Metal Dust Combustion Dynamics &
Novel Concepts of Explosion Protection Application

By

Nicholas Reding

Submitted to the graduate degree program in Chemical and Petroleum Engineering Department and the Graduate Faculty of the University of Kansas in partial fulfillment of the requirements for the degree of Doctor of Philosophy.

_____

Committee Chair: Mark B. Shiflett

_____

Aaron M. Scurto

_____

Alan M. Allgeier

_____

Christopher D. Depcik

_____

Kevin C. Leonard

Date Defended: 22 November 2021

The thesis committee for Nicholas Reding certifies that this is the
approved version of the following dissertation:

Metal Dust Combustion Dynamics &
Novel Concepts of Explosion Protection Application

_____

Committee Chair: Mark B. Shiflett

Date Approved: 22 November 2021

ABSTRACT

Combustible dust explosions continue to present a significant threat toward an extensive range of industries processing, storing, or pneumatically conveying metal dust hazards. Upon ignition within a contained enclosure volume and propagation of flame toward interconnected vessels, metal dust deflagrations demonstrate a reactive explosion risk relative to organic dusts due to well-documented amplified heat of combustion, burning temperature, flame speed, rate of pressure rise, maximum explosion overpressure, and ignition sensitivity.

Addition of non-combustible inert material to combustible dust mixtures, either through pre-mixing or high-rate injection as the incipient flame front begins to develop, is common practice for preventative inhibition or explosion protection via active suppression, respectively. However, inhibition efficiency of suppressant agents utilized for active mitigation is shown to be reliant on comparative explosibility, discrete burning mechanism, and combustion temperature range, and thus may be increasingly variable depending on the fuel in question. For this reason, mitigation of metal powder deflagrations at moderate total suppressed pressures (relative to the overall strength of the enclosure) and at low agent concentrations has remained challenging. This report reviews applicable thermal analytical techniques and large-scale suppression testing in Fike Corporation's 1 m^3 sphere combustion chamber to evaluate the efficacy of multiple suppressant agents for the mitigation of contained iron and aluminum powder deflagrations.

Following ignition of suspended fuel within a primary enclosure volume, propagation of flame and pressure fronts toward upstream/downstream interconnected enclosures may result in devastating secondary explosions if not impeded through an appropriate isolation mechanism. In such an occurrence, accelerated flame front results in flame jet ignition within the secondary vessel, greatly increasing the overall explosion severity. Unlike an isolated deflagration event with

quantifiable reduced pressures, oscillation of pressure between primary and secondary process vessels leads to overpressure that is often unpredictable by conventional prescriptive means. As a supplementary investigation, the authors advocate and demonstrate the use of FLame ACceleration Simulator (FLACS) computational fluid dynamics modeling to provide reliable consequence predictions for specific passive protection application scenarios involving dust explosions within interconnected equipment.

Through recent years, investigations have thoroughly shown the influence of particle size, polydispersity, and chemical composition on dust explosion sensitivity and severity. However, studies characterizing the effect of particle shape (or morphology) on metal dust explosibility are limited and merit further consideration in order to better define the hazard and understand unique allowances for implementation of protection. In this work, high-purity aluminum dust samples of three unique particle morphologies (spherical, irregular, and flake) were examined. Investigations performed in a Kühner MIKE3 minimum ignition energy apparatus and a Siwek 20 L sphere combustion chamber resulted in the direct characterization of explosion sensitivity and severity, respectively, as a function of suspended fuel concentration and variable particle morphology. Such fuel reactivity was modeled as a means of predicting hazardous potential for distinct metal dust processing methods. Applying the shrinking particle theory with reaction and species diffusion limitations, previously reported pressure evolution outcomes were verified through development and implementation of closed-vessel numerical modeling reliant on fundamental mass and thermal balance equations.

Acknowledgments

I must begin by thanking my mentor, Dr. Mark Shiflett. You sparked my graduate career and inspired me to achieve goals I never would have imagined for myself. Nothing has been as rewarding as reaching this milestone, and I can honestly say I would not be here without having had you in my corner – thank you for everything you have done to get us to this point.

Further, I would like to express gratitude to the doctoral program committee members, and to the entire faculty and staff of the Department of Chemical and Petroleum Engineering at the University of Kansas. More specifically, this project recognizes the following individuals: Dr. Michael Branicky at the University of Kansas' Department of Electrical Engineering & Computer Science for consultation on MATLAB script concepts; graphic artist Gilbert Ortiz for the design and creation of remarkable illustrations used for journal cover art and conference demonstrations; and Dr. Olivier Dufaud at the University of Lorraine (France) for his guidance and willingness to collaborate during program development.

Additionally, I would like to acknowledge the contributions from Fike Corporation's remote site staff and combustion lab technicians in executing open-air discharge testing, minimum ignition energy experiments, fuel explosibility analysis, and active explosion mitigation experiments. I gratefully recognize the support of Fike Corporation in providing operational resources, continued project funding, and consent to publish these experimental findings.

Lastly, I would like to thank my family and my wife, Monia, for their love, support, and constant reassurances. You have been my biggest advocates and have given me the strength to overcome any obstacle. I love you all deeply.

Additional Acknowledgements

Table of Contents

List of Figures

List of Tables

Chapter 1: Introduction to Combustion & Unique Metal Dust Hazards

1.1. Recent Metal Dust Explosion Incidents

Metal dust deflagrations continue to pose a critical threat towards plant safety. Upon ignition of a dispersed metal dust cloud containing sufficient oxidizer, serious dust explosions can occur, with extensive loss to life and property. Prominent growth in metal refining, processing, and storage industries demands the development of more effective methods and materials for suppressing metal dust explosions. To fully appreciate the severity of such unpredictable hazards, this work begins with a general review of combustible metal dust deflagration incidents and resultant explosions.

Dispersion and ignition of combustible metal dust clouds constitutes a considerable threat for a broad series of industrial applications, ranging from automotive coatings and electronics to explosives and propellants (Ghanim, 2006). As reported by a Chemical Safety Board (CSB) investigation on combustible dust hazards, there were more than 281 combustible dust incidents within the United States between 1980 and 2005, resulting in 119 fatalities and 718 documented injuries to operating personnel. Due to the heightened ignition sensitivity and reactivity of many metal dust clouds in air, metallic fuels have contributed to a noticeable proportion of these statistics. According to the CSB's tabulation of these occurrences, dusts of metallic nature have accounted for approximately 20% of these 281 explosion incidents (U.S. Chemical Safety and Hazard Investigation Board, 2006). Despite a widened understanding of aluminum combustion behavior, metal dust explosions have continued to exhibit catastrophic intensity through recent years. At the Hayes Lemmerz International-Huntington, Inc. facility in Indiana in 2003, ignition and flame propagation within an aluminum scrap dust collection equipment line led to one fatality and several injuries (U.S. Chemical Safety and Hazard Investigation Board, 2003). In December

of 2010, AL Solutions, Inc. of New Cumberland, WV experienced a severe metal dust explosion following frictional heating within a defective zirconium blender unit, ultimately causing three fatalities and one serious injury (U.S. Chemical Safety and Hazard Investigation Board, 2010). Over a six month period in 2011, the coupled effects of three separate iron powder flash fires and hydrogen explosions at the Hoeganaes scrap metal processing facility in Gallatin, TN resulted in five deaths and three injuries (U.S. Chemical Safety and Hazard Investigation Board, 2011). Described in a comprehensive incident report for 2019, three sieving machine workers were hospitalized in June following self-heating of aluminum powder at a metallic pigment production company in Sweden. Two months later, a producer of atomized aluminum powders and granules in Wales experienced an explosion event leading to two operator injuries (Cloney, 2020). Historically, however, aluminum dust explosions are capable of even greater destruction. Another considerably more devastating incident occurred at an industrial metal polishing plant in Kunshan, China in 2014. Poor plant housekeeping and inadequate isolation techniques led to a succession of consecutive aluminum-alloy explosions and caused 146 fatalities, 114 injuries, and 51 million USD in direct economic losses (Li et al., 2016b).

1.2. Combustion Fundamentals

In the presence of an oxidizer, combustion releases a variety of products depending on the fuel in question. Organic fuel decomposition during oxidative reactions yields predictable products including carbon dioxide, water vapor, and heat. Reaction R1 utilizes a simple sugar complex as an example of an organic dust combustion. Upon ignition under oxygen (O_2), pure metal dusts typically react to produce large quantities of heat and the respective metal oxide component. Reaction R2 utilizes magnesium as a metal combustion example.

$$C_{12}H_{22}O_{11} + 12O_2 \rightarrow 12CO_2 + 11H_2O + Heat \tag{R1}$$

$$2Mg + O_2 \rightarrow 2MgO + Heat \tag{R2}$$
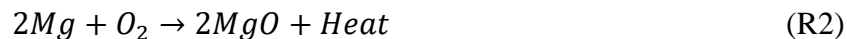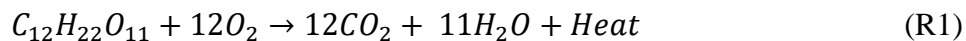
Regardless of the fuel type, in order for an explosion to occur, there are several universal criteria that must be met: (1) combustible dust is present, (2) oxidizing agent is present (O_2 in air), (3) fuel is lofted (dispersed) in suspension, (4) adequate ignition source is available to initiate the reaction, and (5) combustion occurs in a contained enclosure. This concept, also known as the 'Explosion Pentagon', is shown in Figure 1.1. Expanding on these conditions, the fuel concentration must be within the upper and lower explosibility limits, and the particle size distribution must be able to support flame propagation. According to the stoichiometry of the reaction mechanism, the atmosphere must provide sufficient oxygen to sustain combustion. Propagation of the combustion zone (flame front) through the unreacted

Figure 1.1. Explosion Pentagon

medium at a velocity less than the speed of sound is referred to as a deflagration. If allowed to accelerate to velocities greater than the speed of sound, detonation occurs. Deflagration growth within a confined volume is required to produce the pressure effects associated with an explosion. Removal of any one of these five elements is enough to impede initiation of an explosion event.

The combustibility and relative severity of a dust explosion may be assessed from a fuel's experimentally measured explosibility index value, or K_{St}, at stoichiometric burning condition as depicted in Table 1.1.

Table 1.1. Hazard Classifications for Combustible Dust Explosions (Eckhoff, 2003)

K_{St} Range [bar-m/s]	Classification	Relative Intensity
$K_{St} = 0$	St$_0$	Non-combustible
$0 < K_{St} < 200$	St$_1$	Weak
$200 < K_{St} < 300$	St$_2$	Strong
$K_{St} > 300$	St$_3$	Very strong

Scaled by enclosure combustion volume V_{vessel}, K_{St} is directly proportional to the maximum rate of pressure rise as demonstrated by Equation E1:

$$K_{St} = \left(\frac{dP}{dt}\right)_{max} x \ V_{vessel}^{1/3} \tag{E1}$$

The maximum pressure observed during contained, unprotected combustion (P_{max}) represents another explosibility parameter. K_{St} and P_{max} correlate to the combustion kinetics and thermodynamics, respectively, for a given fuel. However, the reader must keep in mind that this cube root law (equation E1) may have limited validity in some cases. Accuracy of results for a certain fuel demand the following to be true: enclosures (test vessel and process vessel in which the fuel is conveyed) must be geometrically comparable, thickness of the flame front must be insignificant in comparison to the enclosure radius, and the burning rate as a function of temperature and pressure must be uniform in all considered volumes. Fuels of the same composition may exhibit varying explosibility due to differences in injection turbulence, moisture content, and effective particle size (Eckhoff, 2003).

Fuel combustion propagation mechanisms are complex and are unsteady in most industrial application settings. Although some metals (such as iron) combust in solely the solid-phase (homogeneous combustion), other metallic flame propagations with extensive heats of combustion and flame temperatures experience multi-phase decomposition. In such a heterogeneous environment, the fuel particulate first begins to absorb energy through conductive, convective, and/or radiative heat transfer methods. Following melting and vaporization of the fuel, the

coexisting phases of the metal particle mix with available oxidizing molecules, leading to ignition and burning of the fuel. Once this fuel source has been exhausted, flame extinction occurs and preheating of subsequent particles begins as the flame front develops further. As observed by Gao et al. (2015), there are two types of flame propagation mechanisms relevant in dust explosions: kinetics-controlled propagation and devolatilization-controlled propagation. Combustion has the potential to transition from one regime to another, depending on variances in bulk volatility or particle size. Metal dust flames are able to propagate via surface reactions, pre-volatilization, or both.

Upon ignition of a suspended dust cloud, metal dust fuels are capable of generating exceedingly high flame temperatures and substantial rates of pressure rise. Reding and Shiflett describe the full extent of the complexities and spontaneity associated with sustained metal dust combustion in a recent review article (Reding & Shiflett, 2018). Taveau further illustrates the distinct combustion characteristics of metallic fuels and comments on the resultant challenges in designing effective explosion protection solutions (Taveau, 2014). As shown in a multitude of extensive comprehensive works, metal dust combustion regimes are considered to be dangerous hazards unless proper prevention and/or protection techniques are established (Eckhoff, 2003; Ogle, 2017). The overarching goal for any plant safety engineer would ideally be to prohibit combustion altogether, effectively eliminating the risk of explosion entirely. With this in mind, Section 1.3 will begin with discussion of methods for explosion prevention for metal dust conveyance processes.

1.3. Review of Current Explosion Prevention Techniques

1.3.1. Housekeeping

The risk of primary explosions within process equipment remains high when the five criteria of the explosion pentagon (shown in Figure 1.1) are met. The initial deflagration event generates a pressure front that can disturb settled dust that has accumulated on the floor and other horizontal surfaces. Once this dust buildup is lofted and ignited, a chain reaction of secondary explosions can occur. One key finding from the hazard study performed by the CSB from 1980 to 2005 was as follows: "Secondary dust explosions, due to inadequate housekeeping and excessive dust accumulations, caused much of the damage and casualties in recent catastrophic incidents" (U.S. Chemical Safety and Hazard Investigation Board, 2006).

Dust layer accumulation has quite an important influence on the amount of dust able to be suspended. According to studies carried out by Eckhoff, a one-millimeter layer of dust with a bulk density of 500 kg/m^3 is capable of generating a 100 g/m^3 dust cloud if fully dispersed through a room five meters in height. Partial dispersion up to only one meter can produce a lofted concentration of 500 g/m^3, as illustrated in Figure 1.2 (Eckhoff, 2003). Based on this analysis, it is clear that it takes little accumulation to reach minimum explosible concentrations if lofted properly. Therefore, suitable housekeeping techniques (such as preventing dust leaks, effectively utilizing dust collection units, and eliminating flat surfaces where dust can collect) are vital towards reducing the risk for secondary explosions.
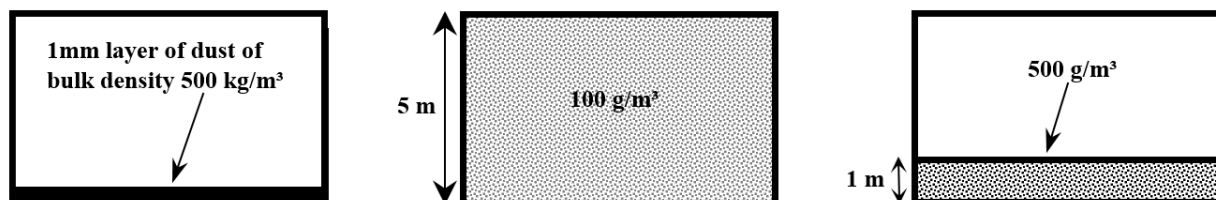
Figure 1.1. Hazard potential for thin layers of dust accumulation

Assuming combustible material cannot be reliably contained within process equipment during operations, the National Fire Protection Agency (NFPA) provides guidance on appropriate strategies to maintain housekeeping standards. For example, NFPA 654 offers direction on preventive housekeeping practices such as recommended cleaning frequency, proper cleaning methods, and requirements for portable vacuum usage (National Fire Protection Association, 2013). According to NFPA 484, however, metal particulate fuels require a more refined approach. In addition to covering the housekeeping measures as depicted in NFPA 654 for organic dusts, NFPA 484 guides the user to refrain from water-based cleaning in areas exposed to alkali or highly reactive metal particulates (National Fire Protection Association, 2015). Even trace amounts of moisture cause concerns when dealing with such materials. Effects of particle moisture content and aggressive reactivity of burning metals with water will be discussed in detail in Section 1.5.3 and 1.6.3, respectively.

1.3.2. Ignition Control

According to the explosion requirements described in Section 1.2, a dispersed combustible dust will only begin to burn once it has been subjected to an ignition source with sufficient energy. Removal of such ignition sources can eliminate the risk of explosions; however, depending solely on ignition source prevention methods is unreliable for fuels with low minimum ignition energies (<10 mJ), as is the case with certain reactive metals. For many hydrocarbon dusts with higher minimum ignition energies, the control of potential ignition sources can have a positive impact on internal risk hazard analysis. Exposure to the following ignition sources can be largely avoided by mandating proper workplace standards and enforcing modifications to existing process operations (Eckhoff, 2003):

- Open flames (smoking, welding, etc.)

- Hot surfaces due to process overheating or inadequate cooling mechanisms

- Self-heating and smoldering nests (porous dust deposits may contain oxidation pockets, generating a high temperature internal reaction zone)

- Exothermic decomposition reactions (release of combustible volatiles)

- Heat produced through mechanical impact (sparks induced by abrupt metal/metal contact)

- Electrical failure and/or electrostatic discharge

Taking precaution regarding the ignition sources mentioned above will not completely guarantee that fire or explosion will not occur. That being said, a firm stance on process safety principles such as grounding all process equipment or establishing intrinsically safe electrical components is nevertheless a noteworthy facet to a thorough prevention design.

1.3.3. Inerting with Non-Flammable Gas

Gas inerting is often utilized as a technique to prevent the formation of an explosive atmosphere by lowering the volume percentage of oxidant within a given operation. Assuming that there are no compatibility concerns between the purge gas and the conveyed process media, introduction of inert gases such as nitrogen (N_2), carbon dioxide (CO_2), or conditioned flue gases into an enclosed process volume can effectively quench the continuance of combustion oxidation reactions. The system should be properly designed to maintain oxidant concentrations low enough that the dust cloud is unable to sustain flame propagation, even if all other criteria of the explosion pentagon are satisfied. The degree to which the oxygen content must be limited is dependent on both the ignition energy provided and the fuel being conveyed. This correlation was studied in further detail by Schwenzfeuer et al. (2001), who developed fitted relationships for limiting oxygen

content (LOC) within an enclosed atmosphere as a function of ignition source capacity and fuel minimum ignition energy (MIE).

As one might anticipate, the severity and sensitivity rise with increasing oxygen content of the gas in which the fuel is processed. This trend continues until saturation is reached, at which point O_2 is in excess. This relationship is presented by Eckhoff for various metal fuels and for organic carbon, as shown in Figure 1.3 (Eckhoff, 2003; Ballal, 1980).
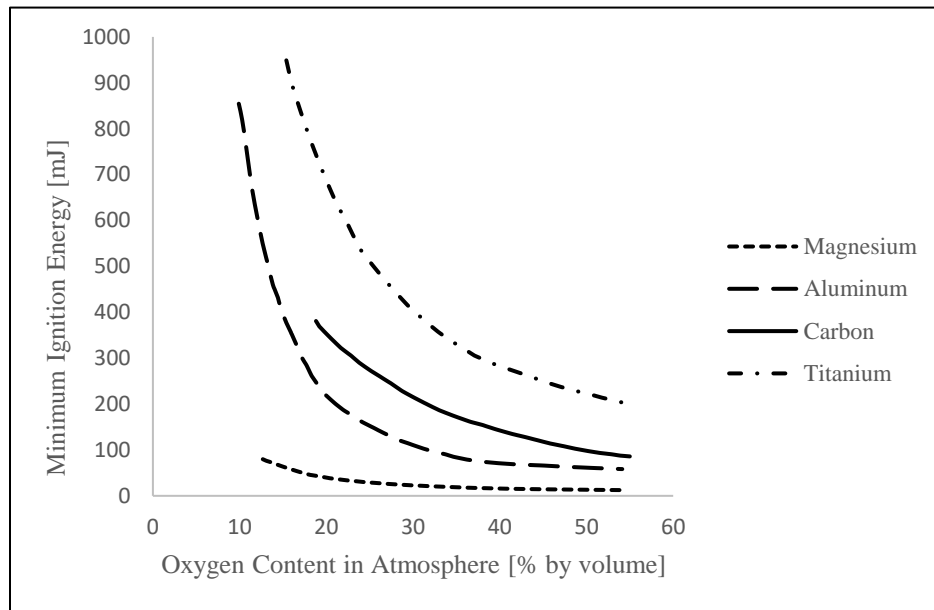
Figure 1.2. Minimum ignition energy as a function of oxygen content for dust clouds of various fuels (mean particle size: 40 µm, initial pressure: 0.2 bar, equivalence ratio: 0.65, MIE defined for 80% ignition probability)

As oxygen content decreases, the corresponding rate of rise of the MIE increases accordingly. The curves for aluminum and titanium most clearly demonstrate this consequence. Oxygen content nears the lower threshold for sustained flame propagation, making the energy requirements of ignition progressively higher.

Despite the clear benefits, gas inerting has some drawbacks. The cost of purchasing the inert gas (or possibly conditioning of pre-existing process flue gas) may be too high to maintain on a large scale. Furthermore, gas inerting may pose unforeseen asphyxiation hazards to personnel in the operations area due to leaks or purges from the process. In addition, the selection of the proper

inert gas for a specific application is another complication to consider. For example, nitrogen gas

is usually appropriate for inerting of aluminum explosion hazards, but rare inert gases such as

argon or helium are required for inerting of magnesium dust to prevent nitride formation. For dust

storage applications with a larger than normal bulk volume (silos, bins, or hoppers), an inert gas

with low permeation may be unsuccessful at preventing the occurrence of internal smoldering

combustion zones (Eckhoff, 2003).

1.3.4. Inerting with the Addition of Non-Combustible Dust

Another form of inerting, known as substitution, involves rendering a combustible mixture

non-ignitable through addition of a non-combustible dust. This process essentially allows for

control of the mixture composition in order to retain non-combustible bulk properties and keep

dust cloud fuel concentrations saturated with solid inertant. If a hazardous material cannot be

completely removed or replaced from the process, this approach could act as a viable alternative.

Completed in a 20 L sphere test vessel, a case study performed by Myers (2008) demonstrated a

significant reduction in ignition sensitivity when flame-retardant material was added to fine

aluminum buffing residue. Ignition sensitivity compares properties of Pittsburgh Seam Coal

(reference material) to properties of the dust in question, as shown in Equation E2:

$$Ignition\ Sensitivity = \frac{[MIExMITxMEC]_{Pittsburgh\ Seam\ Coal}}{[MIExMITxMEC]_{Test\ Dust}} \tag{E2}$$

where MIE represents the minimum ignition energy of a dust cloud, MIT represents the minimum

ignition temperature of a dust cloud, and MEC represents the minimum explosible concentration

of a dust cloud. As noticed by Myers, most impactful on the lowering of ignition sensitivity was

the influence of the flame-retardant additive on the MIE and MIT. Compared to the unadulterated

sample with recorded MIE of 34 mJ and MIT of 350°C, certain fuel/flame-retardant mixtures

yielded MIE and MIT values as high as 452 mJ and 532°C, respectively. However, this analysis was performed on buffing pad residue that was largely organic and contained only trace aluminum content (<10% of the overall mixture). Due to the aggressive nature of metallic dusts, one would expect similar inerting studies on pure metals to return markedly different results. Miao et al. (2016) describes this through investigations of the inerting effect of calcium carbonate on the ignition characteristics (MIE and minimum auto-ignition temperature, MAIT) of metal dusts generated during machining operations. With minimum inerting criteria roughly set at MIE > 1000 mJ and MAIT > 450°C, this study witnessed the effective inerting of Fe alloy and Fe-Al alloy dust using 50% calcium carbonate by mass and the effective inerting of Al alloy dust using 75% calcium carbonate by mass. However, injection of calcium carbonate into pure atomized aluminum, atomized magnesium, or Mg-Al alloy did not demonstrate sufficient increase in MIE or MAIT to qualify successful minimization of ignition risk. Fuels such as aluminum or magnesium are considered highly reactive metals and can be relatively difficult to inert in contrast to normally reactive metal fuels such as irons or other common alloy metals.

An alternate way to exploit non-combustible dusts for the inerting of hazardous metals is to introduce sizeable concentrations of a metal's corresponding metal-oxide, often through mild surface oxidation at low volume percentages of O_2. Oxide content decreases the overall reactivity of the mixture upon potential ignition at a later point by absorbing thermal energy away from a developing combustion. Baudry et al. (2007) demonstrated this through studies confirming the increase in ignition energies of commercial aluminum powder with increasing Al_2O_3 content (increase in oxide content from 0.46 wt % to 6.3 wt % yielded a two-fold rise in required ignition energy). As with aluminum powder, pure titanium can be characterized by comparable explosion severity and sensitivity. Yuan et al. (2014) illustrated the inerting effect of nano-TiO_2 powder on

the MIT of nano and micro titanium dust clouds. The nano metal-oxide inert induced much greater increases in MIT (and equivalent decrease in sensitivity) when mixed with the micro titanium fuel particles. Physical adsorption of the smaller nano-TiO_2 onto the surface of the larger micro titanium particles contributed to limited combustion kinetics by occupying active reaction sites. This substrate inhibition effect was likely not present in the nano-TiO_2/nano-Ti mixtures, as made apparent through minimal increases in MIT even at 90% metal-oxide concentrations.

Studies performed by Bernard et al. (2012) exhibited reduction in flame speed through aluminum dust clouds upon introduction of increasing Al_2O_3 concentrations. The flame velocity experienced an approximate 40% decrease (seemingly linear) when the ignited sample was subjected to mixing with 10 wt % oxide content. A similar effect of decreased flame speed was observed (Gao et al., 2015) for pure 30 µm size zirconium particles coated with iron oxide (Fe_2O_3).

The applicability of chemical suppressants for explosion prevention and suppression of metal dust deflagrations was further investigated by Chatrathi & Going (2000). Monoammonium phosphate (MAP) and sodium bicarbonate (SBC) were ineffective at preventing aluminum ignition, even at minimum inerting concentrations (MIC) as high as 2750 g/m^3. Upon injection of SBC and potassium bicarbonate (PBC) into the combustion test vessel (1 m^3 sphere chamber) following ignition of suspended fuel, aluminum deflagrations (1750 g/m^3 fuel concentration) were suppressed at exceedingly saturated concentrations of agent (average total suppressed pressures as high as 2.08 barg [30.2 psig] at 4.54 kg/m^3 [10 lb/m^3] SBC concentration and 0.035 barg [0.5 psig] activation pressure). The reader should note that pressure is indicated in gauge pressure units, as is common industry practice. Further research is required to properly characterize suppressant agents with greater affinity towards metal dust deflagration suppression. Mitigation of a deflagration through active suppression will be defined in detail within Section 1.4. Understanding

of this topic (explosion protection through mitigation) will be vital toward the experimental analysis performed and discussed within Chapter 2.

These prevention techniques do not come without their disadvantages. Not only does this demand large quantities of what could be a costly inert material, but customers are typically unwilling to sacrifice the purity of their product through contamination with an inert. Depending on the tendency of the fuel to agglomerate, constant attention must be paid to ensure that the inert material and fuel are well-mixed. Differences in particle properties between the fuel and inert substances could lead to significant segregation, leaving some areas exposed to inert concentrations too low to properly impede ignition (Eckhoff, 2003).

Inherently safe process designs demand emphasis on the following key principles: minimization, substitution, moderation, and simplification. For metal dusts especially, institution of such practices requires comprehensive diagnosis of the complexities associated with the hazard in question.

1.4. Inhibitor Properties and Explosion Mitigation Techniques

Inert additives prevent propagation of sustained deflagration through the protected volume via physical or chemical methods. Physical suppressants, such as rock dust, operate by absorbing both thermal and radiant energy from the developing deflagration and by diluting the fuel and oxygen content per unit volume. Energy removed from the ongoing combustion reaction significantly reduces the rate at which unburnt particles are preheated. As the concentration of physical inert increases, the system has less free energy available for unburnt fuel particles to preheat; thus impeding combustion growth and further propagation of the flame front. Depending on the composition of the inhibition material, thermal decomposition may additionally release water and

inert gases (such as carbon dioxide emitted during calcium carbonate decomposition), which act as heat sinks and heighten the physical inerting mechanism. Chemical inhibition implies that the suppressant agent directly hinders the combustion reaction kinetically through disruption of branch chain reactions and detention of free combustion radicals, obstructing standard linear propagation of flame. Certain dry powder suppressant agents, such as sodium bicarbonate and monoammonium phosphate, allow for flame extinction via both physical and chemical means (Chatrathi & Going, 2000).

The efficacy of a dust explosion inhibitor improves with equivalent increase in three key properties of the agent: specific heat capacity, thermal conductivity, and absorptivity (Dastidar et al., 1997). Optimization of these factors allows for increased absorption of the heat and radiant energy generated during combustion, which limits heating of surrounding unburnt fuel particulates. Heat capacity at the particle level is closely related to the characteristics of the inertant chemical composition; however, heat capacity on a bulk scale is directly proportional to the amount of inertant introduced into the application. A higher concentration of inert material within the fuel/agent mixture effectively increases the heat capacity of the system. Thermal conductivity represents the rate at which heat is transferred by conduction through a unit cross-section of a given material, with greater inhibition performance corresponding to increased overall resistance to heat flow. The degree of heat absorptivity is a function of the inert particle surface area, with larger particle surface area promoting greater rates of heat absorption. Surface area itself is a function of both particle shape and size. Irregular, small-sized suppressant agent particles are identified as having greater surface areas. Following analysis of experiments with coal and rock dust mixtures (fuel and inhibitor, respectively) in a 20 L spherical vessel, the authors concluded that decreased suppressant particle sizes yield a reduction in the MIC required to prevent initiation

of oxidative combustion. The aforementioned suppressant properties are applicable to the performance of all solid inhibitors. However, the effectiveness of the material for inerting or suppressive mitigation is also dependent on the properties of the fuel (combustible dust composition, fuel reactivity, particle size, degree of surface oxidation, and suspended concentration). This presents an issue when dealing with reactive metal dust fuels, which commonly exhibit extremely high adiabatic flame temperatures and significant heats of combustion.

In a separate review, Amyotte (2006) discussed complementary parameters influencing the efficacy of non-combustible dusts for the inerting (prevention) or suppression (mitigation) of dust explosions. The variables under investigation included factors representative of the inert material (composition, particle size) and of the application (co-existence of flammable gas, ignition energy, size/geometry of combustion vessel). Even though the large-scale application factors indeed played a role in assessment of the agent's performance, it must be noted that the motivation for this investigation is to examine the effect of material composition on heat of absorption and combustion rate inhibition during fuel oxidation. Inertant powders with varying compositions have fundamental differences in their specific heats, heats of reaction, decomposition temperature range(s), and decomposition rates. As previously mentioned, certain inertant materials with high heat capacities act through physical mechanisms by absorbing thermal energy away from the developing deflagration and restraining continued propagation to other unburnt regions outside of the combustion zone. Depending on the onset of inert decomposition and rate of endothermic decomposition over a specific temperature range, certain inert materials may also exhibit improved performance due to extended "residence time" within the fuel combustion zone. This concept is

the foundation for the theory of chemical inhibition effectiveness, on which much of the subsequent thermal analytical experiments were based (Chapter 2).

Active suppression involves the hindering of deflagration propagation by chemically participating in the combustion reaction and/or physically absorbing heat released from fuel oxidation. Introduction of inert material via active chemical suppression consists of timely, rapid injection of suppressant agent into the protected volume after ignition of the combustible dust cloud has occurred, with the objective of extinguishing the incipient flame front early in the deflagration development, thereby limiting the explosion pressure below the design strength of the vessel. The key stages of suppression system activation can be summarized as follows: (1) Ignition occurs, and the heat of combustion begins to develop pressure within the system. During suppression experiments, full payload of fuel is dispersed into suspension within the contained volume and ignited via chemical igniter. (2) As the deflagration develops, the resultant pressure growth is monitored. Pressure buildup is detected via electronic pressure transducer. Once set point pressures are achieved, system controller triggers high-rate injection and complete dispersion of suppressant agent into the protected volume via responsive opening of a High-Rate Discharge (HRD) container pre-loaded with suppressant and pressurized under nitrogen. (3) The suppressant agent absorbs heat from the developing combustion, quenching the flame front and promptly limiting further pressure growth. Once released into the enclosure, the suppressant agent has primary functions of absorbing heat generated by the incipient explosion and of inerting the unburnt region of the suspended dust cloud. The maximum pressure observed within the vessel during a suppressed deflagration event is reported as the total suppressed pressure (TSP). Explosion protection application design practices require that the TSP be lower than the protected enclosure design strength in order to prevent rupture of the vessel during an event. All powder

loading procedures, HRD container pressurization, and actuation firing mechanism will be discussed in experimental context within Chapter 2 (Section 2.1.1). This technique must be properly designed based on the appropriate capabilities of the hardware (time delay between detection and system activation, injection distribution profile, discharge rate, discharge duration, etc.) and is restricted by its specificity to the application in question.

The measured TSP acts as a direct indicator of the inhibition performance of the suppressant agent during deflagration mitigation and consists of the following components:

$$TSP = P_{act} + P_{N_2} + P_{comb} \tag{E3}$$

where P_{act} signifies the activation pressure (or system response set point) of the detector, P_{N_2} represents the pressure due to injection of nitrogen from the HRD container, and P_{comb} indicates the generation of combustion pressure between system activation pressure and complete extinction of the deflagration.

1.5. Inherent Properties of Combustible Dusts (and their Impacts on Metal Explosibility)

If preventative measures cannot be exercised (or are carried out unsuccessfully), it is crucial that plant engineers fully comprehend the hazards involved with metal dust deflagrations. All combustible dusts have intrinsic properties (propagation behavior, particle size, moisture content) that have the potential to increase the degree of explosibility for that specific fuel. However, the unique presentation of these properties in metal dusts contributes significantly to their complexity and well-developed severity.

1.5.1. Flame Propagation Behavior and Turbulence Effects

The fundamental structure of a particle's propagation mechanism is directly connected to the intensity of its systematic flame growth. For metallic particulates, there are two relevant regions surrounding the particle during combustion: the preheat zone and the combustion zone. The flame propagation pathway through a dispersed aluminum cloud (0.42 kg/m^3 concentration, pure aluminum with a particle size of <18 µm) was experimentally observed by Sun et al. (2006) using high-speed cameras with a microscopic optical system. Based on the results of this study, the burning process of aluminum is depicted as follows. First, the unburnt solid metal particle begins to heat as the oncoming flame front grows near. Once oxidation temperatures are reached, an oxide layer begins to form on the particle surface. As the localized temperature rises further, the solid aluminum particle becomes a liquid/vapor mixture as its melting point is surpassed and the boiling point is approached. The developing vapor phase then positions itself between the liquefied aluminum and the oxide coating. As temperatures continue to increase, prompt liquid expansion within the oxide layer generates pressures and internal stress strong enough to crack the oxide shell. This allows for escape of the vapor phase through the oxidation layer, leading to gas-phase reactions in the combustion zone and an asymmetric burning pattern. This mechanism has significant dependence on combustion temperatures and further qualifies the spontaneity and unpredictability typically associated with reactive metal deflagration propagation. Other noteworthy mechanism proposals for the combustion of aluminum dust are depicted by Puri (2008).

In validation of the aforementioned mechanism by Sun et al., Gao et al. (2017) similarly depicted the flame propagation behaviors of 40-nm titanium, aluminum, and iron dust clouds. Combustion reaction was noted to occur in the liquid phase, gas phase, and solid phase,

respectively. Average propagation flame speeds were obtained as follows: 0.565 m/s for titanium, 0.189 m/s for aluminum, and 0.035 m/s for iron. During liquid- and gas-phase metal particle combustion, the authors noticed the occurrence of "micro-explosions" due to spontaneous interactions with the oxidation products which had formed. Furthermore, through constant pressure combustion, Dreizin & Hoffmann (1999) observed the propagation mechanism for a magnesium dust cloud in a microgravity setting. This study demonstrated the reaction rates within the preheat and combustion zones as having an oscillatory, cyclic pattern; Dreizin & Hoffmann also observed the abnormality of secondary ignition of single-particles following the original propagation.

Combustion duration and flame speed are other factors that illustrate the full profile of a fuel's propagation behavior. In a study by Broumand & Bidabadi (2013), the one-dimensional combustion of micron-sized iron dust was modelled based on energy balances in both the preheat and combustion zones. As a result, correlations for combustion time and flame velocity were derived as a function of particle diameter (combustion time $\propto d^2$; laminar flame velocity $\propto d^{-1}$). In addition, demonstrated within the prior-mentioned study by Sun et al. (2006) is the effect of concentration and combustion time on flame speed during aluminum dust propagation. Assuming that the saturation fuel concentration (above which combustion would have been dampened) had not been reached, flame speed is expected to rise with higher fuel concentrations. Moreover, the flame speed seems to increase exponentially for greater time durations following initial ignition. For applications in which more fuel is available or in which the contained combustion volume is substantial, this could be problematic. In other words, it would take longer for the combustion to run its course, signifying the potential for extremely high flame speeds and amplified likelihood for deflagration to detonation transition (DDT). At the moment at which the flame front catches up with the preceding pressure front, a DDT scenario may result. Deflagrations tend to propagate

through direct heat transfer; on the other hand, detonations propagate by means of pre-compression. Detonations are differentiated from deflagrations due to their devastating properties including accelerated flame speed growth, increased rate of pressure rise, and maximum resultant pressures as high as 20 to 80 barg. Pipeline flame propagation data described by Going & Snoeys (2002) clearly depict the flame speed effects as a function of distance from ignition volume. Commonly transitioning within interconnecting ductwork, deflagrations can easily accelerate to detonation velocities if left unprotected. Ideally, in the absence of effective prevention, an additional solution would be to block propagation pathways via mechanical isolation or timely injection of a chemical suppressant. Further details regarding isolation requirements are described in NFPA 69, the Standard on Explosion Prevention Systems (National Fire Protection Association, 2014). However, large-scale validation testing (activation times, device placement, injection quantities, etc. must be confirmed to provide a stable protection design) is necessary prior to direct application of such guidance to metal dusts in particular.

Turbulence is known to have a prominent impact on deflagration combustion rate. From an application standpoint, internal baffles, partitions, pipeline fittings, and elbows all can act as means of adding turbulence to the system. Completed in a 20 L spherical test vessel, Zhang et al. (2018) illustrated the influence of turbulence and uniformity of dispersion on aluminum powder explosions, as a function of nominal fuel concentration. Agitating the sample within the test vessel prior to ignition, this study revealed direct correlation between turbulence and maximum rate of pressure rise at lower nominal dust concentrations. At higher nominal fuel concentrations, dust dispersion uniformity replaced turbulence as the driving force. Increasing turbulence at higher concentrations often left some localized regions too concentrated with fuel to support combustion, exceeding the upper flammability limit of the aluminum/air mixture. The influence of turbulence

on combustion rate and flame propagation can be modeled analytically. Christill et al. (1989) established a model for the prediction of propagation and pressure growth mechanisms in gas explosions and established the foundation for the development of a comparable model capable of determining effects of turbulence in dust explosions.

1.5.2. Particle Size & Specific Surface Area

Under ideal dispersion conditions, particle size has a primary influence on the overall surface area available for combustive heat generation. As a general trend for most dusts, decreasing particle size demonstrates an inverse relationship with ignition sensitivity and explosion severity. However, for most organics this relationship will not continue indefinitely. Depending on the fuel, there is a limiting particle size below which the dust will not exhibit augmented combustion rate. As described by Eckhoff (2003), the reasoning behind this phenomenon can be illustrated through examination of the steps of a typical organic combustion process: pyrolysis (or devolatilization), gas-phase mixing, and gas-phase combustion. The first step, devolatilization, is considerably influenced by particle size. Yet, if this step were not rate limiting, then further decrease in particle size would have no impact on the overall rate. As described in Section 1.5.1, metal dusts do not devolatilize, but rather exhibit a dissimilar combustion mechanism that encompasses melting, evaporation, and burning of distinct particulates. As a result, the limiting particle size is much larger for organics than for metals. Therefore, further decrease in size of atomized metal powders (or equivalent increase in specific surface area) tends to yield exponential increase in severity parameters such as maximum rate of pressure rise. In Figure 1.4, Eckhoff shows this effect for

silicon/air and aluminum/air mixtures, while allowing for comparison to natural organic materials such as dry starch and protein.
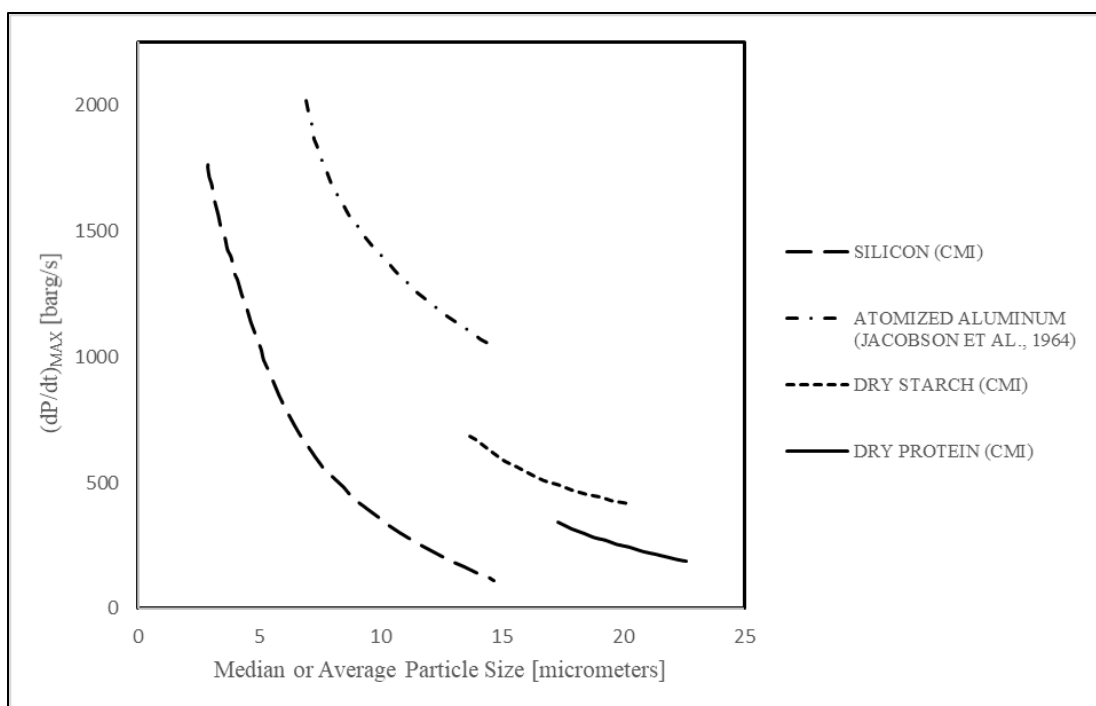
Figure 1.4. Maximum rate of pressure rise as a function of particle size for silicon, aluminum, and organic dust clouds in air; results from Hartmann bomb explosibility vessel (Eckhoff et al., 1986; Jacobson et al., 1964)

Explosibility as a function of particle size was further explored in a research study led by Kadir et al. (2016). Upon testing nano- and micro-sized aluminum particles in a 20 L spherical vessel, the study was able to confirm the increase of K_{St}, MEC, and MIE with decreasing particle size. More notably, this group validated their explosibility testing through transient three-dimensional computational fluid dynamic (CFD) simulations, further supporting their claims of higher turbulent kinetic energy during deflagrations of samples with reduced particle size. Boilard et al. (2013) investigated similar concepts, except through analysis of micro- and nano-size titanium powders. In this study, nano-titanium particles exhibited extremely high ignition sensitivity, demonstrating pyrophoric tendencies (auto-ignition without external ignition source) as soon as the fuel was brought into contact with O_2 concentrations large enough to support combustion.

Krietsch et al. (2015) presented comparable results for a wide variety of metal types, including nano-sized titanium, aluminum, zinc, copper, and iron.

Size alone is not enough to properly define the severity of the hazard. The shape and nature of the dust must also be considered. According to BIA Report 13/97, micrometer-sized aluminum powder has the capability of displaying K_{St} values as high as 1100 barg-m/s, maximum explosion overpressure as high as 12.9 barg, and minimum ignition energies as low as < 1 mJ. In addition, this report collects explosibility parameters for a multitude of other metals and metal alloys of varying particle size, shape, and processing consistencies (Beck et al., 1997). Even aluminum flakes, with a much larger nominal particle size, were able to produce a K_{St} of 600 barg-m/s when utilized in explosion suppression testing investigated by Moore & Cooke (1988).

A variable often overlooked when characterizing the degree of the hazard, dispersity (defined as the heterogeneity of particle sizes in a mixture) can have nearly as dominating of an effect on explosibility as particle size. Centered on a mean size, dispersity represents the magnitude of the full particle size distribution and is pertinent to a majority of dust conveyance applications, in which the particle size of the process media is either unfixed or unknown. Studies by Castellanos et al. (2014a) reported the influence of particle size dispersity on the explosibility parameters (K_{St} and P_{max}) of aluminum dust propagation. At constant mean particle diameter of 15 µm, samples of varying dispersity were prepared and tested in a 36 L explosion test vessel. The sample most concentrated around the mean particle size (lowest dispersity) yielded K_{St} of 179 bar-m/s and P_{max} of 9.15 barg. The sample with the largest dispersity represented an increased explosion hazard, with resultant K_{St} and P_{max} values of 413 bar-m/s and 10.25 barg, respectively. High dispersity in a sample provides increased likelihood for the presence of fine particulates, which

have lower ignition temperatures, and escalates the combustion rate due to their considerable specific surface area.

1.5.3. Moisture Content

In organic dusts, increasing moisture content of an explosible dust powder reduces the ignition sensitivity and explosion severity. As described by Eckhoff (2003), the ability of moisture to inhibit explosibility stems from three major concepts. First, water acts as an inert heat sink, pulling energy away from the developing combustion. Second, upon evaporation the water vapor combines with the pyrolysis vapor allowing for a less reactive mixture in the combustion zone. Third, high moisture content causes the powder to agglomerate together which impedes full particulate dispersion. However, the influence of relative humidity is more complex for metallic dust deflagrations. By examining the impact of aluminum humidity (Case 1) and atmosphere humidity (Case 2) on explosibility, investigations made by Traoré et al. (2009) provide some clarification on these intricacies. As presented by Case 1, results indicate that storage conditions have a detrimental effect on explosion severity. In comparison to dry aluminum powder (median diameter of 7 µm) with a maximum rate of pressure rise of 1530 bar/s, experiments conducted for the same fuel concentration (250 g/cm^3) at 76% relative humidity yielded a maximum rate of pressure rise of more than 2150 bar/s. After treating the aluminum at high humidity for long periods, the water has time to adequately adsorb onto the surface and, upon ignition, reacts with the solid aluminum particle to produce gaseous hydrogen (H$_2$), as demonstrated in Reaction R3.

$$2Al_{(s)} + 3H_2O_{(g)} \rightarrow Al_2O_{3\,(s)} + \ 3H_{2\,(g)} \tag{R3}$$
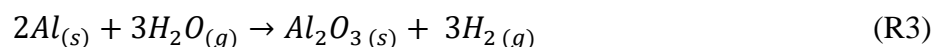
Once the oxide shell is broken (as explained in Section 1.5.1), release and combustion of H$_2$ contributes another fuel source to what is already a reactive metal dust deflagration. In Case 2,

explosion testing of dry aluminum powder was performed with no humidity pretreatment. Instead, the test atmosphere was injected with specific water volumes immediately prior to ignition, with the objective of creating a saturated atmosphere but impeding adsorption of water onto the particle surface. Unlike Case 1, by limiting the water-metal contact time to the explosion duration exclusively (approximately 20 to 70 milliseconds), the explosion severity is significantly reduced. This study saw a decrease in the maximum rate of pressure rise, from 900 bar/s for the dry aluminum powder to 400 bar/s for the aluminum powder in a fully water-saturated atmosphere (0.3 mL in a 20 L sphere test vessel).

These claims were further supplemented through work performed by Bernard et al. (2012). When examining the inhibition effect of partially oxidized aluminum dust, Bernard noticed an interesting phenomenon concerning moisture content. At constant oxide concentration, increases in water concentration from 1.4 to 1.7 wt % coincided with a corresponding rise in flame speed (from 0.25 to 0.30 m/s) and decrease in MIE. Although pre-ignition oxide concentrations generally induce mitigation of the combustion rate, oxides in the presence of saturated water are unable to dampen combustion. On the contrary, increased residual water content within the oxide shell seemed to reflect augmented flame speed and ignition sensitivity.

The above discussion involves elementary properties whose variance reveals an exceptional consequence when dealing with metal dusts. Section 1.6 will explore hazards specific only to combustible metals.

1.6. Hazards Specific to Combustible Metals

Propagation behavior, turbulence, particle size, and moisture content are not the only characteristics capable of enhancing the magnitude of a metal-induced explosion. The following exclusive metal properties qualify metal dusts deflagrations as unique explosion hazards: high heats of combustion, high flame temperature, radiation heat transfer tendencies, and aggressive interactions between water and burning metallic particles.

1.6.1. Heats of Combustion & Flame Temperatures

Heat of combustion represents the energy liberated per mole of O_2 consumed during metal oxidation and combustion decomposition. Assuming the fuel concentration is maintained throughout combustion, the total amount of heat released is directly limited by the presence (or lack thereof) of O_2 within a contained volume. For this reason, standard practice is to scale heat of combustion based on the number of moles of O_2 available to sustain the combustion reaction. Table 2.1 depicts heats of combustion for several of the more common industrial metals. The more reactive metals, such as calcium, magnesium, and aluminum, have heats of combustion as high as 1270, 1240, and 1100 kJ/mole of O_2, respectively. The energy released during the oxidation of these metals is more than twice that of the heat released during combustion of organic fuels (starch at 470 kJ/mole of O_2; carbon at 400 kJ/mol of O_2).

Table 1.2. Heats of combustion per mole of oxygen consumed for common metallic substances (Eckhoff, 2003)

Material	Oxidation Product(s)	Heat of Oxidation (kJ/mole of O_2)
Calcium	CaO	1270
Magnesium	MgO	1240
Aluminum	Al_2O_3	1100
Silicon	Si_2O_3	830
Chromium	Cr_2O_3	750
Zinc	ZnO	700
Iron	Fe_2O_3	530
Copper	CuO	300

The amount of heat liberated during combustion is in direct correlation with the derived adiabatic flame temperature for a given fuel. A constant volume adiabatic flame temperature represents idealistic conditions in which the combustion is complete and in which no internal energy changes occur within the system (in other words, no transfer of heat, work, kinetic energy, or potential energy through the system boundary). As tabulated by NFPA 484, "The Standard on Combustible Metals", maximum adiabatic flame temperatures (in air) for a variety of metals are shown in Table 1.3, with calculations performed by Cashdollar & Zlochower (2007). As a result, aluminum and hafnium exhibit the highest maximum adiabatic flame temperatures (MAFT) of 3790 °C and 4580 °C, respectively.

Table 1.3. Maximum adiabatic flame temperatures for various metals (National Fire Protection Association, 2015)

Metal	Copper	Zinc	Iron	Tungsten	Chromium	Silicon	Boron
MAFT (°C)	1250	1800	2220	2830	2900	2970	3030
Metal	Niobium	Magnesium	Tantalum	Titanium	Aluminum	Hafnium	
MAFT (°C)	3270	3340	3490	3720	3790	4580	

Higher flame temperatures have the tendency to result in larger heat fluxes and signify the thermodynamic potential of a combustion, as previously mentioned. According to ideal gas law relationships, temperature is directly proportional to system pressure. With that said, one could expect a significant rise in maximum explosion pressure (P_{max}) for fuels that display increased burning temperatures. Cashdollar & Zlochower (2007) also compare adiabatically calculated flame temperatures to experimentally determined values. As a general trend, this study noticed that experimental temperatures begin to approach adiabatic temperatures as particle size decreases, revealing that finer metallic samples are more characteristic of intrinsic combustion properties. Increased metal particle volatility and spontaneity of the flame propagation mechanism are a major byproduct of higher flame temperatures.

1.6.2. Radiation Heat Transfer & Harmful Combustion Products

Particle emissivity contributes significantly to the radiative heat flux that exists throughout the combustion zone. As described in experiments by Elsner et al. (1988), the particulate emissivity of solid organic fuels (ash and quartz sand) is complex and dependent on a variety of factors including dust cloud thickness, primary particle specific surface area, solid loading (or dust concentration), adsorption factors, and scatter coefficients.

As demonstrated in Equation E4, the Stefan-Boltzmann law describes the flux of energy (j) radiated across all wavelengths per unit surface area of a black body per unit time:

$$j = k_b T^4 \qquad \text{(E4)}$$

where k_b represents the Stefan-Boltzmann constant. This relationship directly relates radiant emittance to the fourth power of temperature T. Therefore, the influence of radiative heat transfer observed during combustion propagation increases considerably for metals with higher burning temperatures. In a series of qualitative studies by Leuschke (1965), the significance of radiation heat transfer within metal dust clouds was confirmed. In his experimental setup, two transient dust clouds were dispersed at the same time on opposite sides of an insulated double-pane glass window. Upon immediate ignition of one dust cloud, it was observed whether or not the radiation from the ignited dust cloud was sufficient to initiate combustion in the other non-ignited dust cloud. As a result, open-air deflagrations of zirconium, titanium, aluminum, and magnesium generated adequate radiative energy, transmitted through the glass pane, to induce ignition in the other adjacent dust cloud. Primarily dominated by conductive and convective heat transfer mechanisms, low burning temperature metals such as iron and organics (coal) were unable to produce a similar effect. This effectively demonstrates the principal role of radiation heat transfer in combustion growth for high burning temperature metals. As a means of quantifying this concept, Christophe

et al. (2017) designed experiments to effectively measure the radiated flux during flame propagation through aluminum/air mixtures (particle size = 100 µm, fuel concentration = 270 g/m^3, and radiated flux = 40 kW/m^2).

Other groups have investigated this topic from a theoretical, numerical solution perspective. Utilizing a discrete element method, investigations by Moussa et al. (2015) successfully simulate the radiative heat transfer between dust cloud particulates as well as the heat transfer which occurs in the bulk preheat zone. Although some assumptions are made in this methodology (ignition temperature is kept constant; particle motion is ignored; heat generation due to chemical reaction is neglected), the discrete element method presents the basis of what could be a viable alternative for flame propagation modeling of metal dust deflagrations.

The influence of radiation in heat transfer during propagation has been found to be dependent on the scale of the experiment, according to studies performed by Julien et al. (2015). For small-scale studies on ignited aluminum dust clouds, as dust loading increases, there is an absence of equivalent rise in flame speed. This demonstrates negligible effects of radiation heat transfer for small-scale aluminum dust cloud propagation, in which radiation release acts merely as a heat loss mechanism. For large-scale open-air deflagration experiments, the size of the dust cloud is much larger than the effective radiation absorption span, signifying that radiation emitted by the combustion will be sufficiently absorbed by the unburnt metal particles. Along with the effects of localized eddy turbulence, radiative preheating mechanisms contributed to a six-fold increase in flame speed.

Another factor to consider is the toxicity level of the byproducts released during metal fuel decomposition. Unlike organics, which primarily emit carbon dioxide and water during combustion, metal oxidation can produce a wide variety of toxic reaction products. As an example,

several types of magnesium alloys produced in industry contain trace amounts of thorium, a low-level radioactive element. The decay process of thorium (thorium-232 to radium-228 by alpha decay, and radium-228 to actinium-228 by beta decay) is generally isolated within the alloy until the metal is melted or burned. Volatiles of the radioactive thorium are present in the gaseous products released during burning of the alloy particles. Although the half-life of thorium is significantly greater than other more unstable radioactive elements, this factor nevertheless contributes to the severity of lung tissue damage upon inhalation during burning of magnesium alloys (National Fire Protection Association, 2015).

1.6.3. Reactivity with Water

In Section 1.5.3, the discussion was centered around the effect of moisture content on metal dust explosibility. Here, that dialogue is expanded to include discussion of the high reactivity that results when water is introduced to molten metal or pre-existing metal fires. Typically, water on an organic fire will act as a heat sink, depriving heat (and oxygen, if enough water is present) from the ongoing combustion. However, burning metals present a different case in which they react with water at high temperatures to produce explosive volatiles, including diatomic hydrogen. This can lead to violent explosions in a variety of industries, with particular concern in nuclear and metallurgical processes where wet dust collection and water deluge systems are utilized. This was the situation that led to the explosion incident at AL Solutions, as described by the CSB investigation report (U.S. Chemical Safety and Hazard Investigation Board, 2010). In this circumstance, the milling process removed much of the protective oxide coating surrounding zirconium particulates, leading to the exposure of a metal-water interface and promoting increased H_2 formation. Previous risk assessments acknowledged the hazards of water reactivity with

burning metals, but no action was taken to improve housekeeping or challenge the existence of a water-based fire suppression system in the production area.

Studies performed by Wang et al. (2017) demonstrate a viable pretreatment technique to be exploited specifically for wet dust removal applications. Through preparation of the aluminum dust via introduction of dilute chromium potassium sulfate solution, the hydrogen inhibition method (HIM) describes the use of alumina and chromium oxide (Cr_2O_3) inhibition films to successfully prevent the interaction between water and the metallic core. This process treatment procedure offers a relatively inexpensive prevention technique for the inhibition of H_2 formation during wet metal dust removal processes.

Unfortunately, H_2 production is only part of the reason for the violence of this reaction. Although the intensity of the interaction between water and molten metal is not fully understood, *Lees' Loss Prevention in the Process Industries: Hazard Identification, Assessment and Control* describes superheat theories, which serve as a potential explanation (Lees, 2012). Another explanation for the violent nature of such reactions comes from experiments performed by Mason et al. (2015). Using high-speed cameras and molecular dynamics simulation, Mason and his team justify the spontaneity of the heterogeneous reaction between alkali metals (Na/K) and water. Otherwise known as a 'Coulombic Explosion', Mason suggests that instantaneous electron transfer to water molecules leaves an extremely positive alkali ion surface. This instability in charge results in extensive fragmentation of the alkali particle within milliseconds, with increased surface area contributing further to the violent nature of the reaction.

Offering a degree of high-level context for readers, the subsequent section takes a moment to reflect on the organization and relatability of topics to be discussed going forward.

1.7. Scope of Work

Chapter 1 offers a complete analysis of the unique risks and characteristic hazards associated with metal powder combustion mechanisms, in an attempt to provide high-level qualification of the hazards associated to metal powder deflagration propagation. Turning the page to industrial application, current design techniques for reactive metal deflagration prevention and protection rely predominantly on physical heat absorption properties of the inert material. When explosion protection is required, conservative concentrations of suppressant agent are injected into the combustion volume, essentially over-designing the payload of inertant to compensate for the agent's lack of chemical inhibition effectiveness. Selection of inert materials with increased chemical inhibition allows for lower agent concentrations required to achieve equivalent reduced mitigation pressures. Previously executed and analyzed by Reding (2019) [Master's Thesis, University of Kansas], Chapter 2 reviews the examination of unique agent candidates for the suppression of zinc, iron, and aluminum dust deflagrations at both analytical and industrial testing scales. The demonstrated results encourage further research and development of more efficient mitigation solutions tailored to specific metal dust fuel compositions. Prompted by commercial demands for design support, Chapter 3 alternatively explores the application of computational fluid dynamics for consequence prediction of organic dust explosions involving nonstandard interconnected vessels. Persistent with the original theme of metal dust combustion dynamics, Chapters 4 displays the execution and analysis of explosion severity and sensitivity experiments for aluminum powder samples with variable surface morphology. Lastly, applying the experimental explosibility testing performed in Chapter 4, the content of Chapter 5 demonstrates the development and performance of a numerical mathematical model using MATLAB® for the simulation of closed-vessel pressure evolution during contained aluminum dust explosion events.

Chapter 2: Inertant Characterization – Thermal Analysis & Active Explosion Mitigation

2.1. Inerting & Mitigation Studies on Key Suppressant Agent Materials

Sodium bicarbonate (SBC; $NaHCO_3$), potassium bicarbonate (PBC; $KHCO_3$), monoammonium phosphate (MAP; $NH_4H_2PO_4$), diammonium phosphate (DAP; $(NH_4)_2HPO_4$), and sodium chloride (Met-L-X; $NaCl$) were selected as the suppressant agents to be tested analytically. SBC (CASRN 144-55-8) was acquired from Ansul in the form of the suppressant agent "Plus-Fifty C Dry Chemical" (product code 009336), which is primarily composed of SBC with trace amounts of calcium carbonate, attapulgite, and other inert flow-promoting additives. PBC (CASRN 298-14-6) was acquired from Ansul in the form of suppressant agent "Purple-K Dry Chemical" (product code 009335), which is primarily composed of PBC with trace amounts of flow-promoting additives. MAP (CASRN 7722-76-1) was acquired from Amerex in the form of "ABC Dry Chemical Fire Extinguishant" (product code CH555) and contains 90-98% MAP, with trace amounts of inert chemical additives and flow-promoting materials. DAP (CASRN 7783-28-0) was purchased from Parchem at high purity. Met-L-X was also acquired from Ansul (product code 009328) and is composed of 80-90% sodium chloride (CASRN 557-04-0), with trace amounts of a heat-absorbent polymer additive used for desiccation and fluidization of the agent. Decreased particle size yields increased surface area and corresponds to greater inhibition performance of the agent; thus, to eliminate particle size as a potential parameter affecting inhibitor performance, all suppressant agents were ground and sieved to a similar mean size (20 ± 5 µm). Such material pretreatment allowed for adequate consistency in the degree of particle dispersity. Particle size distributions for all suppressant agents were assessed using a CILAS 990 laser diffraction particle size analyzer and are documented within the Appendix (Figures A.5, A.6, A.7,

A.8, and A.9). All relevant statistical data related to suppressant agent particle size are also documented within the Appendix (Table A.1).

2.1.1. Carbonates (Sodium Bicarbonate and Potassium Bicarbonate)

With the use of 20 L sphere testing, Jiang et al. (2018) investigated the effects of sodium bicarbonate particle size on the mitigation and preventative inerting of 5 and 30 μm aluminum dust explosions. This study found a gradual decrease in maximum explosion pressure through increased SBC concentrations and at smaller suppressant particle sizes. For a 5 μm aluminum dust concentration of 300 g/m^3, the MIC of SBC was found to be 1900 g/m^3 and 2100 g/m^3 for suppressant particle diameters of 53 to 75 μm and 110 to 212 μm, respectively. For a 30 μm aluminum dust concentration of 800 g/m^3, the MIC of SBC was found to be 1200 g/m^3 and 1000 g/m^3 for suppressant particle diameters of 53 to 75 μm and 110 to 212 μm, respectively. The inhibition mechanism for sodium bicarbonate occurs in four determinant steps. Firstly, suppressant particles undergo heating due to initiated fuel combustion. Secondly, the agent begins to decompose. Thirdly, gas and solid phase decomposition products are produced. Fourthly, combustion propagation inhibition occurs. The total duration of these four events is designated by t_i. In the case of 5 μm aluminum combustion, since the burning time (t_b) is exceedingly brief in comparison to the aforementioned SBC inhibition process (t_i), particle size reduction had a minimal effect on lowering of the MIC (9.5% decrease in MIC for 5 μm aluminum; 16.7% decrease in MIC for 30 μm aluminum). For situations such as this, in which $t_b \ll t_i$, the inhibition of flame becomes increasingly dependent on thermal mechanisms to account for the relatively slow rate of chemical inhibition modes. Although the chemical decomposition duration may not be optimum for smaller fuel particle sizes, SBC nevertheless appears to play a pivotal function in impeding gas

phase aluminum combustion propagation. For the mitigation of aluminum combustion, the role of SBC in reducing the fuel burning rate is found to rely primarily on thermal heat absorption and oxygen dilution mechanisms. This speculated deficiency in chemical inhibition is expected considering the low-temperature decomposition of sodium bicarbonate (Appendix B; Figure B.1) relative to the high oxidation temperature range and high maximum adiabatic flame temperature (reported at 3790 °C) of aluminum (National Fire Protection Association, 2015).

In another study, Chen et al. (2017) investigated the effect of sodium bicarbonate with varying granulometric distributions (particle dispersity) on 15 μm aluminum dust cloud propagation intensity. Inerting through the addition of suppression agent with wider particle size dispersity yielded limited flame temperatures, destabilized the overall combustion reaction, and inhibited development of the combustion reaction front. Fluctuating suppressant agent agglomeration patterns generated an increasingly non-uniform preheat zone thickness and decreased flame speeds when compared to agents characterized by a specific particle diameter.

Through both burner and 20 L sphere analysis methods, Rockwell & Taveau (2015) investigated the influence of SBC on hybrid flame propagation. In this case, the hybrid mixture under evaluation consisted of 27 μm mean particle size iron powder and gaseous methane-air with an equivalence ratio of one. At fuel concentrations between 25 and 75 g/m^3, this study found a noticeable decrease in turbulent burning velocity and maximum rate of pressure rise upon addition of 27 μm SBC at concentrations between 25% and 75% of the initial iron concentration. During SBC decomposition, the agent effectively interferes with the expansion of the hybrid flame zone by releasing water vapor and carbon dioxide decomposition products, which participate thermally as heat sinks.

Going & Snoeys (2002) examined and contrasted the efficacy of inert powders SBC and PBC for the mitigation of silicon and aluminum metal dust deflagrations using 1 m³ explosion suppression testing. Following explosibility testing at optimum fuel concentration, silicon dust demonstrated a K_{St} of 120 bar-m/s and a maximum pressure developed during a contained deflagration (P_{max}) of 8.16 barg. At 1000 g/m³ suspended silicon concentration, deflagration suppression testing at 0.05 barg activation pressure demonstrated similar TSPs of 0.33 and 0.27 barg for SBC and PBC, respectively, at 2.3 kg/m³ agent concentration. Even at increased PBC concentration of 4.5 kg/m³, results indicate no further enhancement of the suppression performance. On the contrary, the resultant TSP under these conditions increased slightly due to greater injection pressures, implying that the protected volume was fully suppressed at 2.3 kg/m³ agent concentration. Although minimal differences between SBC and PBC suppression performance were apparent for silicon dust deflagration mitigation, the testing for aluminum dust (K_{St} = 300 bar-m/s, P_{max} = 8.50 barg) proved aluminum deflagrations more difficult to suppress but displayed noticeable trends in agent performance. For aluminum dust at 1750 g/m³ fuel concentration (0.05 barg activation pressure), SBC and PBC at 4.5 kg/m³ agent density yielded TSP values of 2.05 barg and 1.25 barg, respectively. Although PBC appears to be more effective at 4.5 kg/m³, both SBC and PBC required higher agent concentration in order to induce complete suppression (at 9.1 kg/m³, TSPs for SBC and PBC were reported at 0.84 barg and 0.89 barg, respectively). For metal dust deflagrations, the TSP correlates strongly with the suspended fuel concentration. Increased heat liberation and pressure generation over the combustion duration require improved physical inhibition (i.e., greater concentrations of suppressant agent) in order to maintain moderate TSPs. On a large-scale application setting, the effectiveness of the agent toward complete suppression of metal dust deflagrations depends on additional factors other than the agent

composition. Bulk material flow limitations such as inverse velocity at specific throw distances, discharge velocity, and injection profile will also exhibit an appreciable influence on system performance and the ability of the agent to suppress deflagrations at higher fuel concentrations (Taveau et al., 2013; Taveau et al., 2015). Aside from this work, PBC has not been investigated as extensively as SBC from an explosion inhibition standpoint; however, it does demonstrate adequate inerting performance when employed as a fire suppressant (Kuang et al., 2011).

2.1.2. Phosphates (Monoammonium Phosphate and Diammonium Phosphate)

Flame retardants containing nitrogen compounds are excellent options for preventative inerting of bulk combustible solids. Nitrogen and nitrogen-phosphorous based solid inertants and their decomposition products exhibit substantially lower toxicity, decreased corrosion, and increased efficiency in comparison to common metallic hydroxide alternatives. The relatively low activity of metal hydroxide flame retardants requires higher minimum concentrations to meet equivalent inhibition performance. Utilized in many polymer and plastic manufacturing industries, nitrogen-based compounds possess high decomposition temperatures, allowing the inert material to be recycled within the process without concern of potential degradation of the physical properties of the polymeric material. Use of halogen flame retardant puts the plastic production process in jeopardy by limiting the potency of polymer stabilizer additives (Horacek & Grabner, 1996).

Studies by Jiang et al. (2018) compared the inhibition of 5 and 30 μm aluminum dust explosions with MAP and SBC. As the concentration of inert material increased, the flame front became increasingly irregular, resulting in restricted flame propagation velocity. At a constant 1000 g/m^3 fuel concentration, MAP exhibited a greater impact on average flame propagation velocity reduction relative to SBC. Flame propagation through a 30 μm aluminum dust cloud was

fully inhibited by addition of MAP at an agent concentration of 1300 g/m^3, while SBC did not completely impede the deflagration until the agent concentration exceeded 2200 g/m^3. Similar performance trends were measured for propagation inhibition through a 5 μm aluminum dust cloud. MAP was able to fully suppress the propagation at an agent concentration of 1600 g/m^3, whereas the minimum inerting concentration for SBC was not obtained, even at agent concentrations as high as 2200 g/m^3. Both agents utilize physical endothermic decomposition within the flame front, absorbing combustion heat used to volatilize nearby particles in the preheat zone. The presence alone of the inert particles within the dispersed fuel/air cloud adds resistance to the direct diffusion of oxygen, blocking further gas-phase single element oxidative combustion. Using kinetic modeling techniques for stoichiometric mixtures of aluminum/air and inhibitor, the authors demonstrated that the MAP inhibition mechanism more effectively competes for oxygen and oxygen radicals, which chemically interrupts the combustive aluminum oxidation and limits temperature rise within the mixture. Luo et al. (2017) examined the effects of ammonia on methane gas combustion dynamics and arrived at similar conclusions regarding the suppressive mechanism of ammonia compounds. For specific volumes of air mixed with of 7, 9.5, and 11 vol % methane, increased ammonia content correlated directly with narrowed fuel explosibility limits, reduced maximum explosion pressures, and decreased rates of pressure rise. Ammonia and amino groups readily consume radicals required to sustain methane combustion due to significantly lower activation energies when compared to methane and methyl group chain reactions.

In other inhibitor inerting investigations, Chatrathi & Going (2000) measured the MIC of SBC and MAP with a variety of fuels. At constant ignition energy and system turbulence, SBC and MAP demonstrated similar minimum agent concentrations required to prevent the development of the flame front (625 g/m^3 and 875 g/m^3 for SBC and MAP, respectively) at the ideal concentration

of suspended cornstarch. However, even at inerting concentrations as high as 2750 g/m^3, SBC and MAP were both unable to prevent sustained deflagration growth upon ignition of aluminum powder at optimal fuel concentration. Despite some accounts of reported ineffectiveness for the mitigation of aluminum dust explosions, MAP demonstrated promise as a candidate for the suppression of iron powder deflagrations, as discussed in the subsequent Section 2.4, through thermogravimetric analysis (TGA) and differential scanning calorimetry (DSC) of iron powder and iron/inhibitor mixtures. Analogous analytical studies on zinc powder combustion directly support claims of amplified chemical inhibition due to alignment of the agent decomposition range with the fuel oxidation temperature range.

Studies by Moore (1996) compared the efficacy of multiple dry chemical powder suppressants, including MAP, SBC, and Dessikarb® (food-grade sodium bicarbonate), for the mitigation of maize dust (K_{St} = 200 bar-m/s) deflagrations via active explosion suppression. At various system activation pressures between 0.05 and 0.3 barg, MAP continued to demonstrate amplified suppression efficiency, as well as equal or lower reduced pressures following complete agent injection into the protected volume. However, tests performed by Amrogowicz & Kordylewski (1991) exposed conflicting conclusions regarding suppression of organic fuels. The effectiveness of MAP and SBC were compared for both inerting and suppression of a variety of deflagration fuels (melamine, wheat flour, wood dust, and coal dust). MAP was found to be more effective for preventative inerting of organic deflagrations, while SBC was more effective for explosion mitigation application.

Unlike MAP, DAP has not been thoroughly studied for either preventative explosion inerting or explosion mitigation. DAP is a suitable fire retardant additive material and shows potential as an effective explosion inhibitor based on its substantial energy absorption capabilities upon

endothermic decomposition to ammonia and water (Camino et al., 1985). Castellanos et al. (2014b) evaluated the efficiency of MAP and DAP for the inhibition of cornstarch combustion propagation using TGA and DSC analytical techniques. Performed under a nitrogen atmosphere and at a 1:1 wt % fuel to agent mixture ratio, analysis of DSC profiles demonstrated that the addition of MAP and DAP limited the heat released during fuel decomposition by 65.5 and 71.5%, respectively. In addition, upon constant heating of the cornstarch and MAP mixture, it was apparent that MAP induced a shift in the onset of exothermic decomposition to lower temperatures, suggesting that this agent may be better suited for explosion mitigation and less appropriate for preventative inerting. Explosibility testing in the 36 L combustion vessel found that DAP yields reduced fuel K_{St} at all inert loading weights/particles sizes and depicted DAP as having greater cornstarch combustion inhibition performance. The amplified heat absorption capacity of DAP can be explained in part by the increased ammonia content released during inertant decomposition in comparison to MAP. The higher vapor pressure of gaseous inert decomposition products generates an oxygen dilution mechanism that reduces the rate of sustained fuel combustion by limiting oxygen diffusion into the flame zone.

2.1.3. Sodium Chloride-Based Suppressant Agent (Met-L-X)

As reported by Zalosh (2008), Met-L-X is a certified Class D fire suppression agent, capable of extinguishing a variety of metal hydride fires. According to NFPA 484, Met-L-X is the preferred extinguishing agent for the suppression of combustible metal fires involving the following pure metals: alkali metals, aluminum, magnesium, niobium, tantalum, titanium, and zirconium (National Fire Protection Association, 2015). Unlike fire suppression agents consisting of water, carbon dioxide, or halogenated material, Met-L-X does not exhibit reactivity concerns when

inhibiting metal hydride fires. Met-L-X is comprised primarily of sodium chloride and a thermoplastic polymer. The polymer additive increases sodium chloride cohesion and allows for more complete agent coverage of the burning metal to prevent further diffusion of oxygen. Many Class D agents such as Met-L-X demonstrate efficiency in extinguishing the initial metal fire; however, they differ in their inability to produce prolonged cooling effects following the preliminary incident, which allows for the possibility of secondary ignition upon reintroduction to the oxidizing atmosphere (Zalosh, 2008). Although it shows prevalence as an effective fire suppression material, sodium chloride has rarely been investigated for use as an explosion suppressant. However, agent decomposition shifted to higher temperatures makes Met-L-X a respectable candidate for aluminum deflagration mitigation due to increased probability for chemical inhibition, as described in Section 2.4.

Cao et al. (2015) explored the influence of NaCl on methane/air explosion suppression using ultrafine water mist in closed vessel combustion experiments. Following addition of 5% NaCl by mass, the water mist suppression technique was noticeably improved due to decreased combustion temperatures within the flame and preheat regions. Additionally, the investigators demonstrated that this consequence ultimately resulted in inhibited reaction kinetics and underdeveloped flame propagation velocities. The presence of sodium and chloride ions within the protected volume actively capture free radicals ($\cdot O$, $\cdot H$, and $\cdot OH$) that would normally participate in the chain reactions of persistent methane explosion propagation, such as the oxidation of carbon monoxide or the generation of water from hydroxide ions.

2.2. Instrument and Experimental Procedure

When appropriately predicting the efficacy of suppressant materials with increased affinity toward mitigation of large-scale flame propagation, two analytical techniques are noteworthy. The first, thermogravimetric analysis (TGA), measures the sample weight change as a function of increasing system temperature. The second, differential scanning calorimetry (DSC), measures the heat flow into or out of the system as a function of increasing temperature. The area beneath a DSC curve indicates the amount of heat released (or absorbed) during exothermic (or endothermic) sample decomposition, which provides an opportunity to quantify the relative capability of compositionally unique inert materials to absorb heat released as a result of metal powder oxidation and to dampen continued fuel combustion.

The use of a TA Instruments SDT Q600 provided simultaneous TGA and DSC measurements from ambient temperature to a maximum operating temperature of 1500 °C. Such measurements were used to predict inhibition viability of the suppressant materials considered in this study, as well as to analyze the combustion characteristics of the candidate fuels. All experiments were performed with ceramic sample pans, under atmospheric pressures, and at a constant heating rate of 10 °C/min. Dust layer thickness for all thermal analytical experiments was maintained below two millimeters to maximize sample exposure to oxygen and to minimize the influence of thermal gradient through the powder. All equipment signals, including TGA weight, DTA baseline, heat flow, temperature, and cell constant, were recalibrated regularly to ensure accuracy of the measurements. Zinc was the metal standard used for all temperature calibrations, and calorimetric precision was confirmed to be within ±2%. Average sample loading weights are provided in Table 3.1, with a fuel to inhibitor mixture ratio held constant at 1:1 by weight. Each mixture trial was thoroughly blended during sample preparation prior to loading; however, the authors acknowledge

non-uniform solids mixing as a potential degree of uncertainty. To account for this, all trials were repeated a minimum of three times to ensure the reproducibility of results.

Heat flow signatures from DSC analysis provide a predictive technique for characterizing the performance of an agent based on its "capacity" to absorb heat. This method was used to rank the effectiveness of the suppressant agents with respect to their ability to absorb heat away from both organic and metallic dust combustion. Before these results are discussed in Section 2.4, subsequent Section 2.3 offers background on the fuel candidates selected for this investigation.

Table 2.1. Average TGA/DSC sample loading weights

Sample Type	Loading Weight [mg]
Inhibitor	10
Fuel	10
Mixture*	20

*Note: Regardless of total sample weight, mixture solids composition was maintained at a 1:1 ratio by weight. Slight variation in total loading weight is acceptable, as all TGA/DSC results are appropriately scaled by mass.

2.3. Fuels under Analysis

Food grade cornstarch $(C_6H_{10}O_5)_n$ was purchased from Ingredion (CASRN 9005-25-8). Cornstarch was selected as the organic fuel for the purpose of establishing a baseline for comparison. Large-scale suppression and preventative inerting results with cornstarch as the fuel are widely publicized in the explosion protection industry. Based on categorized data of existing explosion protection solutions designed by Fike Corporation between 2015 and 2018, greater than 90% of all metal dust active suppression and/or isolation systems involve either iron (steel) or aluminum powder fuels. To satisfy this application demand, pure iron and aluminum powder were thus chosen as clear candidate fuels for the study. Zinc powder was additionally selected as a fuel candidate because its melting and boiling temperatures (420 and 907 °C, respectively) fit well within the maximum temperature limitations of the instrument. However, due to lesser application

demand, zinc powder was utilized for lab-scale analysis exclusively; resources were not available for further large-scale suppression testing with zinc powder. In comparison to normally reactive metal fuels (zinc and iron), processes conveying aluminum powder are considered to be highly reactive explosion risks. Analysis of alloy-type metals was avoided in order to prevent misidentification of the fuel combustion temperature range. Additionally, partially oxidized metals were not considered due to the inert tendencies of a metal oxide (limited contribution toward fuel combustion). Zinc powder (Zn-101; CASRN 7440-66-6), iron powder (Fe-101; CASRN 7439-89-6), and aluminum powder (Al-100; CASRN 7429-90-5) were all purchased from Atlantic Equipment Engineers, a division of Micron Metals, Inc. Prior to explosibility or suppression testing, mean particle sizes for each metal fuel were determined using laser diffraction particle size analysis (CILAS 990). Particle size distributions and statistical particle size results for all fuel powders are provided in the Supplemental Information (Figures A.1, A.2, A.3, A.4, and Table A.1).
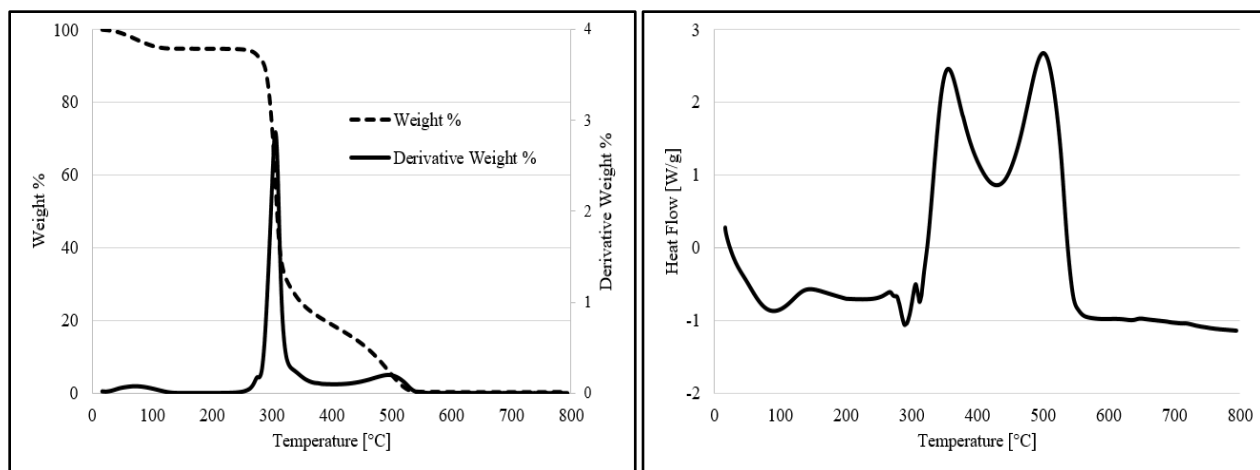
Figure 2.1 (left) & Figure 2.2 (right). Thermogravimetric profile (left) and differential scanning calorimetry profile (right) for cornstarch fuel. Increase in temperature, from room temperature to 800 °C, at a constant 10 °C/min heating rate (in air)

For fuels, the area beneath the exothermic curve measures the quantity of heat released (J/g) during oxidative combustion. This quantity can be obtained through integration of the fuel DSC

signature over the temperature range specific to the fuel combustion zone. For the organic fuel, cornstarch, this combustion region occurs from approximately 250 to 575 °C and is illustrated by TGA and DSC shown in Figures 2.1 and 2.2, respectively. The TGA profile for cornstarch combustion depicts products commonly volatilized during organic fuel decomposition.

The first weight loss peak, at approximately 100 °C, represents the evaporation of water from the sample (1.34 wt % moisture content). Reliant on the dynamic oxygen availability at the reaction surface, the release of complete and incomplete combustion volatiles (CO_2 and CO, respectively) occurs next with maximum derivative weight percentages at approximately 305 °C and 490 °C, accounting for approximately 95% of the total initial sample weight. Integration of the DSC profile over the fixed combustion region for cornstarch yielded 659±41 J/g of heat released during $(C_6H_{10}O_5)_n$ oxidation, relative to 574±14 J/g as measured by Castellanos et al. (2014b).

The zinc combustion mechanism is distinct in comparison to other pure metals, in that flame propagation occurs exclusively in the liquid phase (Poletaev et al., 2018). Therefore, the combustion region of interest for zinc powder can be narrowed to the temperatures immediately succeeding the onset of melting, from approximately 420 to 750 °C, as shown by TGA and DSC analysis in Figures 2.3 and 2.4, respectively.
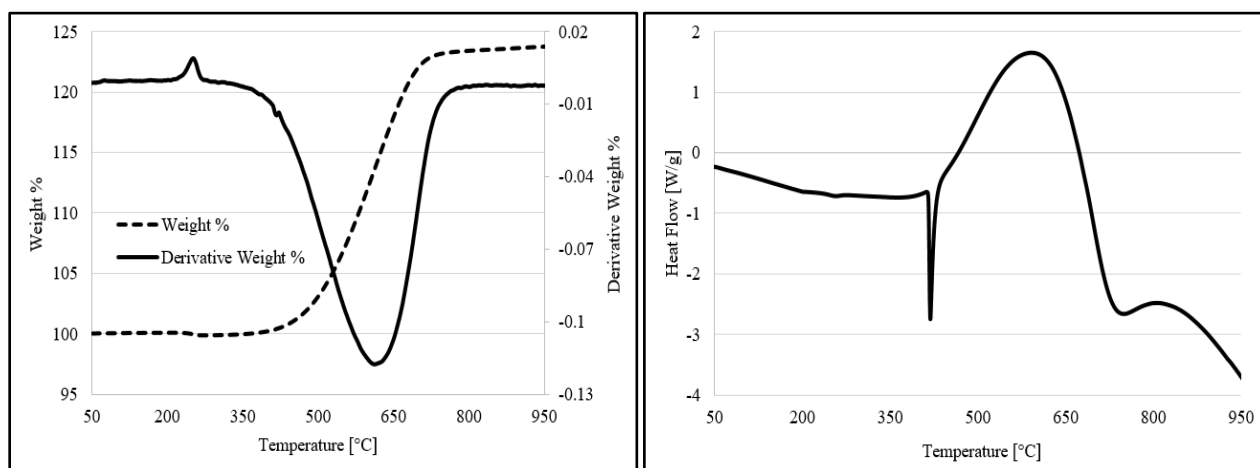
Figure 2.3 (left) & Figure 2.4 (right). Thermogravimetric profile (left) and differential scanning calorimetry profile (right) for zinc powder fuel. Increase in temperature, from 50 to 950 °C, at a constant 10 °C/min heating rate (in air)

Based on the DSC profile, the majority of the heat emitted during oxidation occurs immediately after the endotherm of melting (heat input required for the phase transition), which confirms that zinc combustion takes place in the liquid phase. Following exothermic heat release due to zinc oxidation, the heat flow signature becomes increasingly negative at higher temperatures due to inert material characteristics of metal oxides. The TGA profile for zinc powder combustion indicates sample weight increase during formation of metal oxide, which is characteristic of metal oxidation and aligns directly with the DSC exotherm temperature range. Slight weight decrease, prior to the onset of zinc combustion, occurs at approximately 250 °C and can be attributed to decomposition of trace impurities within the sample. Integration of the DSC profile over the full zinc combustion temperature range yielded 3617±217 J/g of heat emitted during metal oxidation, which is more than five times the energy produced per gram of cornstarch.

The reader might expect the measured explosibility data shown in Table 2.2 to correlate directly with the reactivity and severity of combustion. In other words, augmented explosibility parameters would typically lead one to anticipate an increase in the amount of heat released during fuel combustion. This, however, was not the case. In reality, organic cornstarch exhibited a two-fold increase in the K_{St} during 1 m³ sphere explosibility testing but released five times less energy per gram than zinc powder during combustion. Metal dusts have higher burning temperatures, heats of combustion, and radiation heat transfer rates compared with organic fuels; therefore, the assessment of severity and spontaneity of metal dust propagation using exclusively the explosibility index (K_{St}) is an unreliable means of evaluating overall fuel reactivity potential. The explosibility measurements for iron and aluminum powder fuels are documented in Section 2.8.

Table 2.2. Cornstarch and zinc powder fuel explosibility results at optimum suspended concentration and standard ignition delay, reported via analysis in 1 m³ sphere combustion vessel

Fuel	K_{St} [barg-m/s]	Pmax [barg]
Cornstarch	196	8.48
Zinc	97	5.97

As demonstrated by the iron powder TGA profile in Figure 2.5, sample mass increase due to iron oxidation occurs from approximately 200 to 800 °C (prior to iron's melting point at 1538 °C), verifying that iron is indeed a solid-phase combusting metal (CRC Press, 2005).
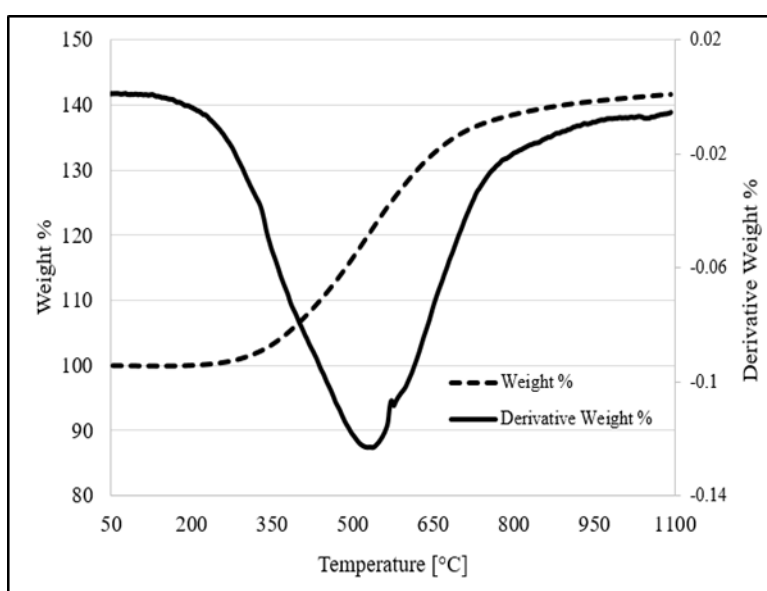
Figure 2.5. Thermogravimetric profile for iron powder fuel. Increase in temperature, from 50 to 1100 °C, at a constant 10 °C/min heating rate (in air)

2.4. Predicted Inhibitor Performances via TGA/DSC

2.4.1. Cornstarch as Fuel

In order to predict the combustion inhibition performance of various suppressant agent inhibitors, 1:1 wt % mixtures of cornstarch and inhibitors were analyzed using TGA and DSC. The heat flow signatures for each DSC profile (Appendix C; Figures C.6, C.7, and C.8) were integrated to calculate the amount of heat released during mixture decomposition. The difference between the heat released by the fuel and the heat released by the mixture directly indicates the

heat effectively absorbed by the suppressant agent. The lower the total heat flow throughout the combustion temperature zone, the more efficient the inhibition during combustion. Prior to integration, all heat flow data were appropriately normalized by treating the cornstarch heat flow signature, before and after the fuel combustion range, as the baseline. The integration results for all cornstarch and inhibitor mixture decompositions are provided in Table C.1. Compared to the heat released during exothermic fuel decomposition (659 J/g), potassium bicarbonate (PBC) mixed with cornstarch exhibited the lowest heat release (-850 J/g) of all five inerting materials tested in this study when integrated from room temperature to 800 °C. The heat absorption performance for sodium bicarbonate (SBC), with a mixture heat release of -184 J/g, was slightly lower compared to PBC.

The DSC profiles for cornstarch and carbonate/cornstarch mixtures are shown in Figure C.6. SBC and PBC display similar behaviors when allowed to decompose in a 1:1 wt % mixture with organic cornstarch. The heat flow profiles for both agent mixtures indicate the release of moisture from cornstarch when heating to 100 °C (endothermic heat flow) and show a catalyzed exothermic mixture decomposition occurring between 250 and 325 °C, which is well before the onset of the characteristic cornstarch combustion range. Not apparent with PBC, the DSC profile for the cornstarch and SBC mixture decomposition produces a secondary fuel combustion step, which corresponds to a narrow, high-magnitude exotherm, at approximately 570 °C. In regard to the way that these agents behave as the mixture degrades, the main difference between PBC and SBC is the slope of the heat signature following the initial heat release for the mixture. For the PBC mixture, a greater negative slope signifies that this inert material has an increased capability to absorb the exothermic heat from the sustained fuel combustion. For higher fuel to agent mixture ratios, the linear segment would be expected to approach a zero slope as the capacity to absorb

additional heat decreases. Confirmed by literature and the corresponding TGA profile shown in Figure B.2, the degradation mechanism for PBC is as follows (Kuang et al., 2011):

$$2KHCO_{3(s)} \rightarrow K_2CO_{3(s)} + CO_{2(g)} + H_2O_{(g)} \tag{R4}$$

$$K_2CO_{3(s)} \rightarrow CO_{2(g)} + K_2O_{(s)} \tag{R5}$$
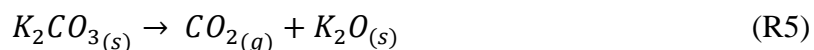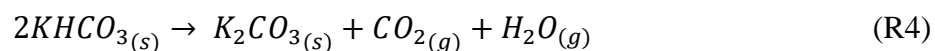
The first inhibitor decomposition step takes place between 100 to 200 °C and produces water vapor and carbon dioxide, which act as gaseous inert heat sinks and offer mass transport resistance by reducing diffusion of oxygen onto the solid surface via dilution. Potassium carbonate (K_2CO_3) is the solid-state material present during the cornstarch decomposition temperature range and has a constant pressure molar heat capacity of 114.4 J/mol^{-1} K^{-1} at 298 K, which is slightly higher than that of sodium carbonate (112.3 J/mol^{-1} K^{-1} at 298 K) and provides potassium carbonate an advantage for thermal inhibition (CRC Press, 2005). The second step involves the dissociation of potassium carbonate at higher temperatures (850 to 1200 °C) into potassium oxide. This decomposition step occurs after the cornstarch combustion temperature range and therefore does not affect the inhibition efficiency of the agent. The mechanism for SBC decomposition is identical to that of PBC, except for the substitution of Na for K.

MAP, DAP, and Met-L-X provided minimal inhibition of cornstarch combustion. The DSC profile for the mixture of cornstarch and Met-L-X (shown in Figure C.8) illustrates that sodium chloride appears to promote intensified exothermic fuel decomposition, with the mixture releasing more heat (986 J/g) than emitted during cornstarch combustion without inhibitor. The inability of these agents to mitigate the fuel combustion may be attributed to the position of their decomposition temperature range. As shown by inhibitor TGA profiles (Figures B.3, B.4, and B.5), the decomposition of these three agents occurs toward the end of the cornstarch decomposition temperature range (or completely afterwards, as in the case of Met-L-X). Principal agent

decomposition at temperatures greater than the fuel combustion temperature range eliminates the potential for chemical inhibition that can reduce free radicals that sustain continued growth of the propagating flame front. In the case of these three agents, the inhibition is primarily physical; inerting relies solely on the heat capacity, thermal conductivity, and absorptivity of the agent but lacks assistance from gaseous volatiles that would normally impede the combustion kinetically.

Oxidation modes for organic fuels are less complex than that of metal powders. Direct overlap of agent and organic fuel decomposition is not always necessary to achieve effective combustion suppression through only physical inhibition. As long as dissociation of the suppressant agent occurs prior to the onset of fuel combustion, inert gas decomposition products have the potential to complement the thermal absorption properties of the agent or of any other solid-state decomposition products. However, metal fuel propagation has more complicated mechanisms of combustion and requires enhanced techniques for inerting, including dependency on chemical inhibition as an effective supplement to standard physical mitigation.

2.4.2. Zinc Powder (Zn-101) as Fuel

Applying the same analytical technique as described in Section 2.4.1, 1:1 wt % mixtures of zinc powder and inhibitors were assessed using TGA and DSC. Similar to the organic fuel/agent mixture evaluation, the DSC profiles shown in Figures C.9, C.10, and C.11 were integrated to yield the effective amount of heat released (or absorbed) during mixture decomposition. Lower heat flow over the combustion temperature zone results in a more efficient the inhibition of the fuel combustion. The DSC peak integrations were performed over the entire liquid-phase zinc combustion range (400 to 750 °C). The cumulative results of these peak integrations are provided in Table C.2.

In comparison to the heat released during zinc decomposition (3617 J/g), suppressant candidates SBC, PBC, and Met-L-X demonstrate limited suppression of zinc combustion due to their predisposition toward physical mitigation (agent decomposition only exists before or after the fuel combustion window). Heat flow signatures for zinc powder mixed with carbonate inhibitors, SBC and PBC, are shown in Figure C.9. The primary mixture combustion exotherm is within the original zinc oxidation temperature range. Physical inhibition (as discussed for SBC and PBC in Section 3.4.1) was effective for cornstarch combustion mitigation, but only slightly reduces the quantity of heat released during zinc powder combustion. The DSC profile for zinc powder mixed with the Met-L-X inhibitor is shown in Figure C.11. The agent appears to catalyze the onset of fuel combustion at lower temperatures and does little to reduce the exothermic heat released during fuel decomposition. Liquid-phase sodium chloride decomposition in the mixture occurred after the metal combustion (between the melting point and 1100 °C), therefore reducing the potential for partial chemical inhibition. The unexceptional efficiency of sodium chloride as a suppressant for zinc combustion relies solely on the thermal absorption properties of the agent, which has a constant pressure heat capacity of 50.5 $J/mol^{-1} K^{-1}$ at 298 K (CRC Press, 2005).

Phosphate-based suppressant agents MAP and DAP exhibit substantially improved suppression performance, reducing the quantity of heat released over the fuel combustion range to 806 J/g and 203 J/g, respectively, as shown in Figure C.10. When the DAP and zinc mixture is heated, the principal exothermic peak is nearly nonexistent, essentially demonstrating full suppression of the fuel oxidation. The efficiency of combustion mitigation can also be assessed by examining the increase in the mass of the mixture as zinc oxide is generated (see zinc/inhibitor mixture TGA profiles, Appendix B). Larger percent mass increase during zinc combustion indicates that the reaction progresses uninterrupted and that the inhibitor is less effective in

dampening the oxidation rate. During combustion, mixtures of zinc fuel with DAP, MAP, SBC, and PBC demonstrate an equivalent rise in mixture mass percent of 4, 7, 9, and 11 wt %, respectively. This trend of increasing sample weight change through the combustion zone correlates well with the increase in heat released (and decrease in inhibition effectiveness), as shown by the integration results in Table C.2. Amplified heat absorption efficiency for MAP and DAP can be explained in part by the corresponding agent decomposition mechanism:

$$(NH_4)_2HPO_{4(s)} \rightarrow NH_{3(g)} + NH_4H_2PO_{4(s)} \tag{R6}$$

$$(NH_4)_2HPO_{4(s)} \rightarrow 2NH_{3(g)} + H_3PO_{4(l)} \tag{R7}$$

$$NH_4H_2PO_{4(s)} \rightarrow NH_{3(g)} + H_3PO_{4(l)} \tag{R8}$$

$$4H_3PO_{4(l)} \rightarrow 2H_2O_{(g)} + 2H_4P_2O_{7(l)} \tag{R9}$$

$$2H_4P_2O_{7(l)} \rightarrow 4H_2O_{(g)} + P_4O_{10(s)} \tag{R10}$$
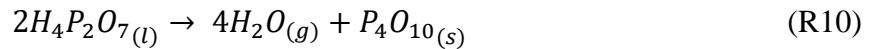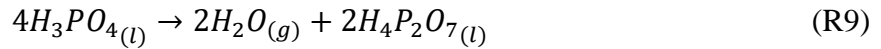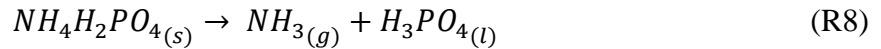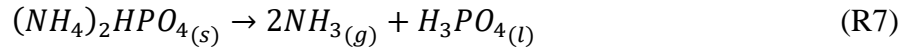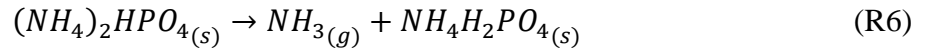
Reaction mechanism steps R6 through R10 are applicable for DAP decomposition, while MAP dissociation occurs exclusively via steps R8 through R10. In comparison to MAP, DAP has a larger constant pressure molar heat capacity (141.4 J/mol^{-1} K^{-1} and 188 J/mol^{-1} K^{-1} for MAP and DAP, respectively, at 298 K) and greater potential for physical heat absorption (CRC Press, 2005; Stephenson & Zettlemoyer, 1994). Both sets of decomposition reactions produce the gaseous ammonia (as per reaction stoichiometry, four times more ammonia generation following DAP dissociation) at concentration below the lower flammability limit, which acts as a buffer against sustained mass and heat transfer on the particle surface. Obstruction of active reaction sites successfully limits diffusion of oxygen, restricting continued fuel particle preheating and volatilization. In industrial prevention or mitigation application, this corresponds to arrested flame temperatures and lower concentrations of oxidant, which thereby introduces significant ignition time delay. However, the ability to inhibit chemically, combined with the aforementioned physical

inhibition characteristics, is what distinguishes the performance of MAP and DAP. The degree of chemical inhibition corresponds to the proximity of primary inert decomposition in relation to the fuel combustion zone. Since the primary agent decomposition (approximately 35% reduction of total sample weight for MAP and 45% reduction of total sample weight for DAP, as supported by TGA profiles in Figures B.3 and B.4, respectively) directly overlaps with the fuel combustion temperature zone (400 to 750 °C), intermediate species of ammonia and amino radicals are actively present to consume oxygen and other free radicals (·O, ·OH, ·H) that would normally prolong fuel propagation. Although these intermediate reactants and products exist in low concentrations due to their relative instability, radical-consuming intermediate reactions compete for oxygen and are nevertheless vital for enhancing the efficiency of chemical inhibition. Unlike the mixture trials containing SBC or PBC, greater availability of oxygen-consuming intermediate reactions during MAP and DAP decomposition allows for reduced oxygen radical concentrations within the reaction zone, resulting in regulated exothermic heat and limited flame temperatures (Jiang et al., 2018). Examples of such transient intermediate mechanisms are shown in Reactions R11 through R15:

$$NH_3 + \cdot OH \rightarrow \cdot NH_2 + H_2O \tag{R11}$$

$$NH_3 + \cdot H \rightarrow \cdot NH_2 + H_2 \tag{R12}$$

$$NH_3 + \cdot O \rightarrow \cdot NH_2 + \cdot OH \tag{R13}$$

$$\cdot NH_2 + O_2 \rightarrow NHO + \cdot OH \tag{R14}$$

$$\cdot NH_2 + \cdot O \rightarrow \cdot NH + \cdot OH \tag{R15}$$

2.4.3. Iron Powder (Fe-101) as Fuel

Preliminary suppression testing on iron powder deflagrations in the 1 m^3 sphere combustion chamber demonstrated nearly equivalent performance for SBC and PBC at the same agent

concentration. Additionally, DAP exhibited poor bulk flow properties upon injection into the combustion volume and lacked functionality on an application setting (minimal agent dispersion results in inadequate flame coverage during system discharge). For these reasons, all continued thermal analysis and eventual suppression testing will utilize SBC, MAP, and Met-L-X as the primary suppressant agent candidates. DSC analysis of iron powder decomposition is overlaid with DSC analysis of iron/inhibitor mixtures in Figure 2.6. Integration of DSC heat flow profiles over the iron powder combustion temperature range (200 to 800 °C) yielded the total heat release during sample decomposition and was performed via analytical techniques, as illustrated in Figure 2.7. Results from the integration of these DSC heat flow signatures are documented in Table 2.3.
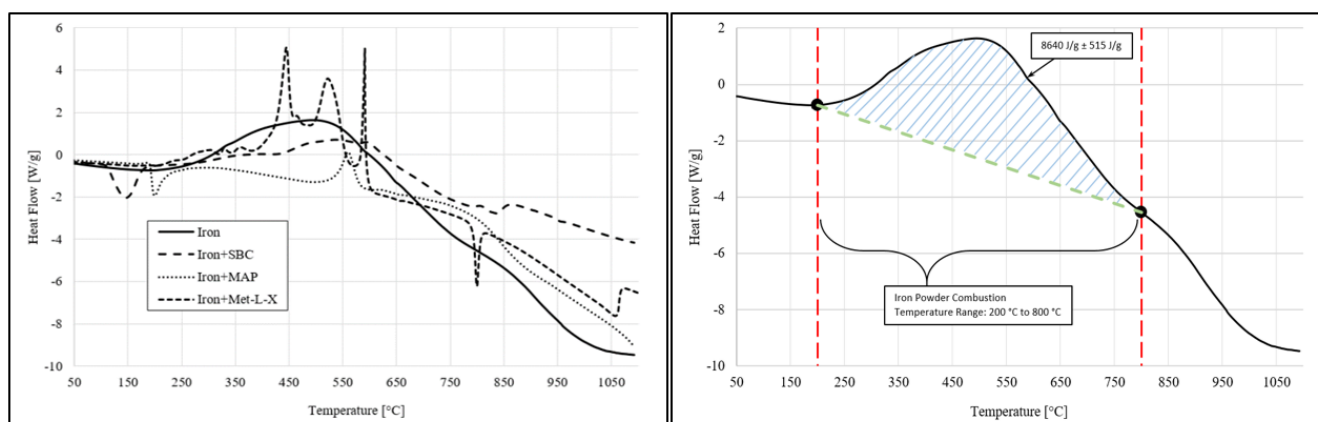
Figure 2.6 (left) & Figure 2.7 (right). Differential scanning calorimetry profile for iron powder fuel and 1:1 wt % iron/inhibitor mixtures (left), and illustration of DSC integration technique (right). Temperature range from 50 to 1100 °C, at a constant 10 °C/min heating rate (in air)

Relative to the heat released during iron powder combustion (8640 J/g), the decomposition of iron/inhibitor mixtures yielded a lower heat release over the temperature range of interest. This consequence is reasonable based on deconstructive interference occurring between exothermic and endothermic heat flow signatures of the fuel and suppressant agent, respectively. The outcome of reduced combustion rate is directly attributable to the degree of physical and chemical inhibition of the inert material. Releasing only 499 J/g through the iron powder combustion range, the

mixture comprised of iron powder and MAP exhibited a substantially improved heat absorption efficiency when compared with suppressant agents SBC and Met-L-X.

Table 2.3. Total heat released per gram of sample during decomposition of iron powder and iron/inhibitor mixtures; integration of Figure 3.6 over the primary iron solid-phase combustion temperature range (200 to 800 °C)

Sample Composition	Σ(Peak Areas within Combustion Range) [J/g]	Average Deviation [J/g]
Fe	8640	515
Fe+SBC	4086	29
Fe+MAP	499	48
Fe+Met-L-X	5649	47

Justification for the increased inhibition efficacy of MAP is hypothesized to be dependent on the extent of overlap between fuel combustion range and the primary decomposition temperature range of the agent. Confirmed through TGA, principal MAP sample mass loss occurs from 500 to 750 °C, directly atop the iron powder combustion region (see TGA profile for MAP, Appendix B; Figure B.3). Such overlap is hypothesized to prompt an amplified chemical inhibition effectiveness due to increased competition for radical intermediates, which would otherwise stimulate continued fuel combustion, by transient MAP decomposition reaction intermediates such as NH_3 or $\cdot NH_2$ (Reding & Shiflett, 2019). Primary endothermic agent decomposition of SBC and Met-L-X, however, occurs outside of the iron powder oxidation window, as confirmed through suppressant agent TGA profiles (Appendix B; Figures B.1 and B.5, respectively), such that the agents are able to operate solely through physical inhibition mechanisms as a result of their solid-state heat capacity and dilution of oxygen content near the fuel particle surface.

2.4.4. Aluminum Powder (Al-100) as Fuel

Similar techniques for the prediction of suppressant agent performance were not possible for aluminum powder fuel due to the high fuel particle burning temperature. Met-L-X (sodium

chloride) decomposes at high temperature in the liquid phase, from approximately 800 to 1000 °C (see the TGA profile for Met-L-X; Appendix B, Figure B.5), and is hypothesized to exhibit improved flame extinction effects during aluminum deflagrations. The shift of agent decomposition toward temperatures closer to high temperature aluminum powder combustion offers an increased likelihood for chemical inhibition effectiveness via introduction of transient sodium and chloride ions. However, such hypotheses were not verifiable through TGA and DSC analysis, as was done with iron powder and iron/inhibitor mixture samples. Figure 2.8 shows partial TGA/DSC of aluminum powder sample under air, carried out on a NETZSCH STA 449 F5 Jupiter simultaneous thermal analyzer equipped with a SiC furnace capable of operating from 25 to 1600 °C.
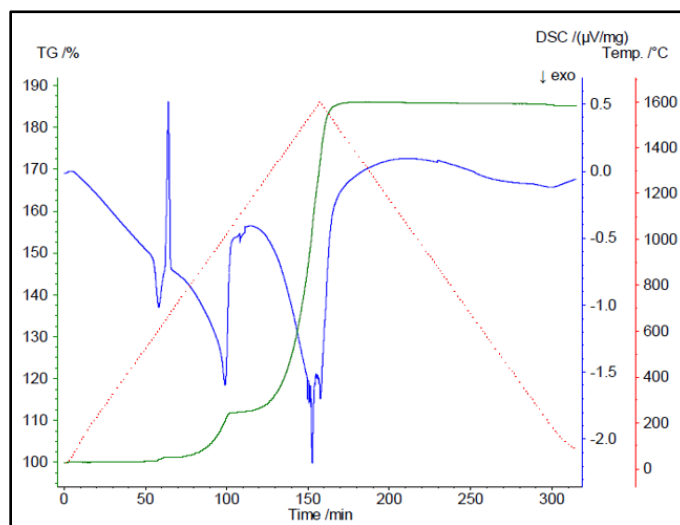
Figure 2.8. Simultaneous thermogravimetric analysis and differential scanning calorimetry profiles for aluminum powder fuel. Temperature range from 25 to 1600 °C, at a constant 10 °C/min heating rate (in air). Results courtesy of NETZSCH testing facilities

Primary sample heat release begins within the liquid phase, following the endotherm of melting at 660 °C (CRC Handbook of Chemistry and Physics, 2005). The sample exhibited three mass gain steps totaling approximately 71% when heated at a constant 10 °C/min rate. All mass gain rate peaks coincide with DSC exotherm peaks at 604 °C, 1017 °C, and 1553 °C. However,

instrument operation up to only 1600 °C was unable to reveal complete sample oxidation; thus, the analysis of aluminum and inhibitor mixtures would not exhibit usable data since higher-temperature liquid- and vapor-phase exotherms are not visible.

2.5. Analysis of Suppressant Decomposition Products via Mass Spectrometry

Prior to suppression testing on a large scale, appropriate measures were taken to assess the toxicity concerns associated with heating a substantial quantity of metal/inhibitor mixture to high burning temperatures. To appropriately identify the agent decomposition volatiles, TGA-DSC experiments were performed, with evolved gas analysis via mass spectrometry (MS). All samples were measured on the NETZSCH STA 449F1 Jupiter thermal analyzer coupled with the NETZSCH QMS 403 Aeolos mass spectrometer. All MS ion-current curves are shown in Appendix D. Such curves for thermal decomposition of SBC under air are displayed in Figure D.1. Evolutions at mass numbers 18 and 44 can be attributed to water (H_2O: MW – 18) and carbon dioxide (CO_2: MW – 44), respectively. Both of these peaks show utmost intensity during the initial decomposition of sodium bicarbonate at approximately 150 °C. Carbon dioxide is evolved at higher temperatures (maximum peak intensity at 669 and 1147 °C) during the secondary decomposition of sodium carbonate. Mass numbers of fragmented ions associated with water (mass number 17) and carbon dioxide (mass number 12) are also present on the MS curve profile. This evolved species analysis aligns directly with literature proposed decomposition mechanism shown in Reactions R16 and R17:

$$2NaHCO_{3(s)} \rightarrow Na_2CO_{3(s)} + CO_{2(g)} + H_2O_{(g)} \tag{R16}$$

$$Na_2CO_{3(s)} \rightarrow CO_{2(g)} + Na_2O_{(s)} \tag{R17}$$
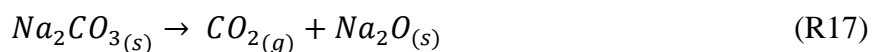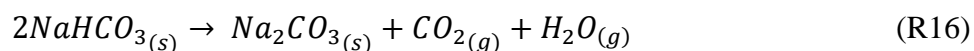
MS ion-current curves for thermal decomposition of Met-L-X under air are displayed in Figures D.2, D.3, and D.4. As with SBC decomposition, thermal degradation of Met-L-X releases CO_2 and H_2O, with greatest peak intensity at multiple temperatures below 600 °C (see Figure D.2). The TGA and associated MS curves for mass numbers 35, 36, 37, and 38 are plotted in Figure D.3. The most probable evolutions attributed to these mass numbers are hydrogen chloride (HCl: MW – 36) and its associated fragmented ions. HCl evolution reaches maximum peak intensities at approximately 270 and 1100 °C. The TGA and associated MS curves for mass numbers 70, 72, and 74 are plotted in Figure D.4. The most probable evolution attributed to these mass numbers is chlorine (Cl_2: MW – 70), or other isotopes of chlorine. Chlorine evolution reaches maximum peak intensity exclusively at the high temperature degradation region (1100 °C), during which approximately 90% of the sample weight loss occurs.

MS ion-current curves for thermal decomposition of MAP under air are displayed in Figures D.5, D.6, and D.7. The TGA and associated MS curves for mass numbers 15, 17, 18, and 19 are plotted in Figure D.5. The most probable evolutions attributed to these mass numbers are H_2O and ammonia (NH_3: MW – 17), as well as accompanying fragmented ions, with maximum peak intensities occurring at 215, 350, and 455 °C. The TGA and associated MS curves for mass numbers 30 and 44 are plotted in Figure D.6. The most probable evolutions attributed to these mass numbers are nitric oxide (NO: MW – 30), nitrous oxide (N_2O: MW – 44), and fragmented ion nitrogen dioxide (NO_2: MW – 30), with trace quantities evolving between 200 and 600 °C. The TGA and associated MS curves for mass numbers 35, 36, 48, and 64 are plotted in Figure D.7. The intensities of these evolutions are trivial relative to other evolved species. The mass numbers can likely be attributed to the species HCl and sulfur dioxide (SO_2: MW – 64), as well as the related fragments of these components. Both SO_2 and fragmented ion SO_2 (mass numbers 64 and 48,

respectively) show maximum peak intensity at 390 and 475 °C. Both HCl and fragmented ion HCl (mass numbers 36 and 35, respectively) show a slight increase in MS signal intensity above 800 °C. Although monoammonium phosphate contains no single molecules of chlorine or sulfur, it is likely that trace quantities of these evolved species are introduced via thermal degradation of the chemical additives and flow-promoting materials present within commercially acquired MAP. The mass loss step at approximately 600 °C does not seem to correlate with a particular mass number intensity change, signifying that the evolved species (likely a form of phosphorus oxide based on original sample composition) may have condensed to liquid phase despite a heated transfer line integrating the TGA with the MS. This evolved species analysis can be compared with the literature proposed MAP decomposition mechanism shown in Reactions R8 through R10.

With hazards appropriately identified, agents are ready for suppression testing on a large scale using a 1 m^3 combustion sphere. The 1 m^3 combustion sphere is allowed to cool to equilibrium following explosibility or suppression testing, and an open exhaust line provides for sufficient ventilation of potentially harmful fuel and agent decomposition products. To maintain personnel safety, use of respirators was required for post-test inspection of combustion chamber internals. Further detail on experimental configuration is introduced in Section 2.7.3.

2.6. Kinetic & Thermodynamic Assessment of Fuel Combustion via DSC

Estimation of the kinetic parameters for the exothermic combustion of cornstarch, zinc, and iron is necessary for understanding of the spontaneity of these fuel decomposition reactions. Aluminum powder combustion was excluded from this assessment, as the full aluminum oxidation temperature range was not visible during DSC analysis up to 1600 °C (discussed in Section 2.4.4). According to ASTM E698 (2001), the relationship between fluctuation in heating rate and

corresponding shift in exotherm peak temperature can be used to approximate the Arrhenius kinetic constants for thermally ignitable materials. To apply this standard, the combustion reactions of cornstarch, zinc, and iron were assumed to follow first-order reaction kinetics. For all fuels, multiple DSC profiles were compiled at heating rates (β) of 5 °C/min, 10 °C/min, 20 °C/min, and 30 °C/min, and the maximum exotherm peak temperatures T_{MAX} were recorded. Cornstarch decomposition consisted of two primary peaks along the exotherm, while zinc and iron powder decomposition each consisted of a single primary peak along the exotherm, as shown by DSC in Figures 2.2, 2.4, and 2.6, respectively. Based on these consolidated data sets, plots of $-ln$ $(\beta/T_{MAX}{}^2)$ versus $1/T_{MAX}$ were created for each exotherm peak. The data were fitted with a linear trend line, and the activation energy E_a for each decomposition peak was determined using the slope, as shown below in Equation E5:

$$slope = -\frac{E_a}{R} \tag{E5}$$

where R is the gas constant. The assumption of first-order kinetics was confirmed based on the linearity of the data points. The pre-exponential factor A was calculated using Equation E6 as described in ASTM E698:

$$A = \beta \frac{E_a}{RT_{MAX}^2} e^{E_a/RT_{MAX}} \tag{E6}$$

The rate constant k as a function of system temperature can be calculated using the activation energy and pre-exponential factor, as shown in Equation E7. This analysis assumes that rate constants are measured in the absence of both internal and external mass transfer limitations.

$$k = Ae^{-E_a/RT} \tag{E7}$$

Once rate constant correlations were established for each exotherm peak, transition state theory and the Eyring-Polanyi equation (Equation E8) were utilized, in which k_B and h_{Planck} represent

the Boltzmann's constant and Planck's constant, respectively (Eyring, 1935). A plot of $-ln$ (k/T_{MAX}) versus $1/T_{MAX}$ was generated for all exotherm peaks. Following linear fitting of the data, the slope was utilized to determine the enthalpy of activation ΔH, and the y-intercept was utilized to determine the entropy of activation ΔS.

$$ ln\left(\frac{k}{T_{MAX}}\right) = -\frac{\Delta H}{R}\frac{1}{T_{MAX}} + Ln\left(\frac{k_B}{h_{Planck}}\right) + \frac{\Delta S}{R} \qquad \text{(E8)} $$

The Gibbs free energy of activation ΔG for each decomposition peak can then be calculated using the following fundamental thermodynamic relationship:

$$ \Delta G = \Delta H - T\Delta S \qquad \text{(E9)} $$

A positive value for Gibbs free energy of activation represents an endergonic reaction, in which the system requires an input of energy. In a dynamic combustion environment, larger values for ΔG signify a product-favored reaction and would promote flame front propagation and heating of surrounding particles. The activation entropy describes how energy must be redistributed through the molecule before reaction initiation is able to occur. Molecular geometry, orientation in space, and quantity of viable degrees of freedom exhibit substantial influence on the entropy of activation. Transition state theory offers explanation for rates of elementary reactions by assuming quasi-chemical equilibrium between reactants and higher-energy activated transition state complexes (Eyring, 1935; Evans & Polanyi, 1935). In support of this concept, activation enthalpy signifies the change in enthalpy from the initial reactant state to the reactant-product hybrid transition state and is typically comparable in magnitude to the activation energy. Higher values of activation enthalpy and activation energy indicate a reduced reaction rate, as is the case for the second peak in cornstarch decomposition (see DSC profile, Figure 2.2). This peak represents incomplete combustion and leads to formation of carbon monoxide due to insufficient presence of oxidizer and poor mixing of the fuel/air interface. Utilizing methodology from ASTM E698 followed by

application of the Eyring-Polanyi equation, kinetic parameters and thermodynamic state functions were modeled for all fuel combustion peaks. Results are shown in Table 2.4 and may be compared with similar analytical investigations by Huang et al. (2014).

Table 2.4. Calculated activation energies and thermodynamic state quantities for cornstarch, zinc, and iron powder combustion; values derived from analysis of DSC heat signatures by means of the technique documented within ASTM E698 and through utilization of the Eyring-Polanyi Equation

Fuels	E_a [kJ/mol]	ΔH [kJ/mol]	ΔS [J/K/mol]	ΔG [kJ/mol]
CS Peak 1	20.4	21.2	-217.1	167.8
CS Peak 2	60.3	60.5	-149.6	179.4
Zinc Powder	41.9	41.5	-207.5	232.0
Iron Powder	32.4	26.4	-236.8	243.8

Other modelling techniques can be additionally employed to assess the degree of combustion rate control by diffusion and kinetics. The shrinking particle model is commonly utilized for simplistic non-catalytic irreversible first-order reactions between solid fuel and surrounding gas film. Another more complicated technique, known as the shrinking unreacted core model, assumes that a reaction front moves from the surface through the solid particle interior and leaves behind a permeable product layer. Unlike the previous model which only considered the chemical reaction rate and diffusion of oxygen through the gas film boundary, the shrinking unreacted core model takes diffusion through a porous product layer (between the gas film and unreacted solid core) into account as well. Depending on the combination of transport and kinetic resistances, a principal aim of these models is to establish correlations for fuel burnout time. From an application standpoint, longer particle burning durations may require extended suppressant agent discharge, such that the inertant injection continues for the entirety of the fuel combustion. These considerations are crucial to large-scale mitigation designs, especially when suppressant agents of varying packed densities tend to exhibit unique dispersion rates and cloud profiles.

2.7. Large-Scale Mitigation - Experimental Objectives and Procedures

2.7.1. Foreword

Metal dusts explosion hazards continue to present a significant threat in a wide variety of process industries. Utilizing the DSC heat flow signature of pure metal fuel sample as a baseline, peak integration analysis showed that the 1:1 wt % mixture of ammonia-based agents (DAP and MAP) with zinc and iron metal powder samples had the greatest reduction in exothermic heat release compared to other suppressant agent materials tested. Significant endothermic DAP and MAP decomposition (>30% of initial sample weight) occurs over the same temperature range during which zinc and iron oxidation takes place. Similar principal decomposition temperature ranges for the fuel and agent provide greater potential to inhibit combustion chemically through consumption of free radicals that would ordinarily sustain ongoing fuel propagation. The results of this study support the need for explosion protection design solutions which exploit particular suppressant materials uniquely tailored toward specific fuel types.

The overlap of fuel and agent decomposition temperature range increases the inhibition effectiveness of the agent and brings industrial applications closer to a refined solution for preventative inerting and active explosion mitigation. An increase in chemical inhibition moderates the necessity for physical (thermal) inhibition. For deflagration mitigation through active suppression, this corresponds with lower agent concentrations required to achieve tolerable (relative to equipment design strength) suppression pressures after system activation. If performance can be maintained by using reduced quantities of inertant material and fewer hardware components, this offers a less expensive and thus more attractive option for customers conveying reactive metal dusts. Currently, active suppression designs for metal dust fuels

commonly utilize SBC at high concentrations, attempting to compensate physically for the agent's lack of chemical inhibition capability.

The notion of heightened chemical inhibition due to overlap of the decomposition temperature range may be applicable to other more reactive metal fuels. Aluminum powder displays a progressively complex and spontaneous combustion mechanism due to failure of the particulate oxide shell at measured ignition temperatures as high as 2100 °C (Beckstead, 2002). As demonstrated in the TGA profile for Met-L-X (Appendix B, Figure B.5), sodium chloride decomposition is shifted toward higher temperatures (800 to 1000 °C), amplifying the probability for chemical inhibition during high-temperature aluminum powder combustion. Inhibition materials best-suited for mitigation of iron and aluminum fuel propagation has been examined further through suppression testing in Fike Corporation's 1 m^3 combustion sphere. Results and discussion pertaining to this effort are presented from this point through the end of Chapter 2. Emphasis on agents with anticipated performance, as predicted from thermal analysis, allows for a more intensive suppression test program. Thus, continued large-scale testing has been performed to assess the efficacy only of suppressant agent candidates SBC, MAP, and Met-L-X.

Material flow properties such as gas permeability, bulk density, cohesiveness, floodability, and compressibility are important characteristics to consider for effectively dispersing agents into the protected volume during high-rate pressurized injection at the onset of deflagration development. Although DAP appeared to exhibit optimal anticipated mitigation performance for mid-range oxidation metals, it does not demonstrate ideal bulk flow characteristics. From an application standpoint, limitation in agent discharge velocity is likely to either put system response time in jeopardy or reduce the rate of agent concentration provided during injection. Suppressant agents SBC, MAP, and Met-L-X seem to demonstrate adequate bulk fluidization with no concerns of

material agglomeration. However, such qualitative observations has been confirmed prior to active suppression experiments. Results pertaining to open-air dispersion testing and high-speed videography analysis are presented in the coming sections.

As described in NFPA 69, active explosion suppression designs shall be based on the following key factors: time required for detection, suppressant discharge pattern, suppressant concentrations as a function of time (injection duration), suppressant efficiency, explosibility of the combustible material, and physical characteristics of the protected enclosure (National Fire Protection Association, 2019). A majority of these variables are limited by the hardware of the explosion protection system manufacturer or by the application in question, but the fourth item in this list (suppressant efficiency) is predominantly dependent on physical and chemical inhibition capacity of the suppressant material, which is the primary focus of this study. In light of costs and escalating doubts surrounding the scalability of sphere explosibility and inerting testing, this work offers a novel analytical technique for characterization and screening of suppression agents based on efficiencies predicted through integration of fuel and fuel/agent mixture DSC heat flow profiles (Cashdollar, 2000; Dastidar, 2004).

2.7.2. Open-Air Dispersion Testing

Suppressant materials of different chemical composition have the potential to exhibit significant variation in physical properties such as cohesiveness, gas permeability, bulk density, compressibility, and floodability. When injected into an open volume under high pressure, these characteristics can often correlate to fluctuating dispersion profiles, flow distributions, and discharge velocities. Before utilizing new inhibitor materials in a contained volume for the mitigation and extinction of developing deflagrations, open-air dispersion testing is necessary to

validate the injection performance of all three suppressant agents (SBC, Met-L-X, and MAP). If a particular agent does not meet expectations during suppression testing, it may be difficult to decide whether the cause is limited dispersion during injection or poor inhibition effectiveness. Open-air discharge testing beforehand will eliminate such doubts. To fairly evaluate suppression data, open-air dispersion shots are required to ensure that the plume of injected inhibition material behaves similarly for all three agents under analysis, with SBC acting as the benchmark for comparison.

A total of six tests were performed, with two identical tests for each agent to confirm repeatability of discharge performance. A 10 L high-rate discharge (HRD) container was utilized for all experiments to retain a uniform agent delivery rate. To maintain equivalent nitrogen headspace volume in all tests, a constant powder volume of 6.8 L was charged into the container. Based on the measured packed densities for all materials (Appendix E, Table E.1), this volume coincides with fill weights of 9.07 kg, 5.90 kg, and 4.08 kg for SBC, Met-L-X, and MAP, respectively. Once loaded with powder and sealed, the HRD container was mounted onto a custom-built test gantry at a firing angle of 45° and pressurized with nitrogen to 900 psig (62.1 barg), which served as the primary driving force for high-rate discharge of suppressant agent through a Fike standard spreader nozzle assembly. The container was equipped with a pressure transducer to measure the pressure inside the HRD headspace as a function of time following system activation. Vertical and horizontal markers with one foot spacing increments were positioned in front of the gantry and are necessary when calibrating high-speed experimental software utilized during post-test videography analysis. Initiation of HRD container discharge in

all tests was a result of gas cartridge actuator (GCA) remote firing via a 24 VDC power supply. A visual representation of the experimental mounting setup is shown in Figure 2.9.
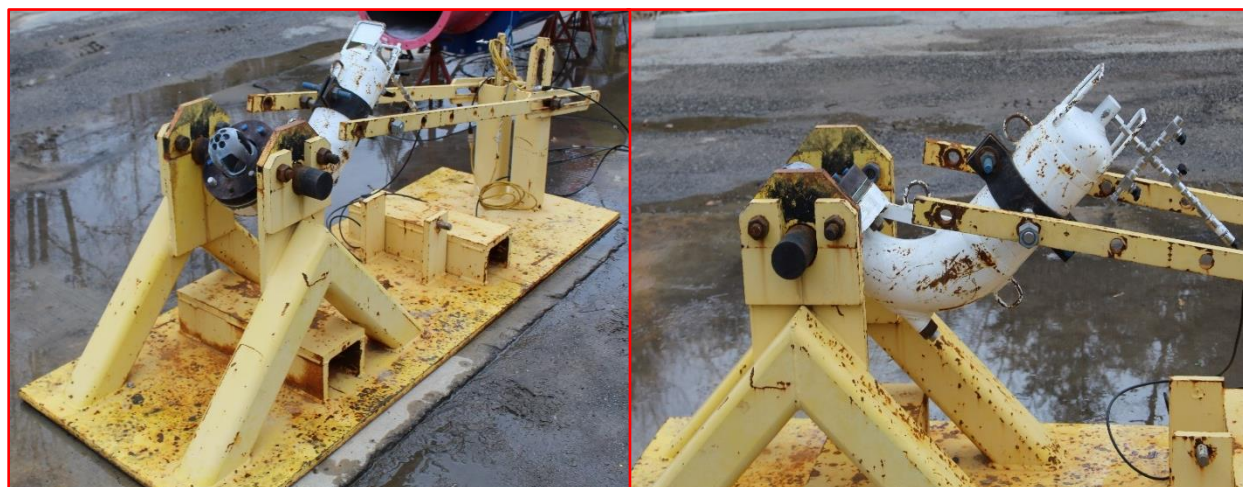
Figure 2.9. Test setup for open-air dispersion testing, overall setup (left) and container detail (right); a 10 L HRD container with a standard Fike spreader nozzle assembly, mounted to the gantry at a 45° firing angle

All tests were recorded with a real-time video camera running at 30 frames per second and with a high-speed video camera running at 1,000 frames per second. High-speed videography was necessary for post-test analysis. A flash bulb, placed in view of the cameras, was activated at the time of GCA initiation, allowing for the synchronization of data acquisition and high-speed video. Using the flash bulb frame as "time zero", reciprocal (inverse) velocity calculations were made at multiple agent throw distances (from origin out to 4.57 meters) based on data points pulled from high-speed video analysis using "i-Speed" software suite.

In addition to inverse velocity measurements, data captured from the HRD pressure transducer and qualitative visual inspection subsequent to discharge were necessary for complete assessment of agent dispersion through comparison of the following post-test deliverables:

- T90, the time required to reduce the nitrogen pressure within the HRD container to 10% of the initial preactuation pressure (90% discharged),

- T03, the time required to reduce the nitrogen pressure within the HRD container to 97% of the initial preactuation pressure (3% discharged),

- Weight of residual powder left in the container following discharge,

- Confirmation that the rupture disc opening is complete and non-fragmenting, and

- Visual comparison of dispersion profile through inspection of high-speed videography at specific time frames

2.7.3. 1 m^3 Sphere Explosibility and Suppression Testing

Displayed in Figure 2.10, the 1 m^3 combustion sphere is a high-strength enclosure (21 barg equipment design pressure) comprised of two carbon steel hemispherical sections and used primarily for closed-vessel fuel explosibility analysis as per international standard ISO 6184-1 (1985) and ASTM E1226 (2010). The 1 m^3 combustion chamber is capable of being reconfigured with HRD container mounting, a requirement for suppression testing. Details on the concept of active suppression as a deflagration mitigation strategy were introduced in Section 1.4. Such discussion includes the potential use of measurable TSP as a direct indicator for suppressant agent performance. For both explosibility and suppression testing, ignition energy was consistently provided using two 5 kJ chemical igniters positioned in the center of the sphere.

Unsuppressed explosibility analysis is essential for determination of fuel reactivity in the form of maximum observed pressure (P_{max}) and deflagration index (K_{St}), which is proportional to the maximum rate of pressure rise within the contained volume during fuel combustion. At constant ignition energy and initial pressure, the deflagration reactivity is dependent on the ignition time delay following initiation of fuel dispersion. Reduced ignition time delay induces more aggressive K_{St} due to added effects of injection turbulence. Increased ignition delay allows turbulence dissipation and a portion of the injected fuel particles to fall out of suspension, leading to suspended concentrations lower than anticipated and resulting in a restricted measurement of K_{St}.

Larger concentrations of suspended fuel require dual dispersion (injection via two separate dispersion vessels) to ensure that all fuel is fully injected into the combustion volume prior to ignition, as was the case for all iron deflagration explosibility and suppression tests performed at an increased suspended fuel concentration of 2,250 g/m³. To guarantee complete injection of fuel, the initial fuel load mass was equally divided among, and simultaneously injected from, each of the two injectors. Fuel injection points were positioned on opposing sides of the 1 m³ combustion sphere, with dispersion nozzles placed at contrary vertical and horizontal orientations in order to provide a uniform distribution of fuel.

Figure 2.10. Fike Corporation 1 m³ combustion test vessel, utilized for fuel explosibility and active suppression testing

2.8. Large-Scale Mitigation – Discussion of Results

2.8.1. Open-Air Dispersion Testing

The results of this test program act as a necessary supplement for continued application of novel agents toward metal dust deflagration suppression research. Despite varying flow properties

and particulate densities, dispersion of all three agents appeared visually sufficient to move forward with suppression testing in the 1 m^3 combustion sphere. Although this study was meant to be primarily a qualitative check on the injection proficiency, quantitative deliverables and analysis mentioned in Section 2.7.2 produced a similar assessment.
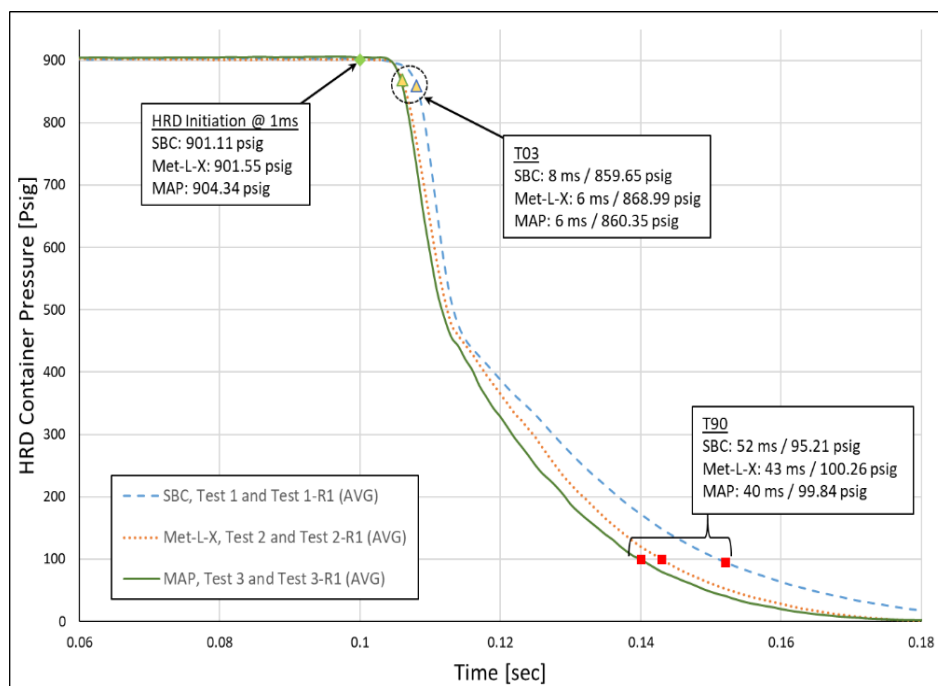
Figure 2.11. Average container pressure as a function of time following HRD initiation (data reported from t = 0.06 to 0.18 s), acting as a qualitative assessment of T03 and T90 differentiations between tests of varying agent types

Pressure transducer measurements of the container headspace pressure as a function of time allowed for determination of T03 and T90 for all tests. Discharge of suppressant agents MAP and Met-L-X exhibited a lower T03 (6 ms) compared to that of SBC (8 ms), likely a consequence of variable powder decompression rates. Immediately following rupture disc opening, bridging of compressed powder begins to propagate toward the headspace volume. As the agent packing begins to break apart, interparticulate expansion and expulsion of bulk agent (as plug flow) promptly follow. Dissimilarities in T03 thus describe differences in the time to effectively fluidize the compressed agent, which is hypothesized to be a function of variable agent particulate

densities. Additionally, the average T90 times for MAP and Met-L-X (40 ms and 43 ms, respectively) were significantly lower than that of SBC (52 ms), a direct result of lesser initial mass charged into the HRD container. The average HRD container pressure as a function of time following HRD initiation is shown in Figure 4.3 for all three suppressant agents under investigation, with T03 and T90 results for each individual test documented in Table 2.5.

Table 2.5. Post-test deliverables for open-air dispersion testing, including measured T90 and T03, suppressant weight left in the container following discharge, and confirmation of complete, non-fragmenting rupture disc opening

Test No.	Container Size	Suppressant Agent	Actual Suppressant Fill Weight (kg)	Measured T90 (ms)	Measured T03 (ms)	Post-Test Residual Powder Weight (lbs)	Complete and Non-Fragmenting RD Opening (Y/N)
1	10L HRD	SBC	9.07	52	8	0.054	Y
1-R1	10L HRD	SBC	9.07	56	8	0.082	Y
2	10L HRD	Met-L-X	5.90	44	6	0.018	Y
2-R1	10L HRD	Met-L-X	5.90	46	6	0.036	Y
3	10L HRD	MAP	4.08	44	6	0.018	Y
3-R1	10L HRD	MAP	4.08	40	6	0.023	Y

Qualitative evaluation of plume geometry likewise demonstrates adequate agent dispersion relative to SBC and eases reservations in regard to continued suppression testing. Figure 2.12 illustrates images captured from high-speed videography at 75 ms following HRD initiation and offers a direct visual comparison of plume distribution for each agent. Plume geometries of SBC and Met-L-X discharge appear nearly identical; all three plume segments are well-formed and comparable in extent. The plume for MAP discharge possesses less distinguishable plume segments (rather, identifies as one single cloud) but still covers roughly the same distances at short times follow system initiation (increased dispersion lag apparent at larger time/throw). Thus, the high-pressure driving force appears to outweigh differences in agent flow properties, such that all agents display similar coverage behavior during discharge.

Figure 2.12. Comparison of plume geometries during open-air discharge testing, including Test No. 1-R1 with SBC (left), Test No. 2 with Met-L-X (middle), and Test No. 3 with MAP (right); images captured at 75 ms following system activation

Figure 2.13 offers visual depiction of a characteristic cloud profile. Subdivisions of the plume are labeled accordingly as Track Point 1 (lower segment), Track Point 2 (middle/primary segment), and Track Point 3 (upper segment). This nomenclature is essential for data set identification and proper review of inverse velocity data. Annotation lines are also evident, on which data points were collected at 5 ms increments following HRD initiation.
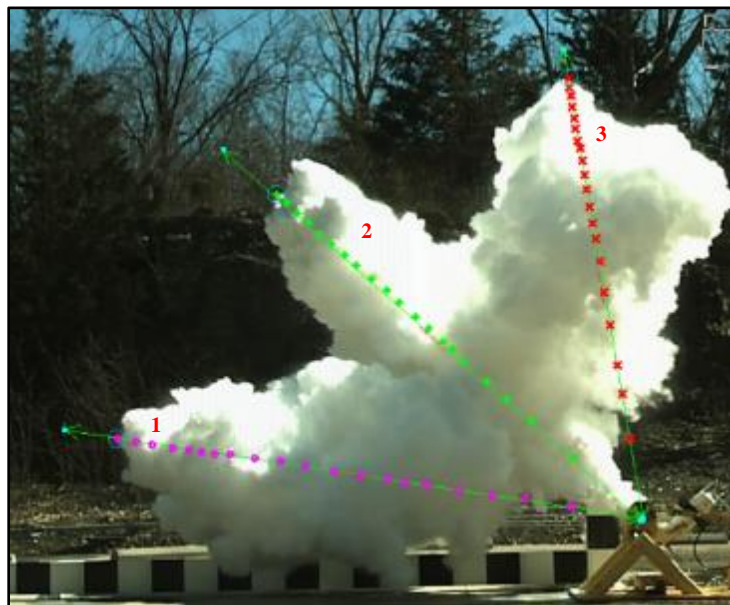
Figure 2.13. Illustration of dispersion profile during open-air discharge testing (Test No. 2-R1, with Met-L-X powder); subdivisions of the plume (Track Point 1, Track Point 2, and Track Point 3) labeled accordingly in red

Table E.2 within Appendix E displays reciprocal velocity data for the central segment of the cloud profile (Track Point 2). The values reported are calculated averages of both the original test and the repeat test for the same agent type. Values are provided at arbitrary throw distances of 0.91, 1.83, 2.74, 3.66, and 4.57 meters. Inverse velocities were determined with respect to the previous frame (instantaneous inverse velocity) and with respect to the user-defined custom origin position (bulk average inverse velocity). This custom origin position is expressed as the location where powder first exits the HRD container. For instantaneous inverse velocity measurements at higher target throw distances, the relative impact of perturbations increases as the dispersed agent loses momentum and is prone to influence by non-stagnant air flow from the surrounding environment.
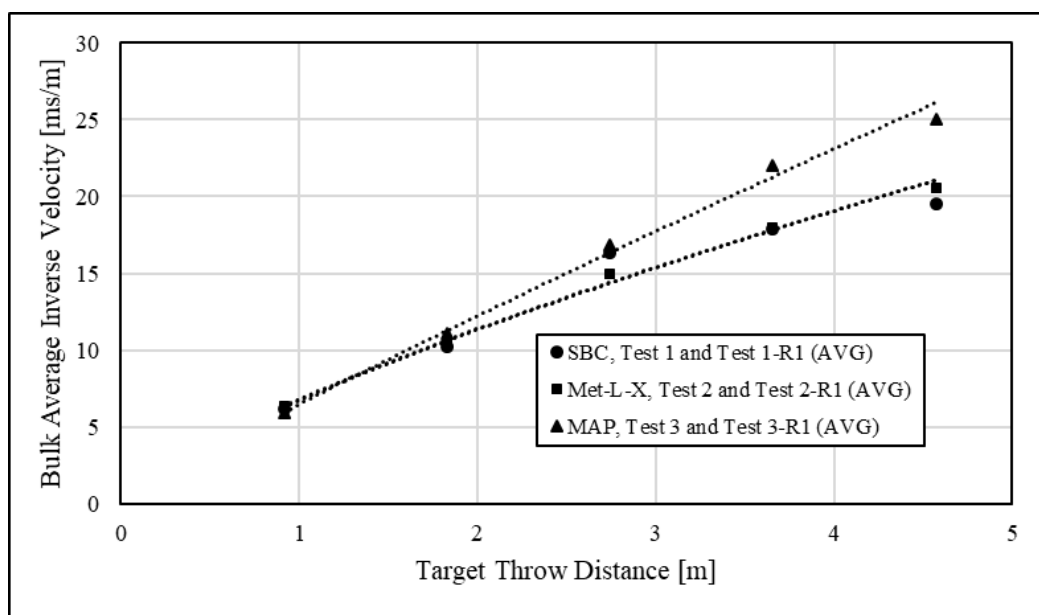
Figure 2.14. Bulk average inverse velocity results (measured with respect to custom user-defined origin) plotted for all suppressant agent as a function of increasing target throw distance

The average bulk inverse velocity data with respect to the custom origin are plotted in Figure 2.14. Results exhibited similar inverse velocities for SBC and Met-L-X. This consistency in inverse velocity between SBC and Met-L-X, even at a larger target throw distance of 4.57 meters

(± 1.44 ms/meter), is seemingly due to comparable particulate crystal densities of 2.20 and 2.16 g/cm³ for SBC and sodium chloride, respectively (CRC Press, 2005). As a result of a considerably lower crystal density (1.80 g/cm³ for MAP), measured inverse velocities for MAP dispersion showed greater deviation from SBC dispersion, more noticeably so at throw distances greater than 2.74 meters (± 4.17 ms/meter at 3.66 meters and ± 5.51 ms/meter at 4.57 meters). At larger target throw distances, the discharge of MAP coincided with an increased time-to-cover and a limited penetration power, again likely due to the significantly lower particulate density compared to the other agents tested. All aforementioned deviations are based on the average bulk inverse velocity data reported in Table E.2 within Appendix E.

Figure 2.15. Post-test evaluation; validation that HRD rupture disc opening is complete and non-fragmenting; Test No. 1-R1 with SBC

Post-test quantification of the residual suppressant weight left in the container was recorded as another auxiliary deliverable and is presented within Table 2.5. All SBC open-air dispersion tests resulted in >0.05 kg of residual powder left in the container (an average of 0.75% of the initial mass), while all MAP and Met-L-X tests resulted in <0.05 kg of residual powder left in the

container (an average of 0.50 and 0.47% of the initial mass, respectively). This minor difference is likely a product of lesser agent mass loaded into the HRD initially; the residual mass in the container in all cases is deemed insignificant, and injection is considered to be full and complete.

Photographs of rupture disc opening were taken for all tests as part of post-test documentation. Discharge of all agent types resulted in complete, non-fragmenting rupture disc opening. An illustration of standard rupture disc opening is provided in Figure 2.15 (Test No. 1-R1; SBC).

Throw distance across the major diameter of the 1 m³ combustion sphere (to be utilized for suppression testing) is approximately 1.24 meters. Upon review of Figure 2.12, all three agents display nearly equivalent bulk average inverse velocities at throw distances less than 2.74 meters, signifying a uniform time-to-cover over this target throw range. In addition to the qualitative plume geometry observations and the deductions rationalized from container pressure transducer measurements, these outcomes encourage the dependability of the 1 m³ sphere suppression test results.

Open-air dispersion testing at particular agent fill weights sets restrictions on the structure of the suppression test plan. Discharge performance and agent injection capability have not been validated for container fill weights larger than that which have been tested. With the lowest crystal density of all agents tested, dispersion of MAP at a 4.08 kg fill weight acts as the limiting factor in this regard. During suppression testing, agent concentrations must remain equivalent for proper comparison of inhibition efficiency. All 10 L HRD containers were filled with no greater poundage of suppressant agent than was tested in this open-air study.

2.8.2. 1 m^3 Sphere Explosibility and Suppression Testing

Explosibility testing in the 1 m^3 combustion sphere, as described in Section 2.7.3, was performed for both iron and aluminum powder fuels prior to suppression testing. K_{St} and P_{max} results, as well as tested fuel concentration and ignition delay, are documented in Table 2.6. Higher concentrations of fuel were preferable, offering a superior representation of the metal dust flame reactivity. Ignition delay was adjusted accordingly over multiple tests in order to confirm that injection and combustion of fuel were complete. Even at high concentration of suspended iron, inspection of dispersion vessels following tests at a 500 ms ignition delay indicated no excess fuel following the event and resulted in no combustion back-pressure through the ball valve. Inspection of the 1m^3 sphere after each explosibility test at this time delay also exhibited complete combustion of all fuel while in suspension, with no smoldering nests or unburnt fuel on the walls or bottom of the vessel. While this time delay is slightly shorter than that used for standard explosibility testing of typical industrial fuels in this particular vessel (600 ms, calibrated to ASTM standard methods), it was deemed necessary to ensure complete combustion as metal dust fuels inject significantly faster than lower density organics that are commonly used for vessel calibration.

Fuel concentration must also be tuned to ensure that the fuel severity was appropriately demanding of the agents. If the fuel is too aggressive, the agents would be overwhelmed, and the deflagration would be unsuppressed. If not challenging enough, it may be difficult to assess deviations in inhibitor performance during suppression testing. At 2,250 g/m^3 fuel concentration, iron explosibility testing yielded an average K_{St} and P_{max} of 61 bar-m/s and 4.52 barg, respectively, while aluminum explosibility testing at only 500 g/m^3 yielded an average K_{St} and P_{max} of 170 bar-m/s and 8.12 barg, respectively. Such an increase in severity at significantly lower fuel

concentration reflects the spontaneity and intensity commonly associated with aluminum powder combustion.

Suppression testing in the 1 m^3 combustion sphere was performed on both iron and aluminum deflagrations with the three agents under analysis (SBC, Met-L-X, and MAP). Test conditions and results from this study are documented for iron and aluminum suppression within Table 2.7 and Table 2.8, respectively. All iron deflagration suppression testing was executed at a 70 mbarg set pressure, and atmospheric pressure as the target ignition pressure, to allow for moderate deflagration development prior to suppression. Based on agent load constraints from open-air dispersion testing, a constant applied suppressant concentration of 4.08 kg/m^3 required a single 10 L HRD to be utilized for all experiments.
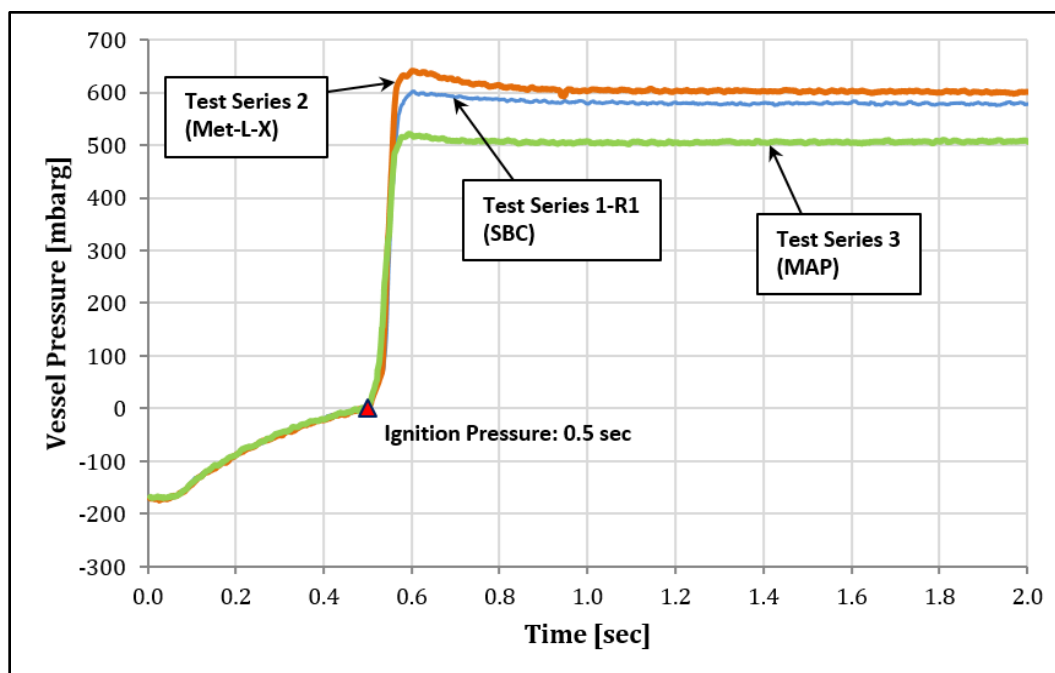
Figure 2.16. Vessel pressure versus time curves for select active suppression experiments with iron powder

Following suppression of iron combustion via injection of SBC and Met-L-X, analysis of vessel pressure versus time curves (Figure 2.16) yielded effective average TSPs of 0.60 barg and 0.62 barg, respectively. Suppression with MAP at the same concentration of agent yielded an

average effective TSP of 0.51 barg. This reduction can be attributed to chemical inhibition, exploited as a supplement to standard physical inhibition. As discussed in Section 2.4.3, thermal analysis of iron and iron/inhibitor mixture samples indicated promising mitigation performance for MAP (which demonstrated nearly 95% reduction in heat released during iron powder combustion) due to amplified degree of overlap between fuel oxidation and primary agent decomposition temperature ranges. Principal decomposition of SBC and Met-L-X occurs either before or after the solid-phase iron powder oxidation range, indicating that these two suppressant agents exhibit roughly the same physical inerting potential and do not function effectively through chemical means for this specific fuel composition.

All aluminum powder deflagration suppression testing was executed at a relatively lower set pressure of 35 mbarg and an agent concentration of $8.16\,kg/m^3$. Atmospheric pressure was targeted as the initial ignition pressure. Compared to applications conveying organic dusts or normally reactive metals, aluminum processing requires protection solutions designed at significantly lower detection thresholds. In the case of ignition of an extremely reactive metal, prompt system activation at low set pressure allows for introduction of suppressant before the deflagration is able to develop energy.

Although suppression with SBC required a single 10 L HRD container, suppression with Met-L-X and MAP, both with decreased particulate density relative to SBC, required simultaneous activation of two 10 L HRD containers to maintain a constant suppressant concentration, to retain adequate nitrogen headspace for accelerating the suppression agents during discharge, and to preserve the same timescale for discharge as with SBC (T90). The $1\,m^3$ combustion chamber setup, equipped with two 10 L HRD containers, is depicted in Figure 2.17. Both HRDs were mounted on

the same hemispherical section of the combustion sphere, so as to not introduce agent throw distance as a potential variable influencing inhibition performance.
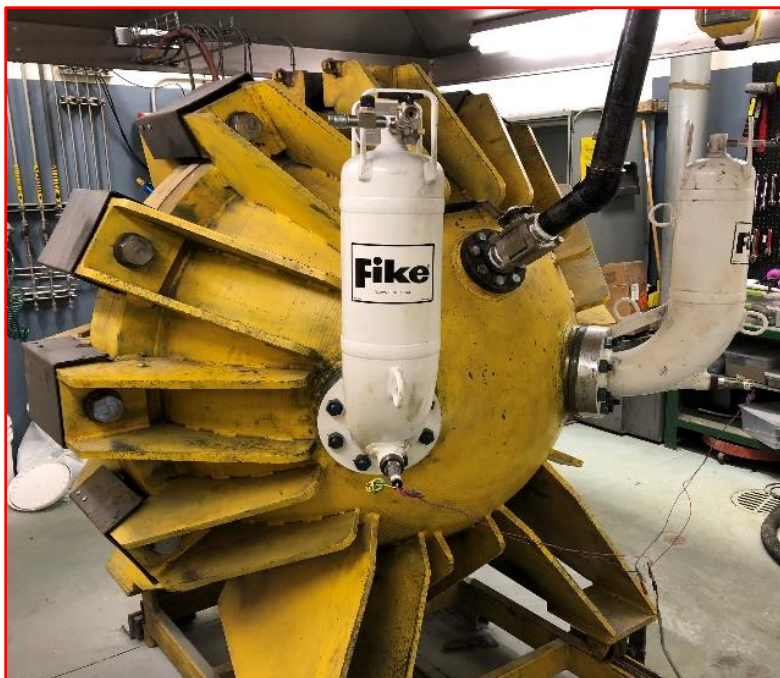
Figure 2.17. Test setup for 1 m^3 suppression testing with two 10 L HRD containers

Following suppression of aluminum combustion via injection of SBC and MAP, the analysis of vessel pressure versus time curves (see Figure 2.18) yielded effective average TSPs of 1.61 barg and 1.63 barg, respectively. Although complete thermal analytical predictive techniques were not available for aluminum powder (see Section 2.4.4), Met-L-X was anticipated to chemically inhibit aluminum combustion due to its high-temperature agent decomposition. However, aluminum deflagration suppression with Met-L-X seemed to demonstrate inconsistent outcomes, with TSPs ranging from 1.33 barg (Test Series 5-R2) to 4.95 barg (Test Series 5).
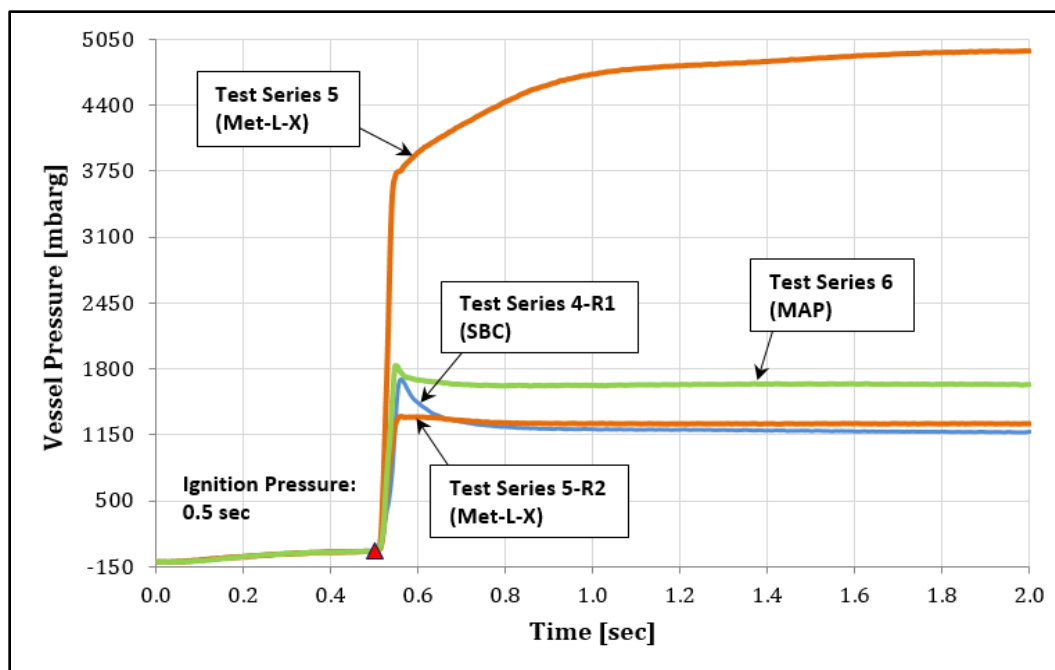
Figure 2.18. Vessel pressure versus time curves for select active suppression experiments with aluminum powder

The post-test combustion residue associated with Test Series 5 is shown in Figure 2.19. As described in Section 2.1.3, Met-L-X is primarily composed of sodium chloride and thermoplastic polymer additive used to form a protective layer preventing further diffusion of oxygen to the burning metal surface. Upon inspection of the burnt mixture internal to the combustion chamber, a dark coating was visible atop a partially oxidized fuel and agent mixture. While effective for fire suppression application, the polymer coating appeared to induce a confined smoldering nest when employed for explosion suppression. Continued partial combustion of unsuspended fuel allowed for steady build of pressure until the end of data collection approximately 1500 ms after the initial ignition of fuel. As long as bulk flow properties are not compromised, removal of the thermoplastic polymer additive from Met-L-X would potentially add performance stability during application as an explosion suppressant. During high-temperature aluminum flame propagation, agent decomposition volatiles likely dissociate and are less inclined to participate chemically in the combustion reaction inhibition. Reliance on physical inhibition and dilution mechanisms, through

increased concentrations of suppressant, is vital for the effective suppression of deflagrations which display increasingly substantial burning temperature and reactivity.

Figure 2.19. Residual combustion deposit following active suppression of aluminum powder deflagration with Met-L-X suppressant agent; Test Series 5

Table 2.6. Iron and aluminum powder fuel particle size statistical analysis and fuel explosibility results via 1 m³ sphere testing, presented as the average of two identical tests.

Fuel Type	Particle Size Distribution			1 m³ Explosibility Testing			
	< 5 um	< 40 um	Mean Size	Fuel Concentration [g/m³]	Ignition Delay [ms]	K_{St} [barg·m/s]	P_{max} [barg]
Al-100	79%	100%	3.51	500	500	170	8.12
Fe-101	11%	76%	26.97	2250	2250	61	4.52

Table 2.7. 1 m³ sphere suppression test results for iron powder fuel (Fe-101), with variable suppressant composition.

Test Series	Fuel Type	Fuel Concentration [g/m³]	Ignition Delay [ms]	Suppressant Type	Suppressant Concentration [kg/m³]	P_{set} [mbarg]	P_{ign} [mbarg]	TSP [barg]
1	Fe-101	2250	500	SBC	4.08 [10L HRD container x1]	70	1.5	0.59
1-R1	Fe-101	2250	500	SBC	4.08 [10L HRD container x1]	70	0.7	0.60
2	Fe-101	2250	500	Met-L-X	4.08 [10L HRD container x1]	70	0.2	0.64
2-R1	Fe-101	2250	500	Met-L-X	4.08 [10L HRD container x1]	70	5.6	0.60
3	Fe-101	2250	500	MAP	4.08 [10L HRD container x1]	70	-0.4	0.52
3-R1	Fe-101	2250	500	MAP	4.08 [10L HRD container x1]	70	1.6	0.50

Table 2.8. 1 m³ sphere suppression test results for aluminum powder fuel (Al-100), with variable suppressant composition.

Test Series	Fuel Type	Fuel Concentration [g/m³]	Ignition Delay [ms]	Suppressant Type	Suppressant Concentration [kg/m³]	P_{set} [mbarg]	P_{ign} [mbarg]	TSP [barg]
4	Al-100	500	500	SBC	8.16 [10L HRD container x1]	35	11.3	1.54
4-R1	Al-100	500	500	SBC	8.16 [10L HRD container x1]	35	7.4	1.68
5	Al-100	500	500	Met-L-X	8.16 [10L HRD container x2]	35	3.0	4.95
5-R1	Al-100	500	500	Met-L-X	8.16 [10L HRD container x2]	35	-5.3	1.85
5-R2	Al-100	500	500	Met-L-X	8.16 [10L HRD container x2]	35	0.4	1.33
5-R3	Al-100	500	500	Met-L-X	8.16 [10L HRD container x2]	35	-2.0	1.98
6	Al-100	500	500	MAP	8.16 [10L HRD container x2]	35	2.9	1.83
6-R1	Al-100	500	500	MAP	8.16 [10L HRD container x2]	35	-8.2	1.42

2.9. Conclusion

Dust explosions induced by the ignition of reactive metal powders continue to present a substantial hazard within metal handling and refining industries. High-rate injection of an inert agent material as the flame front begins to develop (i.e., active suppression) allows for deflagration extinction and effective mitigation of pressure growth within the protected enclosure volume. Inhibition of combustion propagation generally occurs via three routes: physical inhibition, chemical inhibition, and dilution of the preheat zone. However, due to characteristically intense severity and spontaneous burning mechanisms, mitigation of metal powder deflagrations at moderate total suppressed pressures (relative to the overall design strength of the vessel) and at low agent concentrations remains challenging. As demonstrated through TGA/DSC analysis of fuel and fuel/agent mixtures, specific suppressant agent compositions appear to exhibit heightened inhibition performance as a result of the greater overlap between agent decomposition and fuel oxidation temperature ranges. Such overlap prompts increased chemical inhibition effectiveness, which acts as a direct supplement toward standard physical inhibition mechanisms. This study reviews recent metal dust suppression testing in Fike Corporation's 1 m^3 sphere combustion chamber and evaluates the efficacy of multiple suppressant agents (sodium bicarbonate [SBC], sodium chloride [Met-L-X], and monoammonium phosphate [MAP]) for the mitigation of iron and aluminum powder deflagrations at suspended fuel concentrations of 2,250 g/m^3 and 500 g/m^3, respectively.

As predicted from thermal analytical studies, iron deflagration suppression experiments at a 70 mbarg set pressure and with MAP as the discharged suppressant agent yielded marginally lower reduced pressures (average TSP of 0.51 barg) relative to experiments with SBC (average TSP of 0.60 barg). According to the TGA profile for MAP, primary decomposition of the agent occurs

directly atop the solid-phase combustion temperature range of iron powder. Compared to SBC and Met-L-X, whose decomposition temperatures are either above or below the iron combustion temperature window, MAP offers deflagration mitigation by both physical and chemical means, absorbing heat released via fuel oxidation and consuming free radicals that would otherwise prolong the combustion duration. Increased chemical inhibition effectiveness upon use of MAP thus justifies the apparent reduction in TSP. If adopted commercially, it is recommended to modify the composition of the suppressant mixture (increased content of flow-promoting silica) in order to stimulate enhanced dispersion of agent at higher target throw distances more representative of industrial application.

Aluminum deflagration suppression experiments at a 35 mbarg set pressure yielded TSPs greater than 1 barg for all agents tested. Relative to iron powder combustion (normally reactive), aluminum is considered a highly reactive metal and proved more difficult to suppress. Although Met-L-X was anticipated to demonstrate improved inhibition of aluminum combustion due to its high-temperature principal decomposition, suppression testing produced inconsistent results. Suppression of aluminum deflagration with Met-L-X yielded TSP as low as 1.33 barg and as high as 4.95 barg. Inspection of combustion chamber internals following Test Series 5 (Met-L-X, TSP = 4.95 barg) revealed a thin layer of material coating the top of a partially oxidized fuel/agent mixture. In this particular case, it is likely that the thermoplastic polymer additive within Met-L-X created ideal circumstances for a smoldering nest, which continued to burn and gradually generate pressure. As confirmed by the vessel pressure versus time profile for this test, the maximum suppressed pressure did not occur until several seconds after initiation of the event.

Chemical inhibition as a supplement to physical inhibition appeared to be less effective for the suppression of metal fuels with increasing reactivity. The influence of chemical inhibition on iron

powder deflagration extinction was evident but marginal. Fuels such as aluminum display exceedingly high burning temperatures, which may lead to dissociation of agent decomposition volatiles that would normally impede combustion chemically or participate in dilution of the preheat zone. Greater metal fuel reactivity requires over-reliance on physical inhibition mechanisms. From a suppression system design standpoint, this translates to saturation of the combustion volume with inert material at agent concentrations well beyond the standard requirements of an organic dust. For suppression applications requiring high agent concentrations, the use of multiple smaller HRDs rather than a larger one is an effective design approach providing improved agent delivery rate and optimized agent throw distances. Maintaining appropriate response time through low pressure activation set points allows the protection system an opportunity to extinguish the flame front before propagation accelerates to uncontrollable proportions. Combination venting with active suppression is also recommended for extremely reactive hazards in order to keep reduced pressures sufficiently below the enclosure design strength. Appropriate characterization of the hazard and conservative system design procedures are essential for proper protection of industrial processes conveying combustible metal dusts.

Chapter 3: Consequence Prediction for Vented Interconnected Vessels

3.1. Introduction to Explosion Isolation & Existing Prescriptive Guidance

Proper explosion protection strategies are essential for enclosures conveying or storing combustible dusts. Techniques such as explosion venting or active explosion suppression moderate the development of pressure within the protected volume to below the equipment design strength of the vessel. With explosion mitigation in place, the enclosure where ignition originated (primary vessel) may be protected; yet, a separate isolation design may be required to prevent flame and pressure fronts from propagating along upstream or downstream ductwork toward interconnected process units (secondary vessels). Isolation devices can initiate actively, in which system firing is dependent on detection of pressure or flame within the primary enclosure, or passively, during which the valve closure is triggered by a propagating pressure front from the explosion. NFPA 69 (2019) offers industry guidance on the appropriate implementation of alternative forms of explosion isolation. Without such isolation solutions in place, subsequent explosion events in secondary vessels are capable of generating significant energetic behavior. Commonly, a successful isolation design requires hardware to be installed on the ductwork at a minimum distance from the primary explosion volume, ensuring that propagating flame does not escape the isolation barrier location. However, dust-air filtration and bulk product storage processes typically exist with relatively short lengths of ductwork between conveyance vessels, impeding proper implementation of an explosion isolation strategy.

Uninterrupted propagation of flame to interconnected enclosures can result in severe consequences. As the deflagration stretches from primary ignition point into the ductwork and more complicated vessel geometries, increased flame front surface area in contact with suspended unburnt fuel medium coincides with a proportional increase in combustion rate. Acceleration of

flame and additional flow turbulence can lead to a significant rise in system pressure. If allowed to propagate unchecked by a protection system, a deflagration has the potential to accelerate to supersonic speeds, transitioning to detonation and resulting in a rapid increase in explosion pressure. Flame jet ignition within the secondary vessel, as opposed to a standard point ignition source, generates an amplified rate of particulate burning and maximum rate of pressure rise ($\propto$ K_{St}). Another local dynamic effect known as pressure piling induces pre-compression of unburnt fuel medium within interconnected ductwork and secondary vessels; once flame ultimately reaches the secondary vessel volume, ignition of fuel at elevated initial pressure produces local enclosure pressure considerably greater than adiabatic isochoric maximum explosion overpressure generated at atmospheric initial pressure. Both flame jet ignition and pressure piling phenomena are capable of reducing the effectiveness of existing venting or active suppression solutions on the secondary vessel (Bjerketvedt et al., 1997; Zalosh, 2008; Eckhoff, 2003).

The aforementioned phenomena described during propagation of flame between interconnected enclosures has been observed experimentally through remote testing at a large scale. Lunn et al. (1996) performed investigations on coal and toner dust explosions in a combination of contained interconnected vessel systems, connected by a pipe that was 5 meters in length and with vessels volumes ranging from 2 to 20 m^3. In some experimental configurations, the effects of pressure piling and high initial turbulence produced a rise in the measured maximum pressure in the secondary vessel to nearly 20 barg. Holbrow et al. (1996) expanded this study toward dust explosion propagation within interconnected vented vessel systems. Experimentalists observed secondary vessel reduced explosion pressure (P_{red}) up to 6.2 barg, significantly greater than that which could be expected during an event within an isolated enclosure. Maximum pressure within the primary vessel was also intensified but to a lesser extent. Both studies concluded that

the following variables are key factors that influence the observed pressures during propagation of flame between interconnected enclosures: fuel explosibility, interconnected duct diameter and length, ignition location, vessel volume and relative volume ratio, and relief area of the two vessels. A study by Vogl (1994) correlated many of these experimental system parameters, including initial air velocity and pipeline dust concentration, with flame speed and explosion overpressure. Bartknecht (1981) approached the study of explosion behavior in combined vessels from an alternate perspective through analysis of gaseous fuels methane and propane, and observed results similar to those found during investigations with suspended dust fuels. For experiments in which the interconnected enclosed vessels had significantly different volumes, violent pressure oscillations led to unavoidable amplification in maximum rates of pressure rise and peak explosion pressures, with more than a 200% increase in P_{max} within the smaller vessel (compared to an isolated single enclosure) when ignition originated in the larger vessel.

Although many standard calculation methods exist for relief area sizing (NFPA 68, VDI 3673, EN 14491, etc.), most are often exclusive toward deflagration events occurring within a single isolated vessel (NFPA, 2018; Beuth Verlag, 2002; British Standards Institution, 2012). NFPA 68, the Standard on Explosion Protection by Deflagration Venting, provides guidance on deflagration venting of enclosures interconnected with pipelines (Section 8.12), but its usefulness is indeed limited by its specificity. Applicable only to interconnected pipelines with internal diameters of less than or equal to 0.3 meters and length no greater than 6 meters, the following relief venting design guidance is provided:

1) The venting device for the enclosure shall be designed for a burst pressure (P_{stat}) of less than 0.2 barg.

2) Enclosures of volumes within 10 percent of each other shall be vented as determined by NFPA 68 (see Equations 8.2.2 and 8.2.3).

3) If enclosures have volumes that differ by more than 10 percent, the vents for both enclosures shall be designed as if P_{red} were equal to 1 barg or less. The enclosure shall be designed with strength (P_{es}) equal to a minimum of 2 barg.

4) If it is not possible to vent the enclosure with the smaller volume in accordance with this standard, the smaller enclosure shall be designed for the maximum deflagration pressure, P_{max}, and the vent area of the larger enclosure with the larger volume shall be doubled.

5) The larger enclosure shall be vented or otherwise protected as described in NFPA 69 (2019) in order for the deflagration venting of the smaller enclosures to be effective.

For vessels with a large volume difference, an increase in enclosure strength to 2 barg may be difficult to achieve without extensive structural modification to the vessel and ductwork. If the application falls outside of this defined scope (e.g., if hydraulic duct size exceeds 0.3 meters), users are directed toward alternative protection and isolation techniques, as prescribed by NFPA 69 (2019). Active protection solutions are often costly and may require impractical modifications to the process layout or operation conditions. A review by Holbrow et al. (1999) provides additional experimental guidance on venting of dust explosions within interconnected vessels; however, similar limitations in applicability exist according to conditions of the test program, relevant only for compact vessels, dust fuels with P_{max} less than or equal to 10 barg, and duct lengths between 5 to 15 meters.

Through application of a computational fluid dynamics tool with flame propagation solving capability, the objective of this study is to offer an iterative approach toward safe venting design for mitigation of flame and relief of pressure for interconnected process vessels conveying

combustible dusts. For complicated enclosure geometries or applications outside the limitations covered by pertinent vent sizing standards, this nonspecific method provides a reliable manner of confirming minimum relief area requirements to maintain isolated, single-vessel P_{red}'s within an interconnected vessel system.

3.2. Background – Computational Fluid Dynamics Modeling Using FLACS

Reliant on initial conditions and boundary layer assumptions, computational fluid dynamics (CFD) is a form of fluid mechanics that solves fluid flow problems, with or without chemical reaction, through numerical methods and an iterative algorithm approach. The general governing equations for CFD-based numerical analysis include a fixed matrix of fundamental transport equations of mass continuity (E10), motion (E11), and energy (E12). Discretization of the geometry domain into an appropriate mesh allows for sequential, simultaneous examination of fluid flow solutions as a function of fluctuating physical properties (pressure, temperature, density, velocity, and viscosity).

$$\frac{\partial \rho}{\partial t} + (\nabla \cdot \rho \mathbf{v}) = 0 \tag{E10}$$

$$\rho \frac{D\mathbf{v}}{Dt} = -\nabla p - [\nabla \cdot \boldsymbol{\tau_s}] + \rho \boldsymbol{g} \tag{E11}$$

$$\rho \hat{C}_p \frac{DT}{Dt} = -(\nabla \cdot \boldsymbol{q}) - \left(\frac{\partial \ln \rho}{\partial \ln T}\right)_p \left(\frac{Dp}{Dt}\right) - (\boldsymbol{\tau}_{s,i} \nabla \mathbf{v}) \tag{E12}$$

Operating on a Cartesian grid space by means of the finite volume method, the FLame ACceleration Simulator (FLACS) is an experimentally validated three-dimensional CFD tool utilized in a wide variety of process safety applications, including dispersion of flammable or toxic material; blast and shock wave propagation; pool and jet fires; consequence and risk analysis; and gas, mist, and dust explosions (Gexcon AS, 2014). Following the development of sufficient combustion models for dust-air suspension, the latter was made available through Gexcon in 2006

with the release of DESC (Dust Explosion Simulation Code), which is based on the existing FLACS code for simulation of gas explosions. DESC is capable of consequence prediction in the form of reliable estimation of flow, flame propagation, and pressure generation in complex geometries where combustible dust hazard exists (Skjold, 2014). The next section offers a consolidated review of the primary considerations during the development of the DESC modeling platform.

3.3. DESC Model

3.3.1. Multiphase Turbulent Flow

The nature and degree of the turbulent flow have a substantial impact on the combustion rate within a suspended dust cloud. DESC incorporates the use of the Reynolds-averaged Navier-Stokes equations (RANS), supplemented by the ideal gas equation of state and the k-ε turbulence model in order to simulate mean flow characteristics for isotropic turbulent fluid flow conditions (Skjold, 2007). The decay of turbulence, or the rate of dissipation of the dispersion-induced turbulent kinetic energy ε, was appropriately fitted to this RANS model system through comparison with large vessel experimental measurements. Although prediction of transient turbulent states remains challenging, such standardized measurements allowed for extraction of empirical relationships describing both the root-mean square of turbulent velocity instabilities and integral turbulent length scale. In the case of a dust suspension, the concept of particle-laden flow coupled with heterogeneous combustion allowed for further simplification of the fundamental RANS equations. Additional assumptions included thermal and kinetic equilibriums between the continuous (or carrier) phase and dispersed (or particulate) phase, as well as k-ε model results unaffected by the condition of multiphase flow. Consequently, the user must be cognizant that the current version of the DESC software is limited in its inability to provide precise simulation of

agglomeration effects, gravitational loss of particle suspension, and selective division of particles within unique geometry configurations (Skjold, 2007; Skjold et al., 2005).

Since release of the first version, DESC has applied empirical relations to convert accumulated dust layers into particle suspension. Dispersion induced by turbulent flow during a combustible dust explosion is capable of demonstrating an increase in the event severity. DESC utilizes fuel particle specifications and other user inputs to describe the injection of a dust at a particular suspension concentration, leading to an established manner of simulating the dust lifting phenomena (Skjold, 2007).

3.3.2. Combustion Model

Combustion of a suspended fuel is considered as turbulent reactive flow and requires additional models to compensate for chemical reaction that exists during propagation of flame. Development of a comprehensive model for combustion within turbulent dust clouds allowed for a specification of a precise flame front position and reaction conversion rate (Skjold, 2007).

Adopted from an identical flame thickening model (β flame model) as used in the FLACS gas explosion simulator, DESC applies the following correlation by Abdel-Grayed et al. (1987) for modeling the turbulent burning velocity for gas mixtures:

$$\frac{S_T}{S_u} = 0.875 \, K^{-0.392} \frac{u'_{rms}}{S_L} \tag{E13}$$

where S_T is turbulent burning velocity, S_u is laminar burning velocity, u'_{rms} is the root-mean square of turbulent velocity fluctuations, and K is the Karlovitz stretch factor (Arntzen, 1998). Assuming a constant kinematic viscosity and introducing the turbulence integral length scale l_I, this expression can be simplified as follows (Bradley et al., 1992; Popat et al., 1996):

$$S_T = 15.1 \, S_u^{0.784} u'_{rms}{}^{0.412} l_I^{0.196} \tag{E14}$$

Laminar burning velocity S_L data were readily available for numerous gaseous mixtures, but a lack of similar documentation for dust cloud combustion resulted in a need for experimental input from constant-volume explosion vessels used for standardized fuel explosibility testing. This empirical approach requires several estimates for the S_L at variable suspended dust concentrations. As summarized by Skjold, validation testing on a large scale demonstrated reasonable agreement with overpressure results (in consideration of pressure piling phenomena described in Section 1) and pipeline flame speeds estimated by DESC (Skjold, 2014; Skjold, 2007).

Although DESC retains sufficient functionality for prediction of turbulent combustion, the simulator has several shortcomings, including unknown influence of the inert suppressants on fuel propagation mechanisms and an uncertainty in regard to the probability of detonation to deflagration transition during flame propagation within a dust cloud. The model is more accurate when applied toward fuels of increasing combustible dust explosibility ($K_{St} > 100$ bar-m/s). The DESC model is also comprised of thermodynamic equilibria relations limited to describing combustion of exclusively organic materials, or any composition containing carbon, hydrogen, oxygen, nitrogen, or sulfur (no metal or alloy compounds). However, this project examined explosion venting as the mitigation strategy and simulated propagation through an organic dust cloud of moderate reactivity, with relatively low likelihood of detonation; therefore, the aforementioned limitations were assumed to have no impact on the outcome of this investigation (Skjold, 2014; Skjold, 2007).

Considering that the FLACS program is commonly utilized for design of personnel life safety solutions, verification of the accuracy of model predictions through comparison to experimental data is essential. Gexcon has taken care to considerably assess pivotal benchmarks of the simulation package before commercial deployment. As summarized by Skjold, the performance

and accuracy of DESC has been extensively verified through evaluation against numerous reports of experimental test series, validating capabilities of the simulation in regard to fundamental concepts such as pressure piling, influence of obstacles, turbulence intensity, propagation through complex geometries, inclusion of explosibility test results, dust lifting, and venting of large volume deflagrations (Skjold, 2014).

3.4. Simulation Conditions

3.4.1. Geometry & Three-Dimensional Grid Construction

The primary foundational geometry utilized for all simulations consisted of two vessels, one small and one large, interconnected by a two meters long rectangular duct (800 mm x 500 mm cross-sectional area). The smaller cylindrical vessel was constructed with an internal volume of approximately 4 m^3, while the larger cylindrical vessel was constructed with an internal volume of approximately 15 m^3. The FLACS program simulates a dust explosion situation by performing iterations throughout the grid space around solid objects built exclusively as either rectangles or cylinders. For this reason, the cone shape of both hoppers was constructed as a series of short cylinders with progressively smaller major diameters. The final cylinder at the discharge of the hopper was modeled as a solid surface, signifying that the discharge outlet is closed during the deflagration event. Such an assumption acts as a representation of a slide gate or rotary valve, positioned at the product discharge and rated to withstand the maximum explosion overpressure.

A three-dimensional uniform grid space was defined for the calculation, with a refined core domain centralized around the primary geometry and cell size of 0.1 meters. The grid was then stretched toward external boundaries, offering a coarse resolution depiction of simulation deliverables outside of the internal enclosure geometries. Porosities were calculated and verified to ensure that the geometry and the grid were in proper alignment. Upon extension to industrial

application, it is recommended to perform a grid independence study to ensure that simulation results are not reliant on the computational mesh density. Visual portrayal of the principal enclosure geometry, as well as the grid space, is shown in Figure 3.1 (left).
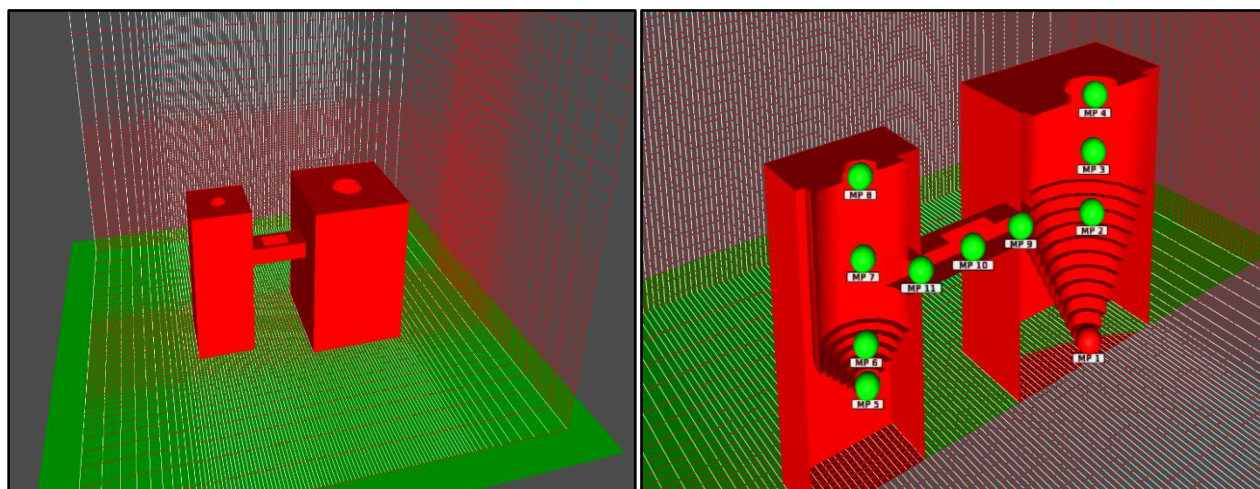
Figure 3.1. Depiction of simulation geometry with view of three-dimensional core domain and extended grid [left]; monitor point locations internal to large vessel (M1 through M4), small vessel (M5 through M8), and interconnecting ductwork (M9 through M11) [right]

3.4.2. Monitor Points & Simulation Deliverables

Eleven monitor points (M1 through M11) were established throughout the primary enclosure volume, as illustrated in Figure 3.1 (right). M1 through M4 were positioned within the large vessel volume along the central vertical axis; M5 through M8 were positioned within the small vessel volume along the central vertical axis; M9 through M11 were positioned within the interconnecting ductwork volume along the central horizontal axis. All monitor points were designated to measure the scalar quantity pressure as a function of time following simulation initiation. Combustion product mass fraction was selected as another independent deliverable, allowing the user to visualize any potential gaps in the system geometry where flame is allowed to escape into a location of improperly aligned grid space. An example of combustion product mass fraction as a three-dimensional field variable output is shown in Figure 3.2.
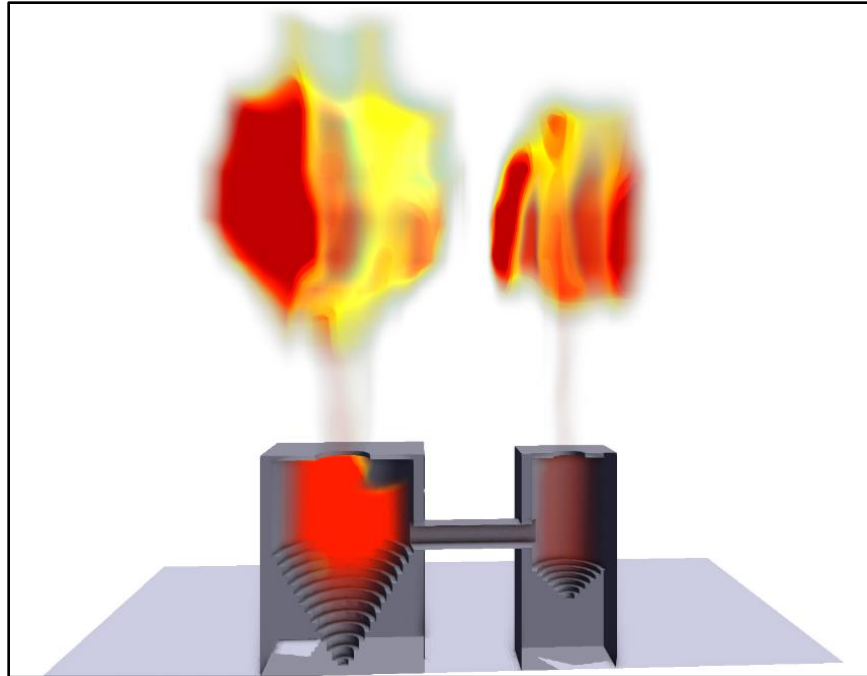
Figure 3.2. Three-dimensional illustration of combustion products (Simulation 1; 750 g/m^3 fuel concentration; ignition in large vessel), image captured at t = 290 ms

3.4.3. Relief Panels

The explosion scenario required the use of active panels to simulate explosion mitigation via relief venting. As shown in Figure 3.3, three popout-type relief panels were created: Panel 1 on the large vessel, Panel 2 on the small vessel, and Panel 3 on the interconnecting ductwork. All relief panels were centralized on the top surface of their respective geometry and were defined with an 8 kg/m² vent mass. All panels were also defined with a 0.1 barg static burst pressure. Once the system pressure at the internal vent face had increased to minimum opening threshold, panel porosity was set to instantaneously increase from zero to one, allowing for linear displacement of the panel and redirection of flame and pressure to locations external to the enclosure. Resistance of the vent opening within the surrounding air was considered through designation of a conservative drag coefficient in all simulation cases.
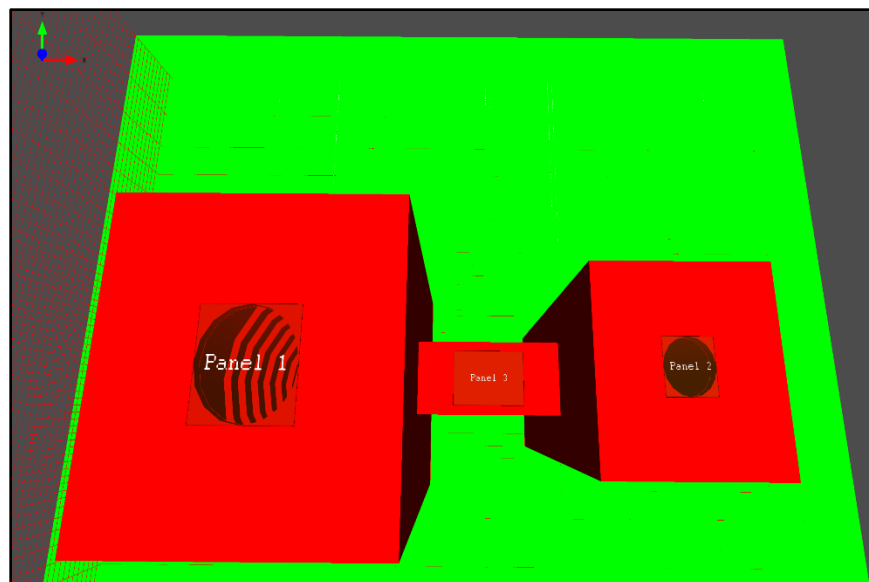
Figure 3.3. Relief panels associated with the large vessel (Panel 1), small vessel (Panel 2), and interconnecting ductwork (Panel 3)

Depending on the simulation in queue, dimensions of each rectangular panel were adjusted to match the size of the corresponding relief holes cut into the enclosure geometry. In accordance with the project objective as defined in Section 3.1, the size of the holes and panels on both the large and small vessel were increased in an attempt to obtain reduced target explosion pressures. Maximum overpressure solutions for a variety of venting configurations are found in Section 3.5.

3.4.4. Initial Conditions & Boundary Type

Prior to running the simulation, the initial conditions were defined including ambient system temperature and pressure. Characteristic velocity was specified at 5 m/s, and relative turbulence intensity was specified at 0.1. The turbulence length scale, which indicated the size of any significant energy-containing eddies within the turbulent flow region, was specified at 0.01 meters. Length scales disproportionately large relative to grid cell lengths commonly yield solution convergence issues and were avoided. The EULER boundary type was advised by Gexcon as a

sufficient fit for most explosion scenarios and was employed in this case to set simulation conditions at the upper and lower extents of the domain (Gexcon AS, 2019).

3.4.5. Fuel Specifications & Ignition Source

Dried maize starch, with a documented deflagration index (K_{St}) of 150 bar-m/s and a maximum pressure developed within a contained optimum deflagration (P_{max}) of 8.6 barg, was selected as the fuel of interest for all simulations. Physical properties of the fuel included a particulate density of 1180 kg/m^3 and a dust particle diameter of 15-µm. The entire enclosure geometry (both vessels and interconnected ductwork) was assumed to be uniformly occupied with suspended fuel prior to ignition, as illustrated in Figure 3.4 (left), at concentrations of either 250 g/m^3 or 750 g/m^3. Laminar burning velocities were specified at 0.223 and 0.250 m/s for suspended dust concentrations of 250 and 750 g/m^3, respectively.
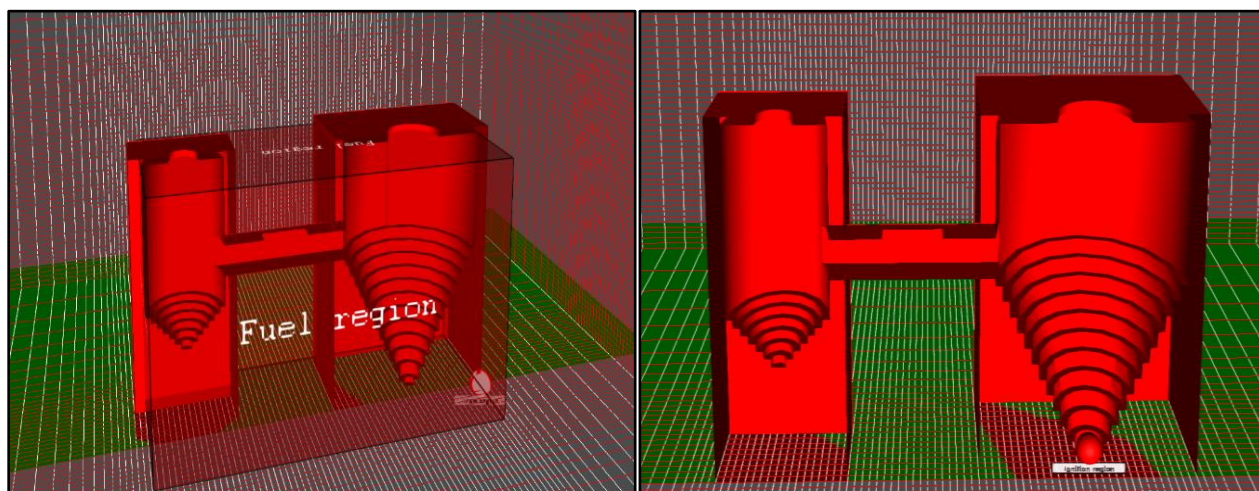
Figure 3.4. Initial suspended fuel region at the time of ignition [left]; point ignition location (x, y, z) at bottom of the hopper of the large vessel [right]

Ignition energy was maintained at 10 kJ for all simulations. As shown in Figure 3.4 (right), ignition location dimensions were positioned at the bottom of either the large vessel hopper or small vessel hopper, in an attempt to demonstrate electrostatic discharge during collection and

dropout of product. Maximum overpressure solutions for all combinations of ignition location and suspended fuel concentration are discussed in Section 3.5.

3.5. Simulation Results

For simplicity, each venting arrangement was assigned a simulation number identifier, as defined in Table 3.1. Depicted by Simulation 1, the initial venting configuration consisted of a 600 mm diameter relief panel on the small vessel and a 1000 mm diameter relief panel on the large vessel, with no venting present on the interconnected ductwork. Under the assumption that each enclosure is isolated with no interconnection to other vessels, vent sizing guidance from NFPA 68 was utilized to predict expected reduced pressures as a reference for comparison ($P_{red} = 0.51$ barg for the small vessel; $P_{red} = 0.26$ barg for the large vessel). Industry convention requires that designer size the vent(s) of an independent enclosure to yield a P_{red} below the strength of the vessel (P_{es}); consequently, this case study maintained the conservative presumption that these predicted P_{red} values were equivalent to the respective enclosure strengths of each vessel. However, propagation of flame through interconnected ductwork allowed for pressure piling and flame-jet ignition effects, resulting in generation of maximum overpressures as high as 2.33 and 2.07 barg in the small and large vessel, respectively, at moderately high concentrations of fuel. Unless saturation has been reached and availability of oxygen becomes limiting, increased fuel content coincides with higher thermodynamic potential, raising both the maximum overpressure and amount of heat liberated during complete combustion. As a result, ignition at high concentration of suspended maize starch yielded a significant increase in the maximum overpressure, with more than a two-fold increase during Simulation 1, regardless of ignition location. Yet, even at relatively low concentrations of suspended maize starch, the maximum overpressure reached 0.90 and 0.88 barg in the small and large vessel, respectively. Thus, for all conditions of ignition location and

fuel concentration, the initial venting configuration was ineffectually designed to maintain system pressures below the originally anticipated P_{red}'s estimated by NFPA sizing methods and was considered to be inadequate for the protection of an interconnected vessel system.

Table 3.1. Simulation numbers assigned to identify the discrete venting arrangements, for both suspended concentrations of maize starch (250 and 750 g/m³). Y/N indicates the presence (or lack thereof) of a relief panel (size: 800mm x 500 mm) on the interconnecting ductwork

Simulation No.	Venting Arrangement [mm] [Small Vessel/Large Vessel/Ductwork]	
	250 g/m³ Fuel Concentration	750 g/m³ Fuel Concentration
1	Ø600/Ø1000/N	Ø600/Ø1000/N
2	Ø600/Ø1000/Y	Ø600/Ø1000/Y
3	Ø600/Ø1200/Y	Ø800/Ø1200/Y
4	Ø600/Ø1400/Y	Ø800/Ø1400/Y
5	N/A	Ø800/Ø1600/Y
6	N/A	Ø1000/Ø1800/Y
7	N/A	Ø1000/Ø2000/Y

Shown in Figure 3.5, two-dimensional representation of the pressure development qualitatively illustrated extensive oscillation of the pressure front between the enclosure volumes. In an attempt to decouple translation of pressure along the interconnected ductwork, the geometry of Simulation 2 implemented pipe venting, as prescribed within NFPA 68 (Chapter 9), in addition to the initial venting configuration defined by Simulation 1. The rectangular vent positioned on the interconnecting duct was created with relief area equal to the cross-sectional area of the duct (800 mm x 500 mm) and was centered along the primary axis of the interconnected duct geometry. However, the maximum observable overpressures were still recorded as high as 1.30 and 1.15 barg in the small and large vessel, respectively. Therefore, pipe venting as a supplement to the initial relief area proved insufficient for maintaining the P_{red} below that which had been predicted for an isolated vessel.
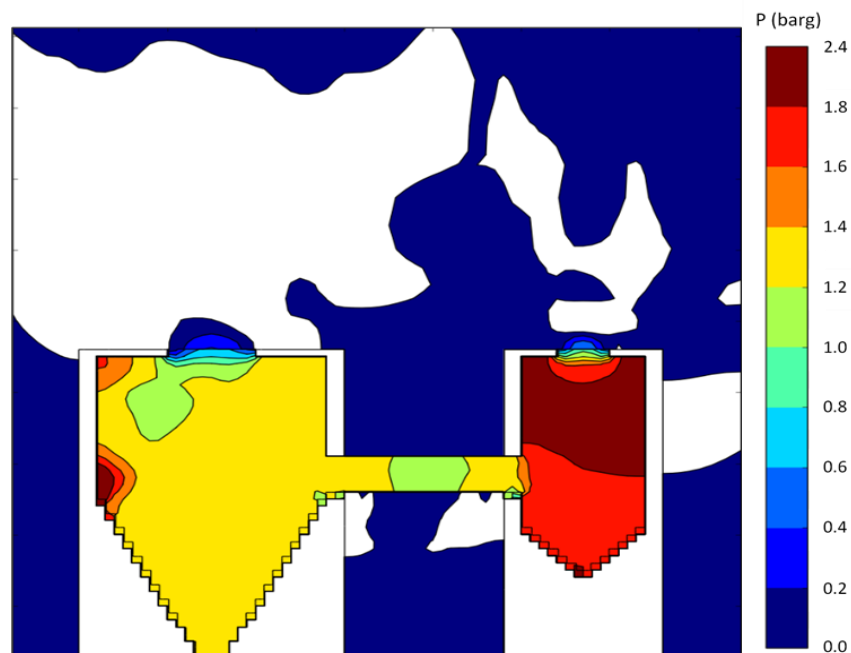
Figure 3.5. Two-dimensional depiction of system pressure (Simulation 1; 750 g/m^3 fuel concentration; ignition in large vessel), image captured at t = 260 ms

Additional simulations were prepared, incrementally increasing the vessel relief area until P_{red} fell below the target values predicted for an event in an isolated enclosure. Tables F-1 and F-2 show the maximum overpressure results for simulations at 250 g/m³ suspended fuel concentration. Tables F-3 and F-4 show the maximum overpressure results for simulations at 750 g/m³ suspended fuel concentration. Each set of tables displays simulation outcomes based on ignition occurring in both the small and large vessel, respectively. Results are illustrated graphically in Figure 3.6 (low fuel concentration) and Figure 3.7 (high fuel concentration). Increased concentration of fuel resulted in a substantial escalation of the explosion severity, thus requiring a more extensive iteration of the relief geometry. The horizontal lines present on both figures represents the target $P_{red,}$ or theoretical enclosure design strength (P_{es}) for each vessel, determined by utilizing the initial venting configurations to predict P_{red} values for an isolated enclosure. Following ignition in the large vessel at 750 g/m³ fuel concentration, the initial venting configuration required a 66% and 80% increase in the relief area on both the small and large vessels, respectively, in conjunction

with venting of the interconnected ductwork, before the P_{red} could be maintained below the corresponding predicted values for an isolated enclosure. Comparably, the simulation scenario in which ignition occurred within the small vessel required a 33% and 100% increase in the initial relief area on both the small and large vessels, respectively. Though increase in pressure with respect to that of an isolated enclosure was consistently apparent throughout the entire interconnected geometry, the largest relative generation in maximum overpressure occurred within the adjacent vessel in which ignition did not occur. In all cases, maximum overpressure monitored within the ductwork was nearly equivalent to the maximum pressures measured within the vessel in which ignition occurred.
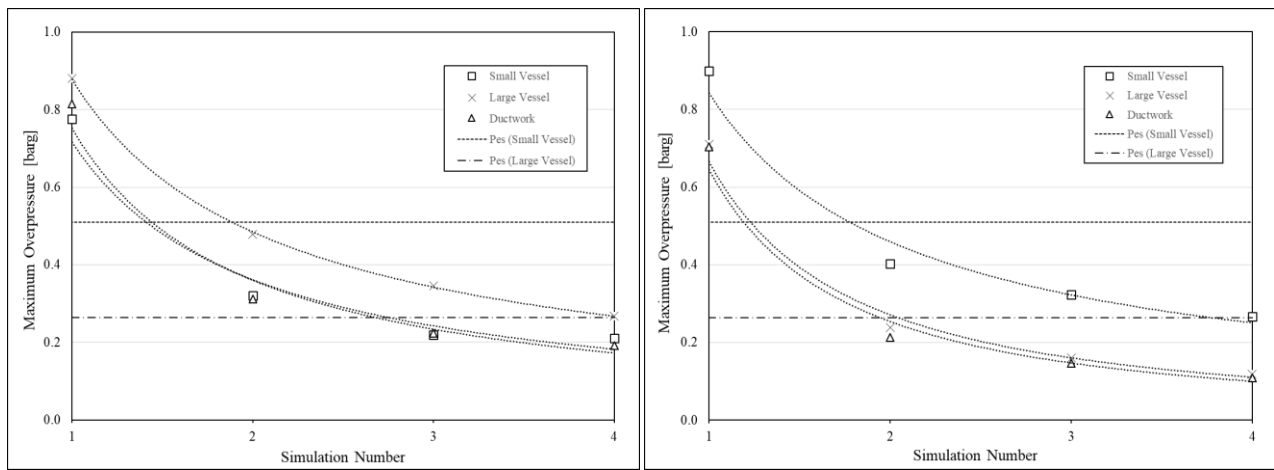
Figure 3.6. Maximum overpressure in the small vessel, large vessel, and ductwork for various venting arrangements; suspended concentration of maize starch of 250 g/m³; ignition in both the small [left] and large [right] vessel
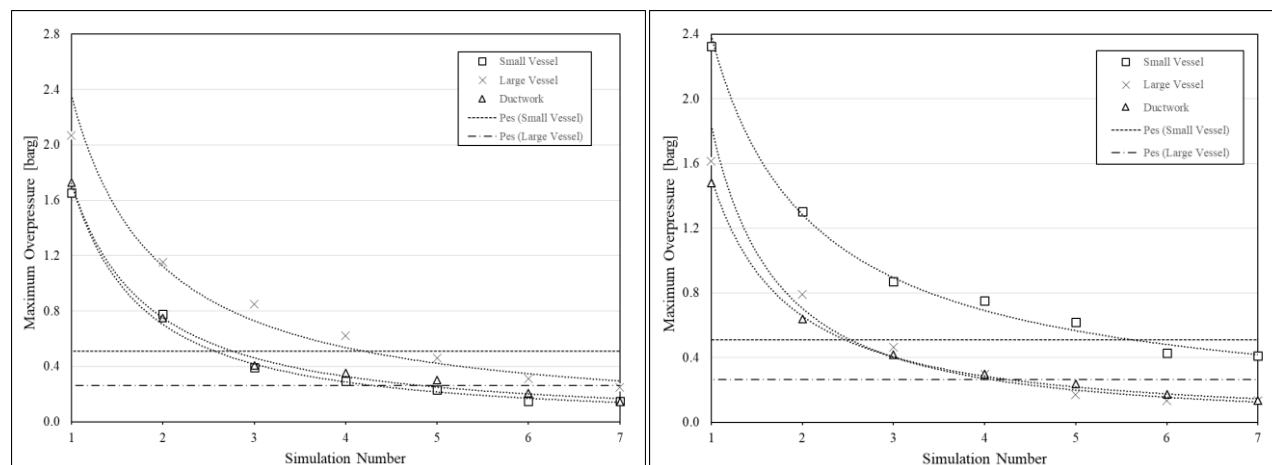
Figure 3.7. Maximum overpressure in the small vessel, large vessel, and ductwork for various venting arrangements; suspended concentration of maize starch of 750 g/m^3; ignition in both the small [left] and large [right] vessel

3.6. Conclusion

If allowed to propagate between interconnected process vessels, a developing organic dust deflagration is known to exhibit flame jet ignition and pressure piling phenomena, which contribute significantly to pressure front oscillation and irregular generation of explosion pressure. Numerical CFD simulation through FLACS was employed to evaluate the influence of these phenomena on maximum explosion overpressure and minimum venting requirements. For all scenarios considered in this work, simulated propagation to a secondary vessel without supplement to the initially designated relief area has returned maximum overpressure results considerably greater than the targeted reduced pressures (i.e., assumed equipment strengths) predicted by the corresponding vent sizing calculations for an isolated enclosure. Although relief sizing standards such as NFPA 68 may provide some recommendation on deflagration venting for interconnected vessel systems, this guidance often lacks flexibility and extends over limited application space. If the end user operates an application that does not adhere to the limitations of relevant regulatory standards or does not possess resources for large-scale validation testing, the suggested process

protection solution may be deemed under- or improperly designed by the authority having jurisdiction.

For nonstandard venting application designs that do not fit the requirements of governing sizing standards, consequence prediction using CFD simulation offers a reliable approach toward estimation of maximum overpressure within complex interconnected geometries. For any venting configuration of interest, maximum overpressure results may be monitored and compared to target enclosure design strengths. End users are encouraged to wait until the computational package is certified by Gexcon (validation of DESC combustion model through characterization of turbulent burning velocity and thermodynamic relationships for non-organic materials) before extending this iterative technique to metal dust combustion simulation. Customers requiring protection against combustible organic dust hazards, however, are recommended to perform internal risk hazard analysis or pursue engineering consultation in the form of a multivariable FLACS assessment, capable of demonstrating conservative minimum venting configurations required to maintain tolerable P_{red}'s within complicated enclosure networks which do not adhere to standard prescriptive guidance.

Chapter 4: Effect of Particle Morphology on Metal Deflagration Sensitivity & Severity

4.1. Background & Research Objectives

Certain minimum criteria must be satisfied for a dust explosion to occur. Suspension of fuel within an oxidized enclosure must see sufficient ignition energy before a deflagration may begin to develop. The physical and chemical nature of the dust fuel itself plays a substantial role in evaluating the hazardous potential of the deflagration. To this end, numerous studies have been performed for the characterization of metal fuel explosibility as a direct function of particulate size (Boilard et al., 2013; Callé et al., 2005; Cashdollar, 2000; Castellanos, 2013; Di Benedetto et al., 2010; Dufaud et al., 2010; Huang et al., 2007; Li et al., 2011; Li et al., 2016a; Mittal, 2014; Soundararajan et al., 1996; Yu et al., 2016; Yuan et al., 2014), polydispersity (Castellanos et al., 2014a; Liu et al., 2018; Wang et al., 2019), and mixture composition (Bernard et al., 2012; Cashdollar et al., 2007; Gao et al., 2017; Hartmann, 1948; Krietsch et al., 2015; Miao et al., 2016). However, investigations regarding the influence of particle shape (or morphology) on metal dust explosion sensitivity and severity are lacking.

A communication on the hazards of combustible dusts released by the Occupational Safety and Health Administration (2009) provided high-level guidance to industry regarding the significance of physical characteristics, commonly formed during material processing, on ignitability and explosibility of a dust cloud. Two separate studies conducted through the Bureau of Mines (Jacobson, Nagy, & Cooper, 1962; Jacobson, Cooper, & Nagy, 1964) examined the effect of particle shape due to various methods of processing on explosibility index and maximum overpressure, for fuels regularly found in the plastics industry and for aluminum dust fuels. Relative to spherical particles with decreased specific surface area, flake powder and other dusts of irregular surface structure with comparable nominal size distribution consistently demonstrated

a greater explosion hazard by offering opportunity for a more complete oxidation of the fuel, as well as lower heat loss over a reduced duration of combustion. Tabulated within BIA Report 13/97 (Beck, Glienke, & Mohlman, 1997), consolidation of metal dust explosibility parameters for particle morphologies that have been processed by a variety of techniques (milling, grinding, atomization, cutting, welding etc.) has exhibited a similar trend in explosion sensitivity and severity results. Illustrated through a series of Hartmann tube experiments by Thomas, Oakley, & Brenton (1991), differences in lycopodium dust morphology induced distinctive dissimilarity in ignition frequency. Textured surface, asymmetric particle shape (Liu et al., 2008), and the state of mixture agglomeration prior to ignition (Fanebust & Fernandez-Anez, 2019) all act as fundamental determinants of particle flowability during dispersion, with significant influence on the behavior of discrete flame front propagation through a suspended dust cloud. Although average particulate surface area was not formally quantified, a study led by Guo et al. (2019) compared the explosion properties of three different samples found within the fiberboard production industry and, in doing so, demonstrated an amplified explosibility index and maximum overpressure for wood dusts that exhibit a slender, fibrous nature. This outcome is an expected consequence of increased surface to volume ratio and non-uniform dispersion during injection of fuel relative to spherically shaped particles. An earlier investigation by Amyotte et al. (2012) corroborated this expectation through explosion severity and sensitivity experiments, as well as geometrical equivalence modeling, for wood and polyethylene samples of both coarse and fine flocculent morphology.

All of the aforementioned investigations report rising explosibility and ignition sensitivity with an increasingly irregular fuel particle morphology. However, a majority of these studies refrained from providing necessary documentation on size or polydispersity of the tested fuels, each a relevant factor that would have a complementary impact on effective surface area and on single-

element fuel combustion. Accurate assessment of this data would require additional acknowledgement of the origin of the powder fuels, either supplied or processed, allowing reviewers to evaluate mixture composition, moisture content, and existence of relative impurities. Qualitative authentication of morphological consistency through assessment of high-resolution scanning electron microscopy (SEM) imaging is equivalently essential. Another more recent study by Bagaria et al. (2019) displayed greater concern for decoupling the influence of particle shape from size and polydispersity. Here, researchers examined the effect of particle morphology on the minimum ignition energy of granular aluminum dusts, while taking care to extensively characterize the physical (particle size distribution, polydispersity, and shape) and chemical (composition) properties of the spherical and irregular dust samples that were tested. Although the investigation did not utilize explosibility testing to study the impact of morphology on pressure generation, the conclusions identified from this study have demonstrated that an increase in specific surface area through particle irregularity is capable of reducing conductive heat transfer within a dispersed dust cloud, while effectively promoting ignition and propagation of flame. This guidance worked toward the optimization of minimum ignition energy prediction modeling and offered industry a keen motivation to avoid dust processing and conveyance with hazardous forms of particle morphology.

Development of explosion prevention techniques and mitigation solutions for the responsive extinction of reactive metal dust deflagrations has proven challenging. Existing literature on dust cloud combustion dynamics has specified the significance of size, polydispersity, and mixture composition but lacks a concise evaluation of the independent effects of the nature of material processing. The research involved with this effort discusses the execution of and results from testing of fully characterized aluminum fuels of distinct surface morphology, with the aim of

investigating the influence of particle shape on metal dust explosion sensitivity and severity parameters. Particle shape and specific surface area are essential factors to consider, and assessment thereof should be recognized as standard procedure during risk/hazard analysis performed for the pneumatic conveyance and metal dust processing industries.

4.2. Experimental Specifications

4.2.1. MIE Test Apparatus & Methods

Explosion sensitivity properties such as limiting oxygen concentration (LOC), minimum explosible concentration (MEC), minimum auto-ignition temperature (MAIT), minimum ignition temperature (MIT), and minimum ignition energy (MIE) are extremely relevant for the design of adequate explosion prevention systems. With specific attention on the latter, the MIE of a dust cloud represents an assessment of ignition likelihood during dust handling and processing. MIE experiments allow for the determination of minimum spark energy necessary to ignite a given sample of dust, during which the ignition is defined as propagation of a flame that separates from the electrode ignition source. Assessment of MIE for all samples was performed using a Kühner MIKE3 apparatus (Figure 4.1), in accordance with test method standard ASTM-E2019-03 (2019). The device consists of a vertical 1.2-L glass Hartmann tube, with sample loading and dispersion configuration located at the bottom of the tube. Forced air through the nozzle assembly raises the charged fuel particulates into suspension. Simultaneously, a high-voltage electric spark is initiated across a designated electrode spark gap located in the center of the tube. All experiments were performed with constant 1 mH inductance. The apparatus permits testing at fixed ignition energy levels ranging from 1 to 1000 mJ and at adjustable ignition time delays of 90, 120, 150, and 180 ms. Detection of ignition (I)/no-ignition (NI) required visual confirmation by the investigator.

Figure 4.1. Kühner MIKE3 minimum ignition energy apparatus (photo at the permission of Fike Corporation)

The standard test procedure began with a dust sample weight of 1200 mg, corresponding to a suspended concentration of 1000 g/m^3, and a distinct ignition energy with high probability for ignition (e.g., 300 mJ). Ignition time delay was maintained at 120 ms for all tests. If ignition occurs, the operator then lowers the energy level, using the same concentration of fuel, until ten successive no-ignitions events are achieved or until ignition is achieved at 1 mJ. At the lowest energy level where ignition still occurs (E_2), testing is continued for higher and lower concentrations of dust – at least five different linear concentrations must be considered in order to calculate the probability

of ignition (Equation E15). At the energy level where no ignition occurs (E_1), testing is continued

for higher and lower concentrations of dust – all concentrations with ignition at energy E_2 must be

validated by ten no-ignition events at energy E_1 at adjacent concentrations until an "upswing" in

ignition energy is identified. Applying the probability of ignition, a statistically derived value for

the MIE (E_S) lies between energy levels E_1 and E_2 and may be calculated as follows:

$$MIE = E_S = 10^{\frac{(\log E_2 - I[E_2])*(\log E_2 - \log E_1)}{((NI+I)[E_2]+1)}} \tag{E15}$$

where $I[E_2]$ signifies the number of tests with ignition at energy level E_2, and $(NI+I)[E_2]$

signifies the total number of tests at energy level E_2.

The above technique was applied for all fuel samples investigated. The apparatus was regularly

calibrated, on a four-month interval, using Niacin powder. Additionally, investigations by Bagaria,

Zhang, & Mashuga (2018) have confirmed that particle breakage and change in size distribution

due to forced dispersion in the Kühner MIKE3 device may be deemed negligible for non-

electrostatic dust materials.

4.2.2. Explosibility Test Apparatus & Methods

The severity of an explosion due to ignition of combustible dust/air mixtures in a contained

combustion chamber is defined by two prominent explosion properties: maximum rate of pressure

rise associated with the expanding flame front and maximum explosion overpressure within a

constant volume (P_{max}). The former is directly proportional to the dust deflagration index, K_{St},

which is normalized by the cube root of the combustion volume as defined below:

$$K_{St} = \left(\frac{dP}{dt}\right)_{MAX} V_{vessel}^{1/3} \tag{E16}$$

Both of these characteristics are essential for developing an understanding of fuel explosibility

behavior and for proper design of explosion protection systems. For all dust morphologies

investigated, these parameters were determined following continuous pressure transducer monitoring during unmitigated, closed-vessel deflagration events within a 20 L Siwek spherical enclosure.
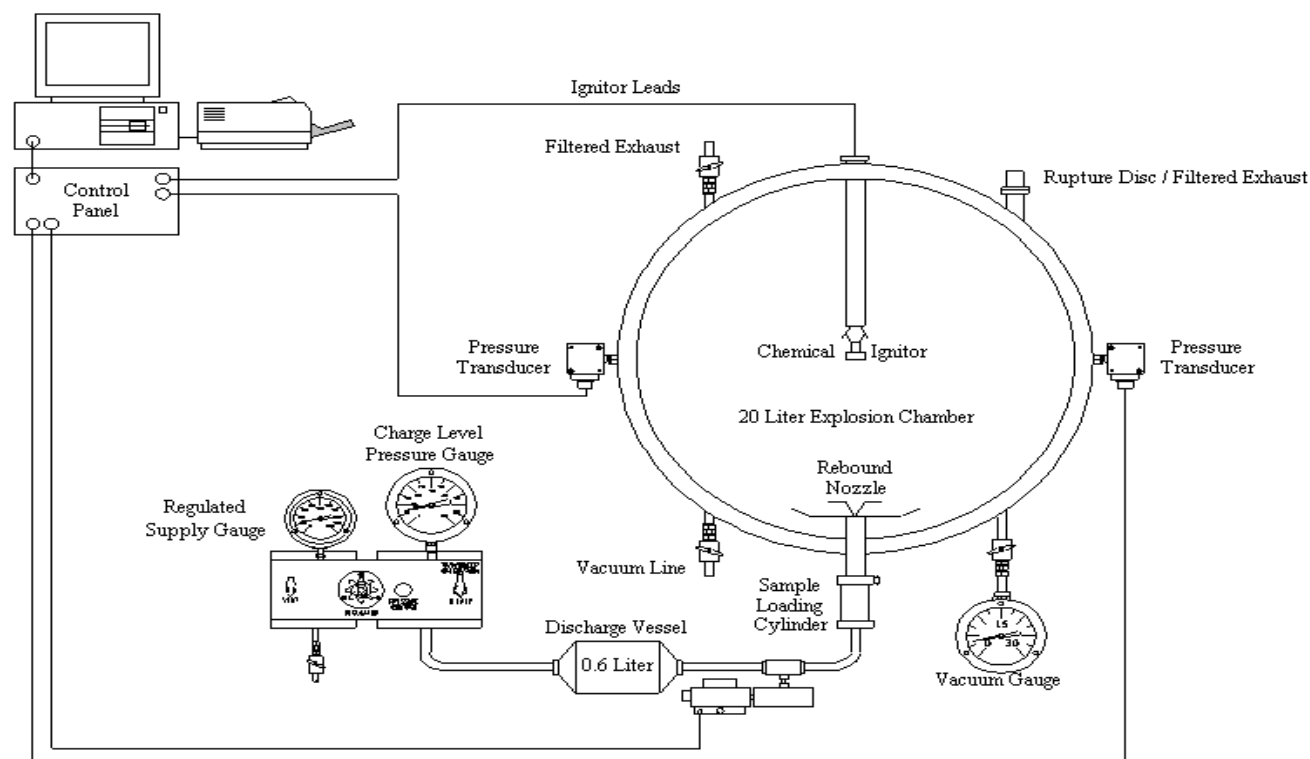
Figure 4.2. Diagram of the Siwek 20 L explosibility chamber and control components (figure reproduced with permission from Fike Corporation)

Prior to injection of fuel, appropriate vacuum level was established in order to achieve a near-atmospheric (± 5 mbarg) initial pressure at ignition. Initially loaded into a pressurized discharge vessel, fuel was then dispersed through a single rebound nozzle at concentrations ranging from 125 to 3000 g/m^3. Once the fuel was suspended, ignition of the dust cloud was consistently implemented by electronic activation of a single 5 kJ chemical igniter located centrally within the combustion volume. The specific time delay between initiation of fuel injection and ignition of the suspended dust/air mixture was maintained constant in order to sustain uniform initial turbulence for all tests performed. A diagram of the Siwek 20 L explosibility chamber, including all

interconnections for pressure detection, vacuum regulation, fuel dispersion, ignition, and control components, is shown in Figure 4.2. All testing of explosion severity was executed in accordance with the requirements of the ASTM E1226 (2019), the standard for dust cloud explosibility test methodology, and international standard ISO 6184-1 (1985). Once system pressure and temperature had stabilized, the deflagration event was considered complete. Before cleaning and recharging, a cooling jacket installed adjacent to the combustion chamber allowed for prompt dissipation of combustion heat. Pressure and combustion off-gas were relieved and exhausted, respectively, to a safe location free from operating personnel.

A vacant 0.25-inch normal pipe thread (NPT) port on the standard 20 L Siwek sphere apparatus was retrofitted to insert a centrally located thermocouple as a means of monitoring the steady state settling temperature following completion of the explosion event before heat was allowed to dissipate from the combustion chamber. In order to sustain the integrity of the thermocouple through numerous test series, an ungrounded closed-bead OMEGA thermocouple (K-type) was utilized, with a maximum allowable operating temperature of 1200 °C. Data acquisition required a single analog input channel for differential measurement of raw voltage – data capture using thermocouple module was avoided due to significantly slower acquisition speeds relative to a voltage module. Signal voltage values were adjusted using a ten-point rolling average to smooth the data set. Change in signal voltage output from the thermocouple corresponded to fluctuation in temperature internal to the combustion volume and may be applied as follows:

$$T_{settling} = T_{cold} + S \times \beta_{sensitivity} \tag{E17}$$

where T_{cold} signifies the cold junction compensation temperature, S represents the measured signal voltage, and $\beta_{sensitivity}$ is the rated thermocouple sensitivity (Seebeck coefficient, 41 $\mu V/°C$). Although the technique allows for a sufficient estimation of a combustion settling temperature

($T_{settling}$), it is important to note the drawbacks of this approach. Measurement of a precise peak flame temperature was deemed impractical due to limited responsiveness of the thermocouple relative to the data acquisition system's capability for sampling over such a brief duration of combustion. Likewise, continuous tracking of the developing flame front temperature was equivalently unfeasible due to highly irregular, non-spherical expansion of flame from the ignition point. Such a phenomenon is characteristic of dust explosibility testing in a non-quiescent atmosphere, an expected consequence of forced injection of fuel from a turbulent dispersion nozzle. Selection of thermocouple hardware mandated a distinct compromise between survivability and speed. A smaller, exposed bead thermocouple would have offered faster sampling but would not have survived the thermal shock associated with intense metal dust deflagration reactivity.

4.2.3. Materials & Fuel Characterization

All investigations within the scope of this study applied high-purity aluminum dust as the principal fuel composition. The three unique morphologies used to investigate the effect of particle shape on dust cloud MIE and explosibility were as follows: spherical granular, irregular granular, and flake. To qualify these distinctions in particle morphology, SEM imaging was recorded for each sample using a Hitachi SU8230 field emission scanning electron microscope, as illustrated in Figure 4.3. The spherical granular aluminum sample was acquired from Valimet, Inc. (product code: H-15). The irregular granular aluminum sample was acquired from Toyal America, Inc. (product code: TCP-20). The flake aluminum sample was acquired from Eckart America Corporation (product code: Chromal IV). Both granular aluminum samples (spherical and irregular) were confirmed to possess a non-volatile composition of free aluminum greater than 99.7% by weight, with trace amounts of iron and silicon. The flake sample was confirmed to

possess 2.35% carbon content by weight, which includes a 1.5% by weight stearic acid coating as required by standard flake manufacturing process protocols. Particulate leafing for the flake sample was documented by the supplier at 84% - the flake was classified as dry, with no alcohol-based solvent or emulsion.
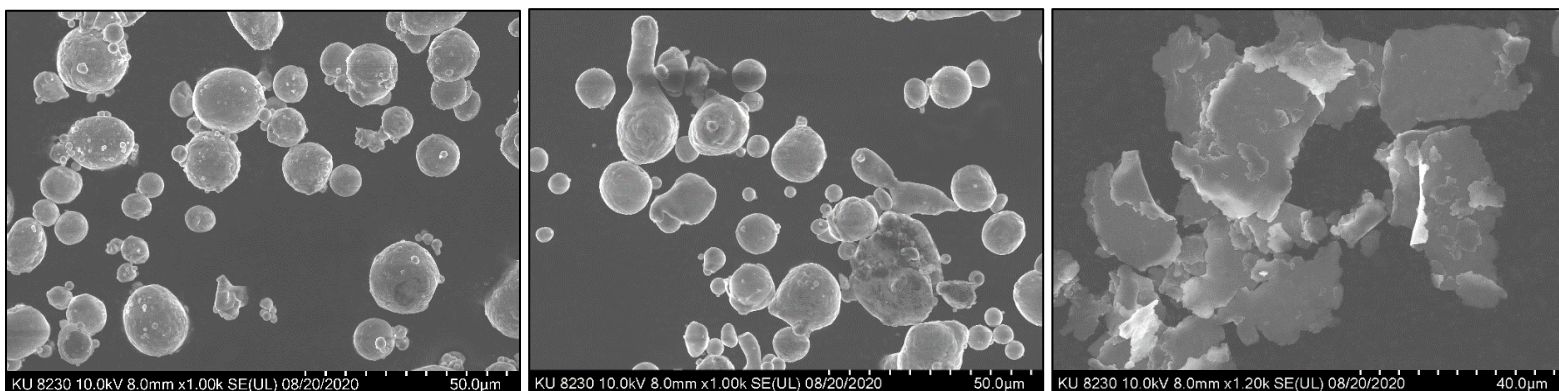
Figure 4.3. SEM imaging for all aluminum particle morphologies (spherical [left], irregular [middle], and flake [right])

To confirm that the effect of particle morphology remained independent from size and polydispersity, size distribution specifications for all samples were evaluated using a Cilas 990 laser diffraction particle size analyzer. Size distribution curves for each sample were overlaid in Figure 4.4. Polydispersity (σ_D), or the degree of heterogeneity of particle sizes within a mixture, is another parameter with significant capacity to influence fuel explosibility characteristics and may be quantified as follows:

$$\sigma_D = \frac{D90 - D10}{D50\ (median)} \tag{E18}$$

For each sample, the particle surface area was obtained through the nitrogen (N_2) physisorption on a Micromeritics ASAP 2020 Accelerated Surface Area and Porosimetry analyzer. All of the tested aluminum samples had negligible micropore volume. Hence, sample loading was maximized in the sample tube to achieve the most accurate results for non-porous samples using the Brunauer–Emmett–Teller (BET) method. Approximately 5 g samples were used to fill up to 75% of the sample tube bulb. To ensure the absence of moisture and unwanted gas molecules, samples were dried at 150 °C in a vacuum oven for 24 h before degassing in the ASAP 2020 at 150 °C for 12 h under vacuum. After the degas step, the N_2 physisorption was performed at -196 °C (77 K) using 50 data points covering adsorption and desorption over a pressure range of 0.01-0.095 of saturation pressure. The saturation pressure was measured every 120 min. BET surface area was calculated using the first nine data points between the pressure range of 0.01-0.23 of saturation pressure. All BET experiments were repeated to guarantee reproducibility of results, with deviations recorded at less than 6%.
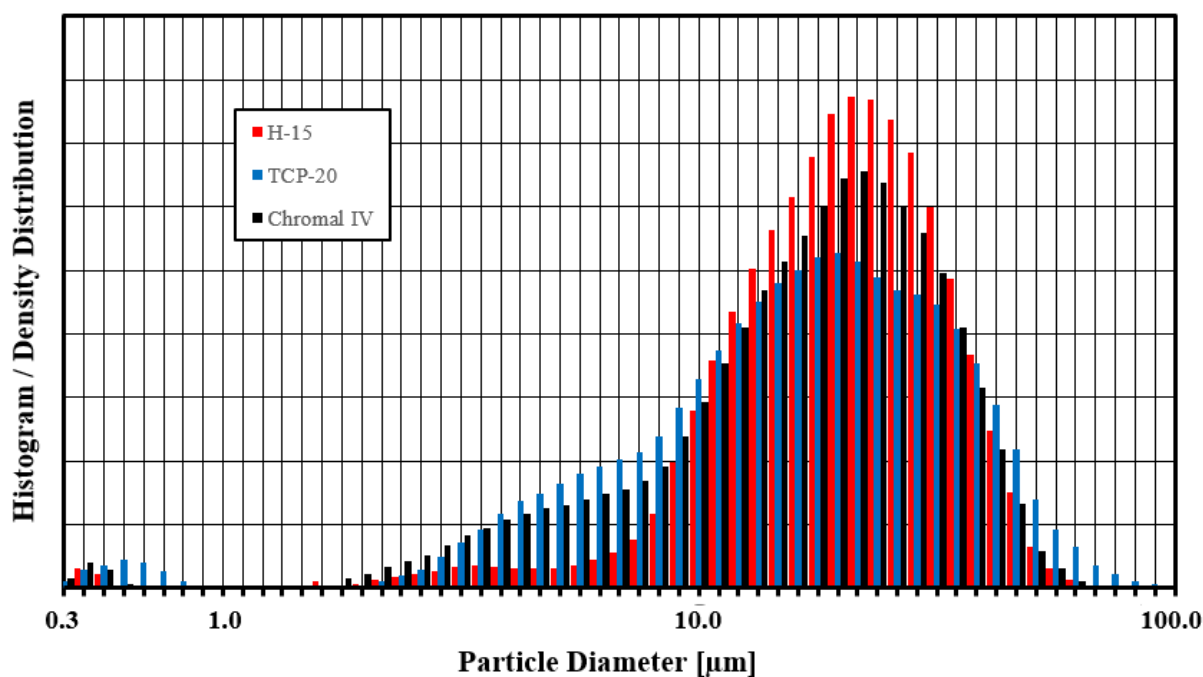
Figure 4.4. Particle size distribution histogram

Granulometric particle size metrics, polydispersity outcomes, and average BET specific surface area measurements are documented in Table 4.1. All particle size statistics (D10, median/D50, D90) and polydispersity values were shown to be similar for the three aluminum morphologies utilized for this investigation. Slight dissimilarities in size distribution and polydispersity are presumed to have a marginal effect on the resultant explosion properties (Castellanos, 2014a). BET specific surface area values demonstrated an increase with fuel particle irregularity. Spherical shaped aluminum exhibited the lowest average specific surface area at 1,960 cm^2/g, with approximately a 15% and 2,630% relative increase in specific surface area for the irregular and flake shaped aluminum samples, respectively. Prior to MIE or explosibility experiments, all samples were confirmed to contain less than 0.1% moisture content by weight.

Table 4.1. Particle size distribution statistics and average specific surface area measurements for spherical, irregular, and flake aluminum dust samples

Morphology:	Spherical Aluminum	Irregular Aluminum	Flake Aluminum
Product Name	H-15	TCP-20	Chromal IV
D10 [μm]	8.29	4.26	4.02
D50 [μm]	20.05	16.89	17.61
D90 [μm]	38.71	42.26	37.51
Polydispersity [σ_D]	1.52	2.25	1.90
Specific Surface Area [cm^2/g]	1,960	2,260	53,618

4.3. Results & Discussion

4.3.1. Explosion Sensitivity

Explosion sensitivity testing for all aluminum samples was performed using MIE analysis methodology as described in Section 4.2.1. The MIE results for the spherical aluminum sample are illustrated in Figure 4.5. Ignition was consistently observed at 100 mJ, with increasing quantity of 'No Ignition' events at the lower and upper ends of the investigated concentration range. No

propagation of flame was apparent at any tested concentration when the ignition energy was lowered to 30 mJ.
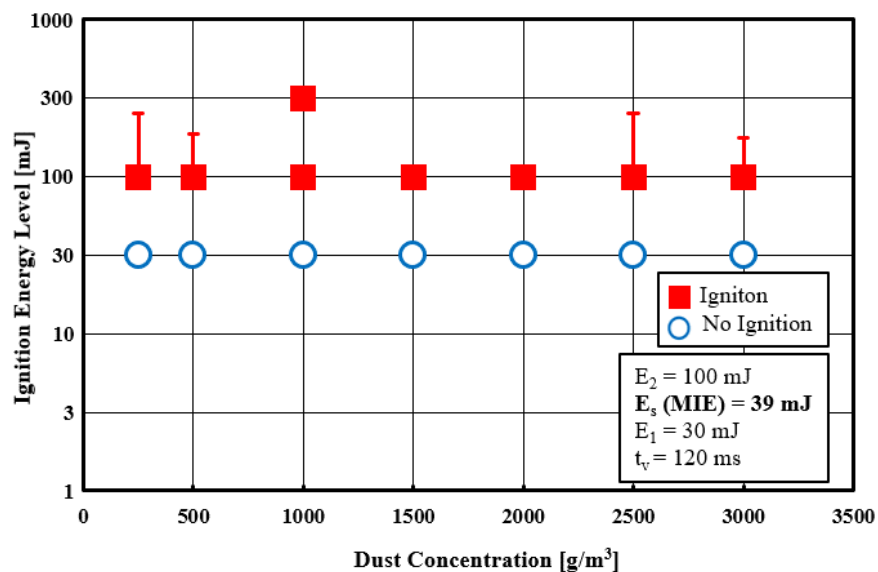
Figure 4.5. Minimum ignition energy results for the spherical aluminum dust sample, H-15

The MIE results for the irregular aluminum sample are illustrated in Figure 4.6. Unlike the spherical morphology, ignition at 30 mJ was effectively observed, with the optimal concentration for ignition located somewhere between 1,000 and 1,750 g/m^3. Any concentration outside of this range achieved ignition only at an energy level of 100 mJ or higher.
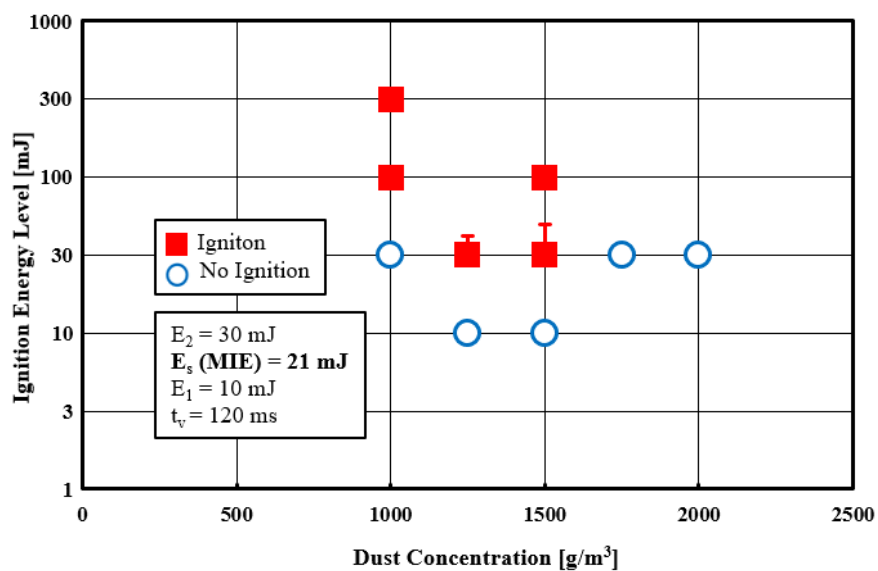
Figure 4.6. Minimum ignition energy results for the irregular aluminum dust sample, TCP-20

The MIE results for the flake aluminum sample are shown in Figure 4.7. Dissimilar to both granular samples, flake aluminum readily exhibited ignition events at 30 mJ for all concentrations. However, lowering the ignition energy to 10 mJ did not yield a continued propagation of flame. It should be noted that the flake powder behaved with conductive tendencies – in many cases, electrical discharge was overwhelmed by the dispersion of fuel. As a result, the Kühner MIKE3 apparatus had difficulties recording the existence of a spark, even when visually confirmed by the operator. With that said, ignition of the flake powder may have been possible at energy levels of 10 mJ or lower. Applying the theory of probability of ignition (Equation E15) for all sets of experiments, the MIE for each dust morphology was estimated to be 39, 21, and 11 mJ for the spherical, irregular, and flake aluminum samples, respectively. These outcomes are displayed in Table 4.2. Similar to results reported by Bagaria et al. (2019), irregularities in fuel morphology at a distinct particle size prompt an increase in specific surface area that promotes amplified rate of discrete particle combustion, thus contributing to higher likelihood of ignition at lower energy thresholds.
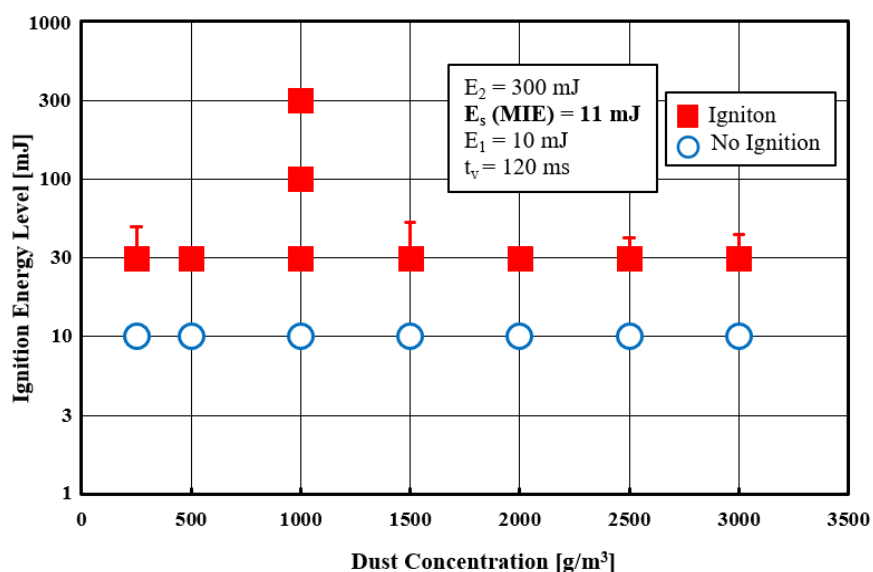
Figure 4.7. Minimum ignition energy results for the flake aluminum dust sample, Chromal IV

Industrial safety guidance provided by Chilworth Technology Ltd. (2013) offers recommendations and issues precaution when handling combustible dusts of a known MIE level. For dusts with MIE documented between 25 and 100 mJ, as was the result for the spherical aluminum sample, it is recommended that all conductive process equipment and personnel shall be bonded and grounded, with a resistance to ground less than 10^8 ohm. For dusts with MIE between 4 and 25 mJ, as was the result for the irregular and flake aluminum samples, the Chilworth report suggests all of the previously stated precautions and in addition recommends measures to control electrostatic discharge ignition from the surface of bulk granular materials. Conveyance of combustible dusts with MIE in this range mandates the implementation of explosion prevention techniques that consider the potential for spontaneous dust cloud ignition within enclosures having free volume greater than 50 m^3. A dust with MIE less than 4 mJ should be considered extremely sensitive to ignition and requires restrictions on the use of insulating materials. The process shall be conservatively designed, as if it were to contain a highly flammable gas or vapor. All risk and hazard analyses that are performed must consider mere suspension of dust (within an enclosure of any size) as a potential source of ignition.

With a substantially larger specific surface area relative to the granular powders, the flake sample offered the greatest amount of free aluminum available for oxidation in the presence of a set ignition energy. Dimensionless number evaluation provides an alternative perspective regarding the effect of morphology on apparent combustion transport mechanisms. The Biot number represents a comparison of conductive to convective heat transfer resistances. Applied more specifically toward the combustion of a singular dust particle, the Biot number signifies a ratio of heat transfer resistance on the interior of the fuel particle to the resistance on the surface

and within the external oxidizing medium. The Biot number, as shown in Equation E19, may be denoted as follows:

$$Bi = \frac{conductive\ heat\ transfer\ resistance}{convective\ heat\ transfer\ resistance} = \frac{h}{\kappa}L \qquad (E19)$$

where κ represents thermal conductivity of the solid body, h represents the convective heat transfer coefficient, and L represents the characteristic length. Since the fuel composition and testing procedure were nearly identical for all aluminum morphologies, differences in characteristic length should be the only aspect influencing the degree of allowable heat transfer during oxidative combustion of a dust cloud (κ and h are expected to be comparable for all dust samples investigated). Taken as the volume of a body divided by the effective surface area, characteristic length will be lower for particle morphologies that demonstrate increasing surface irregularity. Consequently, Biot number is anticipated to be significantly lower for the aluminum flake sample based on the substantial rise in BET specific surface area relative to both the spherical and irregular aluminum samples, as shown in the relationship below (Equation E20):

$$Bi_{spherical} > Bi_{irregular} \gg Bi_{flake} \qquad (E20)$$

A smaller Biot number designates a situation of high allowance for conductive heat transfer. As described by Sun et al. (2006), inspection of the proposed characteristic burning mechanism for an aluminum particle illustrates the impact of an amplified conduction rate on dust cloud MIE. During propagation of flame within an unburnt dust cloud, the solid particles undergo preheating as the flame front expands through the combustion volume from the ignition point. When minimum oxidation temperatures are reached, an oxide layer begins to form on the particle surface. As melting point is exceeded and boiling point is approached, remaining aluminum within the thickening oxide coating transitions to a liquid/vapor mixture. Temperatures continue to rise as oxidation progresses, resulting in a significant generation of pressure due to liquid expansion. A

lesser degree of resistance to conductive heat transfer within metal particulates of irregular surface morphology prompts rapid development of internal stress. Soon thereafter, spontaneous cracking of the oxide shell allows the release of the vapor phase through fissures in the oxidation layer. Gas-phase combustion reactions in the preheat zone induce an asymmetric flame propagation pattern and an increased probability for ignition of adjacent suspended aluminum particles. The aforementioned mechanism is more applicable to aluminum particles of granular nature. For flake morphology, however, radiative heat transfer effects begin to play a larger role by maximizing the ability to preheat surrounding particles via sympathetic ignition. This phenomenon is discussed at more detail within Section 4.3.2.

Resistance to conductive heat transfer on a discrete particle level is not the only factor affecting the likelihood of dust cloud ignition. A recent study by Prasad et al. (2020) has examined the effect of morphology on cloud dispersion dynamics. Incorporating digital in-line holography to a Kühner MIKE3 apparatus, investigators have developed a methodology to measure particle aerodynamic properties within a standard MIE experimental dispersion environment. Particles with irregular morphology were shown to possess greater turbulent velocity and suspended concentration during forced dispersion. The latter dust cloud characteristic was a predictable consequence of enlarged drag force (and reduced terminal velocity) for fuel particles with increased specific surface area. Although dust cloud turbulence has been known to demonstrate an increase in MIE because of heat loss due to convection, this effect was eclipsed by an improved conduction and suspended particle count for irregularly shaped fuels, both of which would raise the possibility of ignition at lower energy levels.

4.3.2. Explosion Severity

Applying the experimental methodology as described in Section 4.2.2, explosion severity testing for all aluminum samples was performed in the 20 L Siwek explosibility chamber. Figure 4.8 demonstrates an example of a typical measured pressure and K_{St} versus time curve using irregular aluminum dust (TCP-20) explosibility at a suspended concentration of 3,000 g/m^3. The combustion test chamber was charged with fuel and sealed under partial vacuum conditions at time zero (t = 0 ms). The aluminum dust dispersion was initiated at t = 53 ms, resulting in pressure rise due to injection through the rebound nozzle and inflow into the vessel. The combustion event was triggered via chemical igniter activation at t = 86.8 ms. Determined through closed-vessel calibration, time delay between commanded fuel injection and ignition was kept constant in order to maintain consistency in both the pressure (target ignition pressure of 1.00±0.05 bar-a) and the degree of turbulence at ignition for all experiments performed. Following ignition, combustion
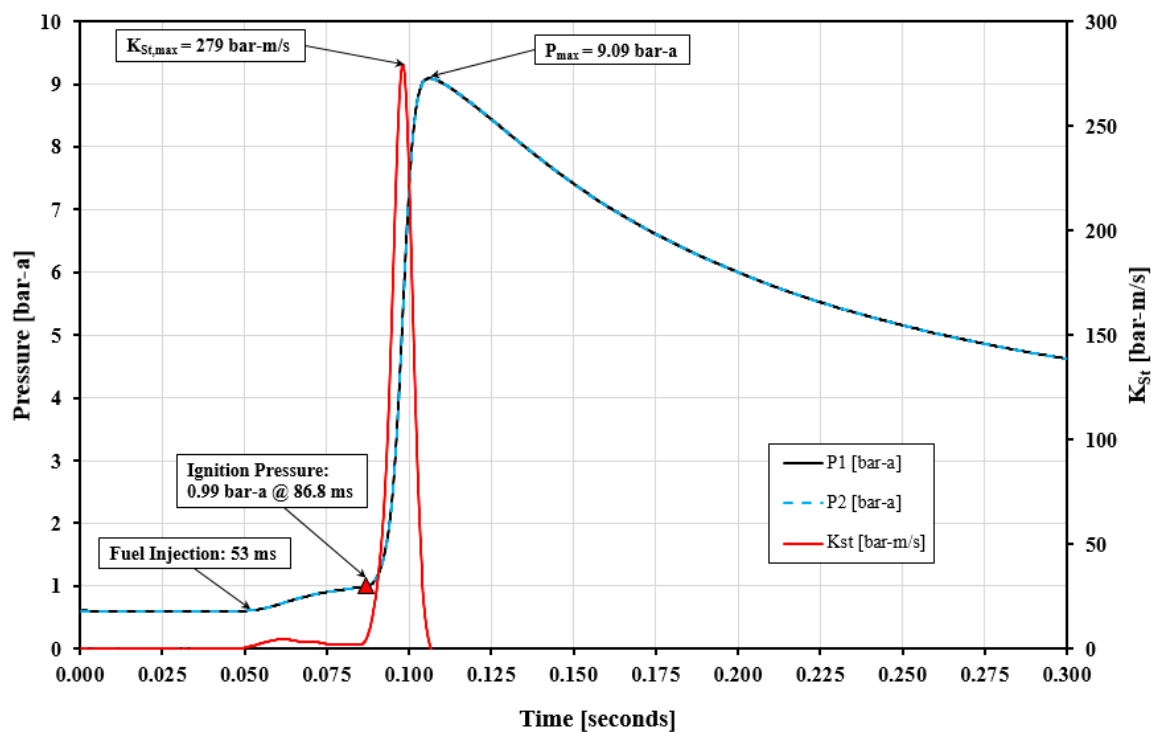
Figure 4.8. An illustration of pressure and K_{St} versus time curves for 20 L sphere explosibility testing; irregular aluminum powder (TCP-20) at 3000 g/m^3 concentration

pressure recording was continued until a distinct peak was apparent, which indicated the onset of deflagration extinction.
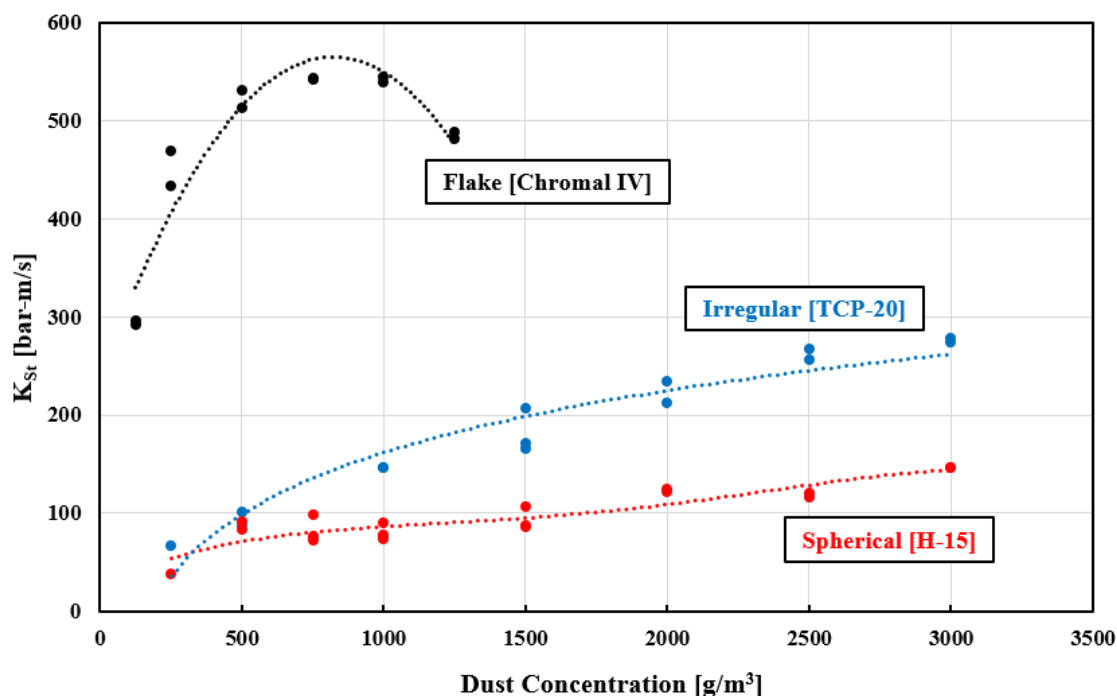
Figure 4.9. Consolidation of maximum K_{St} results for all fuel morphologies as a function of dust concentration

Figures 4.9 and 4.10 provide the consolidated K_{St} and P_{max} results, respectively, for all aluminum dust morphologies as a function of suspended dust concentration. Maximum K_{St} and P_{max} values for each morphology are shown in Table 4.2. Both spherical and irregular aluminum samples displayed a gradual rise in explosion severity as a function of increasing suspended concentration. The spherical aluminum exhibited maximum K_{St} and P_{max} at 163 bar-m/s and 7.29 bar-g, respectively, at the peak dust concentration of 3,000 g/m³. Of the three morphologies investigated, irregular aluminum exhibited intermediate explosibility properties, with a maximum K_{St} and P_{max} of 312 bar-m/s and 8.07 bar-g, respectively. Flake shaped aluminum exhibited the highest explosion severity, with a maximum K_{St} and P_{max} of 624 bar-m/s and 9.67 bar-g, respectively, even at relatively low concentrations of fuel from 500 to 1,000 g/m³. Unlike the spherical and irregular aluminum samples, the flake sample demonstrated a sharp increase in

124

explosion severity at uncharacteristically low suspended dust concentrations (<500 g/m^3). A possible result of dispersion limitations due to the relatively low bulk density, the flake deflagration intensity was observed to decline at dust concentration greater than 1,000 g/m^3. Further explosibility testing at concentrations higher than 1,250 g/m^3 was not permissible - without additional packing, which may compromise the injection performance consistency, the sample loading cylinder was simply unable to hold the full payload of charged fuel.
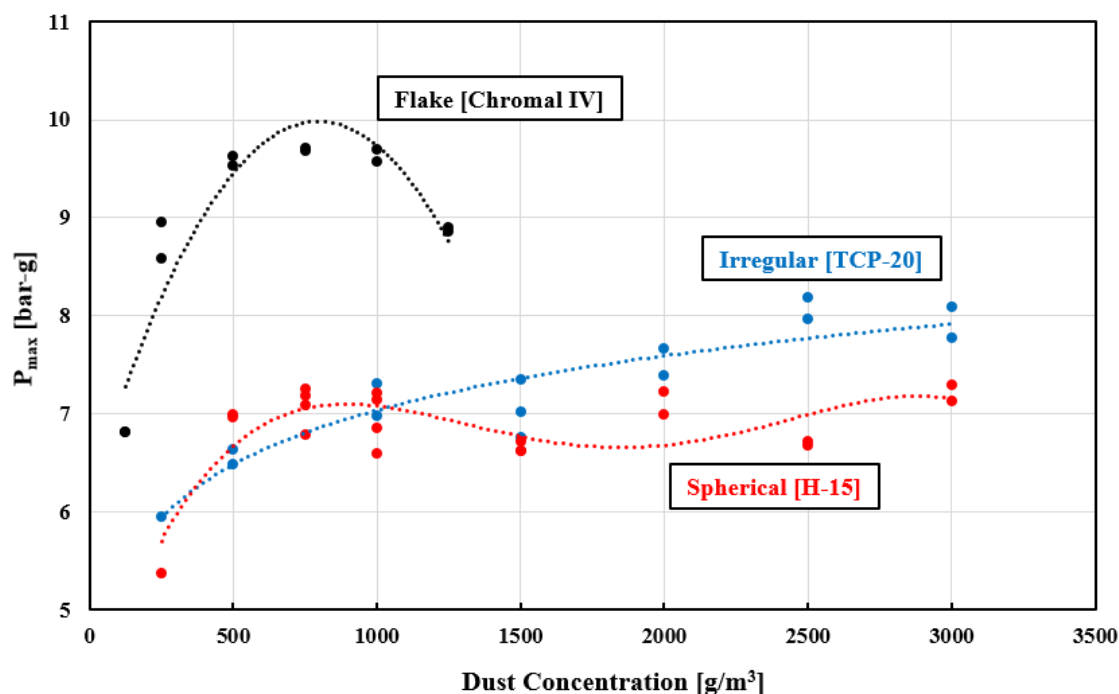
Figure 4.10. Consolidation of P$_{max}$ results for all fuel morphologies as a function of dust concentration

Aforementioned trends in flake explosion severity may be exemplified through discussion of dust cloud burning centered around radiation-based heat transport mechanisms. Erratic increase in measured dP/dt at lean concentrations of fuel indicates impulsive pockets of sympathetic ignition for groups of flake particles increasingly distant from the ignition location. With less obscuration of surrounding particles at low concentration, any given particle has an improved likelihood of positioning itself perpendicular to the incipient flame front (such that the surface area facing the burnt region is maximized) via oblique rotational motion. This orientation unique of metallic flake

promotes the intensification of particle preheating at extended distances via spontaneous radiative heat transfer phenomenon. As concentration of suspended fuel becomes more moderate, the degree of obscuration increases. Thus, at intermediate concentration, the distance at which the radiative component can induce ignition is limited. This occurrence reduces the overall fuel participation by localizing sympathetic ignition to the regions immediately adjacent to the incipient fireball and coincides with the reported drop in K_{St}/P_{max} at concentration greater than 1,000 g/m^3. Explosion severity parameters are expected to rebound and stabilize at extremely rich concentrations of fuel when the system is allowed to reach stoichiometric combustion conditions. Unfortunately, even if dust loading limitations were not present, data collection at high concentration was not possible due to risk of exceeding the design strength of the explosibility test vessel.

Table 4.2. Summary of explosion sensitivity and severity results for spherical, irregular, and flake aluminum dust samples

Morphology:	Spherical Aluminum	Irregular Aluminum	Flake Aluminum
Product Name	H-15	TCP-20	Chromal IV
MIE [mJ]	39	21	11
$K_{St,max}$ [bar-m/s]	163	312	624
P_{max} [bar-g]	7.29	8.07	9.67

Increasing Specific Surface Area

Without use of a multi-wavelength infrared pyrometer (Cashdollar & Zlochower, 2007), thermocouple hardware selection required an appropriate balance between sampling responsiveness and survivability. Thus, measurements simply did not possess the sampling responsiveness necessary to return an accurate peak flame temperature. However, estimations for the combustion settling temperature still managed to contribute insight on the deflagration severity as a function of particle shape. For all three samples, settling temperature began to stabilize at concentrations above 500 g/m^3 once fuel-rich conditions were achieved (i.e., minimum thermal

mass threshold was surpassed). Both the spherical and irregular aluminum morphologies exhibited an average maximum settling temperature of 850 °C (±47 °C at 3000 g/m^3). Flake aluminum exhibited an average maximum settling temperature of 995 °C (±22 °C at 1250 g/m^3). As expected, all values were recorded below the documented maximum adiabatic flame temperature for optimal combustion at constant volume. Elevated settling temperature for the aluminum flake sample supported the existence of a substantial peak flame temperature, as corroborated by the increased P$_{max}$ and thermodynamic potential for combustion relative to the samples with less irregularity. The rise in combustion settling temperature for the aluminum flake morphology is an indication of sizeable difference in fuel reaction participation. Resulting from enhanced drag force for irregularly shaped particles, an increased quantity of dust remained lofted in suspension for extended durations, offering an opportunity for a more complete oxidation of fuel.

For aluminum fuels with highly irregular surface morphology, Section 4.3.1 discusses two principal factors that promote heightened dust cloud ignition sensitivity: less conductive heat transfer resistance and increased suspended concentration due to reduced particle terminal velocity. Each of these attributes additionally stimulates explosion severity by contributing directly to the rate of flame front progression within the combustion volume. Albeit for a MIE dispersion scenario, the study by Prasad et al. (2020) depicted a rise in turbulent velocity for irregular aluminum particles compared to spherical particles, which has been shown to exhibit a considerable influence on explosion severity parameters (Amyotte et al., 1988; Worsfold et al., 2019). Increasing roughness and irregularity of particle shape prompt an asymmetrical dispersion of fuel. Resultant concentration gradient leads to supplementary turbulence effects and non-uniform flame front development, provoking further reactivity during combustion propagation. Following an investigation on the explosive nature of coral-shaped tantalum dust, Matsuda &

Yamaguma (2000) suggested that particles of abstract morphology might also show an increased tendency for fragmentation into fine sizes during forced injection. Although the rebound nozzle assembly utilized for these explosibility experiments has demonstrated no prior evidence of causing particle breakage, substantial alteration to the size distribution could have the capacity to influence both the profile of dispersion and explosion properties as flame front expands through the dust cloud.

4.4. Conclusion

Metal dust deflagrations continue to present a serious threat toward safe operations within a wide variety of metal refining and processing industries. This study investigated the effect of particle shape on the ignition sensitivity and explosion severity of combustible metal dust clouds. Three fully characterized aluminum samples of similar size distribution and distinct morphology (spherical, irregular, and flake) were acquired for testing. Ignition sensitivity analysis was performed in a Kühner MIKE3 apparatus according to ASTM-E2019-03. Explosion severity analysis was performed in a 20 L Siwek explosibility chamber according to ASTM E1226 and ISO 6184-1, with retrofits to support thermocouple data acquisition and estimation of combustion settling temperature. Aluminum fuels with increasing particle shape irregularity demonstrated clear escalation of deflagration sensitivity (lower MIE) and severity (higher K_{St}, P_{max}, and settling temperature). Typical of highly irregular dusts, amplified specific surface area reduces internal conductive heat transfer resistance while influencing dust cloud suspension dynamics during turbulent dispersion. The extent of adjacent particle obscuration within dust clouds with particles of irregular morphology introduces a potential for sympathetic ignition phenomena via radiative heat transfer effects. Collectively, these characteristics enable both a greater probability for

ignition at low energy thresholds and an increasingly aggressive propagation of flame front during a contained explosion event.

Particle shape has proven to be as significant as other more commonly investigated dust properties (particle size, polydispersity, and composition). Documentation of particle morphology is equivalently vital for risk assessment within processes conveying combustible metal dusts. SEM imaging and SSA quantification should be considered a standard practice when conducting hazard analysis for the design of effective explosion protection systems. To improve explosion prevention mechanisms, it is recommended that shape factor approximations be consistently employed for the enhancement of existing predictive MIE models (Bidabadi et al., 2015; Chaudhari et al., 2020; Whitmore, 1992). Using the experimental explosion severity data reported by this investigation, the authors plan to continue this work through development of an experimentally fitted pressure rise model based on thermodynamic fundamentals, with incorporation of relevant specific surface area relationships to capture the effect of particle shape on confined metal dust explosibility.

Chapter 5: Pressure Evolution Model Development

5.1. Introduction

As discussed in Chapter 1, explosion hazards of a metallic nature have unique combustion properties relative to organic dusts and are often denoted as increasingly complex in their oxidation mechanism, making flame extinction more difficult to manage. During a metal dust explosion event, energetic propagation of flame has the capacity to exhibit amplified heat of combustion, flame temperature, flame speed, ignition sensitivity, and explosibility parameters (Reding and Shiflett, 2018; Taveau, 2014; Eckhoff, 2003). Without accurate means of consequence prediction, development of overpressure protection solutions specifically tailored to the mitigation of reactive metal powder deflagrations remains challenging (Yang et al., 2021).

Dust explosion modeling continues to raise major scientific questions. Efforts at modeling dust-air combustion processes typically rely on a fixed developmental scale. At large scale, simulation techniques combine mixture reactivity estimations while considering influence of turbulence for the prediction of flame front position or deflagration overpressure (Nomura and Tanaka, 1980; Skjold et al., 2005; Bind et al., 2012). On a smaller scale, thermo-physical models are employed for the determination of fuel oxidation characteristics at a discrete particle level, such as burnout time, laminar burning velocity, and explosibility parameters (Continillo, 1989; Di Benedetto and Russo, 2007; Di Benedetto et al., 2010; Rockwell and Rangwala, 2013). Although efforts are continuously ongoing, significant progress has been made toward the proposal of combustion models to describe the burning process of a single aluminum particle. Beginning in the 1960s, Brzustowski and Glassman (1964) were among the earliest researchers to introduce the concept of aluminum burning in the vapor phase – the approach implemented model simplifications analogous to those used to denote hydrocarbon droplet combustion (classical *d-*

squared law). Nearly a decade later, Law (1973) produced an analytical diffusion flame model, amended to account for the complications of physical motion and metal oxide condensation, and established fundamental precedent for others looking to apply shrinking droplet theory for the depiction of aluminum particle combustion. Prentice (1974) defined three stages for aluminum combustion: a symmetric vapor phase combustion, an asymmetric phase due to the presence of the alumina cap, and the flame extinction. A study led by Chen and Fan (2005) developed a simplified numerical model to describe two-phase turbulent, reactive flow during flame expansion through aluminum dust injected within a horizontal combustion tube. Another investigation by Dufaud et al. (2010) proposed a mathematical model, reliant on functional mass/heat transport relationships and shrinking core behavior, and was able to achieve respectable agreement with experimental 20 L sphere explosibility data. Yet, particular characteristics of non-ideal aluminum combustion behavior and lack of consideration of transitional heating effects continue to obstruct simulation using a quasi-steady state single-particle oxidation modeling approach. For instance, the condensation and non-uniform deposition of aluminum oxide on the surface encourages fragmentation and asymmetrical distribution of physical quantities around a single burning particle (Beckstead, 2002, 2005; Braconnier et al., 2018; Liang & Beckstead, 1998). Such phenomena limit de facto the use of the classical d-squared law, based on the assumption of a perfectly symmetrical and homogeneous combustion.

Both the physical and chemical properties of a fuel component have significant influence in determining the reactive capacity of a dust deflagration. Although numerous studies exist that illustrate the effect of particle size (Cashdollar, 2000; Callé et al., 2005; Huang et al., 2007; Li et al., 2011; Boilard et al., 2013; Mittal, 2014; Castellanos, 2013; Li et al., 2016b; Yu et al., 2016), polydispersity (Castellanos et al., 2014a; Liu et al., 2018), and fuel composition (Cashdollar et al.,

2007; Krietsch et al., 2015; Gao et al., 2017) on explosion potential, investigations concerning the influence of particle shape (or morphology) on metal dust deflagration severity are limited and merit further attention (Eapen et al., 2004; Jing et al., 2021). Outlined in NFPA 654 (2017), the National Fire Protection Association defines *combustible dust* as a finely divided combustible particulate solid capable of demonstrating a flash-fire or explosion hazard when suspended within the process' oxidizing medium over a range of dispersed fuel concentrations, regardless of particulate size or shape. Identified by an uncharacteristically high energy density (23.3 kWh/L), aluminum dust is industrially processed in substantial range of size distributions and through a variety of manufacturing techniques, from atomization to ball-milling to shredding (Hirata, 1965; Malayathodi et al., 2018). Thus, such a definition of hazard accentuates the relevance of an accurate prediction of dust cloud explosibility and closed-vessel pressure generation for aluminum dust fuels with distinctly irregular morphology. Indeed, modifying the morphology of aluminum particles can lead to significant changes both in the dust dispersion (sedimentation rate, agglomeration effects, etc.) and in the flame propagation dynamics (conduct and radiative heat transfers, adsorption properties, reactivity, flame-particle interactions/stretching, etc.).

The research involved in this work reviews experimental results from recent explosibility testing on aluminum dusts of comparable size distribution and variable morphology (spherical, irregular granular, and flake), with the aim of independently evaluating the influence of particle shape on metal dust explosibility. In consideration of shrinking particle theory, this investigation explores the application of heat and mass balances for development of a mathematical model capable of forecasting pressure evolution during closed-vessel combustion, while accounting for particle surface structure via implementation of discrete geometric equivalence approaches. Suitable fit to the presented experimental data series would allow for prompt extension of

simulation methodology into imminent industrial settings in which immediate dust testing may be impractical, or into combustion testing environments where standard test conditions may be demanding and costly, for the approximation of explosibility parameters and design of effective deflagration mitigation solutions.

5.2. Background – Dust Particle Combustion Phenomena

5.2.1. Non-Catalytic Gas-Solid Particle Reaction Kinetics

From a microscopic perspective, flame propagation within a dust cloud is comprised of local events of discrete particle burning from ignition point source toward surrounding regions of unburnt fuel/air mixture. Consideration of the complexities associated with fundamental physical and chemical phenomena during single-element solid fuel oxidation is an essential first step, before a comprehensive investigation of overall reaction rate during dust cloud combustion may take place.

Transport within a single combusting particle of radius r_p may be defined as a combination of both internal (intra-particle) and external (boundary layer) heat and mass transfer phenomena. Internally, metal fuels are often characterized by higher thermal diffusivity α, and shorter thermal conduction timescale $t_{conduction}$, relative to an organic dust (Ogle, 2017):

$$\alpha = \frac{\kappa}{\rho C_p} \tag{E21}$$

$$t_{conduction} = \frac{r_p^2}{\alpha} \tag{E22}$$

Dimensionless number correlation can likewise be utilized to evaluate external contributions to transport, based on properties of the bulk environment and characteristic length of the reacting

solid particles. As an example, the Ranz-Marshall correlation is commonly used to approximate the degree of convective heat transfer exterior to a spherical particle:

$$Nu = 2 + 0.60 Re^{1/2} Pr^{1/3} \tag{E23}$$

where Nu, Re, and Pr represent the Nusselt number, Reynolds number, and Prandtl number, respectively. Analogous Sherwood number correlations exist to describe the degree of convective mass transfer. As previously mentioned, radiation is another possible mode of heat transfer that is known to exhibit significant influence over the rate of particle preheating. A high-level depiction of aluminum particle burning in a forced convection, free stream environment is illustrated in Figure 5.1 below.
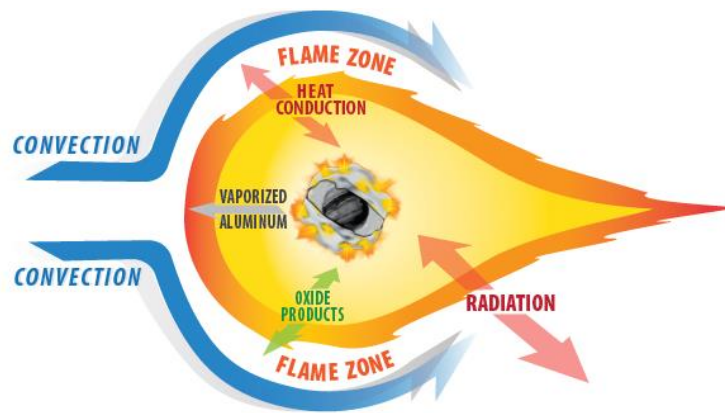
Figure 5.1. A depiction of transport mechanisms for a single burning aluminum particle

Solid fuel combustion normally presents as a combination of both homogeneous and heterogeneous non-catalytic chemical reactions. Unlike homogeneous reaction mechanisms, heterogeneous reactions require further consideration of the mass transport between phases and the discrete contacting patterns of reacting components. Heterogeneous combustion reaction occurs when a gas or liquid medium makes contact and reacts with a solid fuel particle, culminating with the generation of intermediate and final oxidation products. For a particle to continue to burn, oxygen must diffuse through the ambient gas environment, the flame zone, and the surrounding

gas film, then adsorb onto the surface, and finally react with unburnt fuel. Meanwhile, oxidation products desorb from the particle surface. During reaction, solid particles typically exhibit two distinguishable forms of behavior. If an unreacted particle contains impurities that decompose to generate non-flaking ash, or if the products of oxidation possess high yield stress relative to perturbation from surroundings, then the initial solid particle will not undergo change in size through the reaction duration. On the other hand, if flaking ash, no ash, or fluid decomposition product is formed, the solid particle will exhibit shrinkage over time, ultimately disappearing at complete conversion. At this point, it should be noted that the combustion of metal powders will not generate ash, strictly speaking, but rather oxides whose behavior can be quite different.

During non-catalytic gas/solid interaction, a constantly changing particle structure and internal microstructure (e.g., pore distribution network) weighs heavily on the combustion process of both organic and inorganic solids. Three idealized models offer a simplified portrayal of local heterogeneous reaction and diffusion behavior: the progressive conversion model, the shrinking unreacted core model, and the shrinking particle model. The functionality of all three gas-solid reaction models is confined by assumptions that the combusting particle is isothermal, that the oxidation occurs according to irreversible reaction kinetics, first-order with respect to oxygen concentration, and that transport and reaction processes are not influenced by internal particle microstructures. The solid particle is assumed isotropic and continuous in composition. The overall reaction rate is dependent on the existence (and lack) of reaction and species transport resistances R for each particular model case, as generalized below:

$$R_{total} = R_{gas\ film} + R_{ash\ layer} + R_{reaction} \tag{E24}$$

Dominance of any one resistance acts as a direct physical indication of whether the burning mechanism is kinetic-controlled (limited by the rate of gasification, pyrolysis, or devolatilization)

or diffusion-controlled (limited by diffusion of oxidant to the particle surface, through either gas film, product layer, or solid reactant). The former is known as a volatile-type flame, with oxidation typically occurring within the homogeneous gas phase. The latter is commonly referred to as a Nusselt-type flame, where chemical reaction is solely heterogeneous in nature (Eckhoff, 2003). With respect to deflagration of dispersed dust clouds, both types exhibit characteristically thicker flame fronts relative to premixed gas combustion. For volatile-type flame, this thickness may be attributed to burning of volatiles and/or pyrolysis species ejected away from the particle toward the preheat zone. For Nusselt-type flame, on the other hand, increased thickness of the combustion zone is a direct result of reduced molecular diffusion rate external to the particle surface. Experimental and analytical measure of particle burnout time has been shown to suggest the governing transport limitations.

In consideration of the progressive conversion model, the solid particle is assumed to consist of a single fuel component surrounded by a gas film, which serves as a diffusion boundary for reactant gas transport from the bulk free stream to the local solid surface of the particle. Oxygen then penetrates the interior surface and reacts continuously throughout the solid at a rate unique to the location within the particle, with both oxygen concentration and conversion progressively increasing from particle center to exterior. Although this approach to gas/solid reaction and diffusion may not be entirely applicable to the brief timescale of solid-state dust cloud deflagrations, the concepts may be rationally condensed to the fundamental forms of both the shrinking unreacted core model and the shrinking particle model (Ishida & Wen, 1968, 1971a).

Following initial development for particle combustion analysis by Yagi and Kunii (1955), the shrinking unreacted core model considers that the reaction front occupies a thin boundary. Beginning first at the outermost surface of the unburnt fuel particle, the oxidation reaction occurs

at a narrow interface and progresses radially inward toward the particle center, leaving behind a porous inert product layer (also known as an "ash layer") that is permeable to oxygen diffusion. Once the product layer has acquired appreciable thickness, oxygen penetration through this porous medium to the shrinking unreacted core surface results in a supplementary resistance to transport, in addition to diffusion through the gas film separating the particle from the surrounding free stream environment. While reaction progresses, gas-phase reaction products (if any exist) diffuse back through the ash layer to the particle exterior, and then through the gas film to the surroundings. Analogous to the progressive conversion model, and as depicted in Figure 5.2, shrinking unreacted core ideology assumes that the initial particle diameter (including both non-porous unreacted core and product layer accumulation) remains constant while solid is converted, a valid postulate if the bulk densities of the unreacted solid phase and the exterior product layer are equivalent. Although the model operates under isothermal conditions, substantial rate of heat release during combustion is likely to induce significant temperature gradients and mechanical stresses within a particular suspended particle. Noteworthy effects of such non-isothermal behavior have been previously investigated (Shen & Smith, 1965; Ishida & Wen, 1971b).
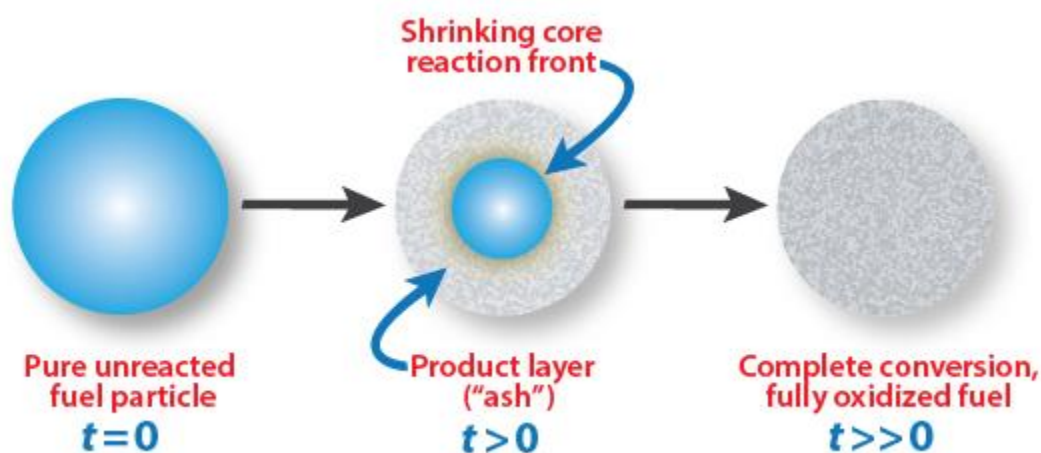

Figure 5.2. Illustration of shrinking unreacted core model for spherical particles of unchanging size

When no ash forms, or if products do not remain on the particle surface following oxidation, the rate of reaction may be depicted by the shrinking particle model. Identical to the shrinking unreacted core model, reaction with oxygen occurs exclusively at the solid surface – the non-porous unreacted particle decreases in size while conversion increases. However, without the presence of an ash layer, only gas film diffusion contributes as the principal resistance to mass transport. As an example of application, consider the following generalized first-order reaction mechanism:

$$O_{2,gas} + bB_{solid} \rightarrow flaking\ ash\ or\ fluid\ oxidation\ products \tag{R18}$$
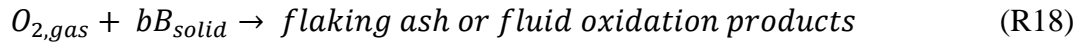
where b is the stoichiometric coefficient for the solid reactant per single mole of oxygen that is consumed. Since the conversion is directly proportional to the remaining surface area of the shrinking particle, one may begin with a mass balance on reacting species O_2 and solid B. If the rate of reaction is less than the rate of diffusion across the surrounding gas film, then the overall rate is limited by reaction kinetics. Under the assumption that reactant consumption rate is chemical reaction controlled:

$$-\frac{1}{4\pi r_p^2}\frac{dN_{O_2}}{dt} = -\frac{b}{4\pi r_p^2}\frac{dN_B}{dt} = bkC_{O_2} \tag{E25}$$

where N_x represents the available moles of species 'x', C_{O_2} signifies the bulk concentration of free-stream oxygen, r_p signifies radius of the spherical shrinking particle at any point in time t following reaction initiation, and k signifies the first-order rate constant for the limiting heterogeneous surface reaction described by Reaction R18. The decrease in moles of solid reactant B shall be denoted using the particle density and a differential on the unreacted particle volume, as follows:

$$-dN_B = -\rho_B d\left(\frac{4}{3}\pi r_p^3\right) = -4\pi\rho_B r_p^2 \cdot dr_p \tag{E26}$$

Substitution of Equation E26 into Equation E25 yields:

$$-\rho_B \frac{dr_p}{dt} = bkC_{O_2} \tag{E27}$$

With the assumption that available oxygen concentration on the surface is not a function of time,

integration from initial particle size R_o to an arbitrary final time t yields:

$$-\rho_B \int_{R_o}^{r_p} dr_p = bkC_{O_2} \int_0^t dt \tag{E28}$$

Solving the above and isolating for time:

$$t = \frac{\rho_B}{bkC_{O_2}} [R_o - r_p] \tag{E29}$$

Next, determine the time for full conversion of the solid particle τ, when $r_p = 0$:

$$\tau = \frac{\rho_B R_o}{bkC_{O_2}} \tag{E30}$$

Dividing Equation E29 by E30, the fractional conversion for a shrinking particle with chemical

reaction limitation is directly related to the shrinking particle radius and can be expressed as:

$$1 - X_B = \frac{volume\ of\ unreacted\ particle}{volume\ of\ initial\ solid\ particle} = \left(\frac{r_p}{R_o}\right)^3 \tag{E31}$$

$$\frac{t}{\tau} = 1 - \frac{r_p}{R_o} = 1 - [1 - X_B]^{1/3} \tag{E32}$$

where fractional conversion X_B represents the fraction of reactant B that has been converted to

products (Levenspiel, 1999). Furthermore, combining Equation E32 with Equation E29, and taking

the derivative with respect to time, leads to the following functional balance expression for reaction

conversion rate:

$$\frac{dX_B}{dt} = \frac{3 \cdot bk}{\rho_B R_o} [1 - X_B]^{2/3} [C_{O_2}]^n \tag{E33}$$

where n represents reaction order (in this case, $n = 1$). Since the existence of an ash layer has no

effect on the conversion progress, the derivation and resultant Equation E33 are also applicable to

the previously described shrinking unreacted core model with chemical reaction limitation. Similar

expressions for fractional conversion and conversion rate may be derived in the case of film diffusion control. For metallic particles, the combustion regime tends to gravitate toward chemical reaction kinetic control as particle size decreases, especially for particles with mean size in the nano-scale (Bouillard et al., 2010).

For the combustion of liquid hydrocarbon in air, the droplet size reduces over the duration in which it is burned, with the burnout time being directly proportional to the square of the original unburnt droplet diameter. This relationship is commonly known as the *d-squared law*. For small particles (Stokes regime), the shrinking particle model under film diffusion limitation has been shown to exhibit burnout behavior equivalent to the d-squared law. Although not derived here, the diffusion flame analysis of liquid droplet combustion serves as an analogous foundation for the burning mechanism of discrete single-element solid fuels. Yet, this proportionality does not always account for uniqueness in a fuel's response to external heating or potential intricacies of solid particle oxidation behavior.

5.2.2. Approximation for Bulk Flame Position & Burn Velocity

Considered vital for the design of suitable explosion protection solutions, two explosibility parameters are necessary to develop an understanding of a dust cloud's unique deflagration potential: the maximum rate of pressure rise $\left(\frac{dP}{dt}\right)_{MAX}$ and the maximum achievable explosion overpressure P_{max} generated within the test chamber at a discrete suspended fuel concentration. The former is proportional to the dust deflagration index K_{St}, and is defined as shown below:

$$K_{St} = \left(\frac{dP}{dt}\right)_{MAX} V_{vessel}^{1/3} \qquad (E34)$$

Normalized by the cube root of the combustion vessel volume V_{vessel}, this relation is known as the *cube-root law* (Eckhoff, 2003). Inaccuracy when applying this law to industrial scenarios is

generally a result of deviation from certain principal theoretical assumptions, including spherical enclosure geometry uniformly charged with unburnt fuel mixture, burning rate independent of vessel volume, quiescent dispersion of unburnt particles, and centrally located point source ignition (Hertzberg & Cashdollar, 1987). The flame region is assumed to expand spherically through the combustion volume away from the initial ignition point, consuming oxidation reactants on the downstream side and leaving behind high temperature combustion products in its path. Unburnt fuel particles are introduced to the oncoming flame (with thickness δ) at a laminar burning velocity S_u and burn for a specific duration of time t_{comb} according to the following relationship:

$$\delta = S_u \cdot t_{comb} \tag{E35}$$

For fuels with high reactivity, time delay between inflection point $\left(\frac{dP}{dt}\right)_{MAX}$ and peak explosion pressure P_{max} becomes increasingly small. A sharp rise in system pressure implies that all unburnt fuel has contributed to the combustion (thermodynamic limitation) very soon after the leading edge of the flame sheet has arrived at the vessel wall (kinetic limitation). Such an implication encourages behavior best characterized by the 'thin-flame model', in which the radially propagating flame resembles an infinitely thin interface (a distinct discontinuity between burnt and unburnt zones) rather than a reaction zone of perceptible thickness. In addition to the expectations outlined by the cube-root law, the 'thin-flame model' assumes ideal gas behavior for both burnt and unburnt mixtures, constant specific heat ratio, adiabatic compression (and corresponding increase in temperature) of the unburnt mixture, and combustion rate based on a simple, irreversible oxidation reaction at the flame boundary. Readers should keep in mind that this assumption is increasingly relevant for combustion of dispersed gas clouds and was made here for the purpose of mathematical simplification – in application, flame zone thickness during propagation through a dust cloud is finite in size, commonly ranging from 15 to 80 cm (Dahoe et al., 1996). Moreover, it

should be emphasized that applying the 'thin-flame model' implies assuming a negligible impact of thermal radiation on the flame geometry. An approximation for the mass fraction of unburnt mixture can be initially defined as a function of experimental pressure rise (Lewis & von Elbe, 1987):

$$\frac{m_u}{m_{u,o}} = \frac{P_{max} - P}{P_{max} - P_o} \qquad (E36)$$

where $m_{u,o}$ and P_o represent the initial suspended mass of fuel and initial system pressure, respectively. Differentiation of Equation E36 with respect to time yields an expression for the rate of pressure rise:

$$\frac{dP}{dt} = -\frac{P_{max} - P_o}{m_{u,o}} \frac{dm_u}{dt} \qquad (E37)$$

To promote increasing functionality, the rate of unburnt mixture consumption $\frac{dm_u}{dt}$ within Equation E37 can be expanded using the surface area and burn velocity of the developing flame front:

$$\frac{dP}{dt} = \frac{P_{max} - P_o}{m_{u,o}} \; 4\pi \, r_{flame}^2 \rho_u S_u \qquad (E38)$$

where ρ_u represents the density of the unburnt dust cloud mixture, and r_{flame} represents the radius of the flame front at any point in time during the explosion event. Next, consider a volume balance around the contents of the combustion vessel:

$$V_{vessel} = \frac{4}{3}\pi \, r_{flame}^3 + \frac{m_u R T_u}{P} \qquad (E39)$$

where T_u represents the unburnt gas mixture temperature and R represents the ideal gas constant. The first term signifies an estimation of the burnt mixture volume using flame radius - the second term signifies an estimation for unburnt mixture volume using ideal gas equation of state. After applying an approximation similar to that shown in Equation E36, the second term of Equation E39 may be re-written as follows:

$$\frac{m_u R T_u}{P} = \frac{4}{3}\pi\, r_{vessel}^3 \left[\left(\frac{\rho_{u,o}}{\rho_u}\right) \frac{P_{max}-P}{P_{max}-P_o} \right] \tag{E40}$$

where $\rho_{u,o}$ represents the initial unburnt mixture density and r_{vessel} represents the combustion vessel radius. Following substitution into Equation E39, the volume balance may be further simplified to the following form, useful for determination of flame radius based on experimental overpressure:

$$r_{flame} = r_{vessel} \left[1 - \left(\frac{\rho_{u,o}}{\rho_u}\right) \frac{P_{max}-P}{P_{max}-P_o} \right]^{1/3} \tag{E41}$$

Assuming unburnt mixture compression is isentropic ($P\rho^{-\gamma} = constant$), substitution of Equation E41 into Equation E38 yields the following dynamic solution for burning velocity (Dahoe et al., 1996; Dahoe & de Goey, 2003; Bradley & Mitcheson, 1976):

$$S_u = \frac{r_{vessel}}{3(P_{max}-P_o)} \left(\frac{dP}{dt}\right) \left(\frac{P}{P_o}\right)^{-1/\gamma} \left[1 - \left(\frac{P_o}{P}\right)^{1/\gamma} \frac{P_{max}-P}{P_{max}-P_o} \right]^{-2/3} \tag{E42}$$

Revisited in Section 5.3, the relationships derived above for flame radius (Equation E41) and burning velocity (Equation E42) are essential for iterative solving of functional thermal balance equalities and for output of resultant model predictions for deflagration pressure as a function of time post-ignition.

5.2.3. Combustion of Metallic Solids

An extensive review of dust explosion dynamics by Ogle (2017) introduces principles of single-element particle modeling for inorganic combustible dusts, including volatile and nonvolatile metallic solids, while taking into account unique phase behavior of oxide components that are formed. Although the initial reduced state often presents a worst-case explosibility scenario, most metallic powders found within industry exhibit significant variation in reactivity

due to differences in mixture composition, particle size, morphology, and degree of oxide coating that has already formed on the particle surface prior to ignition.

Inorganic metal dusts demonstrate a distinct response to external heating. Unlike the pyrolysis of organic solids, in which thermal decomposition products do not see much participation in the combustion reaction, metals experience phase transitioning during heating and readily interact as part of the principal oxidation mechanism. The type of mechanism involved is reliant on factors such as volatility (of both the metal and metal oxide – relative to their melting and vaporization temperatures), flame temperature, and solubility of various metal oxide species within the parent metal of interest. Dependent on the magnitude of the constant pressure adiabatic burning temperature relative to metal and metal oxide melting points, metal dust combustion may exhibit one of three discrete burning modes: low temperature oxidation, combustion on the metal surface, or combustion within the vapor phase (Yetter & Dryer, 2001). The documented flame temperature for a particular metal composition is bounded by the vaporization temperature of the metal oxide component. Increased metal flame temperatures are known to supplement the combustion rate via thermal radiation flux throughout regions of preheating unburnt fuel (Glassman, 1960; Leuschke, 1965). Contribution to metal dust flame propagation from radiative heat transfer is hypothesized to increase considerably for highly irregular particle morphologies (Reding et al., 2021). Indeed, for microparticles, light scattering is notably enhanced by a very irregular shape, whereas the opposite effect is observed for submicron particles (Penttilä & Lumme, 2004). Although simplified by a limited number of reaction intermediates compared to organic solid combustion, metal oxidation retains a degree of complexity with homogeneous and heterogeneous reaction mechanisms (influenced by the growing alumina cap) often occurring in parallel.

Taken from an aggregate of commercial data on existing explosion protection applications, aluminum and iron are the most frequently encountered metal dusts hazards within bulk storage and pneumatic conveyance industries (Clouthier et al., 2019). Coincidently, these two metal compositions additionally represent the full spectrum of recognized metal oxidation kinetics behavior, with aluminum adhering to the shrinking particle theory and iron adhering to the shrinking unreacted core theory. Beginning with the former, the reaction equation for stoichiometric combustion of solid aluminum is as shown below:

$$\frac{4}{3}\text{Al}_{(s)} + \text{O}_{2\,(g)} \rightarrow \frac{2}{3}\text{Al}_2\text{O}_{3\,(s)} \tag{R19}$$
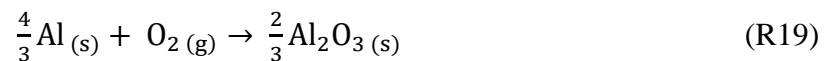
It should be noted that reactions between aluminum and nitrogen to generate aluminum nitrides will not yet be considered. Since the boiling point of aluminum oxide exceeds that of aluminum, it is suggested that aluminum combustion in air occurs predominantly in the vapor phase (Brzustowski & Glassman, 1964). Depicted as a molten droplet surrounded by a halo of oxide combustion products (Grosse & Conway, 1958), the burning mechanism of moderately sized aluminum particles has been shown to demonstrate detached diffusion flame behavior similar to that of liquid hydrocarbon combustion (Kanury, 1975; Ballal, 1983; Bazyn et al., 2007). Before non-idealities are introduced, the approach outlined by the d-squared law has proven to be a reasonable prediction for burnout time during diffusion-controlled volatile metal combustion. However, phase equilibrium has a unique influence on aluminum particle combustion by prompting the condensation of gas-phase reaction products to form an amorphous alumina layer on the particle surface (Dreizin, 1996). Other observed deviations from ideal aluminum burning behavior include incomplete oxidation, asymmetric burning pattern, oxide cap transparency, flame jetting from the particle surface, and fragmentation of particle microstructure (Beckstead, 2002, 2005).

A less reactive explosion hazard relative to aluminum, nonvolatile iron powder combustion relies exclusively on heterogeneous reaction mechanism and displays behavior of the shrinking unreacted core gas/solid kinetic model described in Section 5.2.1. As proposed by Sun et al. (2000), oxygen molecules first diffuse through the surrounding gas film. Assuming the iron particle surface has already undergone a certain extent of natural oxidation before ignition, oxygen is left to adsorb onto the existing iron oxide layer. After dissociating from its diatomic state, oxygen diffusion continues inward to a molten iron reaction zone at the surface of the unreacted solid. As the unreacted core undergoes further conversion and begins to shrink in size, an exterior porous product layer continues to increase thickness. In the case of experimentally observed iron particle combustion, however, the particle size does not remain constant – rather, the overall particle diameter diminishes slightly due to a less dense oxide layer compared to iron (Sun et al., 1998).

5.3. Pressure-Rise Model Development & Outcomes

Simultaneously solving functional mass and heat balance relationships within a numerical MATLAB® computational program, the pressure evolution during unmitigated aluminum dust explosions within a contained 20 L spherical combustion vessel has been modeled as a function of time for aluminum dust morphologies and concentrations that were experimentally investigated during a previous study (see Chapter 4). The severity of all explosion events was experimentally quantified through evaluation of aforementioned principal explosibility parameters, K_{St} and P_{max} – outcomes for all three morphologies are tabulated in Table 5.1 as a function of variable fuel concentration.

Table 5.1. Measured K_{St} and P_{max} values from 20 L Siwek explosibility testing for spherical, irregular, and flake aluminum dust samples (Reding et al., 2021)

Morphology:	Spherical Aluminum		Irregular Aluminum		Flake Aluminum	
Concentration [g/m^3]	K_{St} [bar-m/s]	P_{max} [bar-g]	K_{St} [bar-m/s]	P_{max} [bar-g]	K_{St} [bar-m/s]	P_{max} [bar-g]
125	-	-	-	-	339	6.79
250	41	5.39	68	5.94	516	8.56
500	95	6.96	109	6.62	611	9.53
750	-	-	-	-	624	9.67
1000	81	7.14	163	6.98	624	9.58
1250	-	-	-	-	570	8.81
1500	122	6.72	231	7.34	-	-
2000	136	7.24	258	7.65	-	-
2500	136	6.66	299	7.95	-	-
3000	163	7.29	312	8.07	-	-

For a variety of potential combustion regimes (reaction or diffusion limited, with or without constant particle size), expressions for the chemical conversion rate $\frac{dX}{dt}$ were analytically derived, similar to the mass balance derivation that has been demonstrated in Section 5.2.1. The contained combustion test chamber modeled by the developed program represents a closed-vessel system, in which mass input and output may be set equal to zero. Thus, the reactant disappearance and accumulation rate are equivalent and may be denoted as follows:

$$(-r_{total}) \cdot V_{vessel} = \frac{dN_{Al}}{dt} = \frac{d[N_{Al,o}(1-X)]}{dt} \tag{E43}$$

where r is the overall reaction rate, N_{Al} is the number of moles of aluminum dust in the system at any time t, and $N_{Al,o}$ is the number of moles of aluminum dust initially injected to suspension within the combustion chamber. Applying the fundamentals of shrinking core theory, all mass balance derivations were reduced from the following fractional conversion relationships provided by Levenspiel (1999) for heterogeneous reaction of spherically shaped solid particles:

$$\textit{Film Diffusion Control (constant particle size):} \qquad \frac{t}{\tau} = X \tag{E44}$$

$$\textit{Film Diffusion Control (shrinking particle size):} \qquad \frac{t}{\tau} = 1 - (1-X)^{2/3} \tag{E45}$$

$$\text{\textit{Reaction Control (constant particle size):}} \qquad \frac{t}{\tau} = 1 - (1 - X)^{1/3} \qquad \text{(E46)}$$

$$\text{\textit{Reaction Control (shrinking particle size):}} \qquad \frac{t}{\tau} = 1 - (1 - X)^{1/3} \qquad \text{(E47)}$$

where the time for full conversion of the solid particle (τ) may be described generally as:

$$\tau = f\ (\rho, R_o, k, C_{O_2}) \qquad \text{(E48)}$$

in which k represents the kinetic rate constant according to the Arrhenius law:

$$k = A \cdot \exp\left(-\frac{E_a}{RT}\right) \qquad \text{(E49)}$$

and where A and E_a represent the pre-exponential factor and activation energy of the reaction, respectively, and act as fitted parameters estimated by the MATLAB® program using an *fminsearchbnd* subroutine to provide a degree of numerical resolution. Since aluminum particle burning is presumed to exhibit both oxide phase transition and a readily deforming external product layer, ash layer diffusion control was not considered as a potential combustion regime. General uniform conversion may also be applied by employing the following simplified expression for oxidation conversion rate:

$$\frac{dX}{dt} = bk[1 - X][C_{O_2}] \qquad \text{(E50)}$$

Investigations by Balakrishnan (2014) and Bazyn et al. (2007) have reported transition from diffusion to reaction limited combustion regime for aluminum particles with diameters larger than 7.5 µm. Larger sized particles, like the samples modeled for this investigation, exhibit lower burning temperatures and decreased overall combustion kinetics on the particle surface. Further, as discussed in Section 5.2.3, aluminum particle oxidation has been consistently found to adhere to the fundamentals of shrinking particle theory. Although relationships for extent of reaction rate were derived for all fractional conversion expressions previously noted, for these reasons only the expression analytically derived from Equation E47 (which applied rate control by reaction

limitation and non-constant particle size) was employed as the effective mass balance for all simulations. In this specific case, Equation E48 becomes:

$$\tau = \frac{\rho R_o}{b k C_{O_2}} \tag{E51}$$

The solution sensitivity with respect to user-defined values of pre-exponential factor and activation energy initialization has been additionally investigated through measurement of deviation in model predicted explosibility (K_{St} and P_{max}) and the apparent rationality of fitted kinetic parameters. In order to reduce the likelihood of convergence issues when solutions are unable to circumvent the boundaries of isolated potential wells, a modified multi-start procedure was engaged to cycle through initial kinetic parameter combinations, reporting only simulation outputs that yield a minimized summation of error for an explicit suspended concentration and morphology. Starting points were evenly distributed over the entirety of the defined kinetic parameter search interval.

Particle diameter is a vital characteristic length scale, with significant influence on kinetic and transport processes during dust cloud combustion. Although the conversion-time relationships derived using Equations E44 to E47 were predominantly based on an assumption of spherical particle geometry, flat-plate particle geometry was also considered as a means of achieving greater applicability toward pressure evolution prediction for irregular flake particle morphology. The following relationship for flat-plate particulate burnout history from Levenspiel (1999) was applied for mass balance derivation under film diffusion and reaction limitation constraints:

$$\textit{Flat-Plate Geometry:} \qquad \frac{t}{\tau} = X \tag{E52}$$

in which

$$\tau = f\left(\rho, L, k, C_{O_2}\right) \tag{E53}$$

where L signifies half-thickness as the characteristic particle length scale and was estimated from initial SEM imaging characterization (see Section 4.2.3).

Furthermore, two thermal energy balance relationships were implemented as part of the principal system of equations. First, a heat balance at the interior vessel wall provided an estimate of the wall boundary temperature differential and is dependent on heat loss due to radiation (using the Stefan-Boltzmann Law - Equation E54) and convection (Equation E55) by applying the difference in temperature between the gas content and the combustion chamber wall:

$$\dot{Q}_{radiation} = \varepsilon\, k_b\, A_{flame}\, (T_{gas\,content} - T_{sphere\,wall})^4 \tag{E54}$$

$$\dot{Q}_{convection} = h\, A_{sphere}\, (T_{gas\,content} - T_{sphere\,wall}) \tag{E55}$$

where ε is the particle emissivity, k_b is the Stefan-Boltzmann constant, A_{flame} is the surface area of the expanding flame front, h is the convective heat transfer coefficient, and A_{sphere} is the constant-value surface area of the interior vessel wall. The second functional thermal relationship included a heat balance on the gas content internal to the combustion volume and allowed the program to iteratively evaluate temperature of the bulk combustion medium as a function of time following ignition. Paying similar attention toward radiative and convective heat transfer, the second differential additionally accounts for energy input due to the enthalpy of combustion, dissipation of energy following igniter initiation, and heat capacity of all relevant components (gas species, unburnt reactant solids, oxidation products). Although both the aluminum powder and air initially charged to the combustion chamber are assumed to be entirely dry and free of moisture, a differential balance around the temperature of the gas content allows for consideration of supplementary heat flow due to water vaporization, as well as the capacity for water to participate as a thermal heat sink. Nevertheless, water-metal reactions were not considered by the model.

Aside from the aforementioned mass and heat balances, the final functional equation of the solution matrix included an expanded form of the ideal gas law equation of state to relate gas content temperature to system pressure. For each iteration of time, the program concurrently solves the system of functional equations using ode15s solver (effective for differential algebraic equations with high solving stiffness) and utilizes the expression derived in Section 5.2.2 (Equation E41) to assess the developing flame radius, allowing for calculation of flame front surface area A_{flame} under the assumption that the propagation expands spherically. Variable flame position and surface area can then be used to re-evaluate the heat balance relationships for each subsequent time step. Likewise, developments are underway such that the global heat transfer coefficient h will be re-evaluated during each program iteration, accomplished using dimensionless number analysis and the following modified Nusselt number relationship applicable within the turbulent flow regime (Lawson & Lloyd, 1997):

$$Nu = 0.023 Re^{0.8} Pr^{\frac{1}{3}} \left(\frac{r_{vessel}}{r_{flame}}\right)^{0.14} \tag{E56}$$

Rather than rely exclusively on a single mean size to denote the dust particle shape and wide size distribution variability, several different methods were considered to offer a more precise estimation. For each morphology investigated, experimental particle size distribution statistics were loaded and processed by the MATLAB® program. Once a combustion regime had been designated by the user, the corresponding mass balance expression could then be solved as a weighted-average based on the proportion of particles defined by discrete ranges of size. Since combustion rate is known to depend heavily on active surface area, the program was developed with alternative provisions allowing the user to specify Sauter mean diameter $D(3,2)$ instead, in the case that complete size distribution data is not available:

$$D(3,2) = \frac{6}{\rho A_p} \tag{E57}$$

where A_p signifies specific surface area of the particle, measurements experimentally acquired as described in Section 4.2.3.

Another initial value designated at the user interface was particle emissivity. Aluminum dust explosions have been shown to exhibit higher flame temperature and increased emissive power relative to organic dust deflagrations, even more so for samples with irregular surface structure (Holbrow et al., 2000), which leads to supplemented burning velocity and greater quantity of heat emitted to particles in the preheat zone. Moreover, solid particle emissivity in a dust deflagration is directly dependent on dust cloud thickness, particulate obscuration, concentration of fuel in suspension, and measured absorption and scatter coefficients (Elsner et al., 1988). Until further data can be collected for these fuels specifically, estimations of particle emissivity were assumed constant and were subjectively assigned for each morphology investigated ($\varepsilon = 0.80$ for spherical, $\varepsilon = 0.85$ for irregular, $\varepsilon = 0.95$ for flake) in an attempt to allot a proportional radiation heat transfer contribution to the overall heat flow.

Following simulation of all experimental concentrations of spherical aluminum powder combustion, model predictions for K_{St} and P_{max} exhibited an average percentage deviation of 16% and 8%, respectively, from experimental values. Model predicted values and discrete deviations for spherical aluminum powder are shown in Figure 5.3 below.
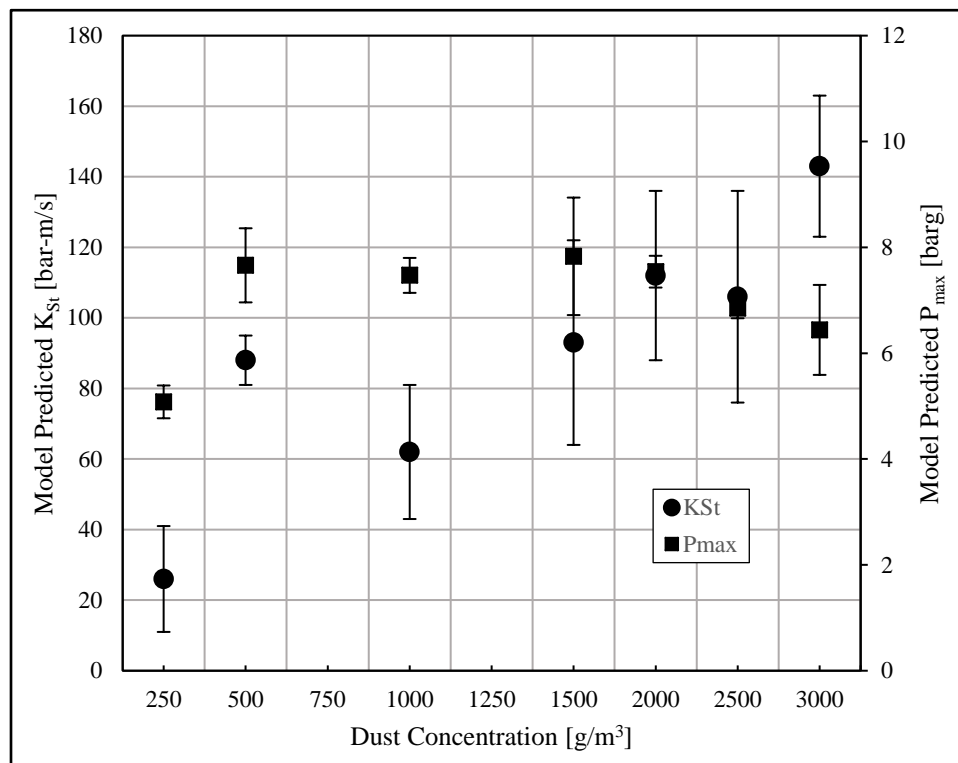
Figure 5.3. Model predicted K_{St} and P_{max} for simulation of spherical aluminum powder combustion, at dust concentrations ranging from 250 to 3000 g/m^3

Agreement between model predicted and experimental pressure evolution was satisfactory but exhibited a degree of divergent behavior for increasingly irregular morphologies, with average error values rising to 17% (K_{St}) and 15% (P_{max}) for irregular aluminum powder combustion and to 20% (K_{St}) and 30% (P_{max}) for flake aluminum powder combustion. Model predictions for irregular and flake morphologies, as well as deviations from experimentally measured explosibility parameters, are displayed in Figures 5.4 and 5.5, respectively. In all cases, simulation agreement at intermediate concentrations proved adequate for the implementation of conservative design explosibility values, with good fitting during pressure generation and marginal conservatism in peak overpressure, as shown in Figure 5.6. For increased suspended fuel concentration, the model generally converged toward increasing values of the fitted kinetic parameters A and E_a for all morphologies. For spherical particles, activation energies range from 8 to 18 kJ/mol, which is

rather low compared to other values from literature (Hu et al., 2021). Nevertheless, it should be

kept in mind that this value corresponds to the global activation energy of a single-step reaction,

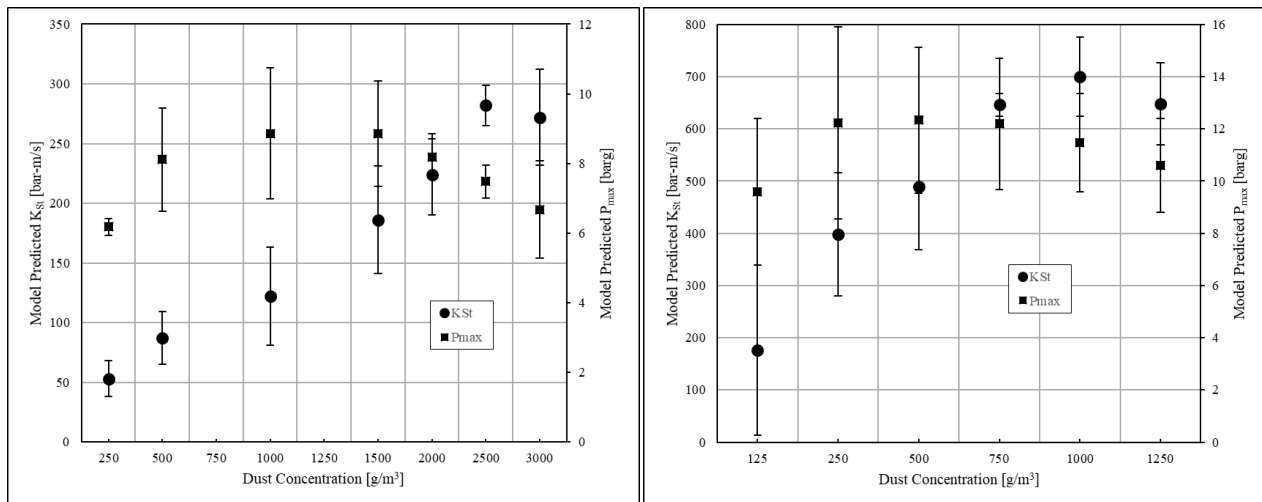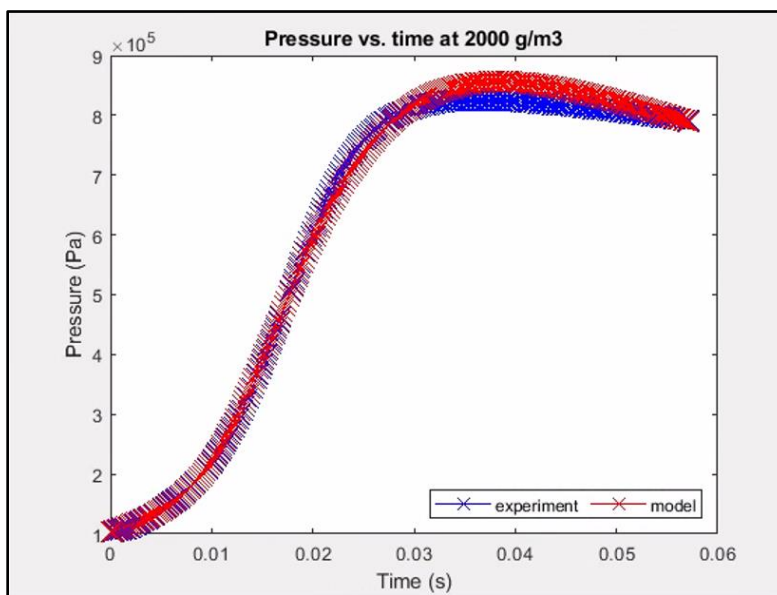which does not aim to describe in detail the different stages of aluminum combustion.

Figure 5.4 (left) & Figure 5.5 (right). Model predicted K_{St} and P_{max} for simulation of irregular (left) and flake (right) aluminum powder combustion, at dust concentrations ranging from 125 to 3000 g/m^3

Figure 5.6. Simulated pressure evolution for spherical aluminum powder combustion at a suspended dust concentration of 2000 g/m^3

For instance, Figure 5.7 shows that a satisfactory agreement can be achieved even at low

powder concentrations ($\leq$ 250 g/m^3); however, the simulation experienced a certain extent of

inaccuracy, as the program can correctly describe maximum pressure or maximum rate of pressure

rise as a function of the initialization, but not both of these parameters. For combustion volumes heavily saturated with fuel (suspended concentrations ≥ 2500 g/m^3), the model seemed to under-predict the maximum explosion overpressure P_{max} at times, as demonstrated by Figure 5.8. The model operates under the assumption that oxidation consistently occurs as a single-step, complete combustion reaction. In reality, greater saturation with fuel increases the likelihood for particle agglomeration, which will increase with surface irregularity. Such phenomena limit the even exposure of oxygen to the particle surface and induce fuel participation by incomplete combustion pathways, which contributes significant thermodynamic limitation to the model functionality. Moreover, as previously stated, reaction between nitrogen and aluminum were not considered, whereas aluminum nitrides are known to be formed under high pressure and temperature (2800 K) (Kwon et al., 2003).
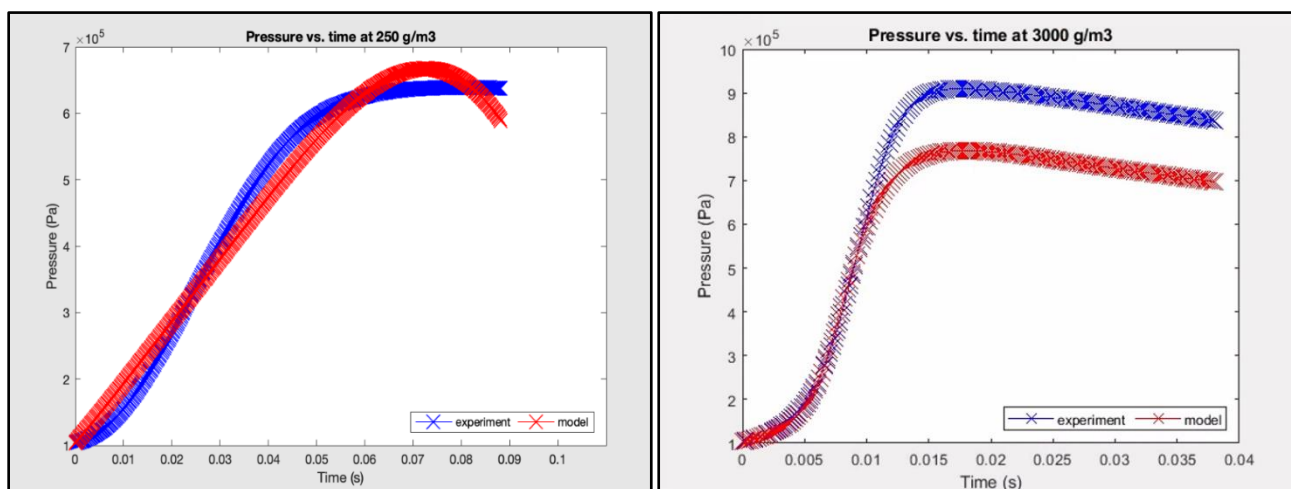

Figure 5.7 (left) & Figure 5.8 (right). Simulated pressure evolution for spherical (left) and irregular (right) aluminum powder combustion at a suspended dust concentration of 250 and 3000 g/m^3, respectively

Experimental inconsistencies may be partially responsible for the deviation. For example, even within a controlled test environment, a majority of metal dust deflagration events at scale involve a certain degree of incomplete fuel combustion. Imprecise timing of fuel injection relative to ignition may induce particle dropout from suspension and consequently lesser participation of fuel

in the combustion, an occurrence that is more perceptible for saturated concentrations of injected fuel. Shortened windows of combustion duration during an incomplete oxidation process reduce the extent of reactant conversion and heat liberation, creating circumstances in which the model could offer a conservative prediction of the overall thermodynamic potential relative to the peak pressure measured from the corresponding experimental scenario. Additionally, the degree of turbulent enhancement is dependent on initial charge of dust, injection pressure, and time delay between injection and ignition initiation – such a parameter may be difficult to quantify and maintain consistent during closed-vessel explosibility experiments. The rate of energy dissipation from the chemical igniter(s) also requires complementary validation and relies heavily on type, quantity, and location of igniters within the combustion volume. Thermal buoyancy due to coexistence of and interaction between hot oxidation products and cold reactants may lead to density differences within the combustion medium and a repositioned geometric center of flame expansion. To compensate experimentally, the point source ignition location must be shifted accordingly to promote a more nearly spherical flame front development. As noted by Julien et al. (2015a, 2015b), the experimental test scale has a significant impact on the isobaric nature of a freely propagating flame front and may similarly undermine the precision of simulation outcomes. Overall, it should also be kept in mind that the typical experimental scattering for tests in the 20L sphere reaches at least ±3% on P_{max} and ±10% on (dP/dt)$_{max}$ (Proust et al., 2007).

Departure from experimental pressure versus time measurements may also be attributed to several open challenges considered during model development. If the tested sample is improperly stored before use, stored for long duration, or directly acquired from an industry application, unquantified oxide accumulation on the surface prior to ignition may increase the fuel's propensity to agglomerate and react according to increasingly nontraditional burning mechanisms. Despite an

assumption of radial propagation expansion, the presence and dissociation of an alumina oxide cap has the capacity to induce fragmentation and fame-jetting behavior, which may lead to significant distortion of flame symmetry to further displacement from anticipated preconceptions of the shrinking core theory (Beckstead, 2002, 2005). The modeled combustion is additionally presumed to occur as a single, simple reaction (as shown in Reaction R19) with no generation of alternative intermediate oxidation products and without concern for the distinct phase or dissociation behavior of the oxide component (Hu et al., 2021). The order of reaction with regard to oxygen is assumed to be 1, which is questionable, especially at high aluminum concentration. Although the heat balance relationship around the gas content may be modified to evaluate the effect of thermal interaction between species, the kinetic model assumes no reaction of aluminum with water or nitrogen, which may be an invalid assumption during oxide condensation and gas-phase reactions at exceedingly high burning temperature.

5.4. Conclusion

Through recent years, and even with continuous advancements in the field of explosion protection, metal dusts processed within pneumatic conveyance and bulk storage industries present a considerable hazard toward operations equipment and personnel. In this work, a closed-vessel mathematical model was developed to predict the pressure growth during aluminum dust explosions characterized by distinct particulate morphology. Applying shrinking core theory to define gas/solid reaction kinetics, the solution methodology relied on application of mass and thermal balance relationships derived analytically under the presumption of chemical reaction or species diffusion limited combustion regimes. Irregular particle surface structure was taken into consideration using novel geometric equivalence methods. Pressure evolution predicted by the model exhibited sufficient agreement with experimental aluminum dust explosibility parameters

K_{St} and P_{max} under specified conditions. Solution deviation and amplified convergence instability was noted for increasingly irregular aluminum morphologies, as well as for rich concentrations of fuel. Potential experimental inconsistencies and considerations for model optimization were examined at length.

Following sensitivity analysis to evaluate the relative influence of initialized user inputs (emissivity, specific surface area, enthalpy of combustion, etc.), the authors propose extension of this numerical simulation to pilot-scale industrial processes where collection of sufficient dust sample may be impractical, or into combustion testing environments where standardized explosibility test conditions may be expensive or difficult to implement repeatedly. Simulation offers test engineers the flexibility to modify key variables (ignition energy, time delay, initial turbulence, suspended concentration, etc.) without the need to coordinate experiments in excess. Accurate consequence prediction for combustible metal dust applications would allow for design of an effective means of deflagration extinction through passive or active explosion mitigation strategies. Depending on the mass balance relationship applied, the model may be readily extended to other metal compositions to ascertain the dominance of specific rate control mechanisms.

Validation experiments will be conducted in the future to monitor the extent of fuel participation during contained aluminum combustion as a function of both injected concentration and scale of the test vessel. Moreover, composition analysis of decomposition products will shed light on effect of aluminum nitride formation. Fuel reactivity further relies on mixture composition and pre-existence of external oxidation layers, but rarely involves combustion of high purity metals, as investigated here. With this in mind, concepts for model expansion include allowances for mixtures with multiple metal alloy components and variable content of oxide. To be used as a benchmark for comparison, parallel experimental efforts are currently underway to evaluate the

explosion severity potential and active suppression effectiveness for variable metal grades, alloy mixtures, and oxidation levels.

Nomenclature

A [=] pre-exponential factor

A_{ext} [=] exterior particle surface area, m^2

A_{flame} [=] flame front surface area, m^2

A_p [=] specific surface area of dust sample, m^2/kg

A_{sphere} [=] interior vessel wall surface area, m^2

b [=] stoichiometric reaction coefficient for solid reactant component

Bi [=] Biot dimensionless number

C$_i$ [=] bulk phase molar concentration of component i, mol/m^3

C_P [=] constant-pressure specific heat capacity, J/kg/K

DAP [=] diammonium phosphate

$D10$ [=] diameter at which 10% of the sample has a smaller particle size, µm

$D50$ [=] median particle diameter, µm

$D90$ [=] diameter at which 90% of the sample has a smaller particle size, µm

$D(3,2)$ [=] Sauter mean diameter, µm

D_f [=] effective diffusivity of oxygen transport through gas film to particle surface

D_A [=] effective diffusion coefficient of oxygen in the product ash layer

E_a [=] activation energy, J/mol

E_S [=] statistically derived value for MIE, mJ

g [=] acceleration due to gravity, m^2/s

h [=] convective heat transfer coefficient, W/m^2/K

h_{Planck} [=] Planck's constant, m^2-kg/s

j [=] radiant emittance, W/m^2

k [=] reaction rate constant under chemical reaction control

K [=] Karlovitz stretch factor

k_b [=] Stefan Boltzmann constant, $W/m^2/K^4$

k_g [=] mass transfer coefficient between bulk fluid phase and particle surface

K_{St} [=] deflagration explosibility index, bar-m/s

L [=] characteristic length [for a flat plate geometry, L=half-thickness], m

l_I [=] turbulence integral length scale, m

MAP [=] monoammonium phosphate

m_u [=] mass of unburnt fuel mixture, kg

n [=] order of reaction

$N_{i,o}$ [=] initial number of moles of species i

N_i [=] number of moles of species i

Nu [=] Nusselt number

P [=] pressure, barg

PBC [=] potassium bicarbonate

P_{act} [=] suppression system activation pressure, barg

P_{N_2} [=] additive pressure due to injection of nitrogen from HRD container, barg

P_{comb} [=] generation of combustion pressure between system activation and flame extinction, barg

$\frac{dP}{dt}$ [=] rate of pressure rise, bar/s

P_{max} [=] maximum explosion overpressure in a contained volume, barg

Pr [=] Prandlt number

P_{red} [=] vessel reduced pressure, barg

P_{es} [=] vessel design strength, barg

$\boldsymbol{q}$ [=] heat flux vector

$\dot{Q}_{convection}$ [=] heat loss due to convection, J/s

$\dot{Q}_{radiation}$ [=] heat loss due to radiation, J/s

Q_{O_2} [=] oxygen diffusion flux to reaction surface at any point r within the ash layer, mol/m^2/s

$Q_{O_2,core}$ [=] oxygen diffusion flux to reaction surface at r = r$_c$, mol/m^2/s

$Q_{O_2,surface}$ [=] oxygen diffusion flux to reaction surface at r = R, mol/m^2/s

r [=] radius, m

r_{total} [=] overall reaction rate, L/mol/s

r_{flame} [=] flame front radius, m

r_p [=] particle radius, m

r_c [=] unreacted core radius, m

r_{vessel} [=] combustion test vessel radius, m

R [=] ideal gas constant, L-bar/K/mol

Re [=] Reynolds number

R_o [=] initial unburnt fuel particle radius, m

SBC [=] sodium bicarbonate

S_u [=] laminar burning velocity, m/s

S_T [=] turbulent burning velocity, m/s

t [=] time, s

t_{comb} [=] combustion duration, s

$t_{conduction}$ [=] thermal conduction timescale, s

T [=] temperature, K

T_{cold} [=] cold-junction compensation temperature, K

T_{MAX} [=] maximum exotherm peak temperature, K

TSP [=] total suppressed pressure during suppression explosion mitigation, barg

$T_{settling}$ [=] combustion settling temperature, K

T_u [=] unburnt mixture temperature, K

T03 [=] time required to reduce nitrogen pressure within HRD container to 97% of initial, ms

T90 [=] time required to reduce nitrogen pressure within HRD container to 10% of initial, ms

u'_{rms} [=] root-mean square of turbulent velocity fluctuations, m/s

v [=] mass average velocity

V [=] unreacted particle core volume, L

V_{vessel} [=] volume of the combustion test vessel, L

X [=] conversion, or extent of reaction

$\frac{dX}{dt}$ [=] reaction conversion rate, s^{-1}

Greek Symbols

α [=] thermal diffusivity, m^2/s

β [=] heating ramp rate during TGA/DSC, °C/min

$\beta_{sensitivity}$ [=] rated thermocouple sensitivity (Seebeck coefficient)

δ [=] flame front thickness, m

ε [=] flame emissivity

ΔH [=] enthalpy of activation, kJ

$\Delta H_{combustion}$ [=] molar heat of combustion, kJ/mol

ΔG [=] Gibbs free energy of activation, kJ

ΔS [=] entropy of activation, J/K

κ [=] thermal conductivity, W/m/K

ρ [=] density, kg/m^3

$\rho_{u,o}$ [=] initial unburnt mixture density, kg/m^3

ρ_u [=] unburnt mixture density, kg/m^3

$\boldsymbol{\tau_s}$ [=] viscous momentum flux (or stress) tensor

τ [=] time to reach complete conversion of reactant, s

σ_D [=] polydispersity

γ [=] specific heat ratio

Funding

References

(1) Abdel-Gayed, R. G., Bradley, D., Lawes, M. (1987). Turbulent Burning Velocities: A General Correlation in Terms of Straining Rates. *Proceedings of the Royal Society of London A*, *301*, 389-413.

(2) Amrogowicz, J.; Kordylewski, W. (1991). Effectiveness of dust explosion suppression by carbonates and phosphates. *Combustion and Flame*, *85* (3-4), 520-522.

(3) Amyotte, P. R.; Chippett, S.; Pegg, M. J. (1988). Effects of turbulence on dust explosions. *Progress in Energy and Combustion Science*, *14* (4), 293-310.

(4) Amyotte, P. R. (2006). Solid inertants and their use in dust explosion prevention and mitigation. *Journal of Loss Prevention in the Process Industries*, *19*, 161-173.

(5) Amyotte, P. R.; Cloney, C. T.; Khan, F. I.; Ripley, R. C. (2012). Dust explosion risk moderation for flocculent dusts. *Journal of Loss Prevention in the Process Industries*, *25*, 862-869.

(6) Arntzen, B. J. (1998). Modelling of turbulence and combustion for simulation of gas explosions in complex geometries. Dr. Ing. Thesis. NTNU, Trondheim, Norway.

(7) *ASTM E698, Standard Test Method for Arrhenius Kinetic Constants for Thermally Unstable Materials Using Differential Scanning Calorimetry and the Flynn/Wall/Ozawa Method*; American Society for Testing and Materials: West Conshohocken, PA, 2001.

(8) A*STM E1226-19, Standard Test Method for Explosibility of Dust Clouds*; American Society for Testing and Materials: West Conshohocken, PA, 2019.

(9) *ASTM E2019-03, Standard Test Method for Minimum Ignition Energy of a Dust Cloud in Air*; American Society for Testing and Materials: West Conshohocken, PA, 2019.

(10) Ballal, D. R. (1980). Ignition and flame quenching of quiescent dust clouds of solid fuels. *The Royal Society Publishing*, *369* (1739).

(11) Ballal, D. R. (1983). Flame propagation through dust clouds of carbon, coal, aluminum and magnesium in an environment of zero gravity. *Proceedings of the Royal Society of London*, *A385*, 21-51.

(12) Bagaria, P.; Zhang, J.; Mashuga, C. (2018). Effect of dust dispersion on particle breakage and size distribution in the minimum ignition energy apparatus. *Journal of Loss Prevention in the Process Industries*, *56*, 518-523.

(13) Bagaria, P.; Prasad, S.; Sun, J.; Bellair, R.; Mashuga, C. (2019). Effect of particle morphology on dust minimum ignition energy. *Powder Technology*, *355*, 1-6.

(14) Bartknecht, W. (1981). Dust Explosions: Course, Prevention, Protection, first ed. Springer-Verlag Berlin Heidelberg: New York.

(15) Baudry, G.; Bernard, P.; Gillard, P. (2007). Influence of the oxide content on the ignition energies of aluminum powders *Journal of Loss Prevention in the Process Industries, 20*, 330-336.

(16) Bazyn, T.; Krier, H.; Glumac, N. (2007). Evidence for the transition from the diffusion-limit in aluminum particle combustion. *Proceedings of the Combustion Institute*, *31*, 2021-2028.

(17) Beck, H.; Glienke, N.; Mohlman, C. (1997). Combustion and explosion characteristics of dust. *BIA Report 13/97*, Hauptverband der gewerblichen Berufsgenossenschaften: Sank Augustin, Germany.

(18) Beckstead, B. W. (2002). A summary of aluminum combustion. Internal Aerodynamics in Solid Rocket Propulsion. RTO/VKI Special Course, Rhode-Saint-Genese, Belgium.

(19) Beckstead, B. W. (2005). Correlating aluminum burning times. *Combustion, Explosion, and Shock Waves*, *41*, 533-546.

(20) Bernard, S.; Gillard, P.; Foucher, F.; Mounaim-Rousselle, C. (2012). MIE and flame velocity of partially oxidized aluminum dust. *Journal of Loss Prevention in the Process Industries*, *25*, 460-466.

(21) Beuth Verlag GmbH, 2002. VDI 3673 (Part 1): Pressure Venting of Dust Explosions, Berlin, Germany.

(22) Bi, H.; Xie, X.; Wang, K.; Cao, Y.; Shao, H. (2021). A risk assessment methodology of aluminum dust explosion for polishing process based on laboratory tests. Proceedings of the Institution of Mechanical Engineers, Part O: *Journal of Risk and Reliability*, *235* (4), 627-636.

(23) Bidabadi, M.; Mohammadi, M.; Poorfar, A. K.; Mollazadeh, S.; Zadsirjan, S. (2015). Modeling ccombustion of aluminum dust cloud in media with spatially discrete sources. *Heat and Mass Transfer*, *51*, 837-845.

(24) Bind, V. K.; Roy, S.; Rajagopal, C. (2012). A reaction engineering approach to modeling dust explosions. *Chemical Engineering Journal*, *207-208*, 625-634.

(25) Bjerketvedt, D., Bakke, J. R., van Wingerden, K. (1997). Gas Explosion Handbook. *Journal of Hazardous Materials, 52* (1), 1-150.

(26) Boilard, S.; Amyotte, P.; Khan, F.; Dastidar, A.; Eckhoff, R. (2013). Explosibility of micron- and nano-size titanium powders. *Journal of Loss Prevention in the Process Industries*, *26*, 1646-1654.

(27) Bouillard, J.; Vignes, A.; Dufaud, O.; Perrin, L.; Thomas, D. (2010). Ignition and explosion risks of nanopowders. *Journal of Hazardous Materials*, *181*, 873-880.

(28) Braconnier, A.; Chauveau, C.; Halter, F.; Gallier, S. (2018). Detailed analysis of combustion process of a single aluminum particle in air using an improved experimental approach. *International Journal of Energetic Materials and Chemical Propulsion*, *17* (2), 111-124.

(29) Bradley, D.; Mitcheson, A. (1976). Mathematical solutions for dust explosions in spherical vessels. *Combustion and Flame*, *26*, 201-217.

(30) Bradley, D., Lau, A. K. C., Lawes, M. (1992). Flame Stretch Rate as a Determinant of Turbulent Burning Velocity. *Philosophical Transactions: Physical Sciences and Engineering*, *338*, 359-387.

(31) British Standards Institution, 2012. EN 14491: Dust Explosion Venting Protective Systems.

(32) Broumand, M.; Bidabadi, M. (2003). Modeling combustion of micron-sized iron dust particles during flame propagation in a vertical duct. *Fire Safety Journal*, *59*, 88-93.

(33) Brzustowski, T. A.; Glassman, I. (1964). Spectroscopic Investigation of Metal Combustion. Heterogeneous Combustion, Academic Press: New York.

(34) Callé, S.; Klaba, L.; Thomas, D.; Perrin, L.; Dufaud, O. (2005). Influence of the size distribution and concentration on wood dust explosion: experiments and reaction modelling. *Powder Technology*, *157*, 144-148.

(35) Camino, G.; Costa, L.; Trossarelli, L. (1985). Study of the mechanism of intumescence in fire retardant polymers: Part V – Mechanism of formation of gaseous products in the thermal degradation of ammonium polyphosphate. *Polymer Degradation and Stability*, *12* (3), 203-211.

(36) Cashdollar, K. L. (2000). Overview of dust explosibility characteristics. *Journal of Loss Prevention in the Process Industries*, *13* (3-5), 183-199.

(37) Cashdollar, K. L.; Zlochower, I. A. (2007). Explosion temperatures and pressures of metals and other elemental dust clouds. *Journal of Loss Prevention in the Process Industries*, *20*, 337-348.

(38) Castellanos, D. (2013). The effects of particle size and crystallinity on the combustion behavior of particulated solids. Doctoral Dissertation. Texas A&M University.

(39) Castellanos, D.; Carreto-Vazquez, V.; Mashuga, C.; Trottier, R.; Mejia, A.; Mannan, M. (2014a). The effect of particle size polydispersity on the explosibility characteristics of aluminum dust. *Powder Technology*, *254*, 331-337.

(40) Castellanos, D.; Lewandowski, A.; Diaz, A.; Mejia, A.; Carreto, V.; Mashuga, C.; Rangwala, A.; Cheng, Z.; Mannan, M. (2014b). Influence of Particle Size and Crystalline Level on the Efficiency of Dust Explosion Inhibitors. *Industrial Engineering & Chemistry Research*, *53*, 11527-11537.

(41) Cao, X.; Ren, J.; Zhou, Y.; Wang, Q.; Gao, X.; Bi, M. (2015). Suppression of methane/air explosion by ultrafine water mist containing sodium chloride additive. *Journal of Loss Prevention in the Process Industries*, *285*, 311-318.

(42) Chaudhari, P.; Ade, N.; Pérez, L. M.; Kolis, S.; Mashuga, C. (2020). Quantitative structure-property relationship (QSPR) models for minimum ignition energy (MIE) prediction of combustible dusts using machine learning. *Powder Technology*, *372*, 227-234.

(43) Chatrathi, K.; Going, J. (2000). Dust Deflagration Extinction. *Process Safety Progress, 19* (3), 146-153.

(44) Chen, Z.; Fan, B. (2005). Flame propagation through aluminum particle cloud in a combustion tube. *Journal of Loss Prevention in the Process Industries*, *18*, 13-19.

(45) Chen, X.; Zhang, H.; Chen, X.; Liu, X.; Niu, Y.; Zhang, Y.; Yuan, B. (2017). Effect of dust explosion suppression by sodium bicarbonate with different granulometric distribution. *Journal of Loss Prevention in the Process Industries*, *49*, 905-911.

(46) Chilworth Technology Ltd. (2013). "Safety Guide: A Strategic Guide to Characterization and Understanding Handling Dusts and Powders Safely". *DEKRA Insight*. Available at: http://dekra-insight.com/images/white-paper-documents/wp_dustguide_us.pdf (Accessed: 18 October 2020).

(47) Christill, M.; Nastoll, W.; Leuckel, W. (1989). Der Einfluss von Strömungsturblenz auf den Explosionsablauf in Staub/Luft-Gemischen. *VDI-Beriche*, *701*, 123-141.

(48) Christophe, P.; Rim, B. M.; Mohamed, G.; Khashayar, S.; Jérome, F. (2017). Thermal radiation in dust flame propagation. *Journal of Loss Prevention in the Process Industries*, *49*, 896-904.

(49) Cloney, C. (2020). "2019 Combustible Dust Incident Report – Version #1". DustEx Research Ltd. Retrieved from https://dustsafetyscience.com/2019-Report

(50) Clouthier, M. P.; Taveua, J. R.; Dastidar, A. G.; Morrison, L. S.; Zalosh, R. G.; Ripley, R. C.; Khan, F. I.; Amyottee, P. R. (2019). Iron and aluminum powder explosibility in 20-L and 1-m^3 chambers. *Journal of Loss Prevention in the Process Industries*, *62*, 103927.

(51) Continillo, G. (1989). A two-zone model and a distributed-parameters model of dust explosion in closed vessels. *Archivum Combustionis*, *9*, 79-94.

(52) *CRC Handbook of Chemistry and Physics*, 86th ed.; Lide, D. R., Ed.; CRC Press: Boca Raton, FL, 2005.

(53) Dahoe, A.; Zevenbergen, J,; Lemkowitz, S.; Scarlett, B. (1996). Dust explosions in spherical vessels: The role of flame thickness in the validity of the 'cube-root law'. *Journal of Loss Prevention in the Process Industries*, *9* (1), 33-44.

(54) Dahoe, A.; de Goey, L. (2003). On the determination of the laminar burning velocity from closed vessel gas explosions. *Journal of Loss Prevention in the Process Industries*, *16*, 457-478.

(55) Dastidar, A. G.; Amyotte, P. R.; Pegg, M. J. (1997). Factors influencing the suppression of coal dust explosions. *Fuel*, *76* (7), 663-670.

(56) Dastidar, A. G. (2004). Influence of Scale on the Inerting of Dust Explosions. Ph.D. Dissertation, Dalhousie University.

(57) Di Benedetto, A.; Russo, P. (2007). Thermo-kinetic modelling of dust explosions. *Journal of Loss Prevention in the Process Industries*, *20* (4-6), 303-309.

(58) Di Benedetto, A.; Russo, P.; Amyotte, P.; Marchand, N. (2010). Modelling the effect of particle size on dust explosions. *Chemical Engineering Science*, *65* (2), 772-779.

(59) Dreizin, E. (1996). Experimental study of stages of aluminum particle combustion in air. *Combustion and Flame*, *105*, 541-546.

(60) Dreizin, E.; Hoffman, V. (1999). Constant Pressure Combustion of Aerosol of Coarse Magnesium Particles in Microgravity. *Combustion and Flame*, *118*, 262-280.

(61) Dufaud, O.; Traoré, M.; Perrin, L.; Chazelet, S.; Thomas, D. (2010). Experimental investigation and modelling of aluminum dusts explosions in the 20 L sphere. *Journal of Loss Prevention in the Process Industries*, *23*, 226-236.

(62) Eapen, B. Z.; Hoffmann, V. K.; Schoenitz, M.; Dreizin, E. L. (2004). Combustion of aerosolized spherical aluminum powders and flakes in air. *Combustion Science and Technology*, *176* (7), 1055-1069.

(63) Eckhoff, R. K.; Parker, S. J.; Gruvin, B. (1986). Ignitability and Explosibility of Silicon Dust Clouds. *Journal of the Electrochemical Society*, *133*, 2631-2637.

(64) Eckhoff, R. K. (2003). Dust Explosions in the Process Industries, third ed. Gulf Professional Publishing: Amsterdam.

(65) Elsner, T.; Koneke, D.; Wheeler, R., V. (1988). Thermal radiation of gas/solid mixtures. *Chemical Engineering and Technology*, *11*, 237-243.

(66) Eyring, H. (1935). The activated complex in chemical reactions. *Journal of Chemical Physics*, *3*, 107-115.

(67) Evans, M. G.; Polanyi, M. (1935). Some applications of the transition state method to the calculation of reaction velocities, especially in solutions. *Transactions of the Faraday Society*, *31*, 875-894.

(68) Fanebust, I.; Fernandez-Anez, N. (2019). Influence of particle size and moisture content of wood particulates on deflagration hazard. *Fire Protection Research Foundation*: Western Norway University of Applied Sciences.

(69) Gao, W.; Mogi, T.; Yu, J.; Yan, X.; Sun, J.; Dobashi, R. (2015). Flame propagation mechanisms in dust explosions. *Journal of Loss Prevention in the Process Industries*, *39*36 186-194.

(70) Gao, W.; Zhou, Q.; Sun, J. (2015). Flame propagation through zirconium particles coated with different ratios of Fe_3O_4. *Fuel*, *148*, 231-237.

(71) Gao, W.; Zhang, X.; Zhang, D.; Peng, Q.; Zhang, Q.; Dobashi, R. (2017). Flame propagation behaviours in nano-metal dust explosions. *Powder Technology*, *321*, 154-162.

(72) Gexcon AS (2014). FLACS v10.2 User's Manual, Bergen, Norway.

(73) Gexcon AS (2019). CASD Pre-Processor I – Defining Scenario, Bergen, Norway.

(74) Ghanim, A. N. (2006). Production of Aluminum Flake Pigments by Ball Mill. *The Iraqi J. for Mech. and Mat. Eng.*, *6*, 44-51.

(75) Glassman, I. (1960). Combustion of metals: physical considerations. *Solid Propellant Rocket Research, Progress in Astronautics and Aeronautics*, *1*, 253-258.

(76) Going, J.; Snoeys, J. (2002). Explosion Protection with Metal Dust Fuels. *Process Safety Progress*, *21* (4).

(77) Grosse, A. V.; Conway, J. B. (1958). Combustion of metals in oxygen. *Industrial Engineering Chemistry*, *50*, 663-672.

(78) Guo, L.; Xiao, Q.; Zhu, N.; Wang, Y.; Chen, X.; Xu, C. (2019). Comparative studies on the explosion severity of different wood dusts from fiberboard production. *Bioresources*, *14* (2), 3182-3199.

(79) Haipu, B.; Xie, X.; Wang, K.; Cao, Y.; Shao, H. (2021). A risk assessment methodology of aluminum dust explosion for polishing process based on laboratory tests. *Proceedings of the Institution of Mechanical Engineers, Part O: Journal of Risk and Reliability*, *32*, 1748006X2098737.

(80) Hartmann, J. (1948). Recent research on explosibility of dust dispersions. *Industrial Engineering Chemistry*, *40* (4), 752-758.

(81) Hertzberg, N.; Cashdollar, K. L. (1987). Introduction to dust explosions. In *Industrial Dust Explosions, ASTM STP 958*. American Society for Testing and Materials, Philadelphia.

(82) Hirata, T. (1965). Study on manufacturing aluminum powder by atomization. *Journal of the Japan Society of Powder and Powder Metallurgy*, *12* (5), 183-186.

(83) Holbrow, P., Andrews, S., Lunn, G. A. (1996). Dust Explosion Propagation in Interconnected Vented Vessels. *Journal of Loss Prevention in the Process Industries*, *9* (1), 91-103.

(84) Holbrow, P., Lunn, G. A., Tyldesley, A. (1999). Dust Explosion Protection in Linked Vessels: Guidance for Containment and Venting. *Journal of Loss Prevention in the Process Industries*, *12* (3), 227-234.

(85) Holbrow, P.; Hawksworth, S. J.; Tyldesley, A. (2000). Thermal radiation from vented dust explosions. *Journal of Loss Prevention in the Process Industries*, *13*, 467-476.

(86) Horacek, H.; Grabner, R. (1996). Advantages of flame retardants based on nitrogen compounds. *Polymer Degradation and Stability*, *54*, 205-215.

(87) Huang, Y.; Risha, G.; Yang, V.; Yetter, R. (2007). Combustion of bimodal nano/micron-sized aluminum particle dust in air. *Proceedings of the Combustion Institute*, *31*, 2001-2009.

(88) Huang, D. H.; Tran, T. N.; Yang, B. (2014). Investigation on the reaction of iron powder mixture as a portable heat source for thermoelectric power generators. *Journal of Thermal Analysis and Calorimetry*, *116* (2), 1047-1053.

(89) International Organization for Standardization, 1985. *ISO 6184-1, Explosion Protection System – Part 1: Determination of Explosion Indices of Combustible Dusts in Air*: Switzerland.

(90) Ishida, M.; Wen, C. Y. (1968). Comparison of kinetic and diffusional models for solid-gas reactions. *AIChE Journal*, *14*, 311-317.

(91) Ishida, M.; Wen, C. Y. (1971a). Comparison of zone-reaction model and unreacted-core shrinking model in solid-gas reactions – I. isothermal analysis. *Chemical Engineering Science*, *26* (7), 1031-1041.

(92) Ishida, M.; Wen, C. Y. (1971b). Comparison of zone-reaction model and unreacted-core shrinking model in solid-gas reactions – II. Non-isothermal analysis. *Chemical Engineering Science*, *26* (7), 1043-1048.

(93) Jacobson, M.; Nagy, J.; Cooper, A. R. (1962). Explosibility of metal powders. US Department of the Interior, Bureau of Mines.

(94) Jacobson, M.; Cooper, A. R.; Nagy, J. (1964). Explosibility of dusts used in the plastics industry. US Department of the Interior, Bureau of Mines.

(95) Jiang, H.; Bi, M.; Li, B.; Gao, W. (2018). Inhibition of aluminum dust explosion by $NH_4H_2PO_4$ and $NaHCO_3$. In *Proceedings of the Twelfth International Symposium on Hazards, Prevention and Mitigation of Industrial Explosions*, Kansas City, MO, USA, Aug 12-17.

(96) Jiang, H.; Bi, M.; Gao, W.; Gan, B.; Zhang, D.; Zhang, Q. (2018). Inhibition of aluminum dust explosions by $NaHCO_3$ with different particle size distributions. *Journal of Hazardous Materials*, *344*, 902-912.

(97) Jing, Q.; Wang, D.; Liu, Q.; Ren, L.; Wang, Y.; Liu, C.; Shen, Y.; Wang, Z. (2021). Study on transient reaction mechanism and explosion intensity parameters of micron-sized flake aluminum dust in air. *Chemical Engineering Science*, *246*, 116884.

(98) Julien, P.; Vickery, J.; Goroshin, S.; Frost, D. L.; Bergthorson, J. M. (2015a). Freely-propagating flames in aluminum dust clouds. *Combustion & Flame*, *162*, 4241-4253.

(99) Julien, P.; Vickery, J.; Whiteley, S.; Wright, A.; Goroshin, S.; Bergthorson, J. M.; Frost, D. L. (2015b). Effect of scale on freely-propagating flames in aluminum dust clouds. *Journal of Loss Prevention in the Process Industries*, *36*, 230-236.

(100) Kadir, N.; Rusli, R.; Buang, A.; Rahim, N. (2016). 4th International Conference on Process Engineering and Advanced Materials: Investigation of the Explosion Behaviour Affected by the Changes in Particle Size. *Procedia Engineering*, *148*, 1156-1161.

(101) Kanury, A. M. (1975). Introduction to Combustion Phenomena, first ed. Gordon and Breach Science Publishers: New York.

(102) Krietsch, A.; Scheid, M.; Schmidt, M.; Krause, U. (2015). Explosion behavior of metallic nano powders. *Journal of Loss Prevention in the Process Industries*, *36*, 237-243.

(103) Kuang, K.; Chow, W. K.; Ni, X.; Yang, D.; Zeng, W.; Liao, G. (2011). Fire suppressing performance of superfine potassium bicarbonate powder. *Fire and Materials*, *35*, 353-366.

(104) Law, C. K. (1973). A simplified theoretical model for the vapor-phase combustion of metal particles. *Combustion Science and Technology*, *7*, 197-212.

(105) Lawson, K. W.; Lloyd, D. R. (1997). Membrane distillation. *Journal of Membrane Science*, *124* (1), 1-25.

(106) Lees, F. (2012). *Lees' Loss Prevention in the Process Industries: Hazard Identification, Assessment and Control*, 4th ed.; Elsevier Inc.: Waltham, MA.

(107) Lembo, F.; DallaValle, P.; Marmo, L.; Patrucco, M.; Debernardi, M. L. (2001). Aluminum airborne particles explosions: risk assessment and management at Northern Italian factories. ESREL Conference, 85-92.

(108) Leuschke, G. (1965). Beitrage zue Erforschung des Mechanismus der Flammenausbreitung in Staubwolken. *Staub*, *25*, 180-186.

(109) Levenspiel, O. (1999). Chemical Reaction Engineering, 3rd Edition. John Wiley & Sons, Inc.: Oregon, USA.

(110) Lewis, B.; von Elbe, G. (1987). Combustion, Flames and Explosions, third ed. Academic Press: London.

(111) Li, Q.; Lin, B.; Li, W.; Zhai, C.; Zhu, C. (2011). Explosion characteristics of nano-aluminum powder-air mixtures in 20 L spherical vessels. *Powder Technology*, *212*, 303-309.

(112) Li, Q.; Wang, K.; Zheng, Y.; Mei, X.; Lin, B. (2016a). Explosion severity of micro-sized aluminum dust and its flame propagation properties in 20 L spherical vessel. *Powder Technology*, *301*, 1299-1308.

(113) Li, G.; Yang, H.-X.; Yuan, C.-M.; Eckhoff, R. K. (2016b). A catastrophic aluminum-alloy dust explosion in China. *Journal of Loss Prevention in the Process Industries*, *39*, 121-130.

(114) Liang, Y.; Beckstead, M. W. (1998). Numerical simulation of quasi-steady, single aluminum particle combustion in air. *AIAA*, 98-0254.

(115) Liu, S.; Cheng, Y.; Meng, X.; Ma, H.; Song, S.; Liu, W.; Shen, Z. (2018). Influence of particle size polydispersity on coal dust explosibility. *Journal of Loss Prevention in the Process Industries*, *56*, 444-450.

(116) Lunn, G. A., Holbrow, P., Andrews, S., Gummer, J., 1996. Dust Explosions in Totally Enclosed Interconnected Vessel Systems. *Journal of Loss Prevention in the Process Industries, 9* (1), 45-58.

(117) Luo, X.; Wang, T.; Ren, J.; Deng, J.; Shu, C.; Huang, A.; Cheng, F.; Wen, Z. (2017). Effects of ammonia on the explosion and flame propagation characteristics of methane-air mixtures. *Journal of Loss Prevention in the Process Industries*, *47*, 120-128.

(118) Malayathodi, R.; Sreekanth, M. S.; Deepak, A.; Dev, K.; Surendranathan, A. O. (2018). Effect of milling time on production of aluminum nanoparticle by high energy ball milling. *International Journal of Mechanical Engineering and Technology*, *9* (8), 646-652.

(119) Mason, R. B.; Taylor, C. S. (1937). Explosion of aluminum powder dust clouds. *Industrial Engineering Chemistry*, *29*, 626-631.

(120) Mason, P.; Uhlig, F.; Vanek, V.; Buttersack, T.; Bauerecker, S.; Jungwirth, P. (2005). Coulomb explosion during the early stages of the reaction of alkali metals with water. *Nature Chemistry*, *7*, 250-254.

(121) Matsuda, T.; Yamaguma, M. (2000). Tantalum dust deflagration in a bag filter dust-collecting device. *Journal of Hazardous Materials*, *77* (1-3), 33-42.

(122) May, D. C.; Berard, D. L. (1987). Fires and explosions associated with aluminum dust from finishing operations. *Journal of Hazardous Materials*, *17*, 81-88.

(123) Miao, N.; Zhong, S.; Yu, Q. (2016). Ignition characteristics of metal dusts generated during machining operations in the presence of calcium carbonate. *Journal of Loss Prevention in the Process Industries*, *40*, 174-179.

(124) Mittal, M. (2014). Explosion characteristics of micron- and nano-size magnesium powders. *Journal of Loss Prevention in the Process Industries*, *27*, 55-64.

(125) Moore, P. E.; Cooke, P. L. (1988). Suppression of Metal Dust Explosions, Report No. 88/49. *British Material Handling Board*; Ascot, Berkshire, UK.

(126) Moore, P. E. (1996). Suppressants for the control of industrial explosions. *Journal of Loss Prevention in the Process Industries*, *9* (1), 119-123.

(127) Moussa, R.; Guessasma, M.; Proust, C.; Saleh, K.; Fortin, J. (2015). Thermal radiation contribution to metal dust explosions. *Procedia Engineering*, *102*, 714-721.

(128) Myers, T. J. (2008). Reducing aluminum dust explosion hazards: case study of dust inerting in an aluminum buffing operation. *Journal of Hazardous Materials*, *159*, 72-80.

(129) National Fire Protection Association. *NFPA 484: Standard for Combustible Metals*, 2015.

(130) National Fire Protection Association, 2017. *NFPA 654: Standard for the Prevention of Fire and Dust Explosions from the Manufacturing, Processing, and Handling of Combustible Particulate Solids*: Maryland, USA.

(131) National Fire Protection Association, 2018. *NFPA 68: Standard on Explosion Protection by Deflagration Venting*: Maryland, USA.

(132) National Fire Protection Association, 2019. *NFPA 69: Standard on Explosion Prevention Systems*: Maryland, USA.

(133) Nomura, S.; Tanaka, T. (1980). Prediction of maximum rate of pressure rise due to dust explosion in closed spherical and non-spherical vessels. *Industrial & Engineering Chemistry Process Design and Development*, *19*, 451-459.

(134) Occupational Safety and Health Administration (2009). *Hazard Communication Guidance for Combustible Dusts: OSHA 3371-08*.

(135) Ogle, R. (2017). Dust explosion dynamics*,* 1st ed. Elsevier Publishing: Warrenville, IL.

(136) Penttilä, A.; Lumme, K. (2004). The effect of particle shape on scattering – A study with a collection of axisymmetric particles and sphere clusters. *Journal of Quantitative Spectroscopy and Radiative Transfer*, *89* (1-4), 303-310.

(137) Poletaev, N. I.; Khlebnikova, M.Y.; Khanchych, K. Y. (2018). Producing and properties of zinc dust flames. *Combustion Science and Technology*, *190* (6), 1096-1109.

(138) Popat, N. R., Catlin, C. A., Arntzen, B. J., Lindstedt, R. P., Hjertager, B. H., Solberg, T., et al. (1996). Investigation to Improve and Assess the Accuracy of Computational Fluid Dynamics Based Explosion Models. *Journal of Hazardous Materials*, *45* (1), 1-25.

(139) Prasad, S.; Schweizer, C.; Bagaria, P.; Kulatilaka, W.; Mashuga, C. (2020). Effect of particle morphology on dust cloud dynamics. *Powder Technology*. Advance online publication. https://doi.org/10.1016/j.powtec.2020.10.058

(140) Price, D.; Brown, H. (1922). Dust explosions: theory and nature of, phenomena, causes and methods of prevention. National Fire Protection Association, Boston, MA.

(141) Puri, P. Multiscale modelling of ignition and combustion of micro and nano aluminum particles. Ph.D. Dissertation; Pennsylvania State University, 2008.

(142) Reding, N. S.; Shiflett, M. (2018). Metal dust explosion hazards: a technical review. *Industrial & Engineering Chemistry Research*, *57* (34), 11473-11482.

(143) Reding, N. S.; Shiflett, M. B. (2019). Characterization of Thermal Stability and Heat Absorption for Suppressant Agent/Combustible Dust Mixtures via Thermogravimetric Analysis/Differential Scanning Calorimetry. *Industrial & Engineering Chemistry Research*, *58* (11), 4674-4687.

(144) Reding, N. S.; Farrell, T.; Verma, A.; Shiflett, M. B. (2021). Effect of Particle Morphology on Metal Dust Deflagration Sensitivity and Severity. *Journal of Loss Prevention in the Process Industries*, *70*, 104396.

(145) Rockwell, S.; Rangwala, A. (2013). Modeling of dust air flames. *Fire Safety Journal*, *59*, 22-29.

(146) Rockwell, S.; Taveau, J. (2018). Studying the Effect of Sodium Bicarbonate on Hybrid Flames: Burner vs. 20-L sphere experiments. In *Proceedings of the Twelfth International*

Symposium on Hazards, Prevention and Mitigation of Industrial Explosions, Kansas City, MO, USA, Aug 12-17.

(147) Russo, P.; Di Benedetto, A. (2013). Review of dust explosion modeling. *Chemical Engineering Transactions*, *31*, 955-960.

(148) Schwenzfeuer, K.; Glor, M; Gitza, A. Relation between Ignition Energy and Limiting Oxygen Concentration for Powders. In *Proceedings from the 10th International Symposium on Loss Prevention and Safety Promotion in the Process Industry*, Stockholm, Sweden, June 2001; Elsevier: Amsterdam, Netherlands, 2001; 909-916.

(149) Shen, J.; Smith, J. M. (1965). Diffusional effects in gas-solid reactions. *Industrial Engineering Chemistry Fundamentals*, *4*, 293-301.

(150) Skjold, T.; Arntzen, B. J.; Hansen, O. R.; Taraldset, O. J.; Storvik, I. E.; Eckhoff, R. K. (2005). Simulating dust explosions with the first version of DESC. *Process Safety and Environmental Protection*, *83* (B2), 151-160.

(151) Skjold, T. (2007). Review of the DESC Project. *Journal of Loss Prevention in the Process Industries*, *20*, 291-302.

(152) Skjold, T. (2014). Flame Propagation in Dust Clouds: Numerical Simulation and Experimental Investigation. Ph.D. Dissertation; University of Bergen, Norway.

(153) Soundararajan, R.; Amyotte, P.; Pegg, M. (1996). Explosibility hazard of iron sulphide dusts as a function of particle size. *Journal of Hazardous Materials*, *51*, 225-239.

(154) Stephenson, C. C.; Zettlemoyer, A. C. (1994). The heat capacity of ammonium dihydrogen phosphate from 15 to 300 K. The anomaly at the Curie temperature. *Journal of the American Chemical Society*, *66* (8), 1405-1408.

(155) Sun, J. H.; Dobashi, R.; Hirano, T. (1998). Structure of flames propagating through metal particle clouds and behavior of particles. *Twenty-Seventh Symposium (International) on Combustion*. The Combustion Institute, Elsevier: New York.

(156) Sun, J.; Dobashi, R.; Hirano, T. (2006). Structure of flames propagating through aluminum particles cloud ad combustion process of particles. *Journal of Loss Prevention in the Process Industries*, *19*, 769-773.

(157) Sun, J. H.; Dobashi, R.; Hirano, T. (2000). Combustion behavior of iron particles suspended in air. *Combustion Science Technology*, *150*, 99-114.

(158) Taveau, J.; Vingerhoets, J.; Snoeys, J.; Going, J.; Farrell, T. (2013). Explosion Protection with Metal Dust Fuels: New Experimental Evidence. In *Proceedings of the Seventh International Seminar on Fire and Explosion Hazards*, Providence, RI, USA, May 5-10.

(159) Taveau, J. Combustible Metal Dusts: A Particular Class. In *17th Annual International Symposium, Mary Kay O'Connor Process Safety Center*, College Station, TX, Oct 28-30, 2014; 594-606.

(160) Taveau, J.; Vingerhoets, J.; Snoeys, J.; Going, J.; Farrell, T. (2015). Suppression of metal dust deflagrations. *Journal of Loss Prevention in the Process Industries*, *36*, 244-251.

(161) Thomas, G. O.; Oakley, G.; Brenton, J. (1991). Influence of the morphology of lycopodium dust on its minimum ignition energy. *Combustion and Flame*, *85*, 526-528.

(162) Traoré, M.; Dufaud, O.; Perrin, L.; Chazalet, S.; Thomas, D. (2009). Dust Explosions: How Should the Influence of Humidity Be Taken Into Account? *Process Safety And Environmental Protection*, *87*, 14-20.

(163) U.S. Chemical Safety and Hazard Investigation Board. *Investigation Report No. 2004-01-I-IN*; Hayes Lemmerz International, Inc.: Huntington, IN, 2003.

(164) U.S. Chemical Safety and Hazard Investigation Board. *Combustible Dust Hazard Study*, 2006.

(165) U.S. Chemical Safety and Hazard Investigation Board. *Case Study No. 2011-3-I-WV*; AL Solutions, Inc., New Cumberland, WV, 2010.

(166) U. S. Chemical Safety and Hazard Investigation Board. *Case Study No. 2011-4-I-TN*; Hoeganaes Corporation, Gallatin, TN, 2011.

(167) Vogl, A. (1994). The Course of Dust Explosions in Pipes and Pneumatic Systems. In *Proceedings of Sixth International Colloquium on Dust Explosions*, Shenyang, Peoples Republic of China; 535-552.

(168) Wang, Y.; Xu, K.; Li, L. (2017). Inhibition of the reaction between aluminum dust and water based on the HIM. *RSC Advances*, *7*, 33327-33334.

(169) Wang, J.; Meng, X.; Zhang, Y.; Chen, H.; Liu, B. (2019). Experimental study on the ignition sensitivity and explosion severity of different ranks of coal dust. *Shock and Vibration*, 1-11.

(170) Whitmore, M. W. (1992). Prediction of dust cloud minimum ignition energy for organic dusts from modified Hartmann tube data. *Journal of Loss Prevention in the Process Industries*, *5* (5), 305-309.

(171) Worsfold, M.; Amyotte, P.; Marta, M. (2019). "Fires, Explosions, and Combustible Dust Hazards". Minerva Safety Management Education. Retrieved from https://cdn.dal.ca/content/dam/dalhousie/pdf/faculty/engineering/peas/CHEE4773/Fires%2C%20Explosions%2C%20and%20Combustible%20Dust%20Hazards_4773.pdf, (Accessed on 27th of February).

(172) Yagi, S.; Kunii, D. (1955). *Fifth International Symposium on Combustion*. Reinhold, 231.

(173) Yang, M.; Jiang, H.; Chen, X.; Gao, W. (2021). Characteristic evaluation of aluminum dust explosion venting with high static activation pressure. *Process Safety and Environmental Protection*, *152*, 83-96.

(174) Yetter, R. A.; Dryer, F. L. (2001). Metal particle combustion and classification, Chapter 6. In: Microgravity Combustion: Fire in Free Fall. Academic Press: New York, 419-478.

(175) Yu, J.; Zhang, X.; Zhang, Q.; Wang, L.; Ji, K.; Peng, L.; Gao, W. (2016). Combustion behaviors and flame microstructures of micro- and nano-titanium dust explosions. *Fuel*, *181*, 785-792.

(176) Yuan, C.; Amyotte, P.; Hossain, M.; Li, C. (2014). Minimum ignition temperature of nano and micro Ti powder clouds in the presence of inert nano TiO_2 powder. *Journal of Hazardous Materials*, *275*, 1-9.

(177) Zalosh, R. (2008). Dust Explosion Fundamentals: Ignition Criteria and Pressure Development. The Fire Protection Research Foundation; Wellesley, MA.

(178) Zalosh, R. (2008). Metal hydride fires and fire suppression agents. *Journal of Loss Prevention in the Process Industries*, *21*, 214-221.

(179) Zhang, Q.; Liu, L.; Shen, S. (2018). Effect of turbulence on explosion of aluminum dust at various concentrations of air. *Powder Technology*, *325*, 467-475.

(180) Zhang, J.; Sun, L.; Sun, T.; Zhou, H. (2020). Study on explosion risk of aluminum powder under different dispersions. *Journal of Loss Prevention in the Process Industries*, *64*, 104042.

Appendix

Appendix A: **Particle Size Distributions and Statistical Data for All Fuels and Agents**
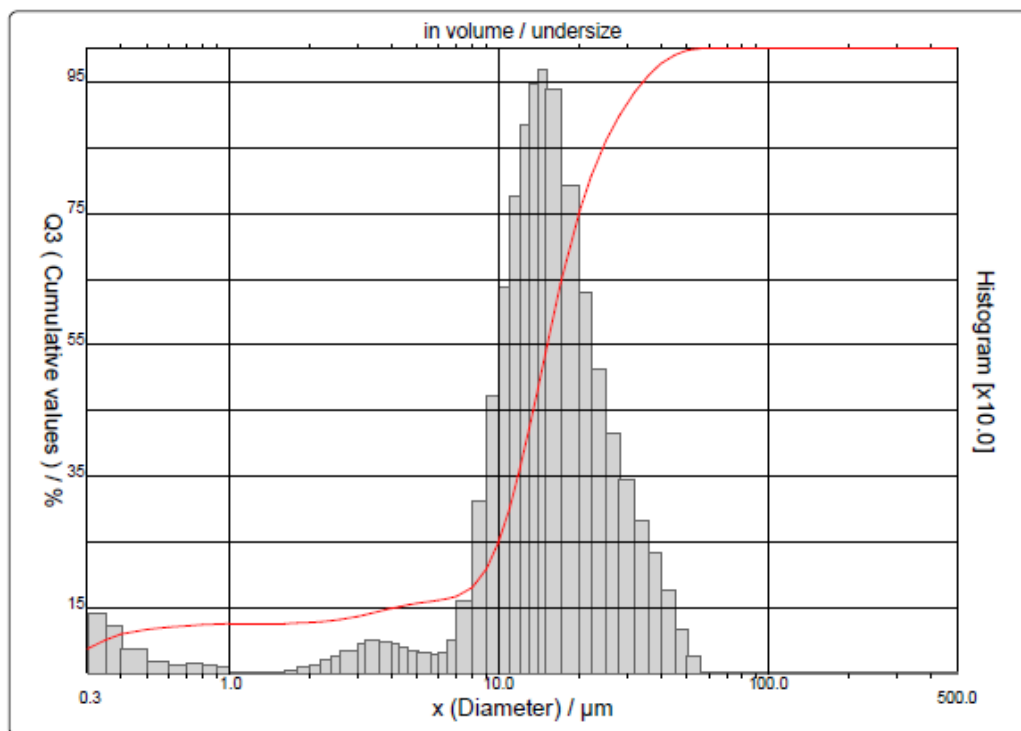
Figure A.1. Particle size distribution for cornstarch [CS].
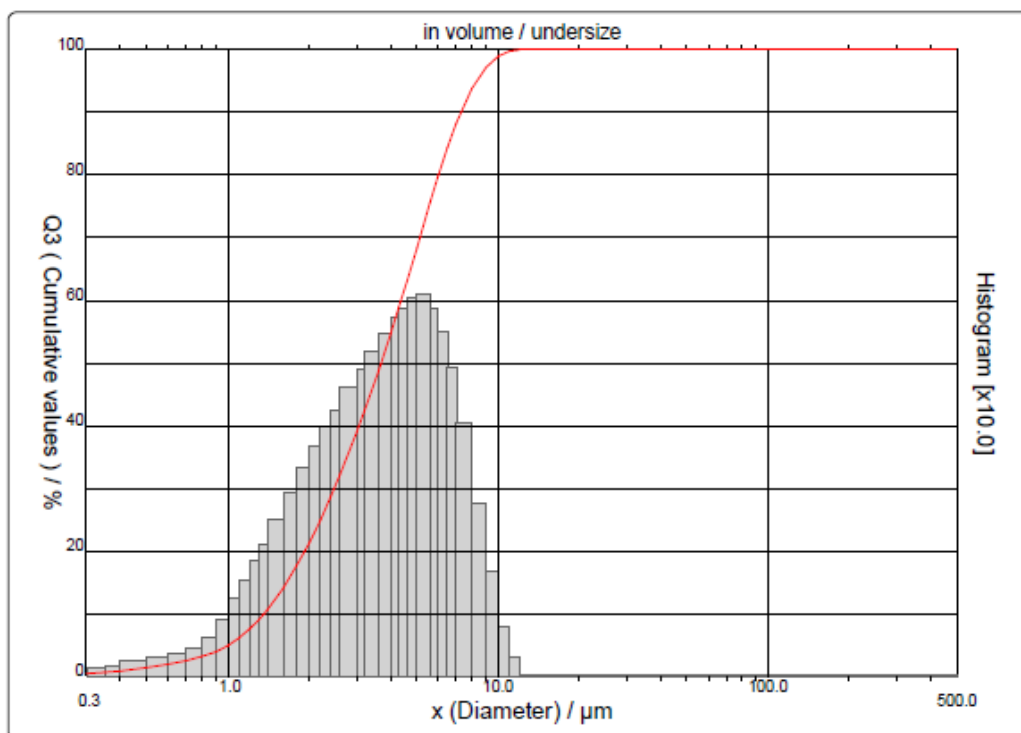
Figure A.2. Particle size distribution for zinc powder [Zn-101].
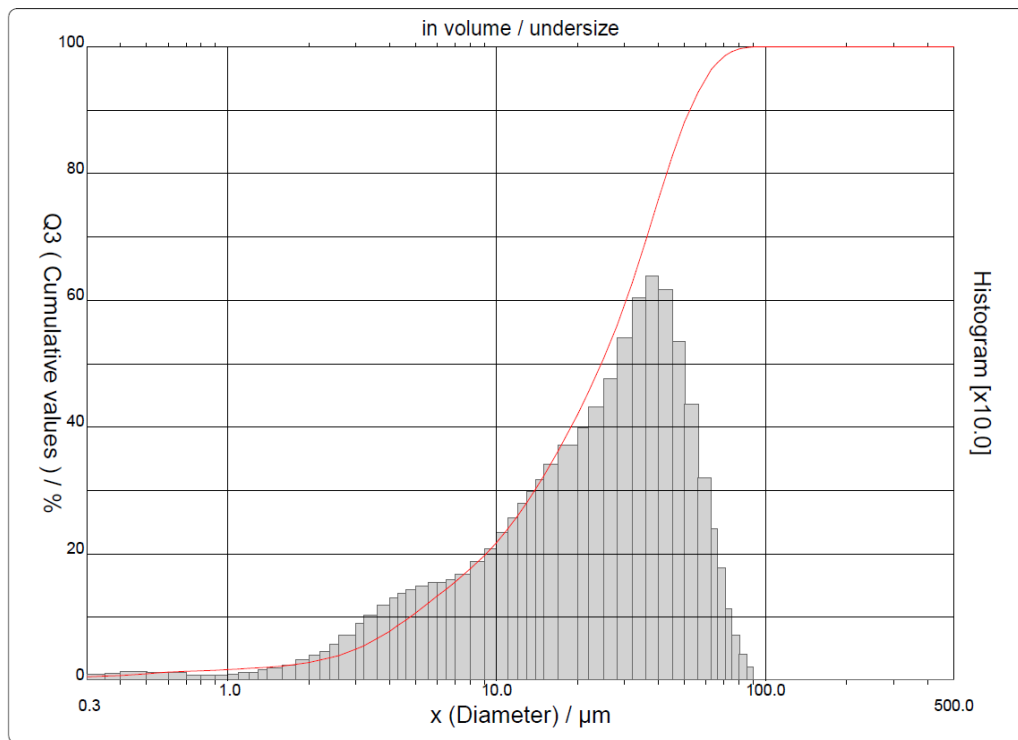
Figure A.3. Particle size distribution for iron powder [Fe-101].
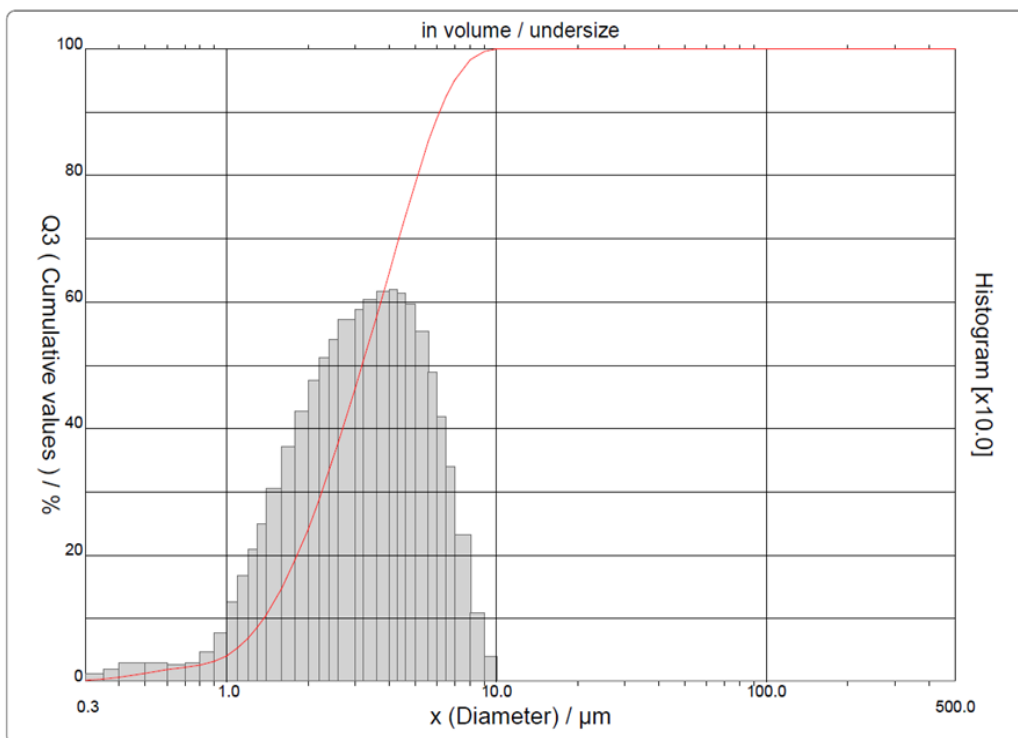
Figure A.4. Particle size distribution for aluminum powder [Al-100].
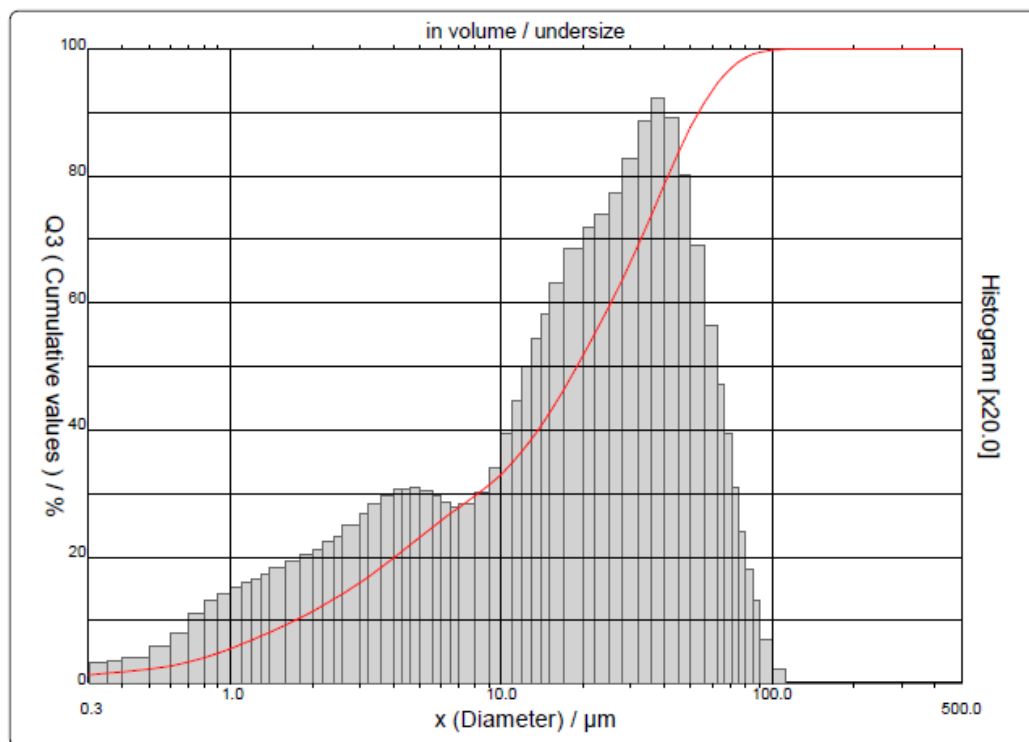
Figure A.5. Particle size distribution for sodium bicarbonate [SBC].
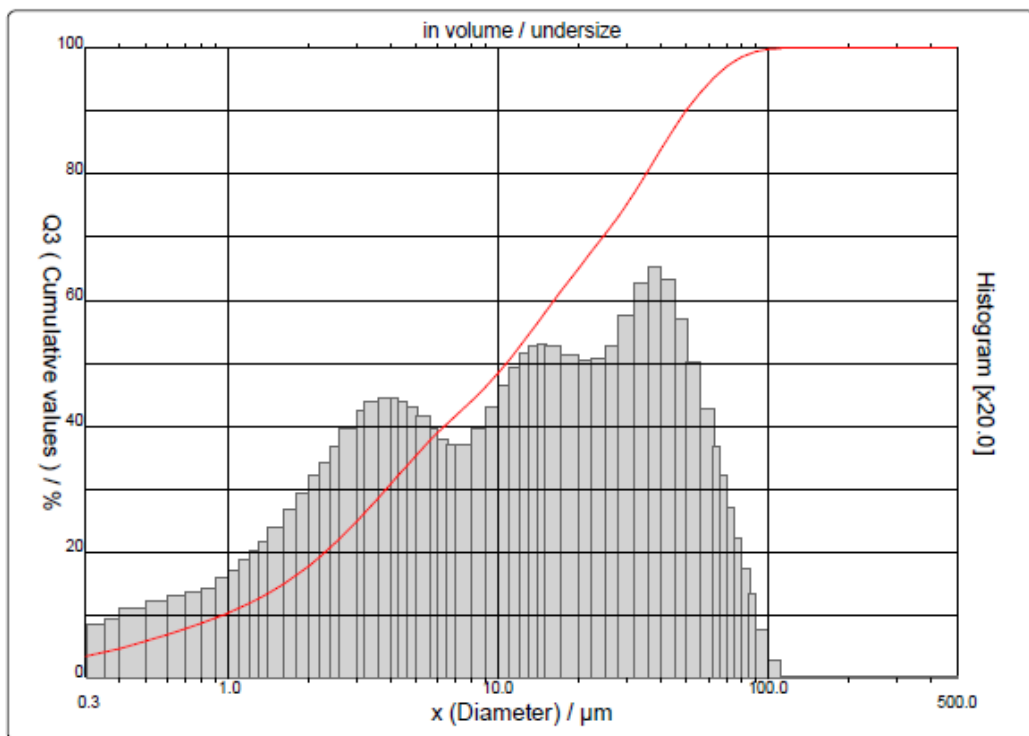
Figure A.6. Particle size distribution for potassium bicarbonate [PBC].
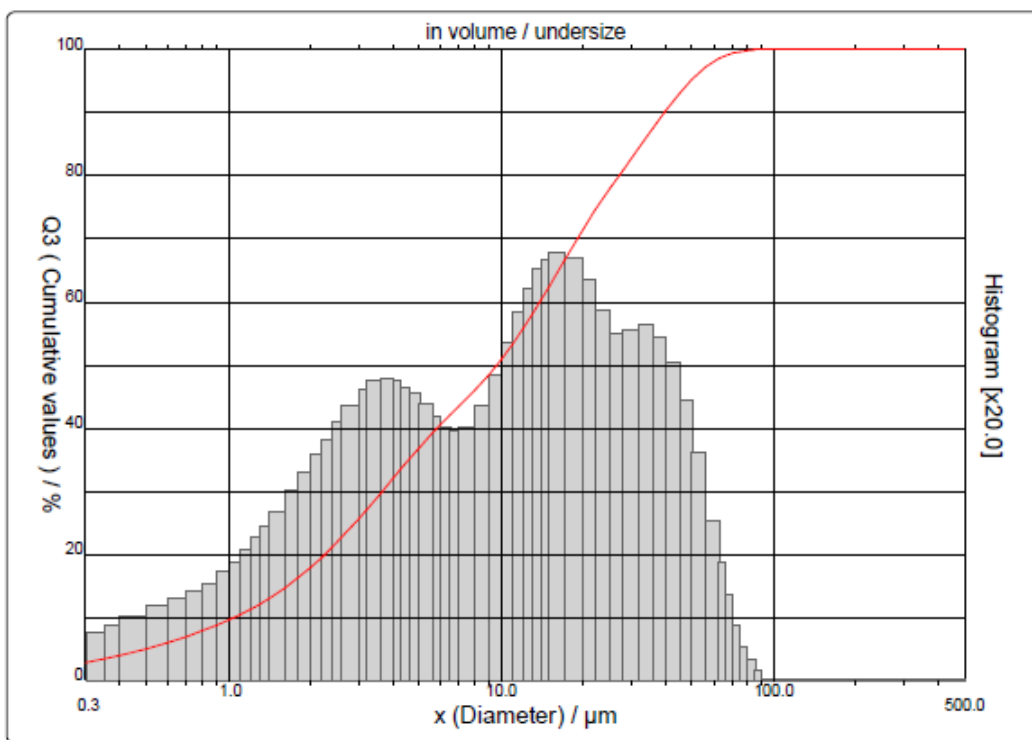
Figure A.7. Particle size distribution for monoammonium phosphate [MAP].
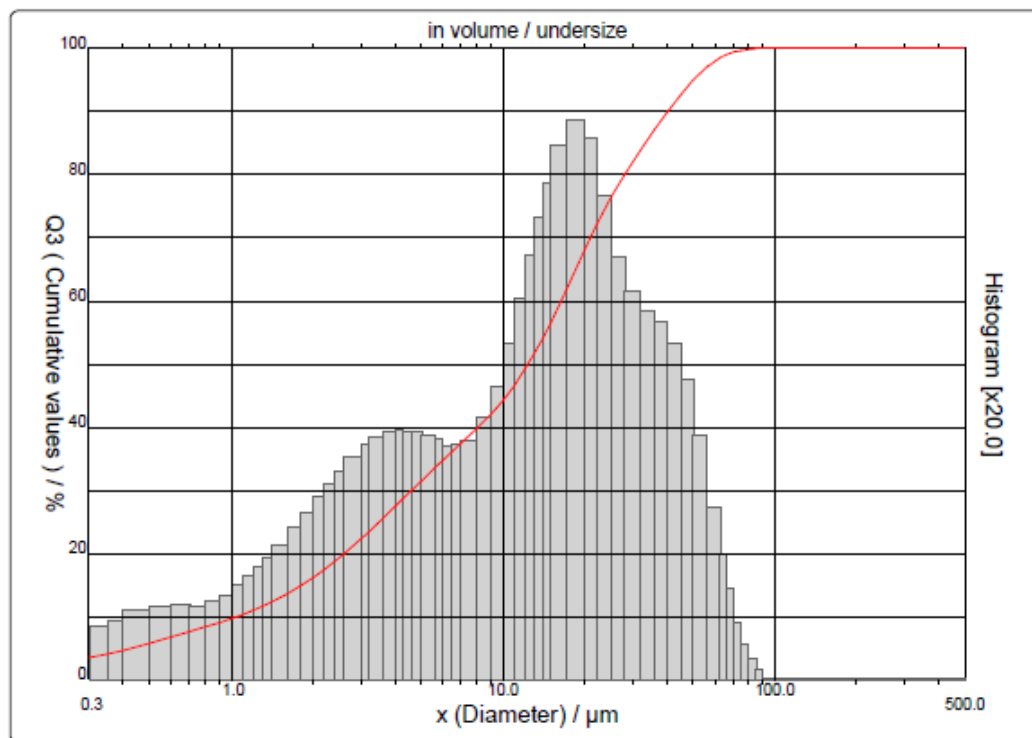
Figure A.8. Particle size distribution for diammonium phosphate [DAP].
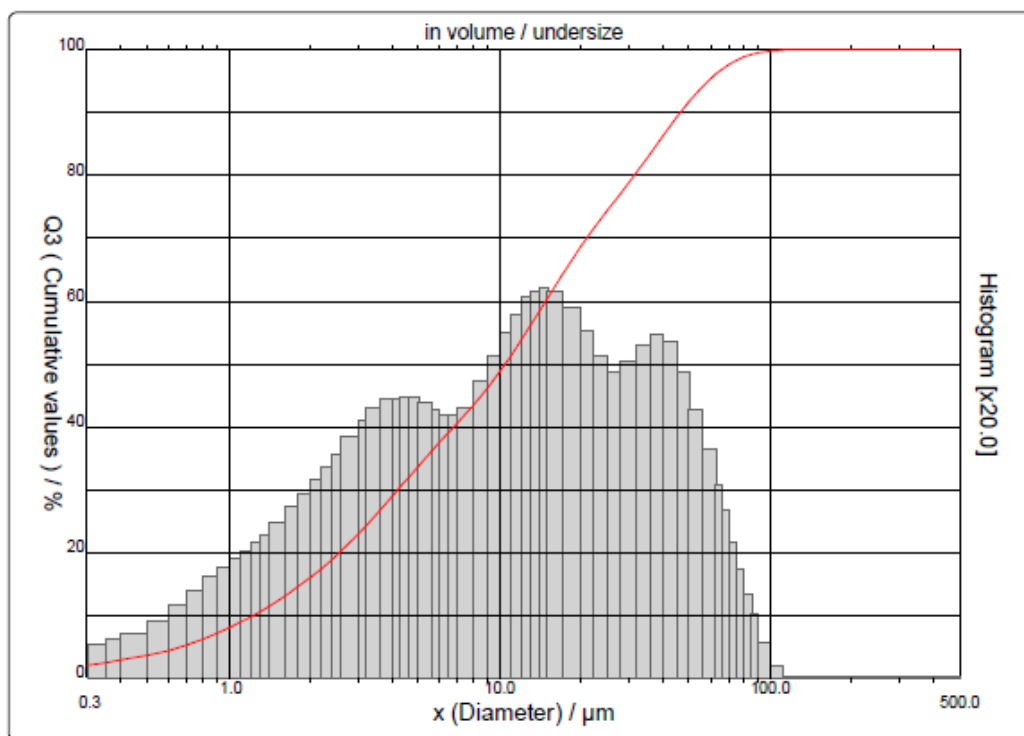
Figure A.9. Particle size distribution for Met-L-X.

Table A.1. Particle size statistical data for all suppressant agent powders.

Suppressant:	SBC	PBC	MAP	DAP	Met-L-X
D10 [μm]	1.72	0.96	1.04	1.04	1.23
D50 [μm]	19.03	10.75	9.61	12.34	10.47
D90 [μm]	53.56	49.58	39.55	40.29	46.34
Mean Diameter [μm]	23.75	18.89	15.27	16.54	17.63

Table A.2. Particle size statistical data for all fuel powders.

Fuel:	Cornstarch (CS)	Zinc (Zn-101)	Iron (Fe-101)	Aluminum (Al-100)
D10 [μm]	0.34	1.36	4.76	1.37
D50 [μm]	14.29	3.68	24.49	3.18
D90 [μm]	28.18	7.31	52.30	6.15
Mean Diameter [μm]	15.28	4.04	26.86	3.51

Appendix B: Mass Loss Profiles (TGA) for All Inhibitors and 1:1 Fuel/Inhibitor Mixtures
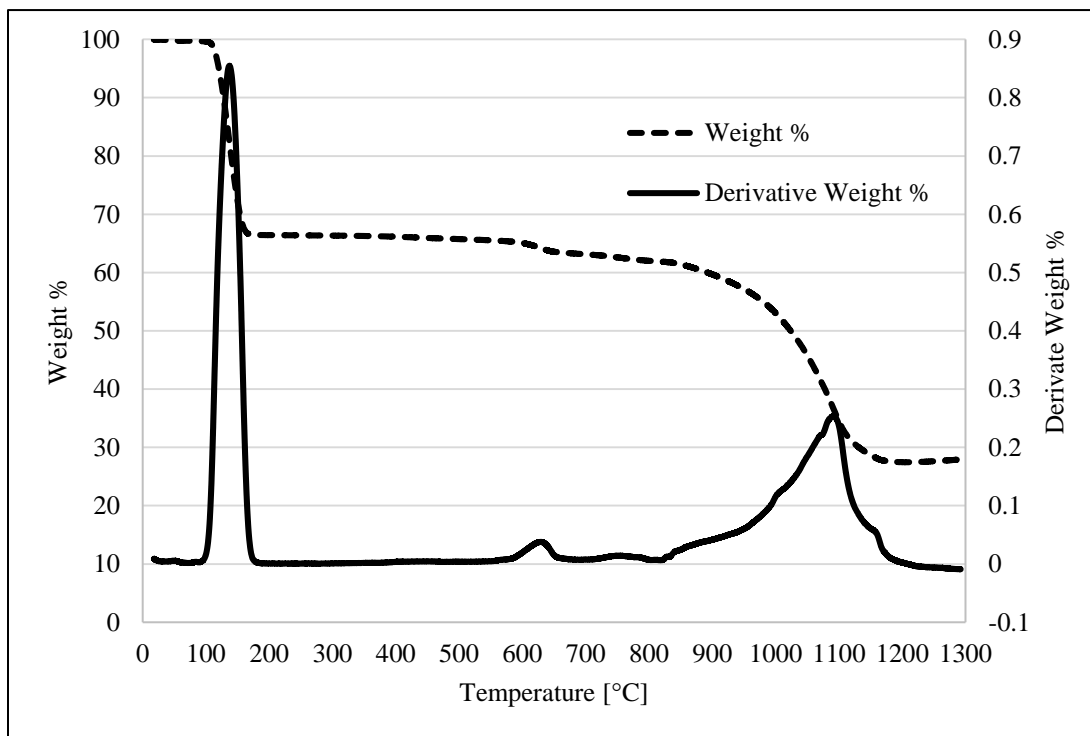
Figure B.1. Thermogravimetric profile of sodium bicarbonate. Increase in temperature, from room temperature to 1300 °C, at a constant 10 °C/min heating rate (in air).
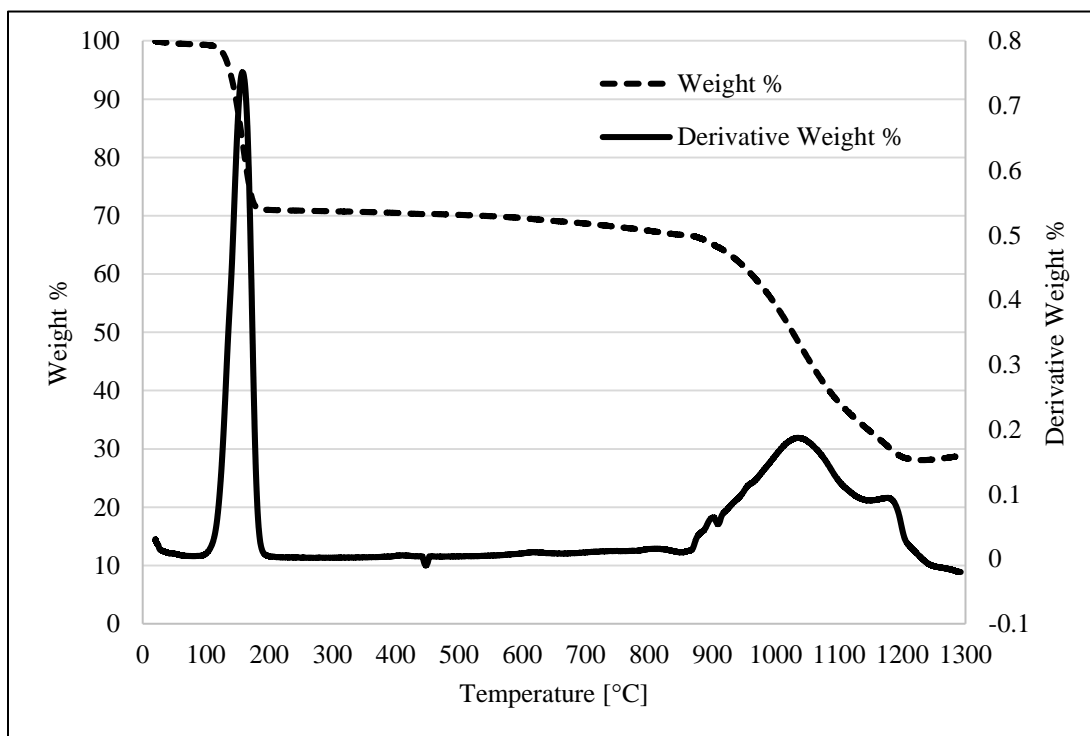
Figure B.2. Thermogravimetric profile of potassium bicarbonate. Increase in temperature, from room temperature to 1300 °C, at a constant 10 °C/min heating rate (in air).
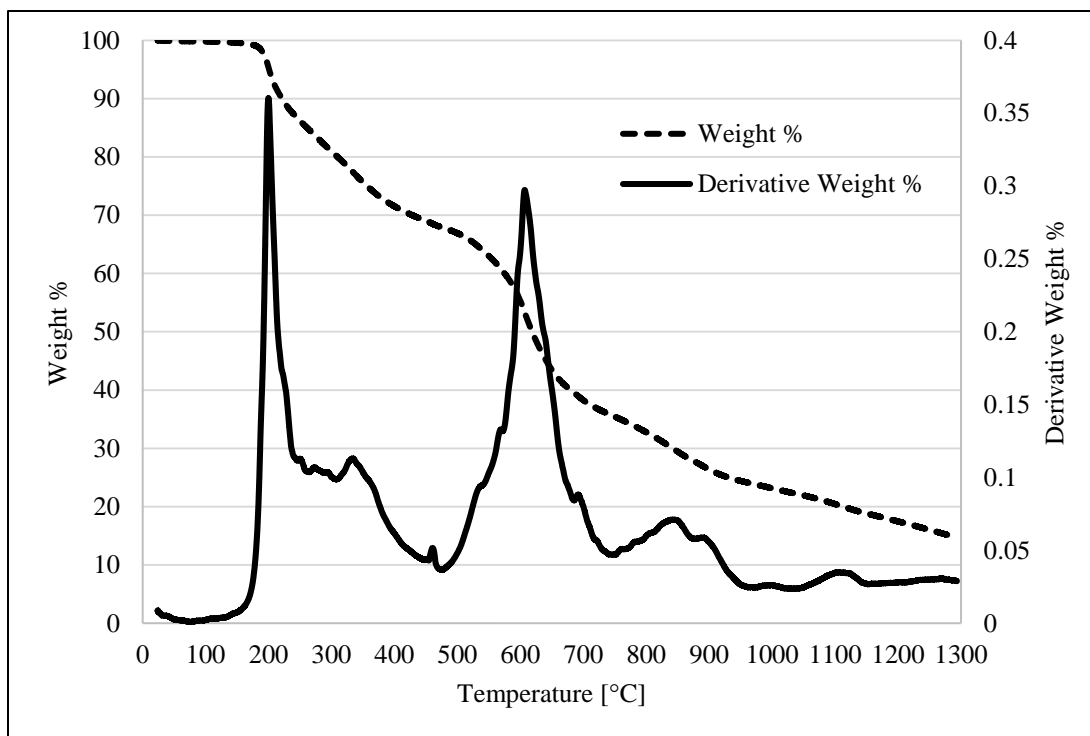
Figure B.3. Thermogravimetric profile of monoammonium phosphate. Increase in temperature, from room temperature to 1300 °C, at a constant 10 °C/min heating rate (in air).
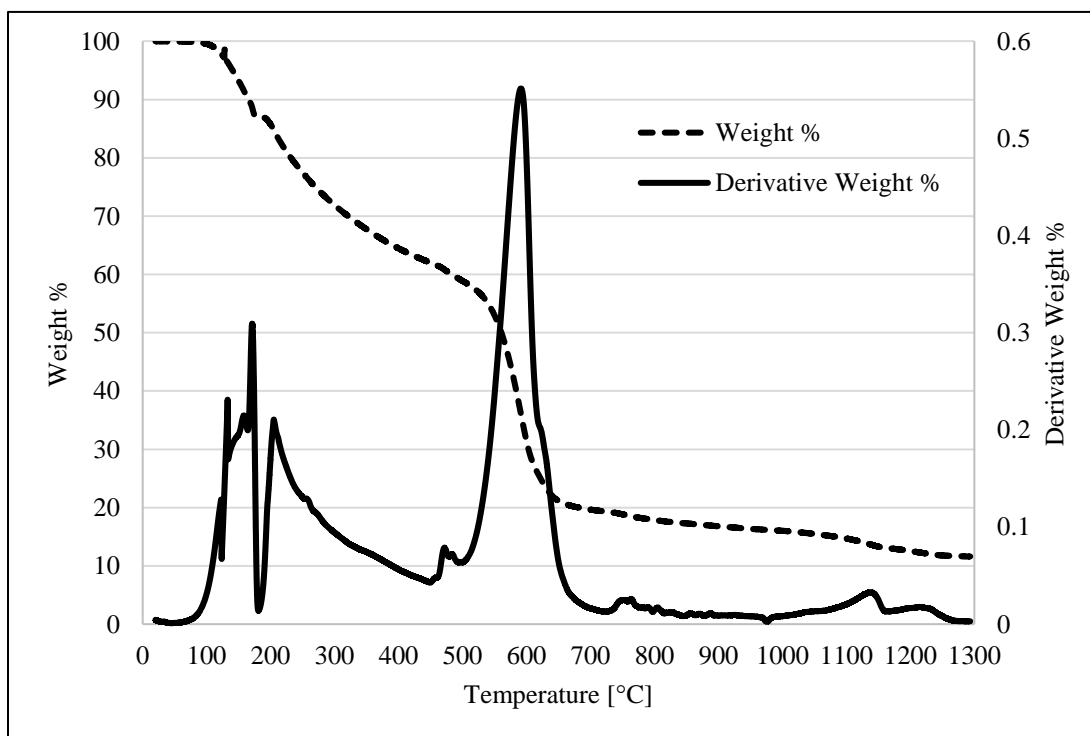
Figure B.4. Thermogravimetric profile of diammonium phosphate. Increase in temperature, from room temperature to 1300 °C, at a constant 10 °C/min heating rate (in air).
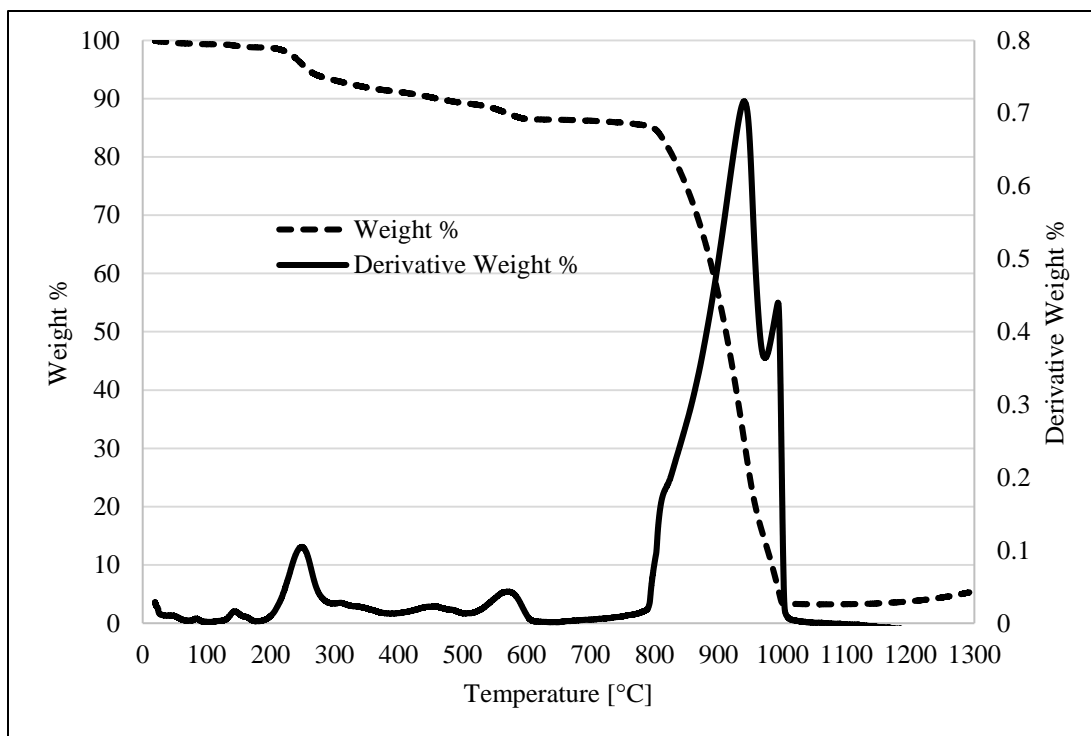
Figure B.5. Thermogravimetric profile of Met-L-X. Increase in temperature, from room temperature to 1300 °C, at a constant 10 °C/min heating rate (in air).
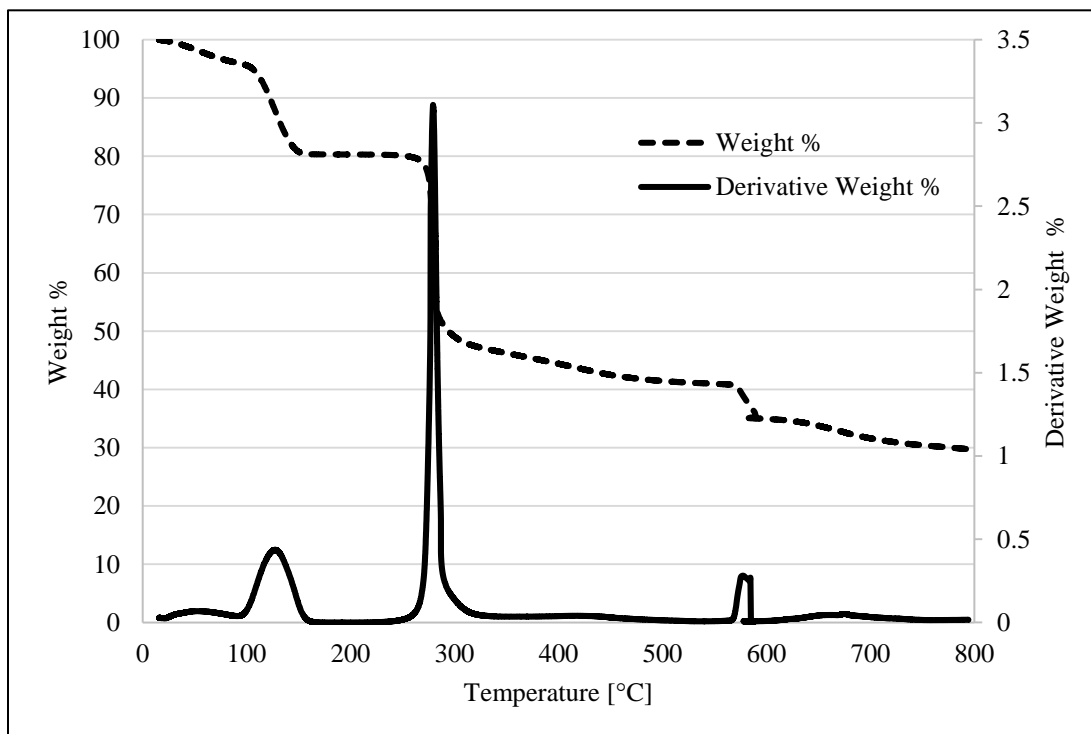
Figure B.6. Thermogravimetric profile of cornstarch mixed with sodium bicarbonate (1:1 ratio by weight). Increase in temperature, from room temperature to 800 °C, at a constant 10 °C/min heating rate (in air).
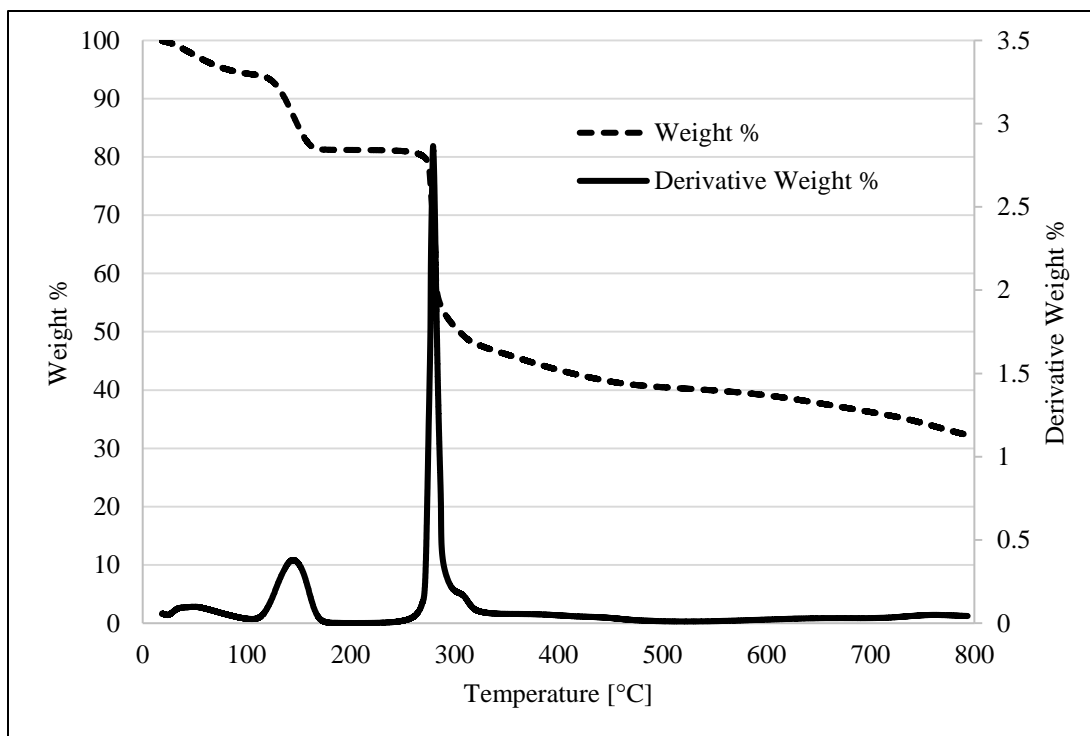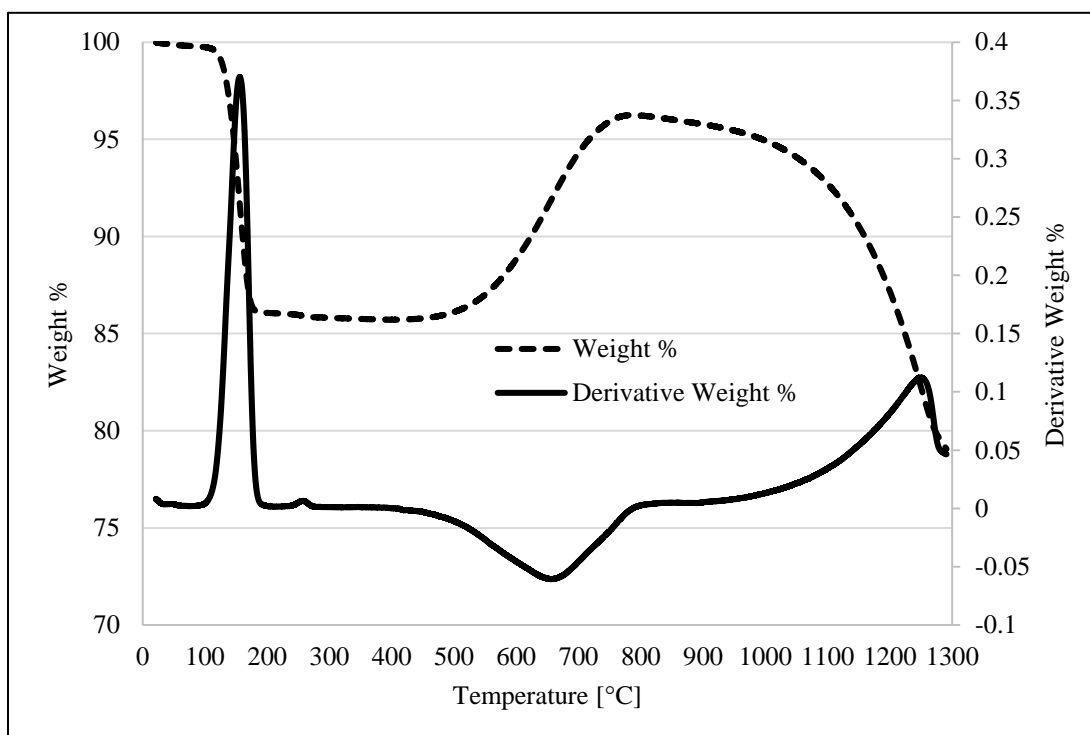
Figure B.7. Thermogravimetric profile of cornstarch mixed with potassium bicarbonate (1:1 ratio by weight). Increase in temperature, from room temperature to 800 °C, at a constant 10 °C /min heating rate (in air).
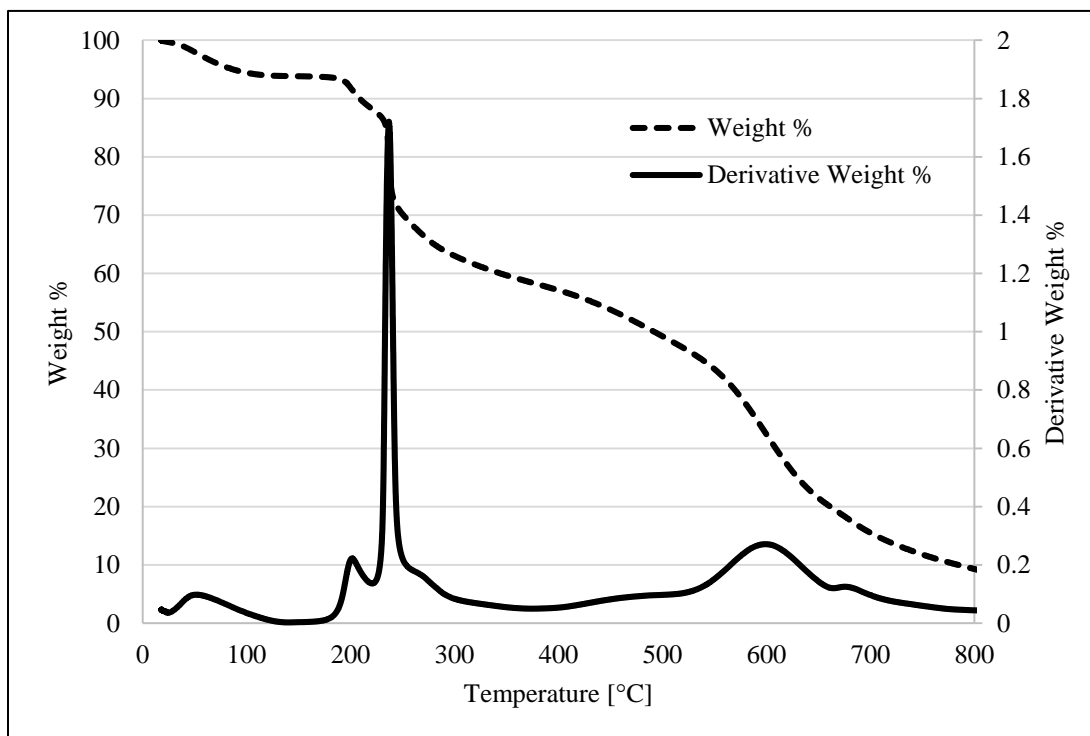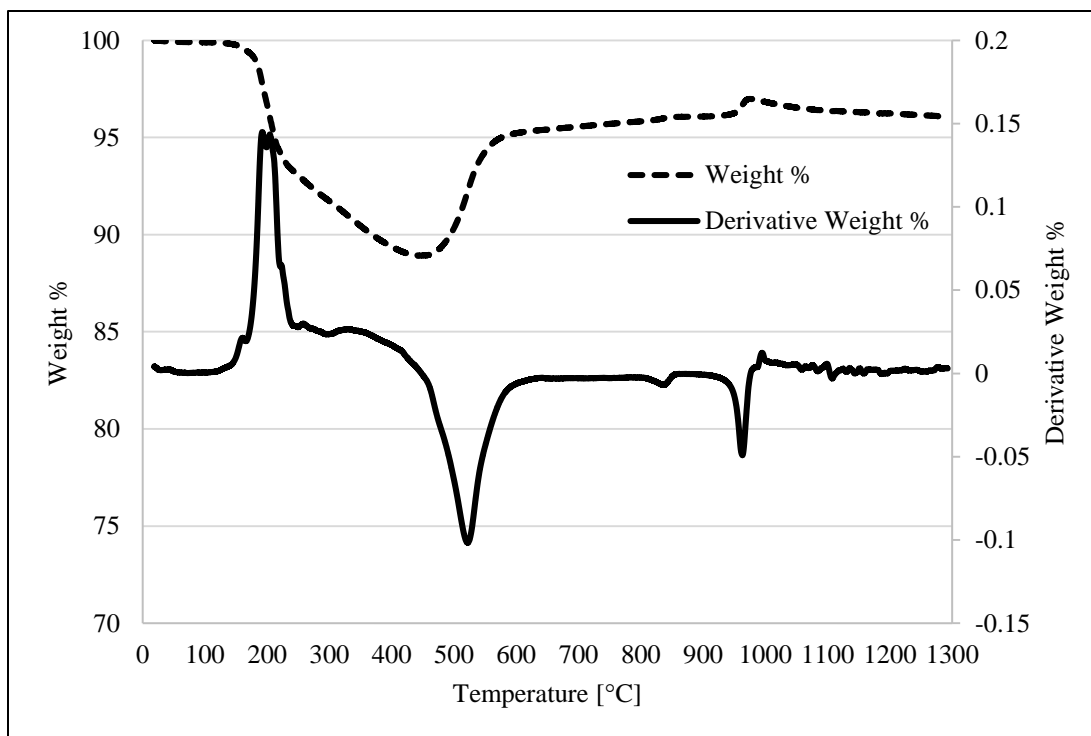

Figure B.8. Thermogravimetric profile of cornstarch mixed with monoammonium phosphate (1:1 ratio by weight). Increase in temperature, from room temperature to 800 °C, at a constant 10 °C /min heating rate (in air).
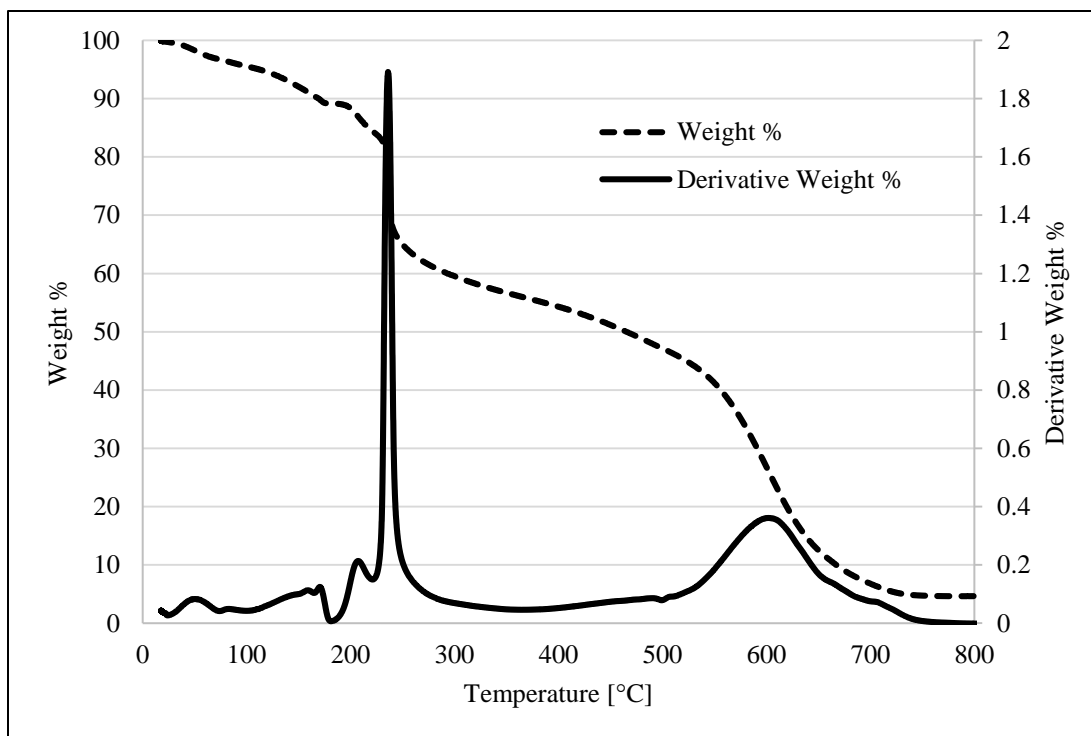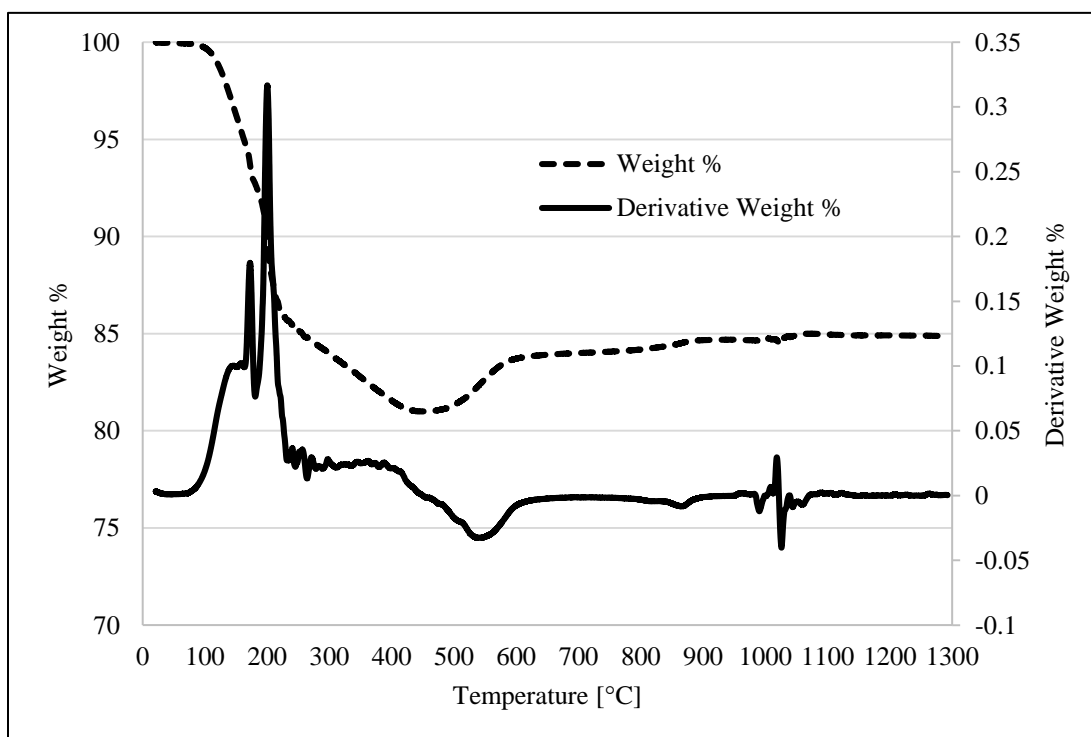
Figure B.9. Thermogravimetric profile of cornstarch mixed with diammonium phosphate (1:1 ratio by weight). Increase in temperature, from room temperature to 800 °C, at a constant 10 °C /min heating rate (in air).
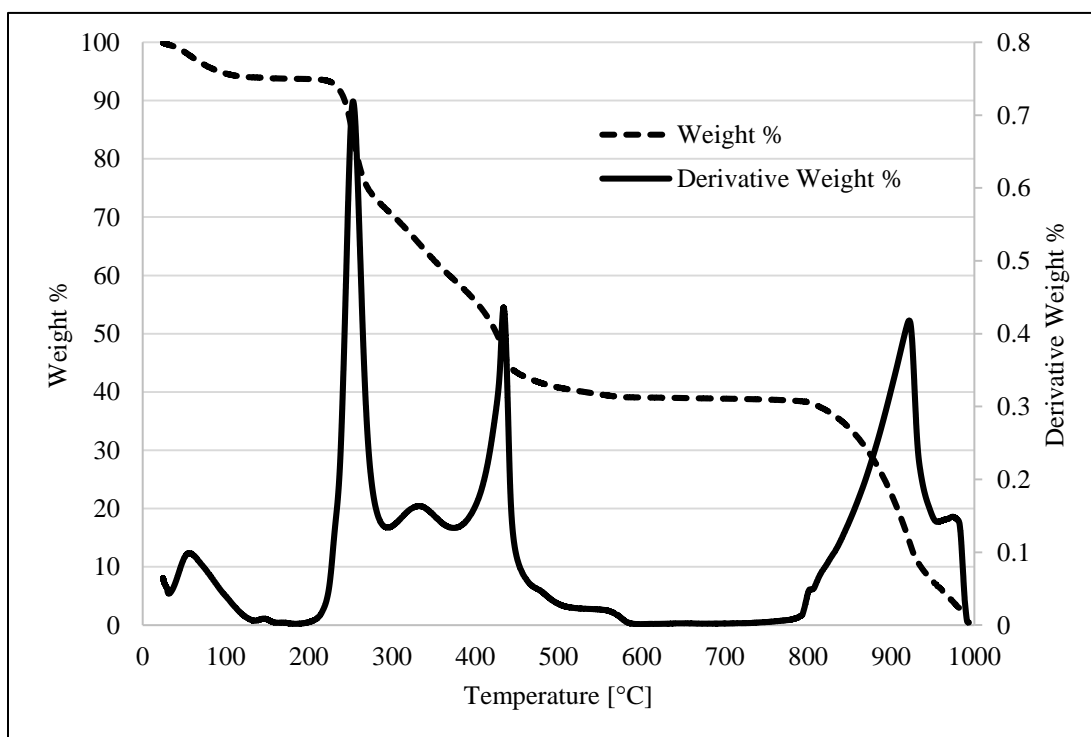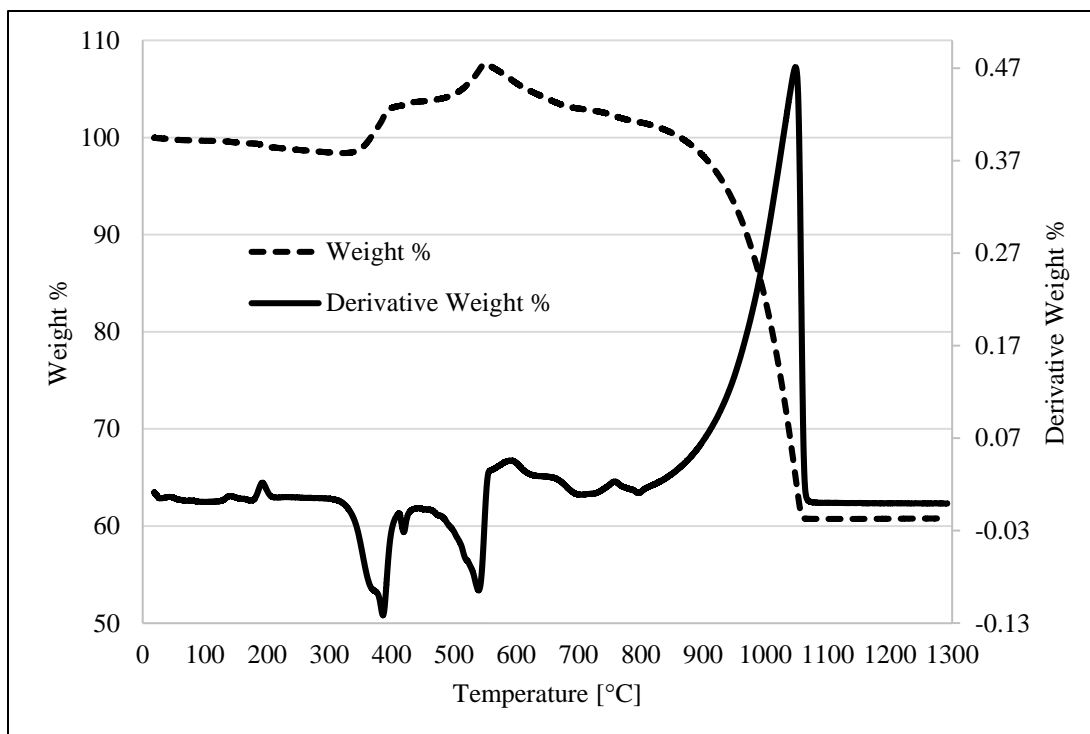

Figure B.10. Thermogravimetric profile of cornstarch mixed with Met-L-X (1:1 ratio by weight). Increase in temperature, from room temperature to 1000 °C, at a constant 10 °C /min heating rate (in air).
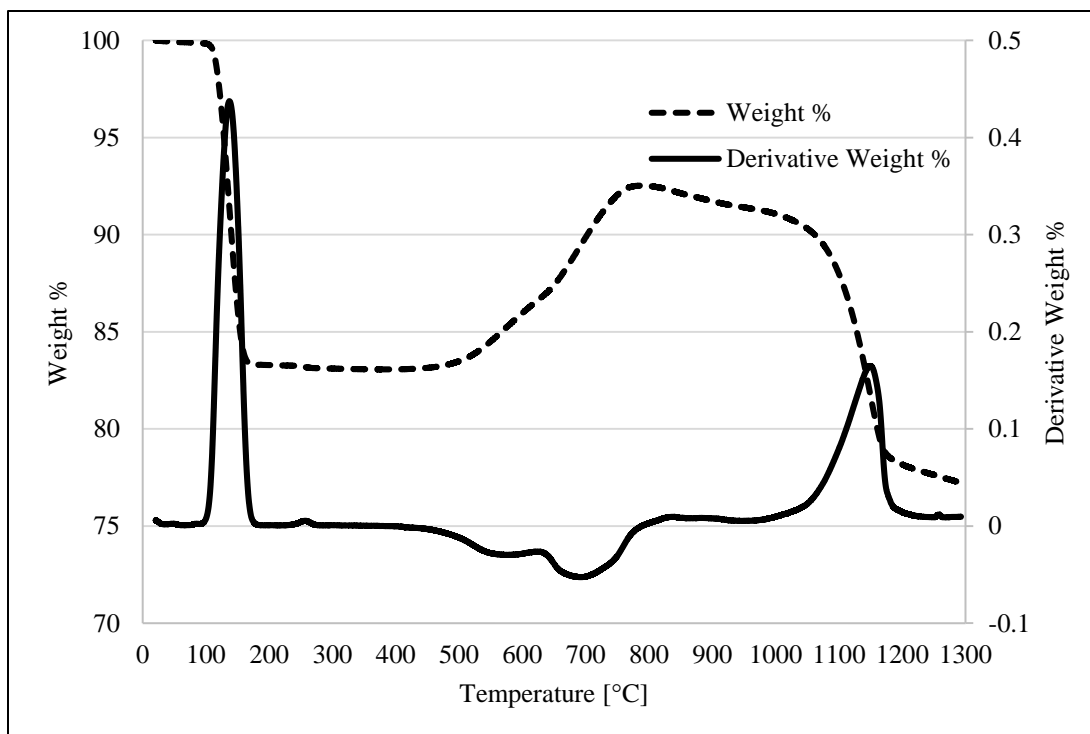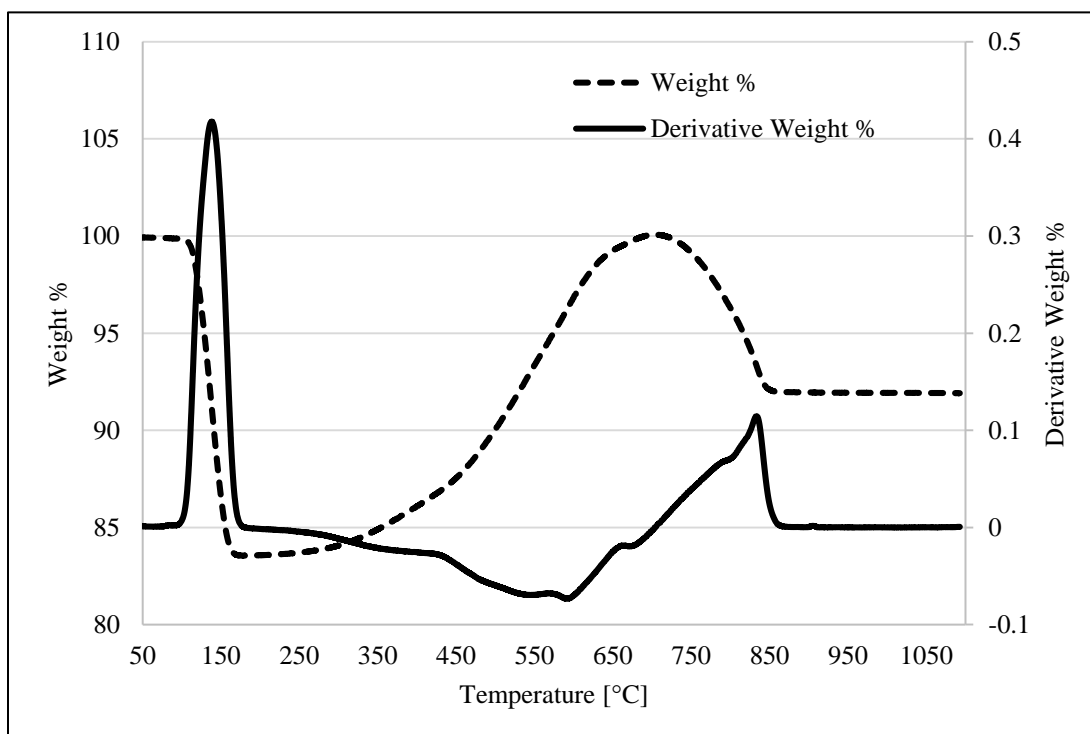
Figure B.11. Thermogravimetric profile of zinc powder mixed with sodium bicarbonate (1:1 ratio by weight). Increase in temperature, from room temperature to 1300 °C, at a constant 10 °C /min heating rate (in air).

Figure B.12. Thermogravimetric profile of zinc powder mixed with potassium bicarbonate (1:1 ratio by weight). Increase in temperature, from room temperature to 1300 °C, at a constant 10 °C /min heating rate (in air).
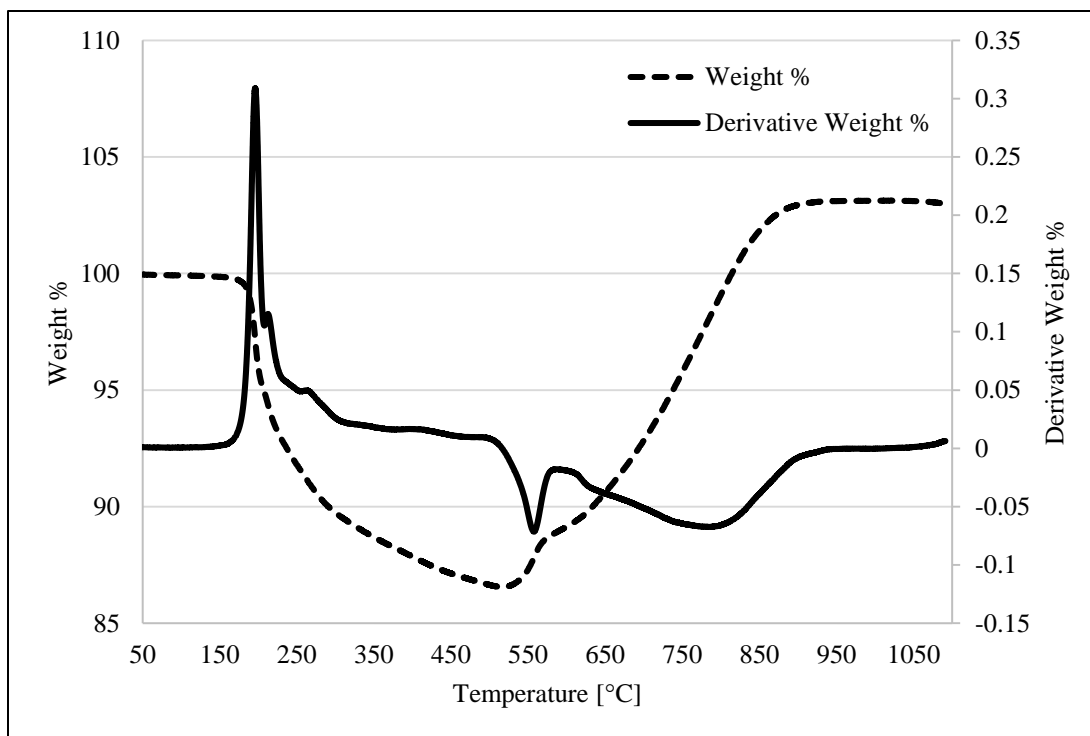
Figure B.13. Thermogravimetric profile of zinc powder mixed with monoammonium phosphate (1:1 ratio by weight). Increase in temperature, from room temperature to 1300 °C, at a constant 10 °C /min heating rate (in air).

Figure B.14. Thermogravimetric profile of zinc powder mixed with diammonium phosphate (1:1 ratio by weight). Increase in temperature, from room temperature to 1300 °C, at a constant 10 °C /min heating rate (in air).
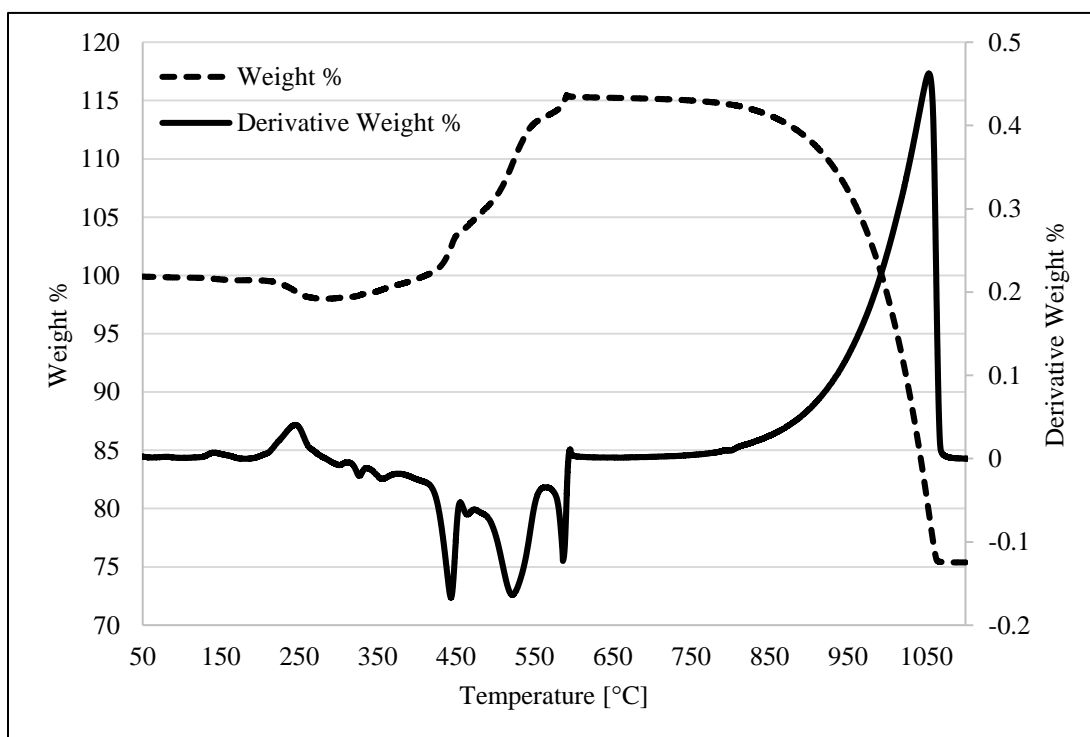
Figure B.15. Thermogravimetric profile of zinc powder mixed with Met-L-X (1:1 ratio by weight). Increase in temperature, from room temperature to 1300 °C, at a constant 10 °C /min heating rate (in air).

Figure B.16. Thermogravimetric profile of iron powder mixed with sodium bicarbonate (1:1 ratio by weight). Increase in temperature, from 50 to 1100 °C, at a constant 10 °C /min heating rate (in air).

Figure B.17. Thermogravimetric profile of iron powder mixed with monoammonium phosphate (1:1 ratio by weight). Increase in temperature, from 50 to 1100 °C, at a constant 10 °C /min heating rate (in air).

Figure B.18. Thermogravimetric profile of iron powder mixed with Met-L-X (1:1 ratio by weight). Increase in temperature, from 50 to 1100 °C, at a constant 10 °C /min heating rate (in air).
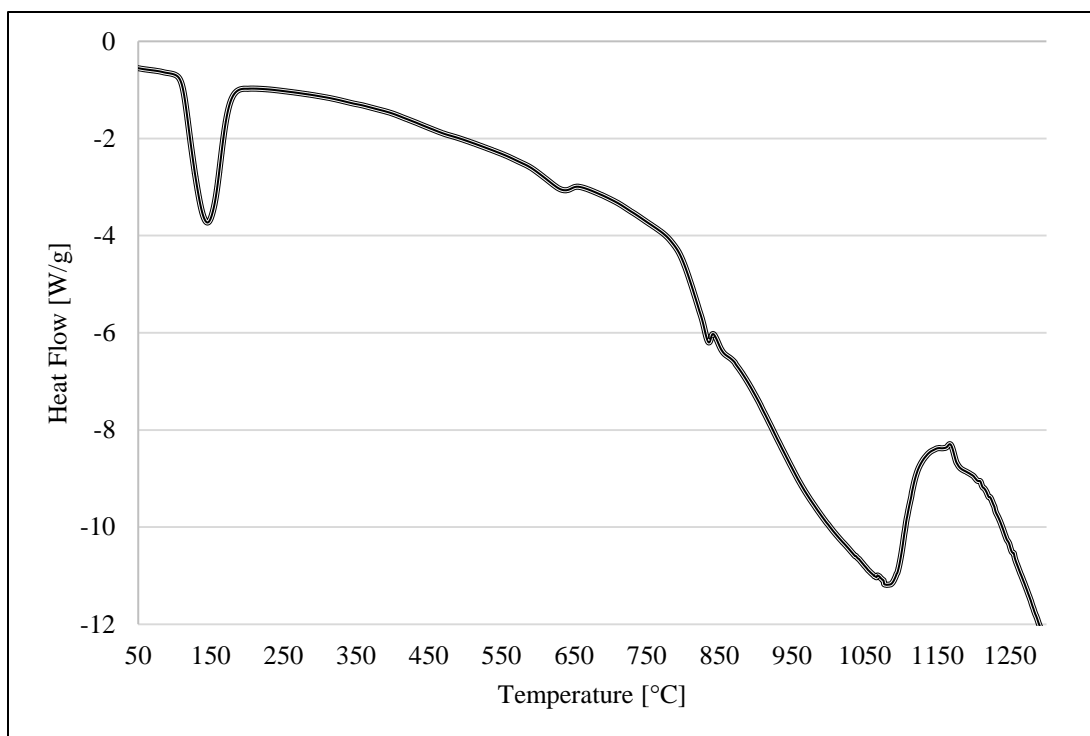
<u>Appendix C</u>: DSC Profiles for All Inhibitors and 1:1 Fuel/Inhibitor Mixtures

Figure C.1. Differential scanning calorimetry profile for sodium bicarbonate. Increase in temperature, from 50 to 1300 °C, at a constant 10 °C/min heating rate (in air).
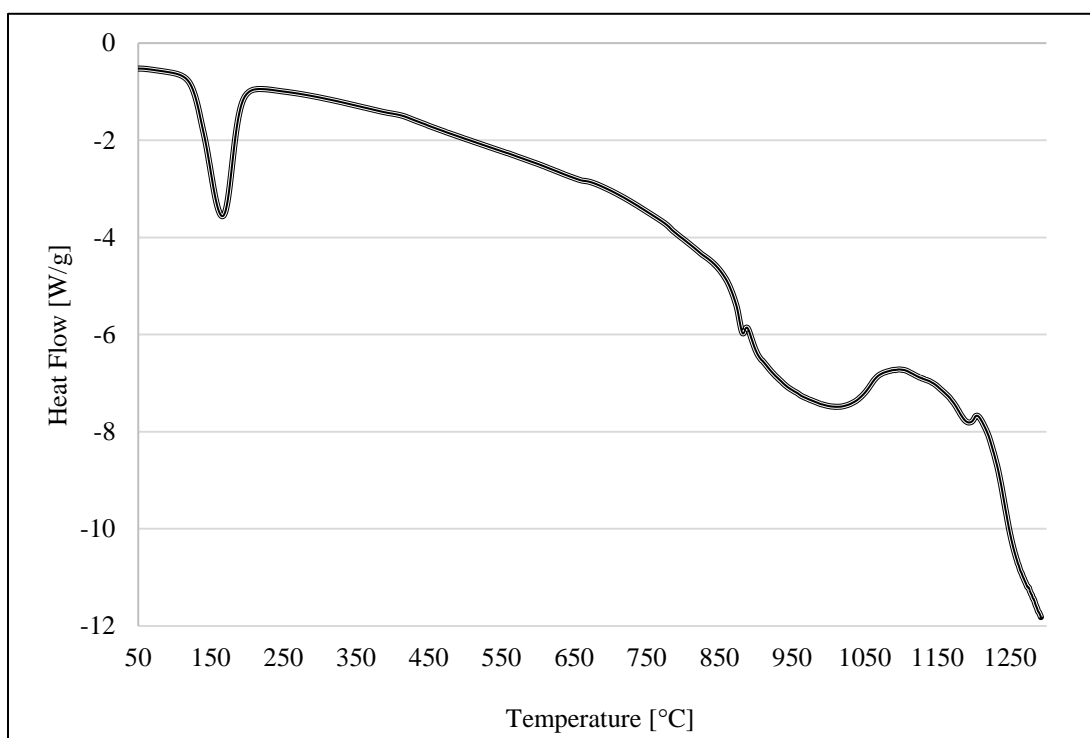

Figure C.2. Differential scanning calorimetry profile for potassium bicarbonate. Increase in temperature, from 50 to 1300 °C, at a constant 10 °C/min heating rate (in air).
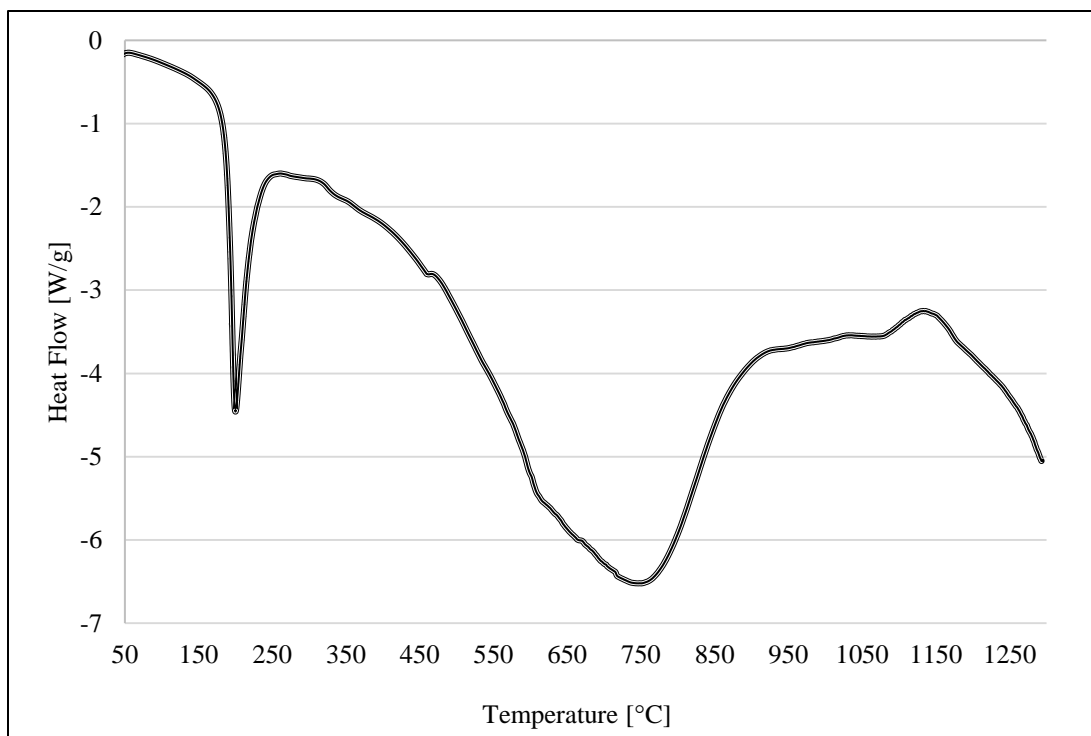
Figure C.3. Differential scanning calorimetry profile for monoammonium phosphate. Increase in temperature, from 50 to 1300 °C, at a constant 10 °C/min heating rate (in air).
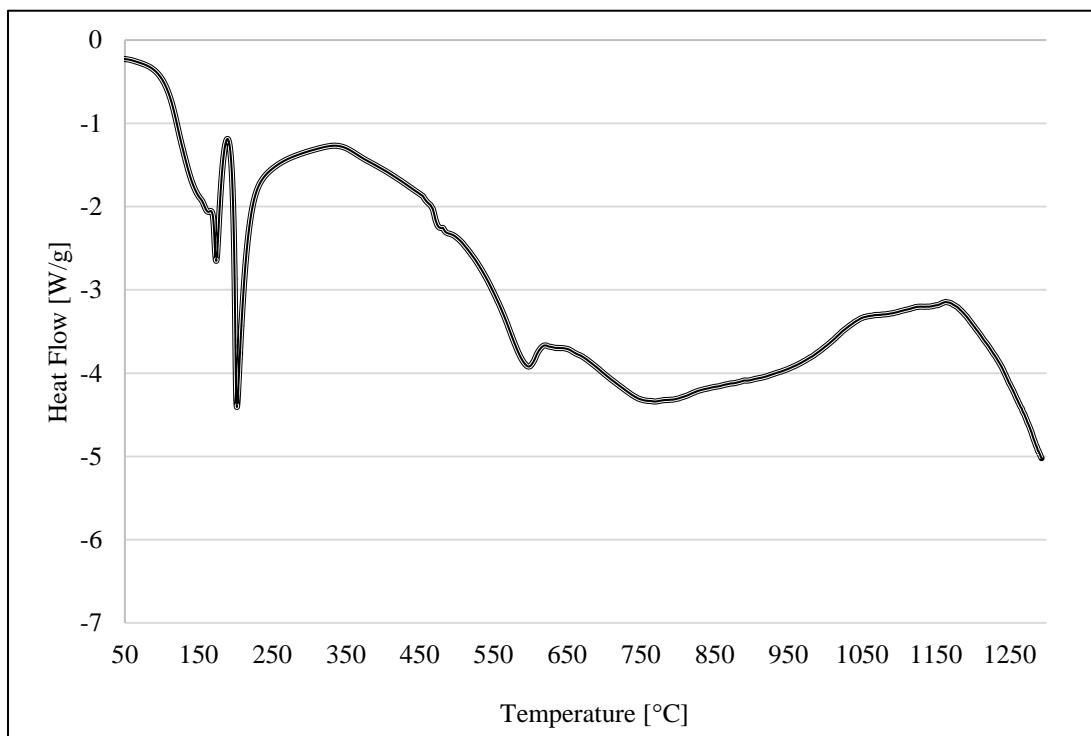

Figure C.4. Differential scanning calorimetry profile for diammonium phosphate. Increase in temperature, from 50 to 1300 °C, at a constant 10 °C/min heating rate (in air).
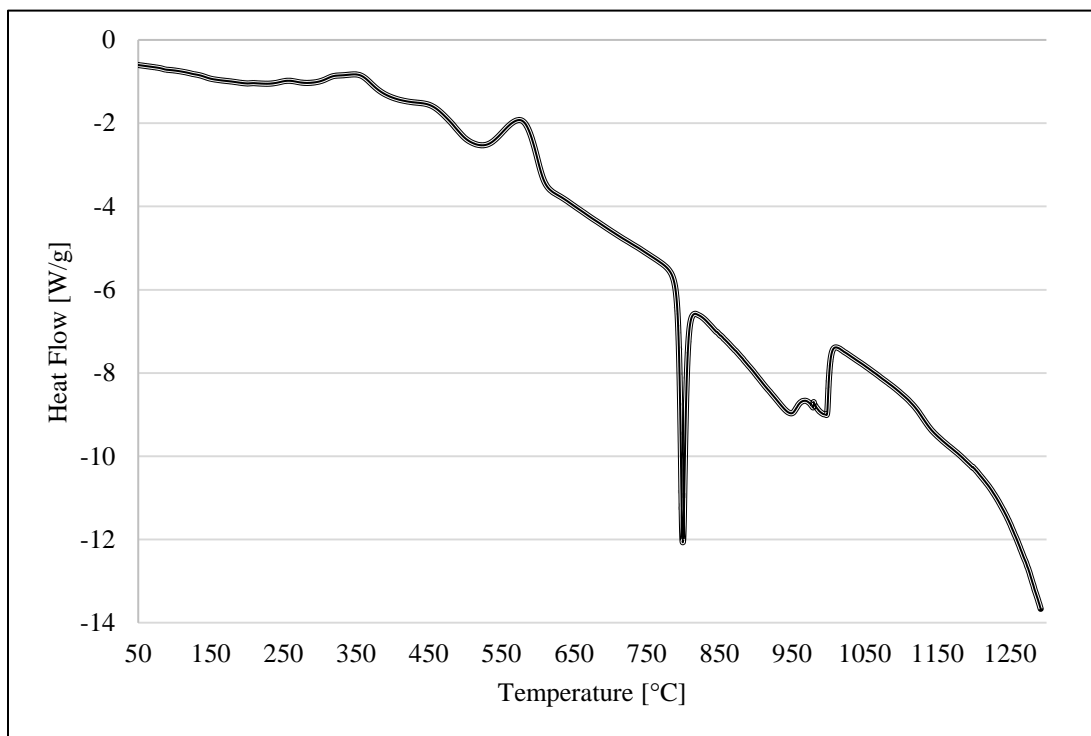
Figure C.5. Differential scanning calorimetry profile for Met-L-X. Increase in temperature, from 50 to 1300 °C, at a constant 10 °C/min heating rate (in air).
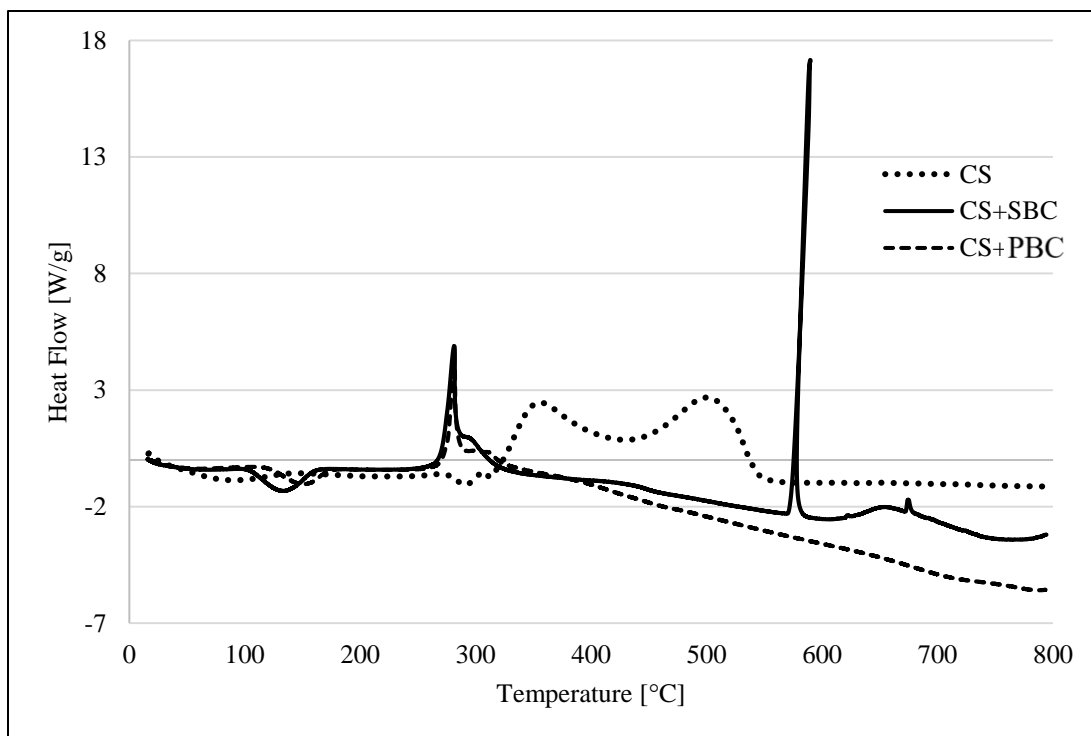

Figure C.6. Differential scanning calorimetry profile for cornstarch and cornstarch/carbonate inhibitor mixtures. Increase in temperature, from room temperature to 800 °C, at a constant 10 °C/min heating rate (in air).
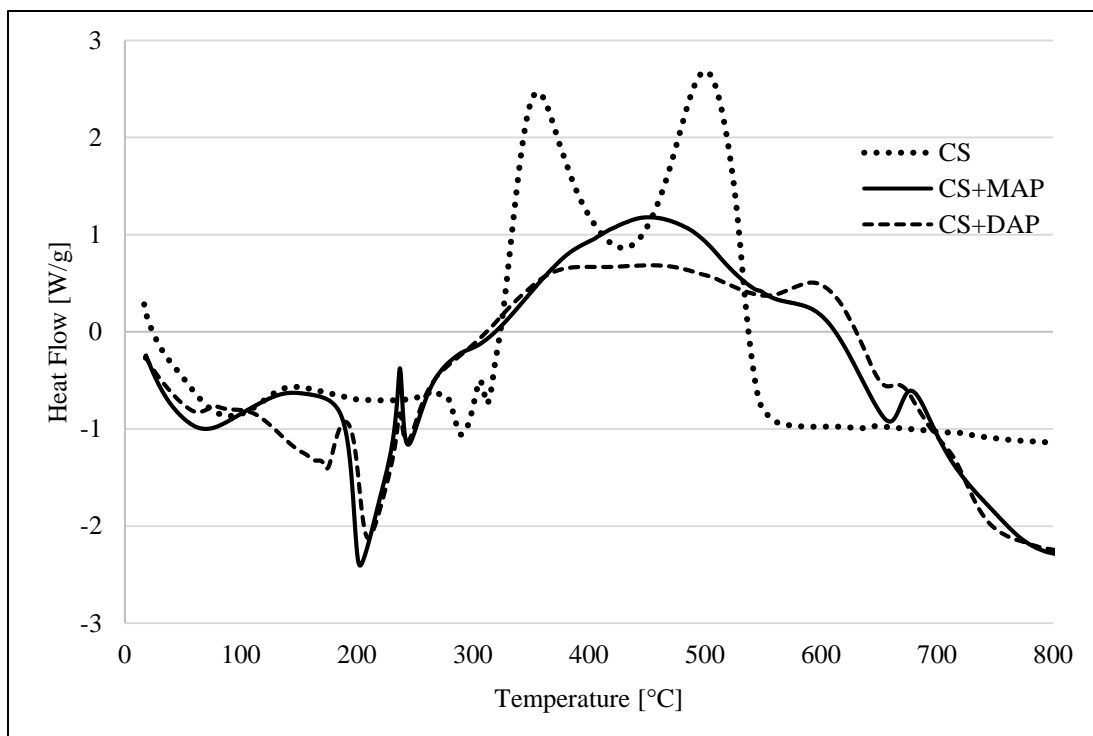
Figure C.7. Differential scanning calorimetry profile for cornstarch and cornstarch/phosphate inhibitor mixtures. Increase in temperature, from room temperature to 800 °C, at a constant 10 °C/min heating rate (in air).
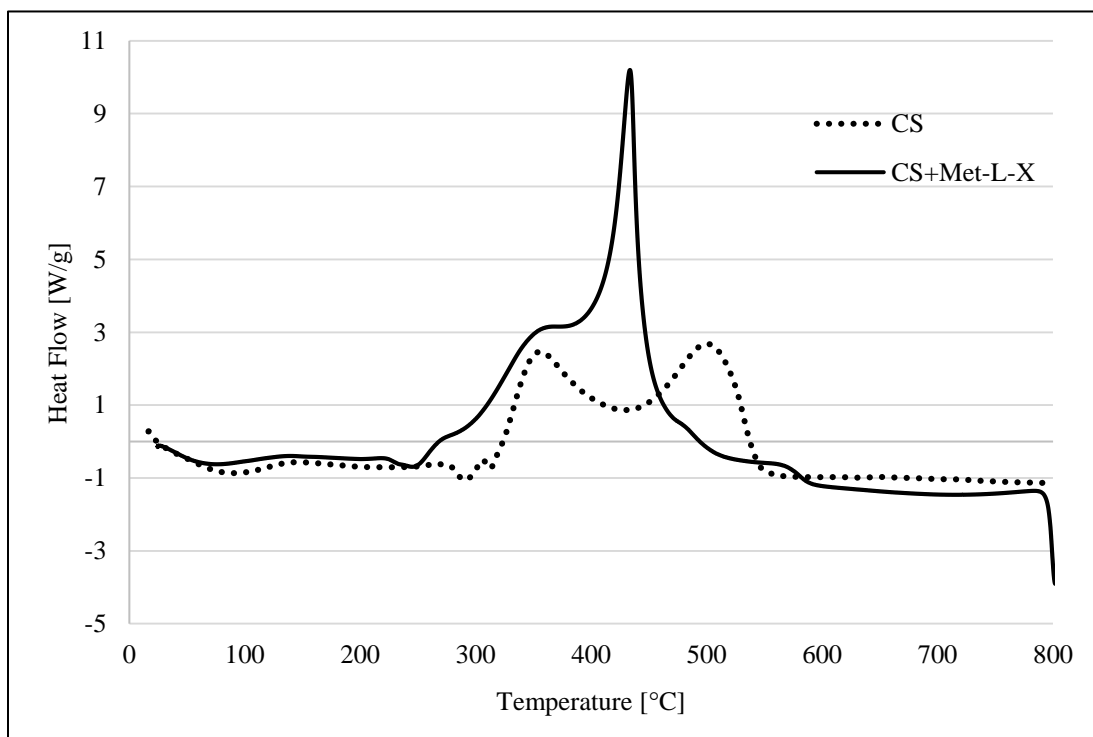

Figure C.8. Differential scanning calorimetry profile for cornstarch and cornstarch/Met-L-X inhibitor mixture. Increase in temperature, from room temperature to 800 °C, at a constant 10 °C/min heating rate (in air).
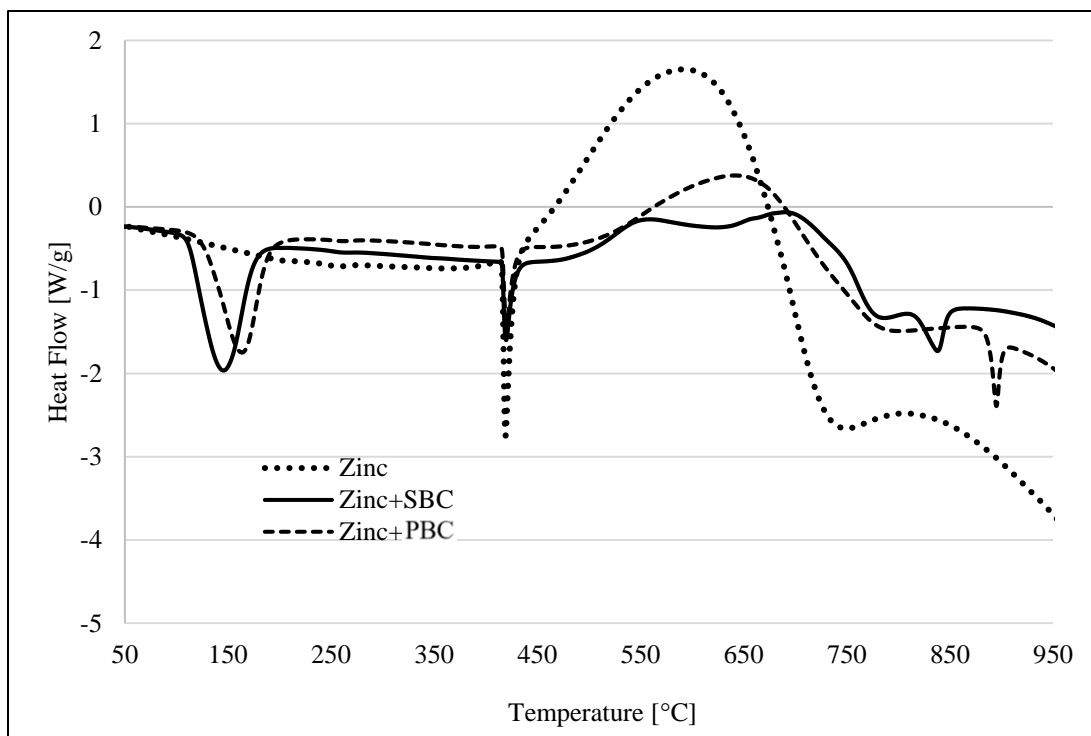
Figure C.9. Differential scanning calorimetry profile for zinc powder and zinc/carbonate inhibitor mixtures. Increase in temperature, from 50 to 950 °C, at a constant 10 °C/min heating rate (in air).
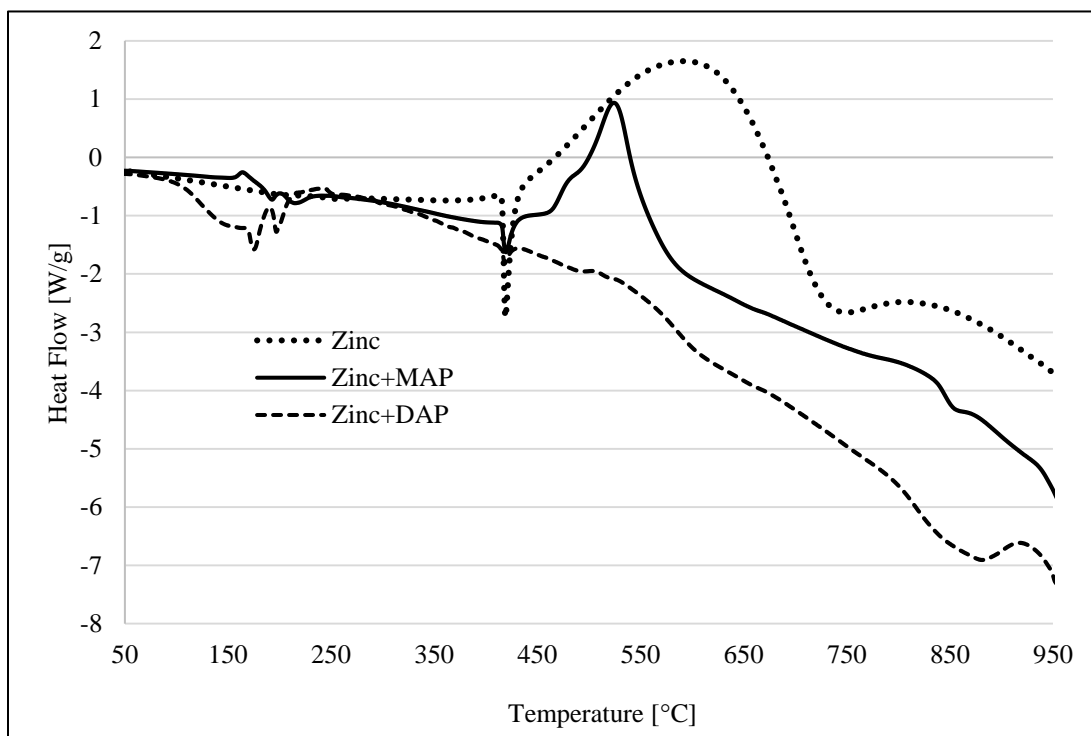

Figure C.10. Differential scanning calorimetry profile for zinc powder and zinc/phosphate inhibitor mixtures. Increase in temperature, from 50 to 950 °C, at a constant 10 °C/min heating rate (in air).
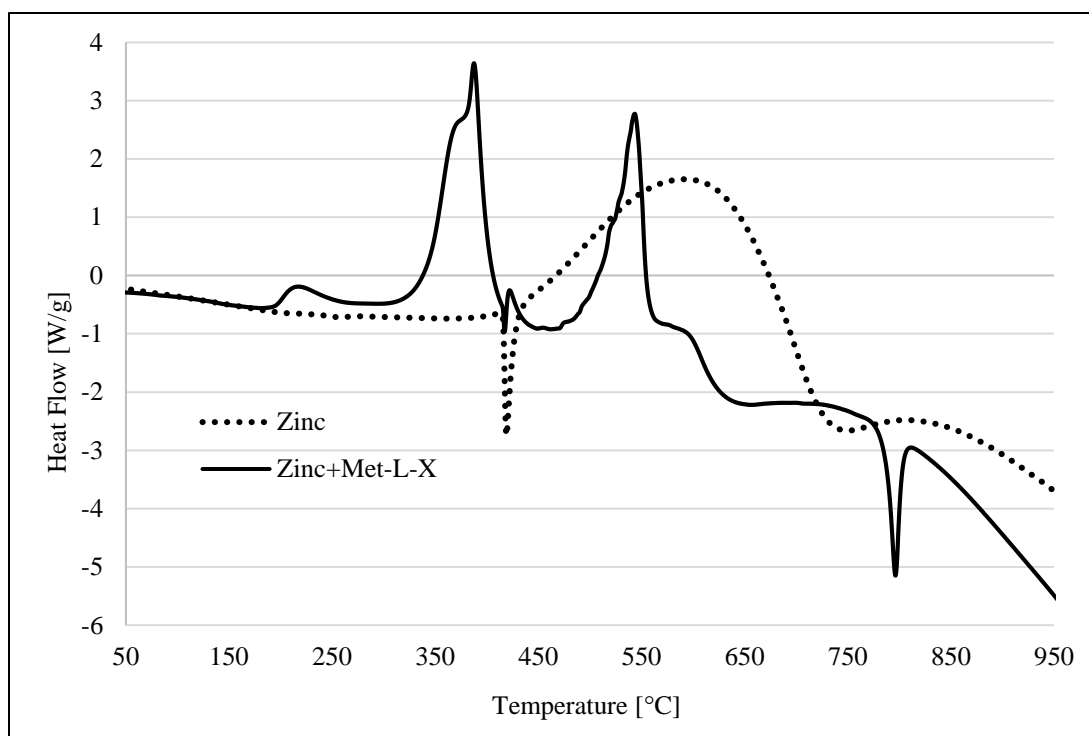
Figure C.11. Differential scanning calorimetry profile for zinc powder and zinc/Met-L-X inhibitor mixture. Increase in temperature, from 50 to 950 °C, at a constant 10 °C/min heating rate (in air).

Table C.1. Total heat released during decomposition of cornstarch and cornstarch/inhibitor mixtures; normalized integration of Figures C.6, C.7, and C.8, from room temperature to 800 °C.

Fuel/Inhibitor Mixture	Normalized DSC Curve Area [J/g]	Average Normalized Deviation [J/g]
CS	659	41
CS+SBC	-184	1
CS+PBC	-850	139
CS+MAP	528	1
CS+DAP	681	194
CS+Met-L-X	986	61

Table C.2. Total heat released during decomposition of zinc powder and zinc/inhibitor mixtures; integration of Figures C.9, C.10, and C.11 over the zinc liquid-phase combustion range (400 to 750 °C).

Fuel/Inhibitor Mixture	Σ(Peak Areas within Combustion Range) [J/g]	Average Deviation [J/g]
Zn	3617	433
Zn+SBC	1149	14
Zn+PBC	1342	49
Zn+MAP	806	84
Zn+DAP	203	46
Zn+Met-L-X	1243	41

Appendix D: Suppressant Agent Evolved Gas Analysis via Mass Spectrometry
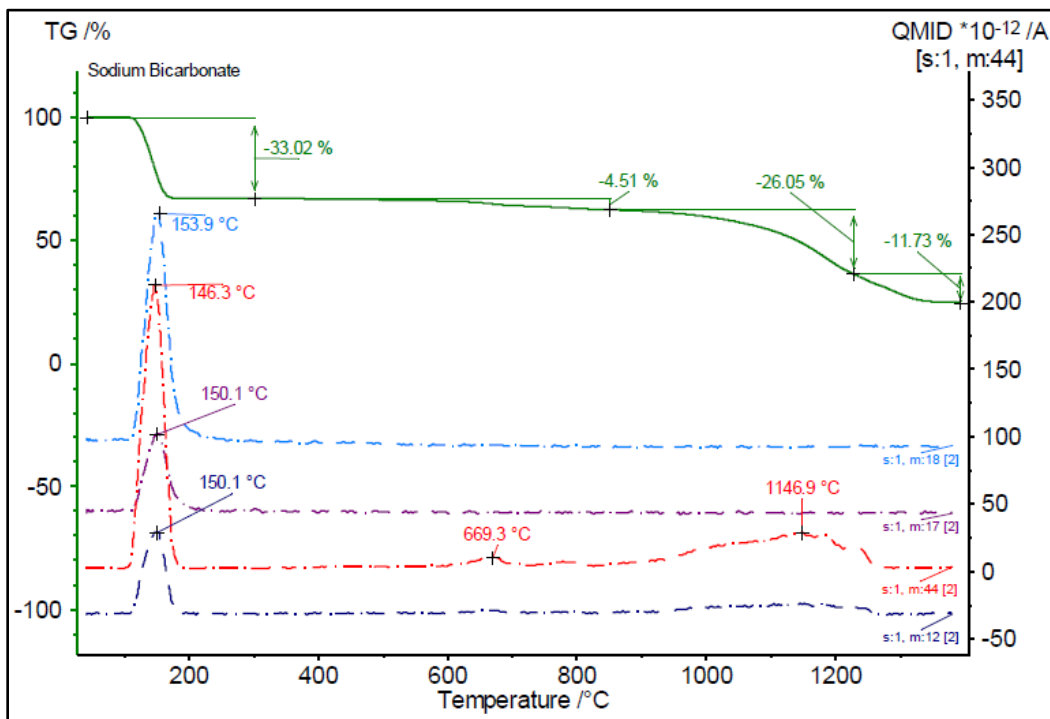

Figure D.1. TGA and MS ion-current curves for mass numbers 12, 17, 18, and 44 in SBC sample, heated from 40 to 1400 °C at 10 °C/min (in air).

Figure D.2. TGA and MS ion-current curves for mass numbers 12, 17, 18, and 44 in Met-L-X sample, heated from 40 to 1400 °C at 10 °C/min (in air).

Figure D.3. TGA and MS ion-current curves for mass numbers 35, 36, 37, and 38 in Met-L-X sample, heated from 40 to 1400 °C at 10 °C/min (in air).

Figure D.4. TGA and MS ion-current curves for mass numbers 70, 72, and 74 in Met-L-X sample, heated from 40 to 1400 °C at 10 °C/min (in air).

Figure D.5. TGA and MS ion-current curves for mass numbers 15, 17, 18, and 19 in MAP sample, heated from 40 to 1400 °C at 10 °C/min (in air).

Figure D.6. TGA and MS ion-current curves for mass numbers 30 and 44 in MAP sample, heated from 40 to 1400 °C at 10 °C/min (in air).

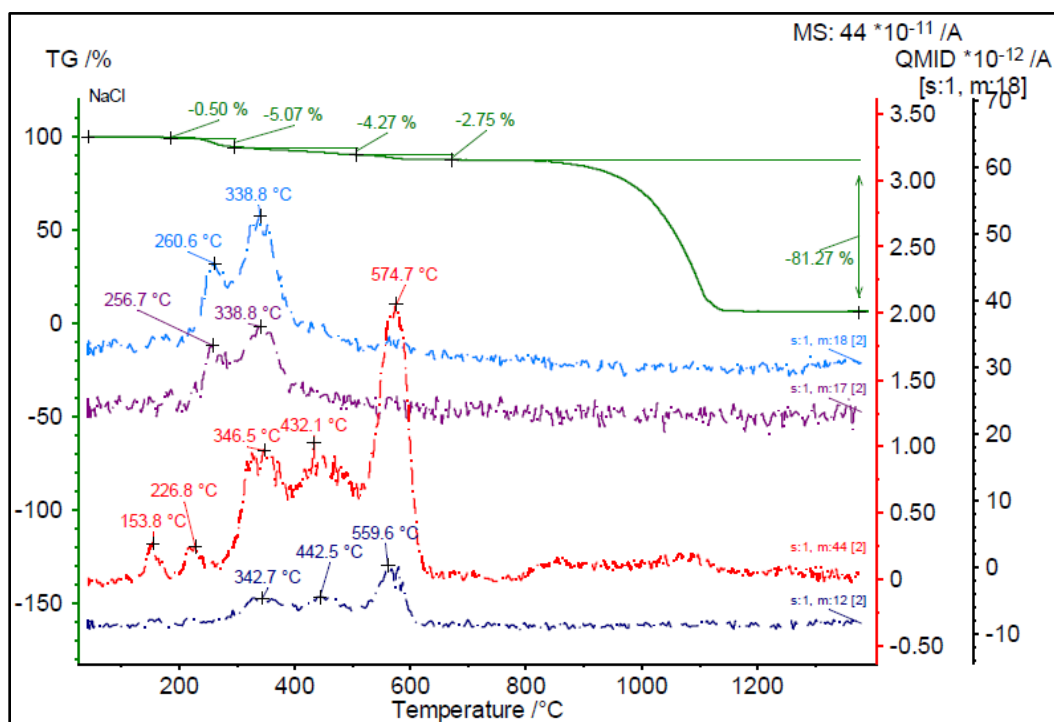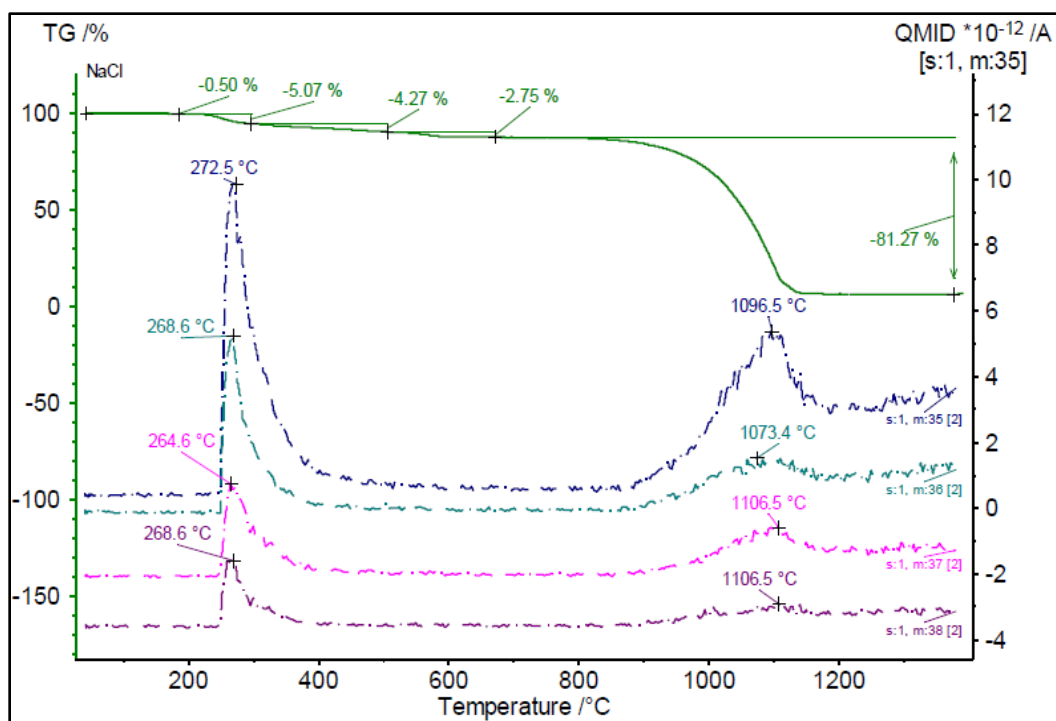**Figure D.7.** TGA and MS ion-current curves for mass numbers 35, 36, 48, and 64 in MAP sample, heated from 40 to 1400 °C at 10 °C/min (in air).
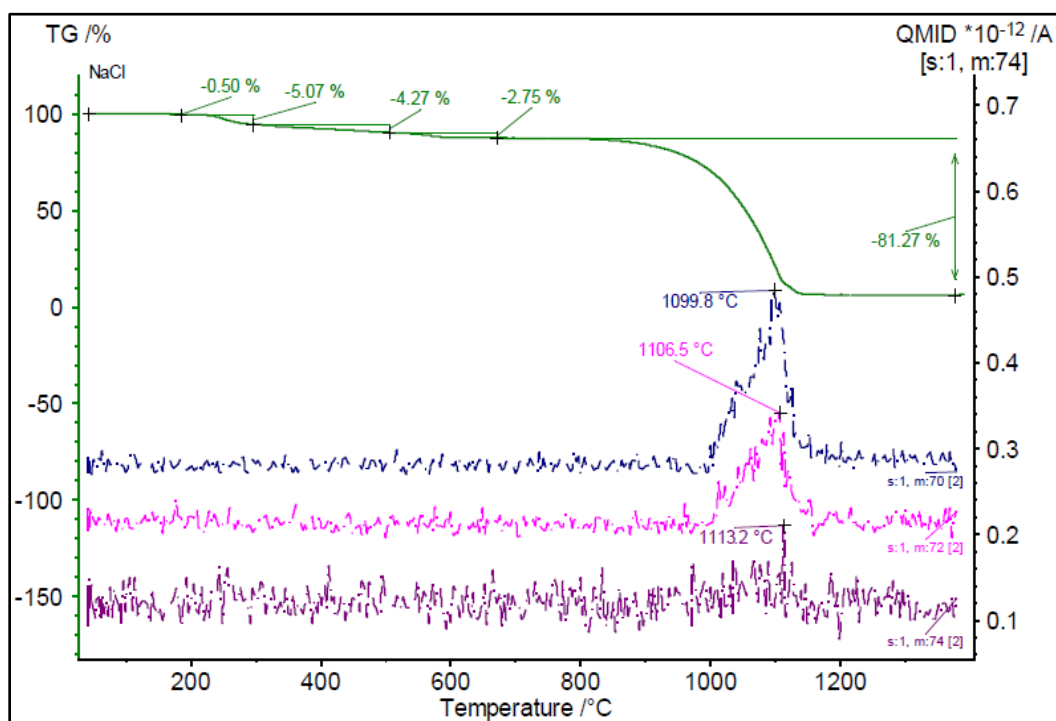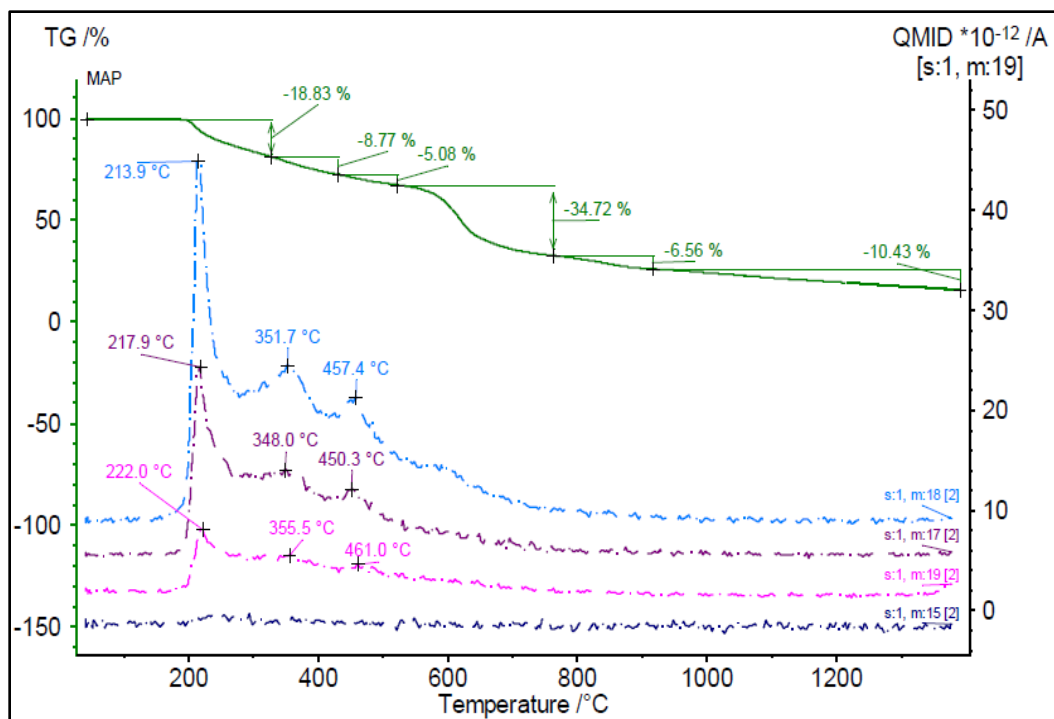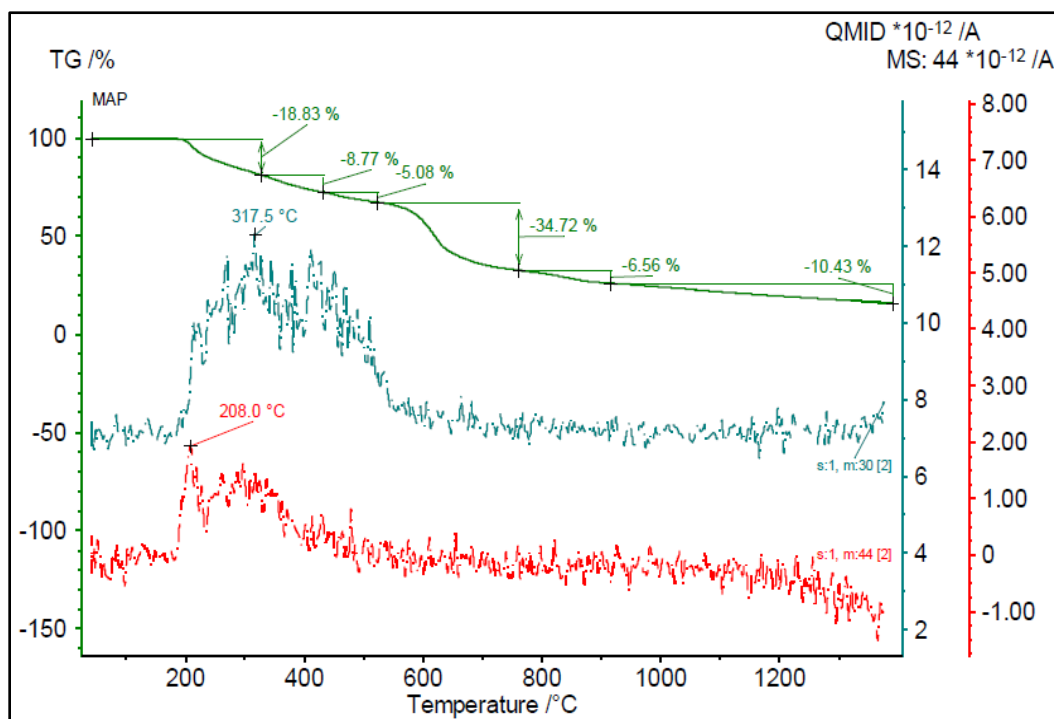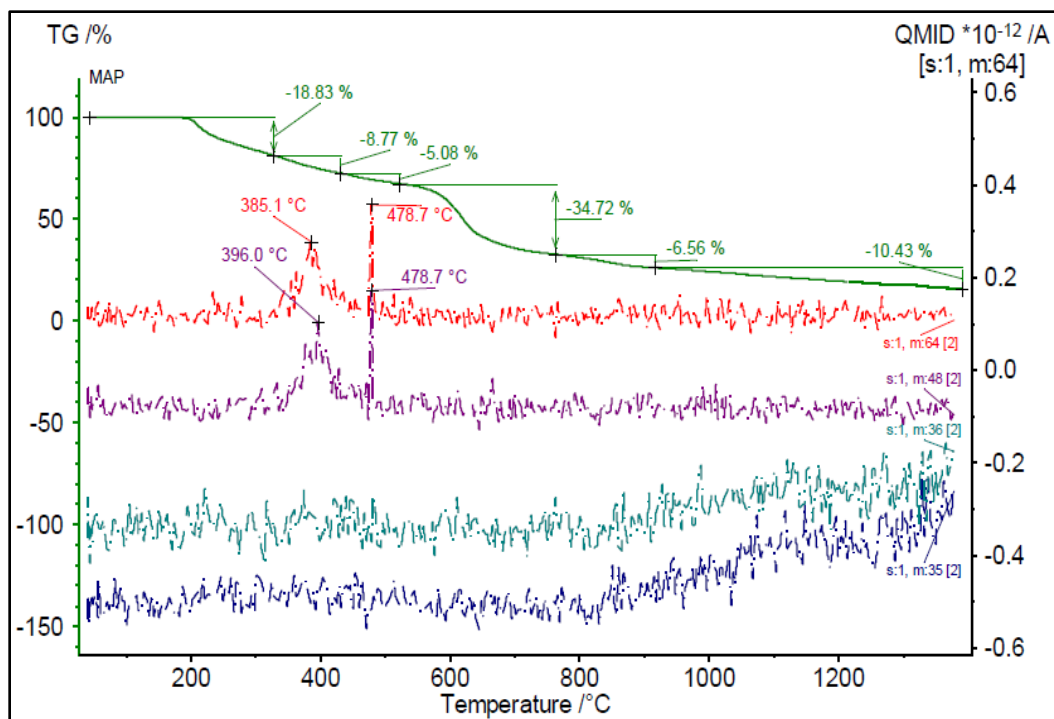
Appendix E: Open-Air Dispersion Data

Table E.1. Measured packed densities for all three suppressant agents, and agent fill weights during open-air dispersion testing.

Suppressant Material	Packed Density (kg/L)	Agent Fill Weight (kg)
SBC	1.33	9.07
Met-L-X	0.89	5.90
MAP	0.63	4.08

Table E.2. Average inverse velocity measurements (in imperial units for open-air dispersion testing, reported exclusively along the central plume axis (Track Point 2) with respect to previous frame (instantaneous) and custom origin (bulk) reference states.

Target Throw Distance (ft)	SBC (Test 1 & 1-R1, AVG)		Met-L-X (Test 2 & 2-R1, AVG)		MAP (Test 3 & 3-R1, AVG)	
	Instantaneous Inverse Velocity	Bulk Inverse Velocity	Instantaneous Inverse Velocity	Bulk Inverse Velocity	Instantaneous Inverse Velocity	Bulk Inverse Velocity
	Inverse Velocity (ms/ft)	Inverse Velocity (ms/ft)	Inverse Velocity (ms/ft)	Inverse Velocity (ms/ft)	Inverse Velocity (ms/ft)	Inverse Velocity (ms/ft)
3	1.95	1.88	2.10	1.93	1.86	1.81
6	5.50	3.11	5.76	3.20	8.12	3.38
9	7.81	4.99	7.39	4.55	10.45	5.13
12	7.65	5.44	8.64	5.48	11.24	6.71
15	8.89	5.96	9.87	6.27	16.81	7.64

Appendix F: Supplementary FLACS Analysis Data

Table F.1. Maximum overpressure in the small vessel, large vessel, and ductwork for various venting arrangements; suspended concentration of maize starch of 250 g/m^3 and ignition in the small vessel. Y/N indicates the presence (or lack thereof) of a relief panel (size: 800mm x 500 mm) on the interconnecting ductwork.

Simulation	Venting Arrangement [mm] [Small Vessel/Large Vessel/Ductwork]	Small Vessel [barg]	Large Vessel [barg]	Ductwork [barg]
1	Ø600/Ø1000/N	0.78	0.88	0.82
2	Ø600/Ø1000/Y	0.32	0.48	0.31
3	Ø600/Ø1200/Y	0.22	0.35	0.22
4	Ø600/Ø1400/Y	0.21	0.27	0.19

Table F.2. Maximum overpressure in the small vessel, large vessel, and ductwork for various venting arrangements; suspended concentration of maize starch of 250 g/m^3 and ignition in the large vessel. Y/N indicates the presence (or lack thereof) of a relief panel (size: 800mm x 500 mm) on the interconnecting ductwork.

Simulation	Venting Arrangement [mm] [Small Vessel/Large Vessel/Ductwork]	Small Vessel [barg]	Large Vessel [barg]	Ductwork [barg]
1	Ø600/Ø1000/N	0.90	0.71	0.70
2	Ø600/Ø1000/Y	0.40	0.24	0.21
3	Ø600/Ø1200/Y	0.32	0.16	0.15
4	Ø600/Ø1400/Y	0.27	0.12	0.11

Table F.3. Maximum overpressure in the small vessel, large vessel, and ductwork for various venting arrangements; suspended concentration of maize starch of 750 g/m^3 and ignition in the small vessel. Y/N indicates the presence (or lack thereof) of a relief panel (size: 800mm x 500 mm) on the interconnecting ductwork.

Simulation	Venting Arrangement [mm] [Small Vessel/Large Vessel/Ductwork]	Small Vessel [barg]	Large Vessel [barg]	Ductwork [barg]
1	Ø600/Ø1000/N	1.65	2.07	1.73
2	Ø600/Ø1000/Y	0.78	1.15	0.75
3	Ø800/Ø1200/Y	0.39	0.85	0.41
4	Ø800/Ø1400/Y	0.29	0.62	0.35
5	Ø800/Ø1600/Y	0.23	0.46	0.30
6	Ø1000/Ø1800/Y	0.15	0.31	0.21
7	Ø1000/Ø2000/Y	0.15	0.25	0.14

Table F.4. Maximum overpressure in the small vessel, large vessel, and ductwork for various venting arrangements; suspended concentration of maize starch of 750 g/m^3 and ignition in the large vessel. Y/N indicates the presence (or lack thereof) of a relief panel (size: 800mm x 500 mm) on the interconnecting ductwork.

Simulation	Venting Arrangement [mm] [Small Vessel/Large Vessel/Ductwork]	Small Vessel [barg]	Large Vessel [barg]	Ductwork [barg]
1	Ø600/Ø1000/N	2.33	1.61	1.48
2	Ø600/Ø1000/Y	1.30	0.79	0.64
3	Ø800/Ø1200/Y	0.87	0.46	0.42
4	Ø800/Ø1400/Y	0.75	0.30	0.30
5	Ø800/Ø1600/Y	0.62	0.17	0.24
6	Ø1000/Ø1800/Y	0.43	0.13	0.17
7	Ø1000/Ø2000/Y	0.41	0.13	0.13

Appendix G: Fluid-Particle Kinetics - Fractional Conversion Derivations

G.1. *Shrinking Unreacted Core Model (Constant Particle Size) – Chemical Reaction Control*

This derivation is in reference to Reaction R18 as the proposed stoichiometry for the heterogeneous gas/solid particle reaction of interest. The reaction extent is unaffected by the existence of external ash layer on the surface. The overall rate is directly proportional to the unit surface area of unreacted core of radius r_c. Under the assumption that reactant consumption rate is chemical reaction controlled, reactant disappearance rate can be expressed as follows:

(1)
$$-\frac{b}{4\pi r_c^2}\frac{dN_{O_2}}{dt} = -\frac{1}{4\pi r_c^2}\frac{dN_B}{dt} = bkC_{O_2}$$

where k is the first-order rate constant for the oxidation at the reaction surface and C_{O_2} is the oxygen concentration within the bulk fluid (remains constant as oxygen diffuses through gas film and ash layer). The decrease in moles of solid reactant B may be denoted using the particle density and a differential on the shrinking unreacted core volume, as follows:

(2)
$$dN_B = \rho_B dV = \rho_B d\left(\frac{4}{3}\pi r_c^3\right) = 4\pi\rho_B r_c^2 \cdot dr_c$$

Substitution of Equation 2 into Equation 1 yields:

(3)
$$-\rho_B\frac{dr_c}{dt} = bkC_{O_2}$$

With the assumption that available oxygen concentration on the surface is not a function of time, integration from initial unreacted core size R_o to an arbitrary final time t yields:

(4)
$$-\rho_B \int_{R_o}^{r_c} dr_c = bkC_{O_2}\int_0^t dt$$

Solving the above and isolating for time:

(5)
$$t = \frac{\rho_B}{bkC_{O_2}}[R_o - r_c]$$

Next, determine the time for full conversion of the solid particle τ, when $r_c = 0$:

(6)
$$\tau = \frac{\rho_B R_o}{bk C_{O_2}}$$

Dividing Equation 5 by Equation 6, the fractional conversion under chemical reaction limitation is directly related to the shrinking unreacted core radius and can be expressed as:

(7)
$$1 - X_B = \frac{volume\ of\ unreacted\ core}{volume\ of\ initial\ solid\ particle} = \left(\frac{r_c}{R_o}\right)^3$$

(8)
$$\frac{t}{\tau} = 1 - \frac{r_c}{R_o} = \mathbf{1 - [1 - X_B]^{1/3}}$$

where fractional conversion X_B represents the fraction of reactant B that has been converted to products (Levenspiel, 1999).

G.2. *Shrinking Unreacted Core Model (Constant Particle Size) – Gas Film Diffusion Control*

This derivation is in reference to Reaction R18 as the proposed stoichiometry for the heterogeneous gas/solid particle reaction of interest. During gas film diffusion control (and assuming that the oxidation is irreversible), there is zero oxygen content available at the particle surface. The overall rate is directly proportional to the surface area of the unreacted core of radius r_c. Reactant disappearance rate remains constant and can be expressed as follows:

(1)
$$-\frac{1}{A_{ext}}\frac{dN_B}{dt} = -\frac{1}{4\pi R_o{}^2}\frac{dN_B}{dt} = -\frac{b}{4\pi R_o{}^2}\frac{dN_{O_2}}{dt} = bk_g C_{O_2} = constant$$

where A_{ext} is the unchanging exterior particle surface area, R_o is the constant particle radius (including thickness of generated ash layer), and k_g is the mass transfer coefficient between bulk fluid phase and particle surface. The decrease in moles of solid reactant B may be denoted using the particle density and a differential on the unreacted core volume, as follows:

(2)
$$dN_B = \rho_B d\left(\frac{4}{3}\pi r_c^3\right) = 4\pi \rho_B r_c^2 \cdot dr_c$$

Substitution of Equation 2 into Equation 1 yields:

(3)
$$-\frac{1}{A_{ext}}\frac{dN_B}{dt} = -\rho_B \frac{r_c^2}{R_o^2}\frac{dr_c}{dt} = bk_g C_{O_2}$$

With the assumption that available oxygen concentration on the surface is not a function of time, integration from initial unreacted core size R_o to an arbitrary final time t yields:

(4)
$$-\frac{\rho_B}{R_o^2}\int_{R_o}^{r_c} r_c^2 dr_c = bk_g C_{O_2}\int_0^t dt$$

Solving the above and isolating for time:

(5)
$$t = \frac{\rho_B R_o}{3bk_g C_{O_2}}[1 - \left(\frac{r_c}{R_o}\right)^3]$$

Next, determine the time for full conversion of the solid particle τ, when $r_c = 0$:

(6)
$$\tau = \frac{\rho_B R_o}{3bk_g C_{O_2}}$$

Dividing Equation 5 by Equation 6, the fractional conversion with gas film diffusion limitation (and the assumption of constant particle size) is directly related to the shrinking unreacted core radius and can be expressed as:

(7)
$$1 - X_B = \frac{volume\ of\ unreacted\ core}{volume\ of\ initial\ solid\ particle} = \left(\frac{r_c}{R_o}\right)^3$$

(8)
$$\frac{t}{\tau} = 1 - \left(\frac{r_c}{R_o}\right)^3 = \boldsymbol{X_B}$$

where fractional conversion X_B represents the fraction of reactant B that has been converted to products (Levenspiel, 1999).

G.3. *Shrinking Unreacted Core Model (Constant Particle Size) – Ash Layer Diffusion Control*

This derivation is in reference to Reaction R18 as the proposed stoichiometry for the heterogeneous gas/solid particle reaction of interest. For gas/solid systems, begin by applying steady state assumption to define a constant rate of disappearance of oxygen relative to its diffusion rate (or flux Q) toward the reaction surface:

(1)
$$-\frac{dN_{O_2}}{dt} = 4\pi r^2 Q_{O_2} = 4\pi R_o{}^2 Q_{O_2,surface} = 4\pi r_c{}^2 Q_{O_2,core} = constant$$

Next, define the flux of oxygen at any location within the ash layer using Fick's law for equimolar counter-diffusion, where D_A signifies the effective diffusion coefficient of oxygen during transport through the ash product layer:

(2)
$$Q_{O_2} = D_A \frac{dC}{dr}$$

Combining Equations 1 and 2:

(3)
$$-\frac{dN_{O_2}}{dt} = 4\pi r^2 D_A \frac{dC}{dr} = constant$$

Upon integration across the ash layer thickness, from R_o to r_c:

(4)
$$-\frac{dN_{O_2}}{dt} \int_{R_o}^{r_c} \frac{dr}{r^2} = 4\pi D_A \int_{C_{O_2}}^{0} dC$$

(5)
$$-\frac{dN_{O_2}}{dt} \left[\frac{1}{r_c} - \frac{1}{R_o} \right] = 4\pi D_A C_{O_2}$$

Consider an unreacted core changing size with time:

(6)
$$-\rho_B \int_{R_o}^{r_c} \left(\frac{1}{r_c} - \frac{1}{R_o} \right) r_c^2 dr_c = b D_A C_{O_2} \int_0^t dt$$

Solving the above and isolating for time:

(7)
$$t = \frac{\rho_B R_o{}^2}{6 b D_A C_{O_2}} \left[1 - 3 \left(\frac{r_c}{R_o} \right)^2 + 2 \left(\frac{r_c}{R_o} \right)^3 \right]$$

Next, determine the time for full conversion of the solid particle τ, when $r_c = 0$:

(8)
$$\tau = \frac{\rho_B R_o{}^2}{6 b D_A C_{O_2}}$$

Dividing Equation 7 by Equation 8, the fractional conversion with ash layer diffusion limitation is directly related to the shrinking unreacted core radius and can be expressed as:

(9)
$$\frac{t}{\tau} = 1 - 3 \left(\frac{r_c}{R_o} \right)^2 + 2 \left(\frac{r_c}{R_o} \right)^3 = 1 - 3(1 - X_B)^{2/3} + 2(1 - X_B)$$

where fractional conversion X_B represents the fraction of reactant B that has been converted to products (Levenspiel, 1999).

G.4. *Shrinking Particle Model (Non-Constant Particle Size) – Gas Film Diffusion Control*

This derivation is in reference to Reaction R18 as the proposed stoichiometry for the heterogeneous gas/solid particle reaction of interest. At any intermediate particle size r, the decrease in moles of solid reactant B may be denoted using the particle density and a differential on the particle volume:

(1) $$dN_B = \rho_B dV = 4\pi\rho_B r^2 \cdot dr$$

Comparable to the expressions used during gas film diffusion control under constant particle size assumption (shrinking unreacted core theory), reactant disappearance rate may be expressed as follows:

(2) $$\frac{1}{A_{ext}}\frac{dN_B}{dt} = \frac{\rho_B 4\pi r^2}{4\pi r^2}\frac{dr}{dt} = \rho_B\frac{dr}{dt} = bk_g C_{O_2}$$

For small particles in the Stokes Regime, correlations for mass transfer coefficient k_g reduce to the following form, reliant on the effective diffusivity D_f of oxygen transport through the external gas film to the particle surface:

(3) $$k_g = \frac{D_f}{r}$$

Combining Equations 2 and 3, integration from initial particle size R_o to an arbitrary final time t yields:

(4) $$\int_{R_o}^{r} r\, dr = \frac{bD_f C_{O_2}}{\rho_B}\int_0^t dt$$

Solving the above and isolating for time:

$$(5) \qquad t = \frac{\rho_B R_o{}^2}{2bD_f C_{O_2}} \left[1 - \left(\frac{r}{R_o}\right)^2\right]$$

Next, determine the time for complete disappearance of the solid particle τ, when $r = 0$:

$$(6) \qquad \tau = \frac{\rho_B R_o{}^2}{2bD_f C_{O_2}}$$

Dividing Equation 5 by Equation 6, the fractional conversion (assuming non-constant particle size and Stokes Regime for small particles) with gas film diffusion limitation is directly related to the shrinking particle radius and can be expressed as:

$$(8) \qquad \frac{t}{\tau} = 1 - \left(\frac{r}{R_o}\right)^2 = 1 - (1 - X_B)^{2/3}$$

where fractional conversion X_B represents the fraction of reactant B that has been converted to products (Levenspiel, 1999).